

Über die Beeinflussung der elektronischen Eigenschaften offenschaliger Komplexe der Gruppe 10 Metalle eines 1,4- Terphenyldithiophenolat-Liganden

Dissertation

der Mathematisch-Naturwissenschaftlichen Fakultät

der Eberhard Karls Universität Tübingen

zur Erlangung des Grades eines

Doktors der Naturwissenschaften

(Dr. rer. nat.)

vorgelegt von

Dipl.-Chem. Nicole Michaela Mews

aus Bad Friedrichshall

Tübingen

2019

Gedruckt mit Genehmigung der Mathematisch-Naturwissenschaftlichen Fakultät der Eberhard Karls Universität Tübingen.

Tag der mündlichen Qualifikation: 21.08.2019

Dekan: Prof. Dr. Wolfgang Rosenstiel

1. Berichterstatter Prof. Dr. Doris Kunz

2. Berichterstatter PD Dr. Andreas Berkefeld

Vorwort

Diese Arbeit wird zur Erlangung des Doktorgrades rerum naturalis (Dr. rer. nat.) in Chemie an der Universität Tübingen eingereicht. Sie entstand im Zeitraum Oktober 2015 bis Juni 2019 unter der Aufsicht von PD Dr. Andreas Berkefeld. Die Finanzierung erfolgte durch das Eliteprogramm für Postdoktoranden der Baden-Württemberg-Stiftung.

Die folgende Arbeit beinhaltet eine Einführung in die Eigenschaften von offenschaligen Ligand-Radikal-Komplexen, eine Zusammenfassung der Ergebnisse und die daraus resultierenden Veröffentlichungen.

Teile dieser Arbeit wurden auf nationalen und internationalen Konferenzen und Treffen in Vorträgen und in Poster-Beiträgen präsentiert.

Danksagung

Mein besonderer Dank gilt PD Dr. Andreas Berkefeld, der mir die Möglichkeit gab sowohl meine Diplomarbeit als auch meine Promotion in seinem Arbeitskreis durchführen zu können. Unter seiner Anleitung und sein Wissen habe ich mehr über Synthese und analytische Methoden gelernt als irgendwo sonst. Ich möchte mich auch für die Unterstützung und Möglichkeit meine Ergebnisse auf Konferenzen im In- und Ausland vorstellen zu dürfen bedanken.

Prof. Dr. Reiner Anwander möchte ich besonders danken für die Möglichkeit meine Ergebnisse sowohl im Seminar als auch bei den jährlichen Gruppenausflügen vorstellen zu dürfen.

Besonders danken möchte ich auch Prof. Dr. Holger Bettinger und Dr. Markus Scheele für die Möglichkeit ihre UV/Vis/NIR-Spektrometer nutzen zu dürfen. Ohne diese Messungen wäre diese Arbeit nicht möglich gewesen.

Andreas Früh und Prof. Dr. Thomas Chassé danke ich für die Möglichkeit und Hilfe Raman- und Einkristall-IR-Messungen durchführen zu können.

Den Arbeitsgruppen Wesemann und Mayer möchte ich für die herzliche Aufnahme in ihren Laboren und die Bereitstellung von Chemikalien und Gerätschaften danken.

Bei der Anwander-Gruppe möchte ich mich bedanken für die konstruktiven Diskussionen und die schönen Gruppen-Aktivitäten.

Auch möchte ich bei allen Bewohnern der Ebene 7 für die tolle Arbeitsatmosphäre und wundervolle Zeit bedanken.

Simon Schundelmeier und Prof. Dr. Bernd Speiser danke ich für Einführung in die Cyclovoltammetrie, die anregenden Diskussionen und die Hilfe beim Aufbau einer eigenen Cyclovoltammetrie-Messeinheit.

Gerald Hörner und Mark Reimann danke ich für die Durchführung und Analyse der theoretischen Berechnungen.

Hartmut Schubert danke ich für die Durchführung der Einkristallstruktur-Analyse.

Dr. Klaus Eichele, Kristina Strohmeier, Priska Kolb und Paul Schuler danke ich für die Bereitstellung und Wartung der NMR-Geräte und Ausführen von nicht-standard NMR-

Messungen. Auch möchte ich Paul Schuler für die Durchführung der ESR-Messungen und konstruktiven Vorschlägen danken.

Dr. Dorothee Wistuba und Wolfgang Bock möchte ich für die Ausführung der hochauflösenden Massenspektrometrie und der Elementaranalyse danken.

Den Metall- und Elektronik-Werkstätten sowie der Glasbläserei möchte ich für die schnelle Hilfe bei akuten Problemen und konstruktiven Vorschläge bei Langzeitprojekten danken.

Ich möchte meinen Modulpraktikanten, vor allem Annika Stetter, für die konstruktive Zusammenarbeit und für den Beitrag zur dieser Arbeit danken.

Ein besonderer Dank geht an die Fachschaft Chemie WS07/08 bis SoSe09 für die wundervolle Zeit, die ich mit Euch verbringen durfte. Ich werde Euch nie vergessen.

Mareike Binder danke ich für die moralische Unterstützung und die tolle Zeit in Japan.

Dennis Meisel möchte ich von ganzem Herzen für die wundervollen und anregenden Diskussionen am frühen Morgen, wenn sonst noch keiner im Labor ist, danken.

Felix Koch danke ich für den wundervollen Zusammenhalt in der doch kleinen Arbeitsgruppe und die anregenden Diskussionen.

Besonders möchte ich bei meiner Familie bedanken ohne deren Unterstützung meine Chemiestudium und die Promotion nicht möglich gewesen wäre. Ganz besonders danke ich meinen Eltern, die bei jeder meiner Entscheidungen hinter mir stehen trotz ihrer getrennten Lebenswege.

Andree, ich danke dir für die Unterstützung auch in den schwersten Zeiten und für die wunderschönen Momente, die wir zusammen schon erleben durften.

Vorwort	I
Danksagung	II
Abkürzungen	V
Abstract	VI
Zusammenfassung	VII
Publikationen	VIII
Beiträge	X
1. Einleitung	1
2. Zielsetzung	12
3. Ergebnisse und Diskussion	13
3.1. Publikation I: Controlling Near-Infrared Chromophore Electronic Properties through Metal-Ligand Orbital Alignment	13
3.2. Publikation II: Tuning of Thiyl/Thiolate Complex Near-Infrared Chromophores of Platinum through Geometrical Constraints	16
3.3. Publikation III: Influencing Factors on the Electronic Structures of Complex Radical- Ligand Ions of Group 10 Metal Triad	20
4. Schlussfolgerung	23
5. Literatur	26
Publikationen I-III	30

Abkürzungen

BArF ⁻	Tetrakis[3,5-bis(trifluoromethyl)phenyl]borat
bpy	2,2'-Bipyridin
CR	Charge-Resonanz
CV	Cyclovoltammetrie
cw	continuous wave
Cy	Cyclohexyl
DMF	Dimethylformamid
ESR	Elektronen-Spin-Resonanz
Fc	Ferrocen
Fc''	1,1'-Diacetylferrocen
L	Ligand
LLIVCT	Ligand-Ligand-Intervalenz-Charge-Transfer
M	Metall
Me	Methyl
Mes	Mesityl
NIR	Nah-Infrarot
NMR	Kern-Magnet-Resonanz
NTf ₂ ⁻	Bis-trifluormethansulfonimid
Ph	Phenyl
py	Pyridin
^t Bu	<i>tert</i> -Butyl
UV/vis	Ultraviolett/Sichtbar
VT	Variable Temperatur
XRD	Röntgendiffraktion

Abstract

Due to their extraordinary electronic and chemical properties, ligand-centered radical complexes are of particular interest in the development of novel materials such as catalysts^[1] and NIR chromophores^[2] and in the elucidation of biological processes^[3]. In the class of non-innocent ligand complexes sulfur-centered radical complexes are of special interest. Due to the strong admixture of sulfur to the metal orbitals in the case of transition metals^[4] and due to its weak +M effect^[5] in thiolates, the boundary between ligand and metal-centered radicals in oxidized bisdithiolate systems becomes blurred. This makes them excellent systems for investigating the metal-ligand interaction. The interaction can be influenced by the geometry as well as by the electronic structure. Unfortunately, the amount of such isolated and crystallographically investigated thiol/thiolate complexes is small.^[6] Due to the *cis*-dithiolate ligand used, the complexes are both limited in their geometric arrangement and highly symmetrical, so that the geometric parameter is difficult to investigate.

In this work, 1,4-terphenyldithiophenolate ligands were used to achieve and isolate for the first time a pure *trans*-position of the thiolates in a cationic radical complex of group 10 metals. The used ligand offers a flexible third coordination site by the bridging system of the terphenyl unit. The binding to the π -system can be controlled by the number of co-ligands and thus indirectly influences the geometric position of the metal coordination sphere. Due to the variation of the metal, the tilting of the metal coordination plane and the steric interaction between main and co-ligand, it is now possible to investigate the interaction between geometric and electronic parameters and their effects on the metal-ligand interaction. In particular, the NIR absorption band has shown that the electronic properties of the system can be strongly influenced by even the smallest geometric changes and that the electronic structure of the metal plays a decisive role in the development of these properties.

Through this work, it is now possible to better estimate the influence of steric and electronic factors and their interaction on the properties of radical complexes. This contributes to the understanding of catalytic systems in nature and in industry

Zusammenfassung

Ligand-zentrierte Radikal-Komplexe sind durch ihre außergewöhnlichen elektronischen und chemischen Eigenschaften in der Entwicklung von neuartigen Materialien wie Katalysatoren^[1] und NIR-Chromophoren^[2] und bei der Aufklärung von biologischen Prozessen^[3] von besonderem Interesse. Dabei stellen Schwefel-zentrierte Radikal-Komplexe eine Besonderheit dar. Durch die starke Mischung zwischen Schwefel- und Metallorbitalen im Falle der Übergangsmetalle^[4] und auf Grund seines schwachen +M-Effekts^[5] in Thiolaten verschwimmt in oxidierten Bisdithiolat-Systemen die Grenze zwischen Ligand- und Metall-zentriertem Radikal. Dies macht sie zu hervorragenden Systemen um die Metall-Ligand-Wechselwirkung zu untersuchen. Dabei kann die Wechselwirkung sowohl durch die Geometrie als auch durch die elektronische Struktur beeinflusst werden. Leider ist die Zahl solcher isolierten und kristallographisch untersuchten Thiyl/Thiolat-Komplexe gering.^[6] Durch den eingesetzten Liganden mit *cis*-ständigen Thiolaten sind die Komplexe sowohl in ihrer geometrischen Anordnung beschränkt als auch hoch symmetrisch, so dass der geometrische Parameter nur schwer untersuchbar ist.

In dieser Arbeit konnte mit Hilfe von 1,4-Terphenyldithiophenolat-Liganden zum ersten Mal eine reine *trans*-Stellung der Thiole in einem kationischen Radikal-Komplex der Gruppe 10 Metalle erreicht und isoliert werden. Dabei bietet der eingesetzte Ligand eine flexible dritte Koordinationsstelle durch das verbrückende π -System der Terphenyl-Einheit an. Die Bindung zum π -System kann dabei durch die Anzahl der Co-Liganden gesteuert werden und beeinflusst damit indirekt die Lage der Metall-Koordinationssebene. Durch die Variation des Metalls, der Verkipfung der Metall-Koordinationssebene und die sterische Wechselwirkung zwischen Haupt- und Co-Ligand ist es nun möglich das Zusammenspiel zwischen geometrischem und elektronischem Parameter und deren Auswirkungen auf die Metall-Ligand-Wechselwirkung zu untersuchen. Dabei hat sich besonderes in der Lage der NIR-Absorptionsbande gezeigt, dass sich das System schon durch kleinste geometrische Änderungen stark in seinen elektronischen Eigenschaften beeinflussen lässt und die elektronische Struktur des Metalls eine entscheidende Rolle bei der Ausprägung dieser Eigenschaften spielt.

Durch diese Arbeit ist es nun möglich den Einfluss von sterischen und elektronischen Faktoren und deren Zusammenspiel auf die Eigenschaften von Radikal-Komplexen besser einschätzen zu können. Sie leistet damit einen Beitrag zum Verständnis der katalytischen Systeme in der Natur und Industrie.

Publikationen

Veröffentlichungen

- Publikation I Mews, N. M.; Berkefeld, A.; Hörner, G.; Schubert, H., Controlling Near-Infrared Chromophore Electronic Properties through Metal-Ligand Orbital Alignment, *J. Am. Chem. Soc.* **2017**, *139*, 2808
- Publikation II Mews, N. M.; Hörner, G.; Schubert, H.; Berkefeld, A., Tuning of Thiyl/Thiolate Complex Near-Infrared Chromophores of Platinum through Geometrical Constraints, *Inorg. Chem.* **2018**, *57*, 9670
- Publikation III Mews, N. M.; Reimann, M.; Hörner, G.; Schubert, H.; Berkefeld, A., Influencing Factors on the Electronic Structures of Complex Radical-Ligand Ions of the Group 10 Metal Triad, unveröffentlichtes Manuskript

Posterpräsentationen

- Poster I Mews, N. M.; Berkefeld, A.; Hörner, G.; Schubert, H., Synthesis and Redox-Properties of Group 10 Metal Complexes from a 4-Terphenyldithiophenol Ligand, *6th EuChemMS Chemistry Congress*, Sevilla, 11.-15. September, **2016**
- Poster II Mews, N. M.; Berkefeld, A.; Hörner, G.; Schubert, H., Über die Eigenschaften von Komplexen des Platins eines gemischt-valenten 1,4-Terphenyldithiophenol-Liganden, *13. Koordinationschemie-Treffen*, Potsdam, 5.-7. März, **2017**
- Poster III Mews, N. M.; Hörner, G.; Schubert, H.; Berkefeld, A., How to Fine Tune the Electronic Properties of Radical-Ligand-Complexes, *19. Tagung der Wöhler-Vereinigung*, Regensburg, 24.-27. September, **2018**

Vorträge

- Vortrag I Mews, N. M.; Berkefeld, A.; Hörner, G.; Schubert, H., Redox Non-Innocent Behaviour of 1,4-Terphenyldithiolato Ligands of Platinum Complexes, *3. Inorganic Chemistry Conference Erlangen*, Erlangen, 5.-8. September, **2017**
- Vortrag II Mews, N. M.; Berkefeld, A.; Hörner, G.; Schubert, H., Über den Einfluss der Koordinationsgeometrie auf die elektronischen Eigenschaften von NIR-chromophoren Ligand-Radikal-Komplexen des Platins, *14. Koordinationschemie-Treffen*, Heidelberg, 11.-13. März, **2018**
- Vortrag III Mews, N. M.; Hörner, G.; Schubert, H.; Berkefeld, A., Steuerung der Eigenschaften von Gruppe-10-Metall-Komplexen eines radikalischen Thiophenolato-Liganden, *Anorganisch-Chemisches Kolloquium*, Tübingen, 7. Mai, **2018**
- Vortrag IV Mews, N. M.; Hörner, G.; Schubert, H.; Berkefeld, A.; How to Fine Tune the Electronic Properties of Radical-Ligand-Complexes (Kurzvortrag), *19. Tagung der Wöhler-Vereinigung*, Regensburg, 24.-27. September, **2018**

Beiträge

Publikation I: Controlling Near-Infrared Chromophore Electronic Properties through Metal-Ligand Orbital Alignment

Synthesen und Analysen wurden von mir geplant und ausgeführt. Die analytischen Methoden umfassen 1D- und 2D-NMR- (^1H , $^{13}\text{C}\{^1\text{H}\}$, ^{31}P , ^{135}Pt , ^1H , ^{13}C -HSQC, ^1H , ^{13}C -HMBC), CV-, X-Band cw-ESR- und VT-UV/vis/NIR-Messungen. Die Elementaranalysen wurden von Wolfgang Bock und die HR-ESI-MS von Dr. Dorothee Wistuba durchgeführt. Die Publikation beinhaltet sowohl die Synthesevorschriften für die Platin-Komplexe mit den Co-Liganden PPh_3 und PMe_3 , die in meiner Diplomarbeit etabliert und dieser Doktorarbeit optimiert wurden, als auch die in meiner Diplomarbeit durchgeführten CV-Messungen. Die theoretischen Berechnungen wurden von Dr. Gerald Hörner ausgeführt und interpretiert. Die Kristallstruktur-Analysen von Einkristall-Röntgendiffraktometrischen Messungen wurden von Dr. Hartmut Schubert durchgeführt. Die Publikation wurde gemeinsam mit PD Dr. Andreas Berkefeld, Dr. Gerald Hörner und mir verfasst.

Publikation II: Tuning of Thiyl/Thiolate Complex Near-Infrared Chromophores of Platinum through Geometrical Constraints

Synthesen und Analysen wurden von mir geplant und ausgeführt. Die analytischen Methoden umfassen 1D- und 2D-NMR- (^1H , $^{13}\text{C}\{^1\text{H}\}$, ^{31}P , ^{135}Pt , ^1H , ^{13}C -HSQC, ^1H , ^{13}C -HMBC), CV-, X-Band cw-ESR-, IR- und VT-UV/vis/NIR-Messungen. Die Elementaranalysen wurden von Wolfgang Bock durchgeführt. Die theoretischen Berechnungen wurden von Dr. Gerald Hörner ausgeführt und interpretiert. Die Kristallstruktur-Analysen von Einkristall-Röntgendiffraktometrischen Messungen wurden von Dr. Hartmut Schubert durchgeführt. Die Publikation wurde gemeinsam mit PD Dr. Andreas Berkefeld, Dr. Gerald Hörner und mir geschrieben.

Publikation III: Influencing Factors on the Electronic Structures of Complex Radical-Ligand Ions of the Group 10 Metal Triad

Synthesen und Analysen wurden von mir geplant und ausgeführt. Die analytischen Methoden umfassen 1D- und 2D-NMR- (^1H , $^{13}\text{C}\{^1\text{H}\}$, ^{31}P , ^{135}Pt , ^1H , ^{13}C -HSQC, ^1H , ^{13}C -HMBC), CV-, X-Band cw-ESR-, IR- und VT-UV/vis/NIR-Messungen. Die Elementaranalysen wurden von Wolfgang Bock durchgeführt. Die Publikation beinhaltet sowohl die Synthesevorschriften für $^{\text{Mes}}\text{Pd-R}$ ($\text{R} = \text{PPh}_3$, PCy_3), die in meiner Diplomarbeit und im Rahmen meines Modulpraktikums eingeführt und in dieser Doktorarbeit verfeinert wurden als auch die elektrochemische Untersuchung von $^{\text{Mes}}\text{Pd-Ph}$ aus meiner Diplomarbeit. Die DOSY-Messungen und deren Auswertungen wurden von PD Dr. Andreas Berkefeld durchgeführt. Die theoretischen Berechnungen wurden von Mark Reimann und von Dr. Gerald Hörner ausgeführt und interpretiert. Die Kristallstruktur-Analysen von Einkristall-Röntgendiffraktometrischen Messungen wurden von Dr. Hartmut Schubert durchgeführt. Der Text der Veröffentlichung wurde gemeinsam mit Mark Reimann, PD Dr. Andreas Berkefeld, Dr. Gerald Hörner und mir geschrieben.

1. Einleitung

Liganden, die an Redoxreaktionen in einem Metallkomplex beteiligt sind und dabei eine eindeutige Bestimmung der Oxidationszahlen im Komplex nicht mehr ermöglichen, galten vor den 1960er Jahren als Kuriosität.^[7] Mit der Entwicklung der ESR-Spektroskopie und der Etablierung von theoretischen Berechnungen gelang es in den 1960ern am Beispiel von Bisdithiolato-Komplexen der Übergangsmetalle zu zeigen, dass die Oxidationen dieser Komplexe hauptsächlich Ligand-zentriert sind.^[8] Dies entfachte einen regen Diskurs darüber, welche weiteren Liganden bevorzugt oxidiert werden^[9], dieser flaute jedoch in den 1970ern wieder ab.

Mit der Untersuchung von aktiven Zentren in Enzymen, biologischen Transport-Systemen und der Photosynthese wurde schnell klar, dass die Fähigkeit eines Komplexes sowohl die Liganden als auch das Metall an Redoxsystemen teilhaben zu lassen eine entscheidende Rolle in den biologischen Prozessen spielt.^[3a,3b,10] Bekannte Beispiele sind das Oxyhäm-System^[11], die Cu-S-Einheit in Plastocyanin^[3b,3d] und NO^{*} in Guanylyl-Cyclasen^[12]. Auch bei der Reaktivität von synthetischen Katalysatoren spielt diese Eigenschaft eine entscheidende Rolle.^[1b-e,13] Ein Beispiel dafür ist der Knölker-Katalysator, der an das aktive Zentrum von eisenhaltigen Hydrogenasen erinnert. Für die katalytische Hydrierung von Aldehyden und Ketonen zu primären und sekundären Alkoholen ist die Fähigkeit des Cyclopentadienon-Liganden als Elektronenreservoir die Reduktion von Fe^{II} zu Fe⁰ zu ermöglichen entscheidend für den Katalysezyklus.^[1b]

Isolierte Ligand-zentrierte Radikal-Komplexe zeigen dabei außergewöhnliche elektronische^[14] und magnetische^[15] Eigenschaften, die für die Anwendung als Molekül-Magnete^[15-16] oder als Elektronen-Loch-Leiter^[17] entscheidend sind. Die für ein Ligand-Radikal typische NIR-Absorption findet sowohl in der Telekommunikation als auch in der Medizin Anwendung.^[2a,2b,2d,2e] Darüber hinaus sind redoxaktive Liganden ein wichtiger Baustein in der Darstellung von Biomimetika^[3a,3e,3g,10b,18]. Durch dieses breite Anwendungsspektrum sind Ligand-zentrierte Radikal-Komplexe für die Forschung von besonderem Interesse.^[19] Um die Eigenschaften offenschaliger Komplexe gezielt beeinflussen zu können, ist ein tiefes Verständnis der Metall-Ligand-Wechselwirkung entscheidend. Denn ab wann verhält sich ein Ligand redoxaktiv? Ist dies immer der Fall oder kann dies gezielt gesteuert werden? Dies sind zentrale Fragen bei der Entwicklung neuer offenschaliger Komplexe.

Nicht-unschuldige Liganden

Die Definition des unschuldigen Liganden führte Jørgensen 1966 ein. Wobei Liganden dann als unschuldig gelten, wenn sie die Bestimmung der Oxidationszahlen des Zentralatoms erlauben.^[20] Dies impliziert, dass nicht-unschuldige oder „verdächtige“ Liganden redoxaktiv sein müssen. Aus der Weiterentwicklung der analytischen Methoden, vor allem auf dem Gebiet der Röntgenabsorptionsspektroskopie und der Röntgendiffraktometrie, sowie der Verfeinerung der theoretischen Berechnungen, ergab sich, dass der Ort, an dem die Oxidation in einem Komplex stattfindet, vor allem von der Zusammensetzung der Grenzorbitale abhängt.^[21] Liegen die Metall-Orbitale energetisch höher als die des Liganden und ist die Energiedifferenz ΔE zwischen den beiden groß, so wird ausschließlich das Metall oxidiert (Abbildung 1, links). Dreht sich das Verhältnis um, so ist die Oxidation Ligand-zentriert und man spricht von einem inversen Bindungsschema (Abbildung 1, rechts).^[21a] Dabei hängen die Kovalenz der Bindung, ausgedrückt durch die Energiedifferenz ΔE , und die Orbitalenergien sowohl von der elektronischen Struktur des Metalls als auch von der Art des Liganden ab. So können Veränderungen am Liganden oder der Austausch des Metalls dazu führen, dass auch redoxaktive Liganden unschuldiges Verhalten zeigen können (Abbildung 1, rote Pfeile). Dies berücksichtigen Ward und McCleverty in ihrer Definition von nicht-unschuldigem Verhalten.^[22]

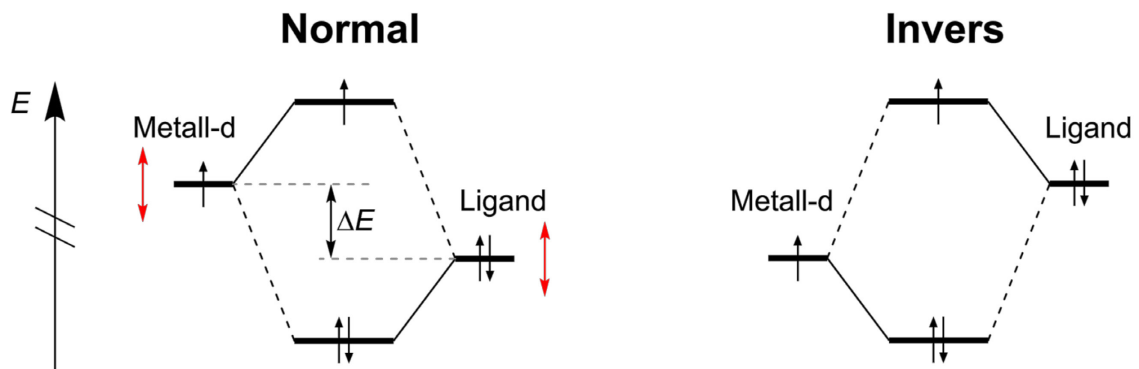
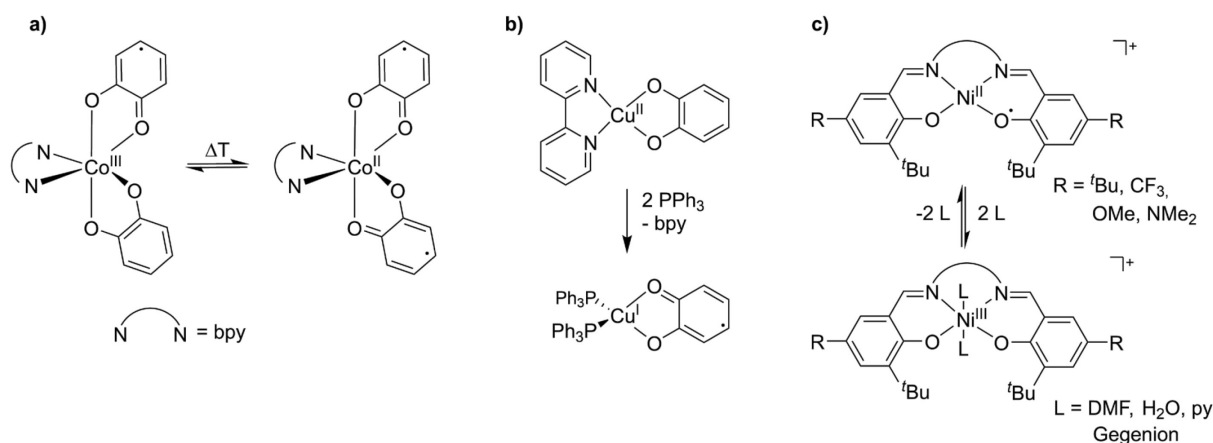


Abbildung 1: Normale (links) und inverse (rechts) Bindungssituation in Metall-Komplexen nicht-unschuldiger Liganden^[21a]. Rot eingezeichnet: Die Variation der Orbitalenergien durch Metallaustausch oder Ligandvariation.

Die entdeckten redoxaktiven Liganden können in drei Kategorien eingeteilt werden: in anionische, neutrale und kationische Radikalliganden. Zu Ersteren gehören die am häufigsten vorkommenden monoanionischen Radikalliganden, die entweder durch Reduktion der Neutralverbindung oder aber durch Oxidation des Dianions gewonnen werden können. Dazu zählen vor allem die für die Natur wichtigen Systeme wie $O_2^{\bullet-}$ ^[11] im Oxyhäm-System ($Fe^{III}/O_2^{\bullet-}$

vs. $\text{Fe}^{\text{II}}/\text{O}_2 \leftrightarrow \text{Fe}^{\text{IV}}/\text{O}_2^{2-}$), und die Triade aus Catechol/Semichinon/Chinon^[23], die vor allem in der Photosynthese und in der Atmung eine Rolle spielen. Darüber hinaus gehören auch die 1,2-Diimine^[7,9c,24], 1,2-Aminophenole^[13b,25], Salene^[3e,26], 1,2-Aminothiolen^[27], 1,2-Dithiolen^[9d,21c,21d,28] und η^n -gebundene π -Systeme von Arylen^[29] zu dieser Gruppe. Für die neutralen Radikalliganden fällt besonders dem NO^\bullet eine bedeutende Rolle in der Regulierung von biologischen Prozessen, wie die Aktivierung von Guanylyl-Cyclasen, zu.^[12] Kationische Radikalliganden hingegen sind selten und dementsprechend nur wenige Beispiele bekannt.^[30]



Schema 1: Beispiele für die Ambivalenz von redoxaktiven Liganden in offenschaligen Übergangsmetall-Komplexen

Die beobachtete Ambivalenz redoxaktiver Liganden in offenschaligen Metallkomplexen ist der Grund für die eingangs erwähnten besonderen Eigenschaften dieser Komplex-Klasse. Sie äußert sich häufig in Gleichgewichten zwischen Valenztautomeren der Form $[(\text{L}^{n-})\text{M}^{(m+1)+}]$ und $[(\text{L}^{(n-1)-})\text{M}^{m+}]$ (Schema 1), wie sie zum Beispiel für Catechol-Komplexe beobachtet werden. Ein Vertreter dafür ist ein high-spin Co^{II} -Semichinon-Komplex, der sich bei niedrigen Temperaturen in einen low-spin Co^{III} -Catechol-Semichinon-Komplex umwandelt (Schema 1a).^[23a,23b] Dieses Verhalten ist auch für einen Mn-Catechol-Komplex bekannt.^[23b,31]

Auch durch die Änderung des Co-Liganden, bei gleichzeitiger Änderung des Ligandenfelds am Metall, kann die Lokalisierung des Radikals beeinflusst werden, wie es für einen Cu-Catechol-Komplex gezeigt wurde (Schema 1b). Wird der κ^2 -N,N'-gebundene 2,2'-Bipyridin-Ligand gegen einen besseren π -Akzeptor-Liganden, wie z. B. das PPh_3 , ausgetauscht, so wandelt sich der quadratisch-planare Cu^{II} /Catecholato- in einen tetraedrischen Cu^{I} /Semichinon-Komplex um.^[32] Ebenso kann die Zugabe zusätzlicher Co-Liganden unter Änderung des

Ligandenfelds zu einer Lokalisierung des Radikals vom Liganden auf das Metall erreicht werden, wie es für Ni-Salen-Komplexe beobachtet wurde (Schema 1c).^[26b,26c,33] In Gegenwart von schwach koordinierenden Liganden, wie z. B. Gegenionen oder Wasser im Lösemittel, kann durch Variation der Temperatur ein Valenzisomeren-Gleichgewicht beobachtet werden.

Je weitreichender die Delokalisierung durch günstige Orbitalüberlappungen ist, desto kleiner wird die Energiebarriere zwischen den tautomeren Formen und das Valenztautomeren-Gleichgewicht geht in eine resonanzstabilisierte Form über.^[30] Bei solchen Komplexen ist es nicht mehr möglich, zwischen einer reinen Metall- oder Ligand-Oxidation zu unterscheiden. Spindichte-Berechnungen eines einfach oxidierten Bis(dithiolato)cobaltat(II)-Komplexes zeigen, dass das entstehende einfach besetzte Molekülorbital in gleichem Maße durch Beiträge von Ligand und Metall bestimmt ist.^[21c] Damit liegt eine Beschreibung der elektronischen Struktur durch Resonanzformen nahe.

Im Fall von elektronisch stark gekoppelten Systemen ist die Zeitskala der gewählten Beobachtungsmethode ausschlaggebend, ob die Lage des Gleichgewichts zwischen Valenzisomeren eindeutig bestimmt werden kann. Ist die Methode zu langsam, um dem Valenztautomeren-Gleichgewicht zu folgen, so werden gemittelte Werte beobachtet. Ist sie hingegen schnell, können zum Teil beide Extremfälle der Radikal-Lokalisation beobachtet werden. Dies ist vor allem dann der Fall, wenn die Überwindung der Energiebarriere zwischen den Isomeren schon durch thermische Anregung erfolgen kann. Das Vorbild für diese Klasse ist das Creutz-Taube-Ion, das im UV/Vis/NIR-Bereich eine typische Absorption für ein delokalisiertes Radikal zeigt.^[34] Auf der Zeitskala von IR- und Raman hingegen wird diese Symmetrie nicht beobachtet und das Elektron ist auf eine Seite des Komplexes lokalisiert.^[34] Damit ist die Suche nach neuen Ligand-zentrierten Radikal-Komplexen vor allem von der Frage nach der Lokalisation des ungepaarten Elektrons geprägt.^[30]

Für Komplexverbindungen mit einem bidentaten oder mehr als einem redoxaktiven Liganden, wie z. B. den Salenen^[26a,35], Bisdithiolaten^[6c] und Bisdiimininen^[25c], können bei Ligand-zentrierten Radikal-Komplexen intensive Absorptionsbanden im NIR-Bereich beobachtet werden. Die Lage und Form Bande geben dabei Aufschluss über die Höhe der Metall-Beteiligung. Aus TD-DFT-Studien an at-Komplexen und kationischen Salen-Komplexen der Gruppe 10 Metalle ist bekannt, dass der für diese NIR-Bande verantwortliche Übergang aus einem reinen Ligand-zentrierten β HOMO in ein Metall-Ligand antibindendes β LUMO stattfindet.^[6c,21c,26b,26c] Der β HOMO- β LUMO-Abstand in einem Ligand-Radikal-Komplex

hängt dabei von der Höhe der Metall-Beimischung am β LUMO ab. Je höher die Metall-Beteiligung ist, desto größer wird der energetische Abstand zwischen β HOMO und β LUMO und desto stärker ist die hypsochrome Verschiebung. Ist der Metall-Beitrag gering, so wird die Energielücke kleiner und die Bande verschiebt sich bathochrom.

Für Gruppe 10 Metall-Komplexe der oben genannten redoxaktiven Liganden zeigt Palladium über alle Ligandarten hinweg den langwelligsten Übergang und die geringste Metall-Beteiligung innerhalb der Gruppe 10 Metalle. Für Nickel und Platin hängt die Beimischung jedoch stark von der Ligandumgebung ab, so dass die NIR-Bandenlage im Verhältnis zu der des Palladiums durch die Wahl des Liganden beeinflussbar ist.

Offenschalige Ligandradikal-Komplexe als NIR-Chromophore

Die UV/vis/NIR-Spektroskopie stellt in der Ermittlung der Lokalisation des Radikals ein wichtiges Werkzeug dar, da sich schon kleine Änderungen in der elektronischen Struktur eines radikalischen Komplexes auf die Lage, Form und Breite sowie auf die Intensität der, wie eingangs beschrieben, charakteristischen NIR-Bande auswirken. Als NIR-Bereich bezeichnet man dabei in der Regel den Bereich zwischen 750 und 2500 nm. Die bei den Ligand-zentrierten Radikalkomplexen auftretenden NIR-Banden sind häufig das Ergebnis eines Interalence-Charge-Transfer-Übergangs zwischen zwei Ligandteilen, vermittelt über das Metall. Wenn es sich hingegen um ein delokalisiertes Radikal handelt, tritt ein dem π - π^* -Übergang in konjugierten π -Systemen ähnlicher Übergang auf.

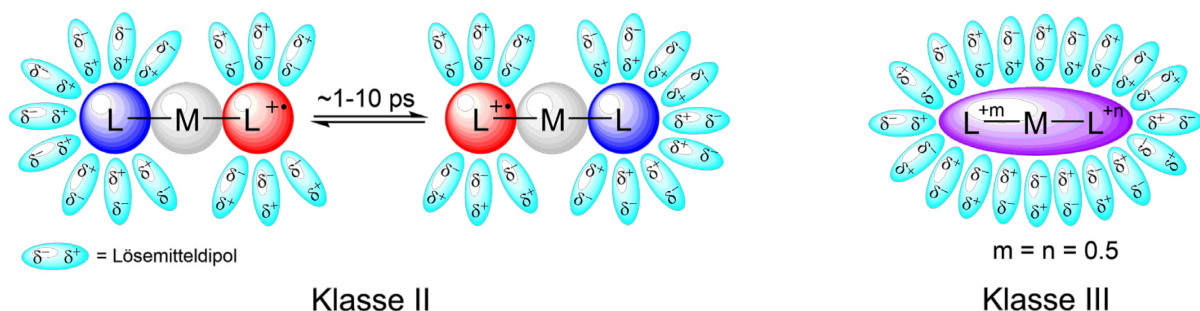


Abbildung 2: Veranschaulichung der Ausrichtung der Lösemitteldipole bei einem Klasse II und einem Klasse III System nach Robin-Day-Klassifizierung am Beispiel eines Ligand-zentrierten Radikals

Gemischt-valente Moleküle bestehen im Allgemeinen aus einem Elektronen-Donor und einem Akzeptor, die durch eine Brücke voneinander getrennt sind.^[36] Im Fall der Creutz-Taube-Ionen bestehen sowohl der Donor als auch der Akzeptor aus Metallzentren, die in verschiedenen

Oxidationsstufen vorliegen. Die beiden Metall-Zentren werden durch einen Elektronenübertragenden Liganden verbrückt. Diese Elektronenübertragung ist nur möglich, wenn es eine elektronische Kopplung zwischen Ligand und Metallen gibt. Für die Ligand-zentrierten Radikal-Komplexe hingegen sind Donor und Akzeptor zwei durch ein Metall verbrückte Liganden oder Ligandteile (Abbildung 3).

Durch den Unterschied in den Oxidationsstufen innerhalb des Moleküls sind die beiden Seiten nicht mehr gleich und es entsteht ein intramolekulares Valenzisomerengleichgewicht mit einer Elektronen-Transfer-Barriere.^[34,36] Nach der Robin-Day-Klassifizierung^[37], die an Creutz-Taube-Ionen entwickelt wurde, kann zwischen lokalisierten und delokalisierten Radikalen unterschieden werden. Dabei weist ein sogenanntes Klasse II System eine lokalisierte Oxidationsstufe und eine messbare elektronische Kopplung zwischen den beiden Ligandteilen auf. Die Geschwindigkeit des intramolekularen Valenzisomerengleichgewichts ist wegen der vorhandenen Umwandlungsbarriere gleich schnell oder etwas langsamer als die Reorientierung der Lösemitteldipole, die circa 1-10 ps beträgt. Dadurch richten sich die Dipole des Lösemittels an dem im Molekül erzeugten Dipol aus (Abbildung 3, links). Das Spektrum wird dabei von einer breiten und Gauß-förmigen Bande geprägt, deren Lage sich bei Änderung der Lösemittel-Polarität merklich verschiebt.^[34,36] Die Bandenbreite, ab der ein Klasse II System vorliegt, kann mit Hilfe der Hush-Analyse berechnet werden.^[38]

Bei einem Klasse III System hingegen gibt es keine Barriere für den Elektronen-Transfer und das Elektron gilt als delocalisiert. Die schmale und zu geringeren Energien stark abfallende Absorptionsbande entsteht durch den Übergang zwischen zwei delokalisierten elektronischen Niveaus.^[34,36] Dadurch wird sowohl der strukturelle als auch der elektronische Unterschied zwischen Donor und Akzeptor aufgehoben, so dass die Wechselwirkung mit den Lösemitteldipolen hauptsächlich durch Dispersionswechselwirkungen bestimmt wird.^[34] Die Reorientierung der Lösemitteldipole kann dabei als gemittelt aufgefasst werden (Abbildung 3, rechts).^[34] Ein sogenanntes Klasse II-III System liegt zwischen den beiden zuvor beschriebenen Systemen. Dabei kann die Reorientierung der Lösemitteldipole nach Meyer *et al.* als zeitlich gemittelt und das Elektron als lokalisiert angesehen werden.^[34] Die auftretenden Banden sind schmal und von der Lösemittelpolarität nahezu unabhängig. Dies macht die Unterscheidung zum Klasse III System schwierig, wenn nicht aus anderen analytischen Methoden, wie z. B. aus Kristallstrukturdaten, auf eine Lokalisation geschlossen werden kann.^[34]

Thiolate als nicht-unschuldige Liganden

In der Reihe der redoxaktiven Liganden stellen die Thiolate eine Besonderheit dar (Abbildung 3). Durch die Eigenschaft des Schwefels sowohl als σ -Donor als auch als σ -Donor- π -Donor-Ligand zu fungieren, sind Thiolate in ihrer Koordinationsfähigkeit sehr vielseitig.^[18b] Der Beitrag der zwei verfügbaren 3p-Orbitale des Schwefels zur M-S-Bindung hängt stark vom Bindungswinkel und von der elektronischen Struktur des Metallions ab. Bei einem Bindungswinkel unter 180° wird die Entartung der 3p-Orbitale aufgehoben und es sind nun sowohl π - als auch σ -Bindungen möglich. Bei der elektronischen Struktur des Metallions sind vor allem dessen effektive Kernladung und die d^n -Elektronenkonfiguration entscheidend.^[3d] Beim Gang zu den schwereren Übergangsmetallen hingegen gewinnen die relativistischen Effekte an Bedeutung. Liegt das Metall in einer hohen Oxidationsstufe vor oder wird durch Kontraktion der Orbitale innerhalb einer Periode oder Gruppe die Elektronenaffinität erhöht, gewinnt die π -Donor-Eigenschaft des Schwefels an Bedeutung.^[18b]

Ist der Schwefel an ein π -System gebunden, wie es bei den Thiophenolen der Fall ist, so kann er mittels eines +M-Effekts mit diesem wechselwirken.^[5] Dieser Effekt ist im Vergleich zu dem in Phenolen oder aromatischen Aminen vermindert. Die für oxidierte N- und O-Donor-Liganden charakteristische chinoide Struktur wird nach der Oxidation von Thiolaten nicht beobachtet bzw. ist nur schwach ausgeprägt.^[9d,21b,27c,27d,39] Verantwortlich dafür ist der Hybridisierungsdefekt, der durch den starken Größenunterschied zwischen 3p- und 3s-Orbitalen hervorgerufen wird.^[40] Die gefundenen Valenzwinkel am Schwefel weichen daher stark von denen einer sp^3 -Hybridisierung, wie sie für Sauerstoff in Phenolen gefunden werden, ab. Dadurch ist das 3p-Orbital des Schwefels gegenüber denen des π -Systems verdreht, so dass der Orbitalüberlapp verringert wird.^[5]

Gegenüber den Übergangsmetallen ist Schwefel ein starker σ -Donor, was zur Ausbildung von sehr kovalenten Bindungen zwischen Metall und Schwefel führt.^[4] Die Ortsbestimmung des ungepaarten Elektrons wird durch den kovalenten Charakter der M-S-Bindung erschwert. Diese Eigenschaften des Schwefels macht sich die Natur zu Nutze, wenn sie schwefelhaltige Liganden in den aktiven Zentren von Enzymen einsetzt. Die Bandbreite reicht von Cu-S-Einheiten in Plastocyanin^[3b,3d] und Ni-S in Hydrogenasen^[3a] hin zu binuklearen schwefelhaltigen Fe-Fe- oder Fe-Ni-Cluster in Wasserstoffreduktasen^[3c,41].

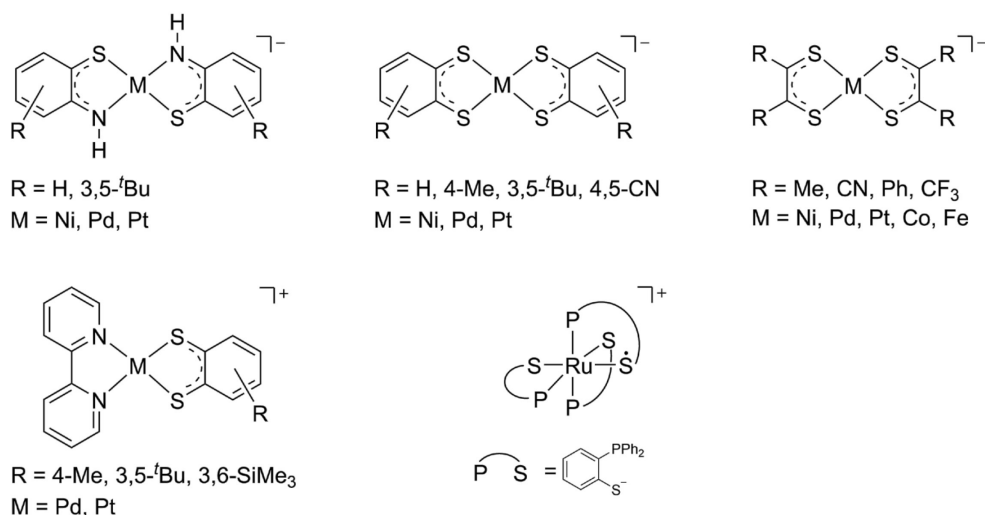


Abbildung 3: Ausgewählte Thiy/Thiolat-haltige Komplex-Strukturen^[6b,6c,8a,9b,21b,27a,27c,27d,42]

Die Bindungssituation in radikalischen Bisdithiolat-Komplexen wurde in den 1960ern von den Gruppen um Gray^[8b,8c,9b,42a,42b,43] und Holm^[8a,44] intensiv untersucht (Abbildung 3, oben), nachdem Schrauzer von einem ungewöhnlichen quadratisch-planaren Ni^{IV}-Bisdithiophenol-Komplex berichtet hatte.^[45] Die Gruppe um Gray stellte in Untersuchungen fest, dass die Verbindungen des 1,2-Maleonitrilthiolats des Ni(II), Co(II), Pd(II), Pt(II), Cu(II) und Zn(II) isomorphe Strukturen besitzen (Abbildung 3, oben rechts).^[9d,42a] Dies ist nur möglich, wenn die Elektronenlücke hauptsächlich am Liganden vorliegt. Dies konnte die Gruppe um Gray an Hand der Ergebnisse von theoretischen Berechnungen und ESR-Messungen zeigen. In der Publikation „The Myth of Ni(III) and Ni(IV) in Planar Complexes“^[8c] postulierten Gray *et al.* daraufhin, dass es sich bei dem von Schrauzer gefunden Komplex um einen Ni^{II}-Bisthiylthiolat-Komplex handeln muss.

In den 2000er Jahren konnten Wieghardt *et al.* mit Hilfe von Schwefel-K- und Metall-K- und L-Röntgenabsorptionsspektroskopie-Messungen sowie DFT-Berechnungen die Befunde von Gray *et al.* weiter untermauern (Abbildung 3, links).^[21,27d,42c] Bei dem von Wieghardt *et al.* untersuchten radikalischen Bis(1,2-thiophenolato-thiyl)-Komplex des Nickels handelt es sich um einen Ligand-zentrierten Radikal-Komplex mit einer DFT-berechneten Spindichte von 34 % am Nickel (Abbildung 3, oben links).^[6c] Die Untersuchungen dieser schwefelzentrierten Radikal-Komplexe waren maßgeblich bei der Entdeckung und Definition des inversen Bindungsschemas beteiligt, deshalb stellen schwefelzentrierte Radikal-Komplexe der Gruppe 10 Metalle ein geeignetes System zur Untersuchung der Metall-Ligand-Wechselwirkung dar.

Beeinflussung der Eigenschaften

Die chemischen und physikalischen Eigenschaften eines Komplexes werden von seiner elektronischen Struktur geprägt. Doch wie beeinflusst man nun die elektronische Struktur? Dabei können zwei Parameter unterschieden werden. Zum einen die Geometrie, die die relative räumliche Orientierung von Metall und Liganden vorgibt. Dadurch wird die Größe des Überlappungsintegrals der Orbitale beeinflusst und somit der Grad der Delokalisierung. Der zweite Parameter ist die Änderung der elektronischen Struktur, die durch Variation des Zentralatoms und der Substituenten am Liganden bewirkt werden kann. Bei der Variation der Ligandstruktur kann zwischen den funktionellen Gruppen am Ligandrückgrat und den Donor-Gruppen, die die Bindung zum Metall eingehen, unterschieden werden. Die Änderung der Substitution findet häufig Anwendung und ist sowohl für die Salen- als auch für die Bisdithiolat-Komplexe systematisch untersucht worden. Substituenten in *para*-Stellung zu den Donor-Gruppen sind dabei von besonderer Bedeutung.^[46] Elektronendonierende Gruppen in dieser Position führen bei einem Ni-Salen-Komplex zu einer verringerten Spindichte am Metall (CAM-B3LYP: *t*Bu: $\rho(\text{Ni}) = 15,7\%$ vs. NMe_2 : $1,7\%$) und zu einer Lokalisierung des Radikals auf den Liganden.^[46b] Der Einfluss der Substituenten auf die Lage der NIR-Absorptionsbande

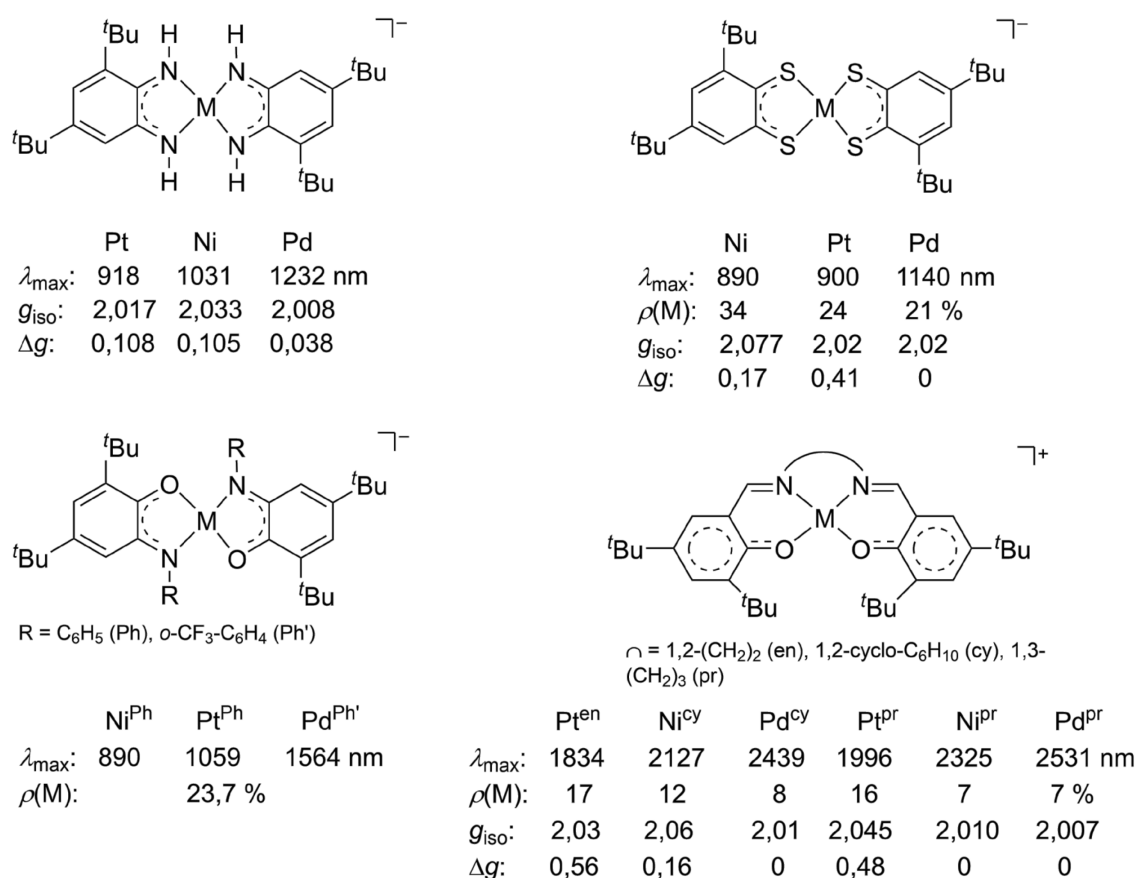


Abbildung 4: Beeinflussung der NIR-Bandenlage und der Spindichte durch sterische und elektronische Veränderungen im Komplex

ist auch für einen ein- bis vierfach substituierten 1,2-Dithiophenol-Liganden in einem Nickel- und in einem Kobalt-Komplex untersucht worden.^[43b] Mit steigender Anzahl der Elektronendonoren am Liganden verschiebt sich in diesen Systemen die NIR-Bande hypsochrom.

Die Fähigkeit eine semichinoide Struktur ausbilden zu können, wird von den am Metall gebundenen funktionellen Gruppen beeinflusst und nimmt in der Reihenfolge $S < N < O$ zu. Mit steigender Ausprägung dieser Struktur findet eine verstärkte Lokalisierung des Radikals im Liganden statt und führt zu einer bathochromen Verschiebung des NIR-Übergangs (Abbildung 4, oben).^[23b,47]

Beim Austausch des Zentralatoms spielt die relative energetische Lage der Metall-d-Orbitale gegenüber dem Liganden eine Rolle. Innerhalb der 4. Periode nimmt bei gleichem Liganden der kovalente Charakter der Metall-Ligand-Bindung mit steigender Ordnungszahl zu. In Bisdithiolat-Komplexen tritt daher bei gleicher Oxidationsstufe des Metalls im Falle des Eisens ein Metall-zentriertes und im Fall des Nickel ein Ligand-zentriertes Radikal auf.^[21b] Die Zunahme der Kovalenz beruht dabei auf der Abnahme der Atomradien bei gleichzeitiger Zunahme der effektiven Kernladung. Innerhalb einer Gruppe steigt der kovalente Bindungscharakter mit zunehmender Ordnungszahl, wie es für Bisdithiolat-Komplexe der Gruppe 9 Metalle gezeigt wurde.^[48] Der Grund dafür ist die Erhöhung der radialen Ausdehnung der $(n-1)d$ -Orbitale durch die steigende Anzahl der radialen Knoten und der damit einhergehenden besseren Überlappung der $(n-1)d$ -Orbitale des Metalls mit denen des Liganden. Mit steigender Kovalenz in Richtung Ir erhöht sich der Metall-Beitrag zum HOMO und führt zu einer Stabilisierung des Ligand-Radikals gegenüber den Co- und Rh-Analogen.^[48]

Der Parameter der Geometrie wurde bislang vor allem durch die Verbindung zweier bidentater Liganden mit Hilfe einer Brücke untersucht (Abbildung 4, unten).^[26a,35] Die Brücke hindert dabei das System zum einen am Wechsel zwischen einer *cis/trans*-Anordnung und zum anderen definiert sie sowohl den maximalen als auch den minimalen möglichen Abstand zwischen Ligand und Metall. Die Einschränkung der Flexibilität resultiert in einer bathochromen Verschiebung der beobachteten NIR-Absorption (Abbildung 4, unten).^[26a,35] Wird die Brücke sterisch anspruchsvoller, so verdrillen sich die Ligandhälften gegeneinander und die Überlappung der Ligand-Orbitale mit denen des Metalls wird beeinträchtigt. Es kommt zu einer weiteren bathochromen Verschiebung. Die Metallbeteiligung nimmt dabei ab, was sich in einer Abnahme der *g*-Anisotropie zeigt (Abbildung 4 unten rechts).^[35b]

Betrachtet man die Auswirkungen der einzelnen Parameter auf die Lage und Intensität der NIR-Bande, so stellt man fest, dass die Verdrillung der Ligandseiten, verursacht durch eine sterisch anspruchsvollere Brücke, die geringste Auswirkung hat. Das Versteifen des Ligandrückgrats, sowie die Änderung des Zentralatoms, beeinflussen die Bandenlage in gleicher Weise und deutlich stärker als die Verdrillung.

2. Zielsetzung

In meiner Diplomarbeit habe ich die Auswirkungen der Geometrie und des Zentralatoms auf die elektronischen Eigenschaften in Gruppe 10 Metall Komplexen eines 1,4-Terphenyldithiophenolato-Liganden untersucht (Abbildung 5). Dabei konnte festgestellt werden, dass beide Faktoren einen beträchtlichen Einfluss auf die zwei beobachteten Oxidationen zeigen. Gleichzeitig ging aus den elektrochemischen Messungen hervor, dass die erste Oxidation für alle untersuchten Komplexe elektrochemisch reversibel ist und somit auch eine Isolation der oxidierten Spezies möglich sein sollte. Ziel meiner Doktor-Arbeit war es nun die Radikal-Komplexe der Gruppe 10-Metalle zu synthetisieren und zu charakterisieren. Bei der Charakterisierung der radikalischen Spezies spielt die Absorptionsbande im NIR-Bereich als Sonde für schon geringe Veränderungen in der elektronischen Struktur der oxidierten Spezies eine besondere Rolle. In wie weit nun die Lage dieser Bande und damit die elektronische Struktur beeinflusst werden können und was für Auswirkungen dies auf die Metall-Ligand-Wechselwirkung hat, wurde in dieser Arbeit untersucht. Die dabei untersuchten Teilaspekte sind im Folgenden aufgelistet.

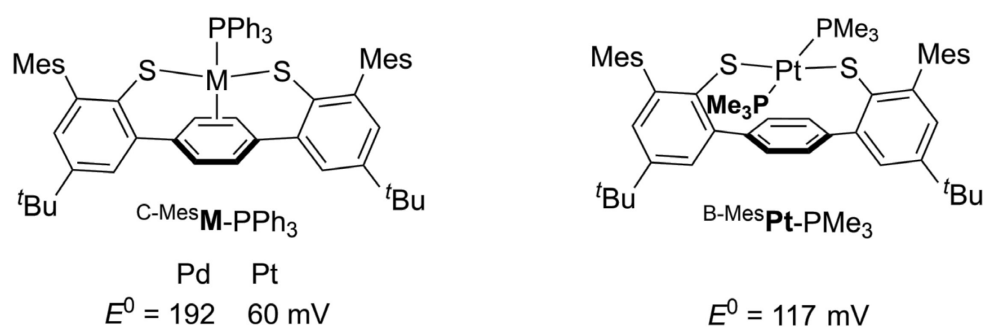


Abbildung 5: In der Diplomarbeit elektrochemisch untersuchte Komplexe mit den Redoxpotentialen E^0 der ersten Oxidation bezogen of Fc/Fc⁺

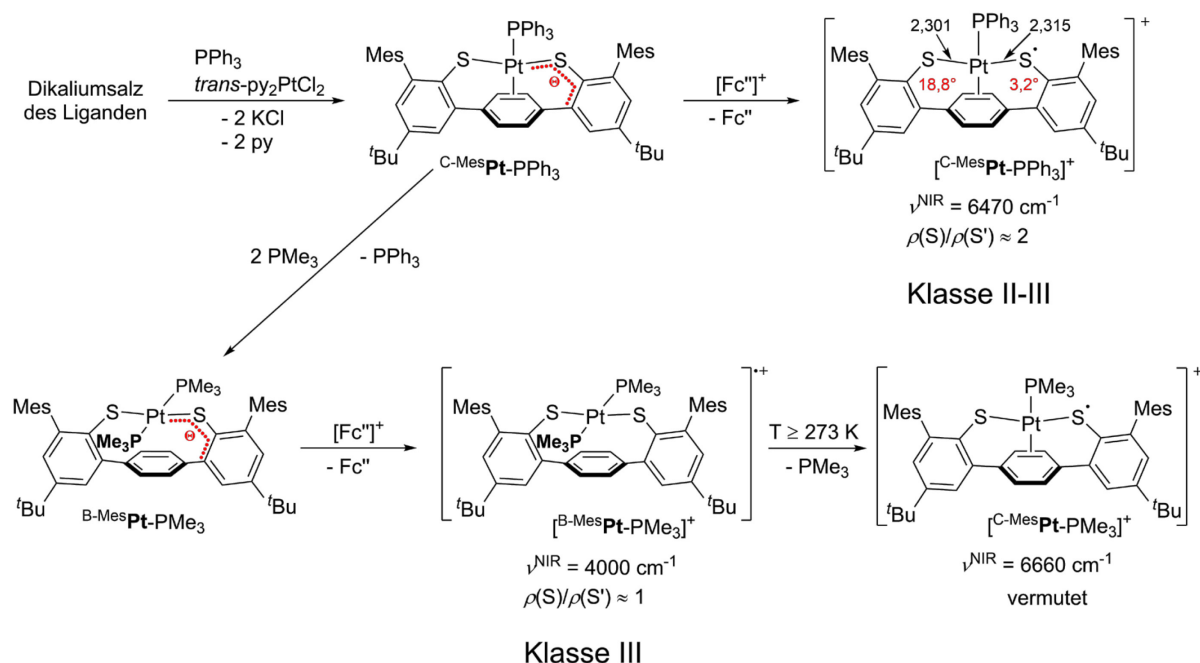
- Synthese von neutralen und oxidierten Thiolat-basierten Gruppe-10-Metall-Komplexen
- Charakterisierung und Bestimmung der elektronischen Struktur der Radikal-Kationen mit Hilfe von X-Band cw-ESR-, CV-, XRD- und UV/vis/NIR-Messungen, unterstützt durch DFT-Berechnungen und Einordnung in die Robin-Day-Klassifizierung
- Untersuchung des Einflusses der Co-Liganden, der Substituenten am Hauptliganden und des Metalls auf die elektronische Struktur der Radikal-Komplexe
- Untersuchung der Auswirkung der geometrischen Anordnung auf die elektronische Struktur des offenschaligen Komplexes im Vergleich zu elektronischen Änderungen im System

3. Ergebnisse und Diskussion

3.1. Publikation I: Controlling Near-Infrared Chromophore Electronic Properties through Metal-Ligand Orbital Alignment

Mews, N. M.; Berkefeld, A.; Hörner, G.; Schubert, H., *J. Am. Chem. Soc.* **2017**, *139*, 2808

Diese Arbeit befasst sich mit den Auswirkungen der verschiedenen Ausrichtungen der Metallkoordinationsebene auf die Eigenschaften von Ligand-Radikal-Komplexen des Platins. Dafür wurden die zwei Metallverbindungen $^{\text{C-Mes}}\text{Pt-PPh}_3$ und $^{\text{B-Mes}}\text{Pt-PMe}_3$ synthetisiert (Schema 2). Die Synthese erfolgt über eine Salzmetathese-Reaktion mit *trans*-py₂PtCl₂ als Vorstufe und dem Dikaliumsalz des 1,4-Terphenyldithiophenolat-Liganden in Toluol unter Zugabe von PPh₃. $^{\text{B-Mes}}\text{Pt-PMe}_3$ wird mittels Ligandenaustausch von PPh₃ durch PMe₃ in Hexan aus $^{\text{C-Mes}}\text{Pt-PPh}_3$ gewonnen. Die Kristallstrukturen der Komplexe zeigen, dass die Anzahl der Co-Liganden entscheidend für eine η^2 -Koordination zum verbrückenden π -System der Terphenyl-Einheit ist. Durch das sterisch anspruchsvollere PPh₃ wird die Koordinationssphäre des Platins durch eine η^2 -Koordinat



Schema 2: Synthese von $^{\text{B/C-Mes}}\text{Pt-R}$ ($\text{R} = \text{PMe}_3, \text{PPh}_3$) und $[\text{B/C-MesPt-R}]^+$ mit Daten der berechneten Spindichte ρ und den in CH_2Cl_2 bestimmten NIR-Banden ν^{NIR} . Rot eingezeichnet der Torsionswinkel Θ in der $\text{Pt-S-(C-C)}_{\text{Ar}}$ -Einheit. Pt-S-Bindungslängen in Å.

π -System gefunden.^[49] Im Unterschied zu PPh₂py wird die Koordination eines zweiten PPh₃ in ^{C-Mes}Pt-PPh₃ nicht beobachtet. Wobei κ -PPh₃ und freies PPh₃ auf der Zeitskala der NMR-Messungen über einen vermutlich assoziativen Mechanismus bei Raumtemperatur schnell austauschen. Die Koordination zum π -System für Strukturen des Typs C wurde auch in Lösung nachgewiesen und ist als ein gemittelttes Singulett mit einem Integral von vier Protonen mit einer ¹³⁵Pt-Kopplung in der ¹H-NMR-Spektroskopie zu beobachten. Bei Temperaturen unterhalb von -60 °C kann auch die η^2 -Koordination durch Aufspaltung in zwei Singuletts beobachtet werden. Bei PMe₃ als Ligand verkippt sich die Koordinationssphäre um 90° und eine Wechselwirkung zum π -System tritt nicht mehr auf.

Bei cyclovoltammetrischen Messungen konnten für beide Verbindungen jeweils zwei Oxidationen beobachtet werden. Die erste Oxidation ist sowohl für ^{C-Mes}Pt-PPh₃ als auch für ^{B-Mes}Pt-PMe₃ elektrochemisch reversibel. Wobei das Redoxpotential der ersten Oxidation von ^{C-Mes}Pt-PPh₃ gegenüber dem von ^{B-Mes}Pt-PMe₃ um 57 mV anodisch verschoben ist. Diese anodische Verschiebung wird durch den Unterschied in der geometrischen Anordnung verursacht und weist darauf hin, dass [^{C-Mes}Pt-PPh₃]⁺ gegenüber [^{B-Mes}Pt-PMe₃]⁺ thermodynamisch stabiler ist. Die chemische Oxidation von ^{C-Mes}Pt-PPh₃ und ^{B-Mes}Pt-PMe₃ erfolgte mit Fe^{III}NTf₂ bei -80 °C in CH₂Cl₂, dabei konnte [^{C-Mes}Pt-PPh₃]NTf₂ in Form von stabilen, kastanienbraunen Kristallen isoliert werden. In der Kristallstruktur von [^{C-Mes}Pt-PPh₃]NTf₂ bleibt auch nach der Oxidation die Anordnung in der Pt-Koordinationssphäre unverändert. Es wird dafür eine Kontraktion der Pt-S-, Pt- π -Aryl und C-S-Bindungslängen bei gleichzeitiger Verlängerung der Pt-P-Bindung beobachtet. Zusätzlich lässt sich auch eine Asymmetrie sowohl in den Pt-S-Bindungslängen als auch im Torsionswinkel Θ erkennen (Schema 2). Diese Asymmetrie spiegelt sich auch in den Spindichten wider, die mittels DFT-Rechnungen (BLYP-35-D3/TZVP/ZORA) erhalten worden sind. Die ^{Ar}S-Pt-S^{Ar}-Einheit trägt dabei >99 % der Gesamtspindichte. Die Spindichte ist auf die Schwefelatome asymmetrisch im Verhältnis 1:2 verteilt, wobei der Schwefel mit der längeren Pt-S-Bindung und dem kleineren Torsionswinkel die meiste Spindichte trägt. Das Platinatom trägt dabei nur 11 % der Spindichte.

Die Isolation von [^{B-Mes}Pt-PMe₃]NTf₂ ist nur bei geringen Temperaturen möglich, da es sich bei Temperaturen über -70 °C zersetzt. Es konnten blauviolette Kristalle aus der Überschichtung einer CH₂Cl₂-haltigen Lösung mit Pentan bei -80 °C erhalten werden. Leider waren diese Kristalle für eine Kristallstrukturanalyse nicht geeignet. Dadurch wurden die DFT-

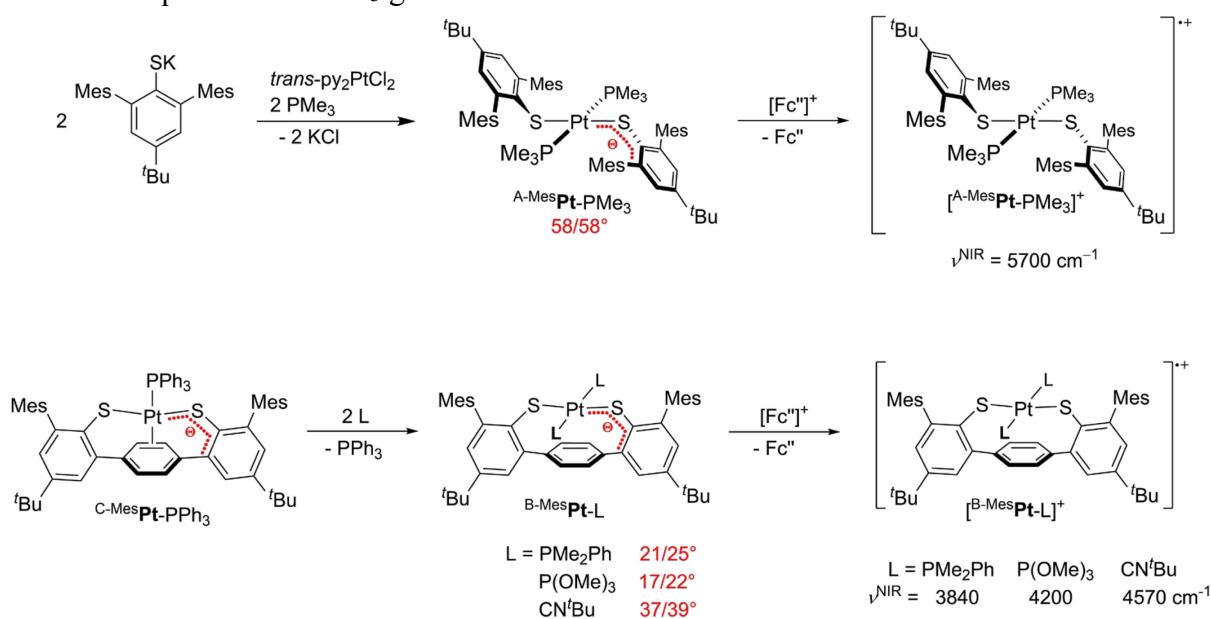
Berechnungen im Gegensatz zu $[\text{C-MesPt-PPH}_3]^+$ auf Grundlage der Neutralspezies durchgeführt. Es zeigt sich, dass auch bei $[\text{B-MesPt-PMe}_3]^+$ die Spindichte sich zu >99 % in der $\text{ArS-Pt-S}^{\text{Ar}}$ -Einheit befindet. Das Platinatom trägt auch hier nur 11 % Spindichte aber der Unterschied zwischen den Schwefelatomen ist nicht mehr gegeben. Man spricht hier deshalb von einem delokalisierten Radikal. Die geringe Metallbeteiligung am SOMO wird unterstützt durch die Ergebnisse der X-Band cw-ESR-Spektroskopie. Die dort beobachtete geringe g -Anisotropie und die Hyperfeinaufspaltung zu ^{195}Pt sind ein Beleg für ein hauptsächlich Ligand-zentriertes Radikal mit Metallbeteiligung. Der Unterschied zwischen beiden Radikalkationen tritt am deutlichsten in der Lage der NIR-Banden auf. Die Verkippung der Koordinationssphäre und der Unterschied in der elektronischen Struktur führen zu einer bathochromen Verschiebung von über 950 nm für $[\text{B-MesPt-PMe}_3]^+$. Die Bandenlage bleibt bei beiden Komplexen von der Lösemittelpolarität nahezu unberührt. Zusammen mit den theoretischen Berechnungen und der Kristallstruktur ergibt sich, dass es sich bei $[\text{C-MesPt-PPH}_3]^+$ um ein Klasse II-III System mit einem LLIVCT und bei $[\text{B-MesPt-PMe}_3]^+$ um ein Klasse III System mit einem CR-Übergang handelt. Bei Temperaturen über 0 °C jedoch wandelt sich $[\text{B-MesPt-PMe}_3]^+$ in eine neue Spezies mit einer Bande bei 1500 nm um. Durch NMR-Experimente konnte in dieser Veröffentlichung vermutet werden, dass eine Umwandlung in $[\text{C-MesPt-PMe}_3]^+$ bei Temperaturen über -70 °C unter Abspaltung eines PMe_3 stattfindet (Schema 2). Durch Zugabe von freiem PMe_3 werden die Spezies quantitativ zu B-MesPt-PMe_3 reduziert. Diese Umwandlung konnte in späteren Arbeiten mit weiteren Hinweisen untermauert werden.

In dieser Publikation konnte gezeigt werden, dass die Anzahl der Co-Liganden einen beträchtlichen Einfluss auf die geometrische Ausrichtung der Metallorbitale gegenüber den Ligandorbitalen hat. Dieser Unterschied in der räumlichen Anordnung schlägt sich dabei sichtbar auf die elektronischen Eigenschaften der Radikalkomplexe nieder und gibt damit einen ersten Einblick in den Einfluss der geometrischen Anordnung auf die Veränderung der elektronischen Eigenschaften eines Ligand-Radikal-Komplexes.

3.2. Publikation II: Tuning of Thiyl/Thiolate Complex Near-Infrared Chromophores of Platinum through Geometrical Constraints

Mews, N. M.; Hörner, G.; Schubert, H.; Berkefeld, A., *Inorg. Chem.* **2018**, *57*, 9670

In dieser Arbeit wird der Einfluss des Torsionswinkels Θ entlang der M-S-(C-C)_{Ar}-Einheit (Schema 3) und der Donoreigenschaften des Co-Liganden sowie der freien Rotation des Liganden um die Pt-S-Achse auf die elektronische Struktur von Komplexen des Struktur-Typs $[^{A/B-C-Mes}Pt-R]^+$ untersucht. Die Synthese der Ausgangsverbindungen $^{B-Mes}Pt-L$ mit L = P(OMe)₃, CN^tBu und PMe₂Ph erfolgt analog zu der Synthese von $^{B-Mes}Pt-PMe_3$ ^[50] ausgehend von $^{C-Mes}Pt-PPh_3$ in Hexan durch Ligandaustausch von PPh₃ durch 2 L. $^{A-Mes}Pt-PMe_3$ wird über eine Salzmetathese-Reaktion aus dem Kaliumsalz des Liganden unter Zugabe von *trans*-py₂PtCl₂ und zwei Äquivalenten PMe₃ gewonnen.



Schema 3: Synthese von $^{A/B/C-Mes}Pt-R$ (R = PMe₃, PMe₂Ph, P(OMe)₃, CN^tBu) und $[^{A/B/C-Mes}Pt-R]^+$ mit den in CH₂Cl₂ bei -80 °C bestimmten NIR-Banden bei ν^{NIR} .

Die Molekülstrukturen der Neutralkomplexe im Einkristall zeigen, dass zwar für alle Komplexe die Koordinationsumgebung für das Platin unverändert ist, aber sie sich in den Torsionswinkeln Θ deutlich unterscheiden. Der Unterschied in den Torsionswinkeln Θ wird dabei vor allem durch die sterische Wechselwirkung zwischen den Mesitylgruppen des Hauptliganden und Co-Liganden bestimmt. Diese Wechselwirkung ist bei P(OMe)₃ maximal, da durch die Einführung der Sauerstoffatome die räumliche Ausdehnung des Liganden deutlich ansteigt und es so zu den kürzesten Abständen zwischen Ligand und Co-Ligand kommt. Um

diese Wechselwirkung zu verringern, ordnet sich das Platin-Atom über einer der Aryl-Bindungen an, so wie es für ${}^{\text{C-Mes}}\text{Pt-L}$ bekannt ist, wobei der Abstand zum verbrückenden π -System ähnlich groß wie für andere ${}^{\text{B-Mes}}\text{Pt-L-Komplex}$ ist. Bei CN^tBu werden die Torsionswinkel Θ auf Grund der nahezu 90° betragenden S-Pt-C_{Isonitril}-Winkel und der daraus resultierenden Wechselwirkung zwischen Haupt- und Co-Ligand am größten. Bei der offenen Form ${}^{\text{A-Mes}}\text{Pt-PMe}_3$ drehen sich wegen einer besseren sterischen Anordnung die Arylreste aus der Koordinationsebene der freien Elektronenpaare des Schwefels heraus ($\Theta = 58^\circ$), so dass nur noch eine geringe Wechselwirkung zwischen Aryl und Schwefel im Thiol stattfinden kann. Dies hat Auswirkungen auf die Spindichtevertellung in $[{}^{\text{A-Mes}}\text{Pt-PMe}_3]^+$, wie DFT-Rechnungen (ZORA/BLYP35-D3/TZVP) zeigen. So reduziert sich die Spindichte im Aromaten von 18 % auf 3 % im Vergleich zu $[{}^{\text{B-Mes}}\text{Pt-PMe}_3]^+$ und konzentriert sich ausschließlich auf die S-Pt-S-Einheit.

Tabelle 1: Spindichten aus DFT-Rechnungen (ZORA/BLYP35-D3/TZVP) und experimentell bestimmter langwelligster Übergang in CH_2Cl_2 bei -80°C für Ligand-zentrierte Radikal-Komplexe des Platins

	$\rho(\text{M})/\%$	$\rho(\text{S})/\rho(\text{S}')$	$\rho(\text{Ar})/\rho(\text{Ar}')$	$\nu^{\text{NIR}}/\text{cm}^{-1}$
$[{}^{\text{A-Mes}}\text{Pt-PMe}_3]^+$	18	1	1	5700
$[{}^{\text{B-Mes}}\text{Pt-PMe}_3]^+$	11	1	1	4000
$[{}^{\text{B-Mes}}\text{Pt-P(OMe)}_3]^+$	9	3,8	3,3	4290
$[{}^{\text{B-Mes}}\text{Pt-CN}^t\text{Bu}]^+$	7	1,7	2,5	4570

Dies führt zu 18 % Spindichte am Platin und ist der höchste gefundene Wert in den untersuchten Komplexen. Er wird sowohl durch eine hohe g -Anisotropie als auch durch eine hypsochrome Verschiebung der NIR-Bande bestätigt. Da die Spindichte gleichmäßig auf beide Ligandarme verteilt und die Bande relativ schmal ist, handelt es sich bei $[{}^{\text{A-Mes}}\text{Pt-PMe}_3]^+$ um ein Klasse III System. Des Weiteren führt der Wechsel von einem bidentaten zu einem monodentaten Liganden zu einer Destabilisierung des Ligandradikal-Komplexes wie eine irreversible erste Oxidation und VT-UV/vis/NIR-Messungen von $[{}^{\text{A-Mes}}\text{Pt-PMe}_3]^+$ im Vergleich zu $[{}^{\text{B-Mes}}\text{Pt-PMe}_3]^+$ zeigen. Für ${}^{\text{B-Mes}}\text{Pt-PMe}_2\text{Ph}$ und ${}^{\text{B-Mes}}\text{Pt-PMe}_3$ konnte gezeigt werden, dass diese Komplexe sich in ihren Eigenschaften sowohl in der Neutral- als auch in der Ligandradikal-Verbindung sehr ähneln und somit auch eine ähnliche elektronische Struktur aufweisen müssen. $[{}^{\text{B-Mes}}\text{Pt-PMe}_2\text{Ph}]^+$ wandelt sich wie $[{}^{\text{B-Mes}}\text{Pt-PMe}_3]^+$ bei $T > -80^\circ\text{C}$ in eine neue Spezies mit einer NIR-Absorptionsbande bei 6700 cm^{-1} um. Diese ist nicht nur wie im

Fall [$^{B\text{-Mes}}\text{Pt-PMe}_3$] $^+$ in VT-UV/vis/NIR-Messungen, sondern auch in VT-ESR-Messungen nachweisbar. Die beobachteten g -Werte, die g -Anisotropie und die Hyperfeinaufspaltungen zu ^{195}Pt stimmen dabei mit einer [$^{C\text{-Mes}}\text{Pt-L}$] $^+$ -Spezies ($L = \text{PPh}_3, \text{PCy}_3$) überein. Dies untermauert die These, dass sowohl der Komplex mit PMe_3 als auch der mit PMe_2Ph unter Abspaltung eines Phosphans eine Bindung zum verbrückenden π -System eingehen.

Vergleicht man die CV-Daten von P(OMe)_3 und CN^tBu mit ihren Donoreigenschaften, so stellt man fest, dass CN^tBu trotz seiner besseren σ -Donor Eigenschaften im Vergleich zu P(OMe)_3 die positive Ladung weniger gut stabilisiert. Dies unterstreicht den höheren Einfluss der Sterik gegenüber den elektronischen Eigenschaften des Co-Liganden. UV/vis/NIR-Messungen bei $-90\text{ }^\circ\text{C}$ und $-80\text{ }^\circ\text{C}$ von [$^{B\text{-Mes}}\text{Pt-P(OMe)}_3$] $^+$ zeigen, dass die bei $-80\text{ }^\circ\text{C}$ breite NIR-Bande aus zwei sich überlappenden Banden besteht. Mit Hilfe von DFT-Rechnungen konnten zwei isomere Strukturen mit einem energetischen Unterschied von 10 kJ mol^{-1} gefunden werden. Die Lokalisierung der Spindichte auf einen Ligandarm und das Beobachten der Isomere sind typisch für ein Klasse II System.

Aufgrund der lokalen D_{2h} -Symmetrie am Platin in $^{B\text{-Mes}}\text{Pt-CN}^t\text{Bu}$ wird für die CN^tBu -Liganden sowohl im Raman-Spektrum eines Einkristalls (2230 cm^{-1} , A_1) als auch im IR-Spektrum im Feststoff (2197 cm^{-1} , B_{2u}) und in Lösung (CH_2Cl_2 , 2212 cm^{-1} , B_{2u}) eine $\text{C}\equiv\text{N}$ -Schwingungsbande gefunden. Dabei reagiert diese Schwingung sensitiv auf die Änderung der Oxidationsstufe des Metalls. Bei der Bindung an ein Mono- oder Dikation wird die Bande gegenüber dem freien Isonitril im IR-Spektrum um 100 cm^{-1} hypsochrom verschoben.^[51] Dies ist auch hier der Fall und ist ein Zeichen dafür, dass das CN^tBu in der Neutralverbindung als reiner σ -Donor agiert.^[51] Die Oxidation von $^{B\text{-Mes}}\text{Pt-CN}^t\text{Bu}$ führt nur zu einer Erhöhung der Frequenz im IR-Spektrum um 13 cm^{-1} . Diese ist deutlich geringer als die dafür erwartete Verschiebung um 100 cm^{-1} für eine Metall-zentrierte Oxidation und unterstützt damit den Befund einer hauptsächlich Ligand-zentrierten Oxidation.

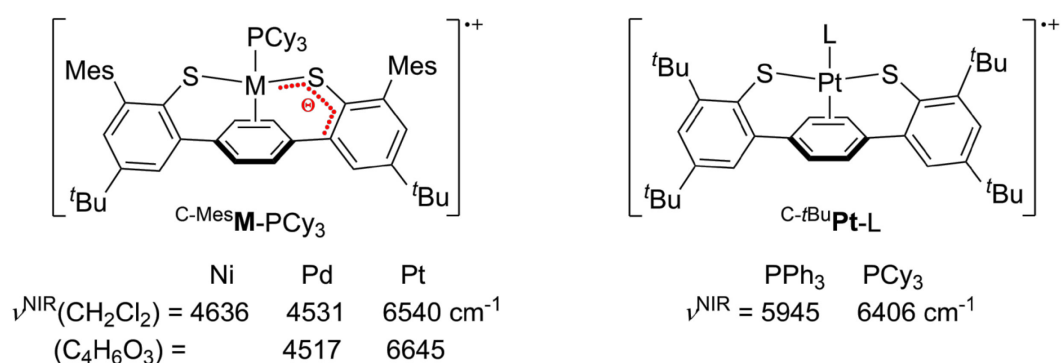
In dieser Veröffentlichung konnte gezeigt werden, dass die Verdrillung der Ligandarme zueinander, ausgedrückt an Hand des Torsionswinkels, einen höheren Einfluss auf die elektronische Struktur ausübt als die Donoreigenschaften der Co-Liganden. Dabei korreliert die Spindichte am Schwefel mit der Größe des Torsionswinkels. Wobei mit steigendem Θ die Spindichte am Schwefel abnimmt. Des Weiteren konnte gezeigt werden, dass das verbrückende π -System durch Einschränkung der Rotation der Ligandarme um die Pt-S-Achse eine verbesserte Überlappung der Schwefelorbitale mit denen des Aryls im Thiophenolat bewirkt.

Dies führt zu einer Verringerung der Spindichte am Metall und zu einer Erhöhung im Aromaten des Thiophenolats. Das verbrückende π -System erhöht darüber hinaus durch Wechsel von einem monodentaten zu einem mehrzähligen Liganden die thermodynamische Stabilität des Radikal-Kations gegenüber der offenen Form.

3.3. Publikation III: Influencing Factors on the Electronic Structures of Complex Radical-Ligand Ions of Group 10 Metal Triad

Mews, N. M.; Reimann, M.; Hörner, G.; Schubert, H.; Berkefeld, A., unveröffentlicht

Diese Veröffentlichung beschäftigt sich mit dem Zusammenspiel zwischen Metall und Ligand und dessen Auswirkung auf die elektronischen Eigenschaften der Thiyli-Thiolat-Komplexe eines 1,4-Terphenyldithiophenolat-Liganden am Beispiel der Gruppe 10 Metalle (Schema 4). Des Weiteren wird der Einfluss des Gegenions, der Co-Liganden und der Substituenten am Hauptliganden auf die elektronischen Eigenschaften untersucht. Die Synthese von $^{C\text{-Mes}/t\text{Bu}}\mathbf{M}\text{-L}$ ($\mathbf{M} = \text{Pd}, \text{Pt}$) erfolgt über eine Salzmetathese-Reaktion, wie sie schon für $^{C\text{-Mes}}\mathbf{Pt}\text{-PPh}_3$ beschrieben ist (Schema 2).^[50] Dabei wird für Palladium *trans*- py_2PdCl_2 als Vorstufe verwendet. $^{C\text{-Mes}}\mathbf{Ni}\text{-PCy}_3$ wird nach der Vorschrift von Berkefeld *et al.* dargestellt.^[52] Ein Vergleich der Kristallstrukturen von $^{C\text{-Mes}}\mathbf{M}\text{-PCy}_3$ ($\mathbf{M} = \text{Ni}, \text{Pd}, \text{Pt}$) zeigt, dass das deutlich kleinere Nickel durch seine kürzeren M-S- und M-Aryl-Bindungen eine Wechselwirkung zwischen dem Co-Liganden PCy_3 und den Mesityl-Gruppen des Hauptliganden forciert. Dies resultiert in einer Verzerrung des Komplexes, beobachtbar durch Unterschiede in den Torsionswinkeln Θ ($4/13^\circ$) und in den Ni-S-Bindungslängen (2,222/2,259 Å). Dabei nimmt der M-P-Abstand im Vergleich zu Platin und Palladium zu. Auf Grund der größeren Atomradien für Palladium und Platin tritt diese Verzerrung nicht auf. Die Größe der Ligandtasche kann durch den Austausch der Mesityl-Gruppen durch *t*Bu verringert werden. Der so erhöhte sterische Druck zwischen Ligand und Co-Ligand führt zu eine Erhöhung der Torsionswinkel Θ um $\sim 10^\circ$ für PCy_3 und PPh_3 .



Schema 4: NIR-Absorptionsbanden bei ν^{NIR} von $[^{C\text{-Mes}}\mathbf{M}\text{-PCy}_3]\text{BArF}$ in CH_2Cl_2 (-90°C) und in Propylencarbonat (-40°C) und von $[^{C\text{-tBu}}\mathbf{Pt}\text{-L}]\text{NTf}_2$ in CH_2Cl_2 bei 20°C . Rot eingezeichnet ist der Torsionswinkel Θ entlang der $\text{Pt-S-(C-C)}_{\text{Ar}}$ -Einheit.

In den CV-Messungen zeigen alle Komplexe zwei oder mehr Oxidationen, wobei für Platin und Palladium die erste elektrochemisch reversibel ist. Der Einfluss der Substituenten und Co-Liganden auf die Formalpotentiale ist im Vergleich zur Variation des Metalls deutlich geringer. Dies ist im Einklang mit einer hauptsächlich Schwefel-zentrierten Oxidation. Die Ursache für die große Potentialdifferenz zwischen Pt und Pd wird durch eine unterschiedlich hohe Metallbeteiligung verursacht. Die Oxidationen von $^{C-Mes}Ni-PCy_3$ sind im Gegensatz zu Palladium und Platin alle elektrochemisch irreversibel und das Produkt der chemischen Oxidation kann nur *in situ* charakterisiert werden, da $[^{C-Mes}Ni-PCy_3]^+$ sich schon bei $-90\text{ }^\circ\text{C}$ merklich zersetzt. Die Beständigkeit der Radikal-Komplexe kann sowohl für $[^{C-Mes}Ni-PCy_3]^+$ als auch für $[^{C-tBu}Pt-Ph_3]^+$ durch den Austausch von NTf_2^- gegen ein schwächer koordinierendes Anion wie $BArF^-$ verbessert werden.

Die Oxidation von $^{C-Mes/tBu}M-PCy_3$ ($M = Pd, Pt$) mit $[Fc^+][NTf_2^-]$ und $[(4-BrC_6H_4)_3N]BArF$ in CH_2Cl_2 liefert nach Eindiffusion von Pentan im Fall der Platin-Komplexe violette und im Fall des Palladiums rotbraune kristalline Verbindungen. Aus den Molekülstrukturen der Kationen im Einkristall ergibt sich, dass die geometrische Struktur unter Kontraktionen der M-S-Bindung erhalten bleibt und die Asymmetrie in den Torsionswinkeln und in den Bindungslängen für $[^{C-Mes}M-PCy_3]^+$ ($M = Pd, Pt$) und $[^{C-tBu}Pt-PPh_3]^+$ gegenüber der Neutralverbindung zunimmt. Der deutliche Unterschied in den S-C-Bindungslängen der ionischen Pd-Verbindung weist auf eine nicht-symmetrische elektronische Struktur hin. X-Band cw-ESR-Messungen zeigen, dass der Austausch von Platin gegen Palladium in $^{C-Mes}M-L$ ($L = PPh_3, PCy_3$) zu geringeren g -Anisotropien und g_{33} -Werten führt. Dies ist im Einklang mit einer Verringerung der Metallbeteiligung im Pd-Fall. Diese Verringerung kann auch durch den Austausch des Mes-Substituenten gegen das sterisch anspruchsvollere tBu erreicht werden, wobei die Auswirkungen im Vergleich zur Metallvariation geringer sind. Dies spiegelt auch die bathochrome Verschiebung um 100 nm von $[^{C-tBu}Pt-PCy_3]^+$ bei gleichbleibender Oszillatorstärke gegenüber $[^{C-Mes}Pt-PCy_3]^+$ wider (Schema 4).

Die UV/vis/NIR-, ESR- und CV-Messungen deuten darauf hin, dass die Beteiligung des Metalls an den Grenzorbitalen in der Reihe $Pt > Ni > Pd$ abnimmt. Die Lage und Form der NIR-Banden von $[^{C-Mes}M-PCy_3]^+$ ($M = Pd, Pt$) bleiben von der Lösemittelpolarität unbeeinflusst (Schema 4). Zusammen mit den DFT-Rechnungen wird $[^{C-Mes}Pt-PCy_3]^+$ der Klasse III und $[^{C-Mes}Pd-PCy_3]^+$ der Klasse II-III zugeordnet. Der Vergleich von $[^{C-Mes}Pt-PCy_3]^+$ mit $[^{C-Mes}Pt-PPh_3]^+$, das ein Klasse II-III System darstellt, zeigt, dass die elektronische Struktur vor

allem von der Lage des Metalls in der Ligandtasche und u.a. an Hand der Größe des Torsionswinkels Θ erkannt werden kann.

In dieser Arbeit konnte gezeigt werden, dass die *trans*-Anordnung der Thiolat-Einheiten, gepaart mit einer flexiblen η^2 -Koordination des verbrückenden π -Systems, es dem komplexierten Metall ermöglicht, den für sich passenden Bindungsmodus einzunehmen. Welcher Bindungsmodus dabei bevorzugt wird, wird durch Größe und elektronische Struktur des Metalls bestimmt. Die Präferenz für einen Bindungsmodus kann mit Hilfe der Interligand-Wechselwirkung zwischen Hauptligand und Co-Ligand durch Wahl geeigneter Substituenten feinjustiert werden. Allein der Austausch von PPh_3 durch PCy_3 ermöglicht den Wechsel von einem System der Klasse II-III zu einem der Klasse III. Dies steht im Kontrast zu den tetradentaten und *cis*-bindigen bidentaten Liganden, die durch ihre Starrheit dem Metall sowohl den Bindungsmodus als auch die Bindungsgeometrie aufzwingen. Aus den DFT-Rechnungen geht hervor, dass die berechnete Metall-Spindichte stark von der Methode und den verwendeten Funktionalen für die Strukturoptimierung abhängt, so dass es zu einer erheblichen Schwankung in der berechneten Metall-Spindichte kommt. Dadurch muss eine Korrelation der Metall-Spindichten mit experimentellen Daten mit Vorsicht genossen werden.

4. Schlussfolgerung

Die Wechselwirkung zwischen Metall und Ligand spielt, wie in der Einleitung erwähnt, eine entscheidende Rolle bei der Ausprägung der chemischen und physikalischen Eigenschaften von Ligand-zentrierten Radikal-Komplexen. Daher ist ein genaues Verständnis der Metall-Ligand-Interaktion wichtig, um Komplexe mit definierten elektronischen Eigenschaften herstellen zu können. Da aber die genauen Mechanismen dieser Wechselwirkung noch nicht abschließend verstanden sind und somit eine kontrollierte Beeinflussung schwierig ist, wurde mit der hier vorgestellten Arbeit ein Beitrag zum Verständnis des Zusammenspiels von geometrischen und elektronischen Faktoren auf die Beeinflussung dieser Wechselwirkung geleistet werden.

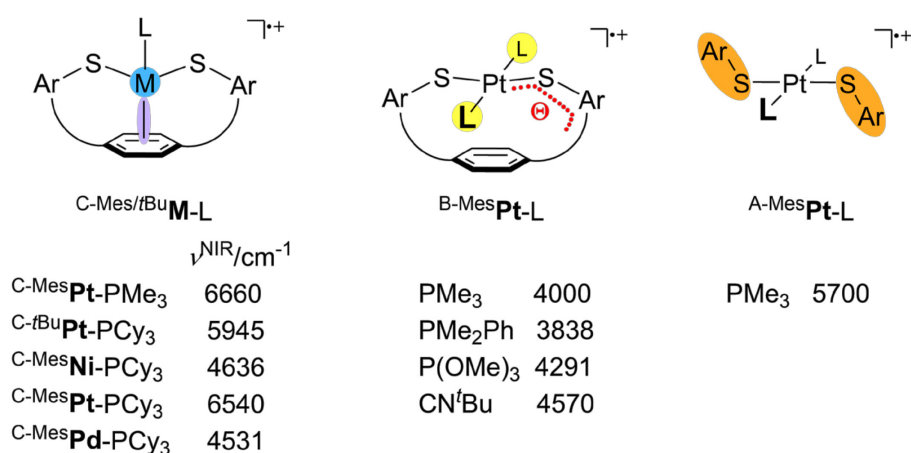


Abbildung 6: Experimentell in CH₂Cl₂ bestimmte NIR-Absorptionsbanden bei ν^{NIR} untersuchter Gruppe 10-Radikal-Komplexe. Rot eingezeichnet ist der Torsionswinkel Θ entlang der Pt-S-(C-C)_{Ar}-Einheit.

Am Beispiel der Thiyl-Thiolat-Komplexe der Gruppe 10 Metalle eines flexiblen 1,4-Terphenyldithiophenolato-Liganden konnte in dieser Arbeit gezeigt werden, welche Rolle die elektronische Struktur und die geometrische Anordnung in der Metall-Ligand-Wechselwirkung spielen. Dabei können fünf Stellschrauben für die Beeinflussung der Eigenschaften der Koordinationsverbindungen unterschieden werden (Abbildung 6, farbige Markierungen). Die erste ist die flexible η^2 -Koordination zum π -System, gesteuert durch die Anzahl der Co-Liganden (Abbildung 6, lila). Die daraus resultierende Verkippung der Koordinationsebene um 90° hat einen starken Einfluss auf die elektronische Struktur des Komplexes, da die Überlappung der Schwefel-Orbitale mit denen des Metalls verändert wird. Es kommt zu einem Wechsel von einem Radikal-Ligand Komplex mit lokalisierter zu einem mit delokalisierten elektronische Struktur und zu einer bathochromen Verschiebung der NIR-Bande um 950 nm im Falle der Komplexe mit dem Co-Liganden PMe₃ (Abbildung 6, links und Mitte).^[50] Einen ähnlich großen Einfluss besitzt die zweite Stellschraube, nämlich die Änderung

der elektronischen Struktur durch Variation des Metalls (Abbildung 6, blau). Obwohl Platin und Palladium ähnliche Atomradien aufweisen, verschiebt sich die Bande des Palladiums auf Grund seiner geringeren Beteiligung an den Grenzorbitalen um 680 nm bathochrom (Abbildung 6, links). Eine weitere Stellschraube ist die Drehbarkeit der Ligandarme um die Pt-S-Achse, die an Hand eines monodentaten Liganden bei gleichbleibender chemischer Umgebung für das Platin untersucht wurde (Abbildung 6, orange).^[53] Durch die Rotationsfreiheit um die Pt-S-Achse verringert sich die Wechselwirkung zwischen Schwefel- und π -Orbitalen des Thiophenolats, so dass die Spindichte weitgehend in der S-M-S-Einheit lokalisiert wird. Durch die Anordnung erhöht sich die Metall-Beteiligung an den Grenzorbitalen und es kommt zu einer hypsochromen Verschiebung um 750 nm der NIR-Bande im Vergleich zur bidentaten Form (Abbildung 6, rechts). Das Ändern der Torsionswinkel Θ durch Variation des Co-Liganden führt im Vergleich zu den anderen Einflussmöglichkeiten zu einer geringeren Verschiebung der NIR-Bande (Abbildung 6, rot, Mitte).^[53] Durch die Änderung des Co-Liganden ändert man nicht nur die Donoreigenschaften und damit die elektronische Struktur, sondern auch den sterischen Anspruch. Es hat sich gezeigt, dass dabei die Änderung des Torsionswinkels einen stärkeren Einfluss besitzt als der elektronische Einfluss des Co-Liganden. Die letzte Stellschraube ist die Ligandtasche, deren Größe durch die Wechselwirkung zwischen den Substituenten am Hauptliganden und den Co-Liganden variiert werden kann (Abbildung 6, gelb). So ändert sich die Bandenlage zwischen den Komplexen $^{C-Mes/tBu}Pt-L$ ($L = PPh_3, PCy_3$) maximal um 177 nm und die Stabilität nimmt durch Einführen der t Bu-Gruppe ab (Abbildung 6, links). Vergleicht man das Zusammenspiel von Metallen mit verschiedenen Atomradien und dem Liganden, so stellt man fest, dass es eine Mindestionengröße gibt, die der Ligand komplexieren kann. Nickel stellt dabei die Größe dar, die gerade noch vom 1,4-Terphenyldithiophenolat-Liganden komplexiert werden kann, was zu einer deutlichen Verzerrung im Komplex und zu einer Instabilität führt.

Fasst man nun die Auswirkungen der fünf Stellschrauben zusammen, so ergibt sich, dass das komplexierte Metall auf Grund seiner elektronischen Struktur und Größe eine Präferenz für einen Bindungsmodus besitzt. Durch die *trans*-Anordnung der Thiolat-Einheiten und die flexible η^2 -Anbindung an das π -System kann der Ligand mit geeigneten Co-Liganden dem bevorzugten Bindungsmodus des Metalls entsprechen. Diese Flexibilität in der Komplexierung von Metallen stellt eine Neuerung in den Radikal-Komplexen dar. Die zurzeit bekannten bidentaten und tetradentanten Systeme (Schema 1, Abbildung 3 und Abbildung 4) zeichnen sich durch ihre Starrheit in der Komplexierung von Metallen aus. Die *cis*-Anordnung der

Heteroatome in den bidentaten Liganden schränkt sie sowohl im Bisswinkel als auch in ihrer Torsionsfähigkeit ein. Diese Starrheit wird bei den tetradentaten Liganden noch verstärkt. Dadurch ist die Bandbreite an möglichen Eigenschaften und die Feinjustierung gegenüber dem hier vorgestellten System deutlich eingeschränkt.

Die hier vorgestellten Komplexe eignen sich durch ihre Flexibilität daher dazu in weiterführenden Studien die Auswirkungen des sterischen Faktors auf die Reaktivität systematisch zu untersuchen. Zusammen mit den Ergebnissen aus meiner Doktorarbeit sollte es dann möglich sein, die Auswirkungen des sterischen Faktors bei der Synthese von Biomimetika oder anderen Komplexen mit dezidierten Eigenschaften einschätzen und berücksichtigen zu können.

5. Literatur

- [1] a) P. J. Chirik, K. Wieghardt, *Science* **2010**, *327*, 794-795; b) V. K. Praneeth, M. R. Ringenberg, T. R. Ward, *Angew. Chem. Int. Ed.* **2012**, *51*, 10228-10234; c) V. Lyaskovskyy, B. de Bruin, *ACS Catalysis* **2012**, *2*, 270-279; d) O. R. Luca, R. H. Crabtree, *Chem. Soc. Rev.* **2013**, *42*, 1440-1459; e) J. Jacquet, K. Cheaib, Y. Ren, H. Vezin, M. Orio, S. Blanchard, L. Fensterbank, M. Desage-El Murr, *Chemistry* **2017**, *23*, 15030-15034.
- [2] a) Y. Qi, Z. Y. Wang, *Macromolecules* **2003**, *36*, 3146-3151; b) M. D. Ward, *J. Solid State Electrochem.* **2005**, *9*, 778-787; c) P. Deplano, L. Pilia, D. Espa, M. L. Mercuri, A. Serpe, *Coord. Chem. Rev.* **2010**, *254*, 1434-1447; d) R. J. Mortimer, *Annu. Rev. Mater. Res.* **2011**, *41*, 241-268; e) W. Kaim, *Coord. Chem. Rev.* **2011**, *255*, 2503-2513.
- [3] a) M. A. Halcrow, G. Christou, *Chem. Rev.* **1994**, *94*, 2421-2481; b) E. I. Solomon, R. K. Szilagyi, S. DeBeer George, L. Basumallick, *Chem. Rev.* **2004**, *104*, 419-458; c) P. Venkateswara Rao, R. H. Holm, *Chem. Rev.* **2004**, *104*, 527-559; d) E. I. Solomon, S. I. Gorelsky, A. Dey, *J. Comput. Chem.* **2006**, *27*, 1415-1428; e) M. Orio, O. Jarjayes, H. Kanso, C. Philouze, F. Neese, F. Thomas, *Angew. Chem. Int. Ed.* **2010**, *49*, 4989-4992; f) W. Kaim, B. Schwederski, *Coord. Chem. Rev.* **2010**, *254*, 1580-1588; g) Y. Yu, C. Cui, X. Liu, I. D. Petrik, J. Wang, Y. Lu, *J. Am. Chem. Soc.* **2015**, *137*, 11570-11573; h) J. A. Denny, M. Y. Darensbourg, *Chem. Rev.* **2015**, *115*, 5248-5273; i) C. Hu, Y. Yu, J. Wang, *Chem. Commun.* **2017**, *53*, 4173-4186.
- [4] W. Kaim, *Coord. Chem. Rev.* **1987**, *76*, 187-235.
- [5] P. J. Blower, J. R. Dilworth, *Coord. Chem. Rev.* **1987**, *76*, 121-185.
- [6] a) K. Ray, T. Weyhermüller, A. Goossens, M. W. Craje, K. Wieghardt, *Inorg. Chem.* **2003**, *42*, 4082-4087; b) H. Alves, D. Simão, I. Cordeiro Santos, V. Gama, R. Teives Henriques, H. Novais, M. Almeida, *Eur. J. Inorg. Chem.* **2004**, *2004*, 1318-1329; c) K. Ray, T. Weyhermüller, F. Neese, K. Wieghardt, *Inorg. Chem.* **2005**, *44*, 5345-5360; d) K. Ray, A. Begum, T. Weyhermüller, S. Piligkos, J. van Slageren, F. Neese, K. Wieghardt, *J. Am. Chem. Soc.* **2005**, *127*, 4403-4415; e) K. Ray, E. Bill, T. Weyhermüller, K. Wieghardt, *J. Am. Chem. Soc.* **2005**, *127*, 5641-5654.
- [7] F. Feigl, M. Fürth, *Monatsh. Chem.* **1927**, *48*, 445-450.
- [8] a) A. Davison, N. Edelstein, R. H. Holm, A. H. Maki, *J. Am. Chem. Soc.* **1963**, *85*, 2029-2030; b) S. I. Shupack, E. Billig, R. J. H. Clark, R. Williams, H. B. Gray, *J. Am. Chem. Soc.* **1964**, *86*, 4594-4602; c) E. I. Stiefel, J. H. Waters, E. Billig, H. B. Gray, *J. Am. Chem. Soc.* **1965**, *87*, 3016-3017.
- [9] a) F. Rohrscheid, A. L. Balch, R. H. Holm, *Inorg. Chem.* **1966**, *5*, 1542-1551; b) H. B. Gray, *Coord. Chem. Rev.* **1966**, *1*, 156-163; c) A. L. Balch, R. H. Holm, *J. Am. Chem. Soc.* **1966**, *88*, 5201-5209; d) R. Eisenberg, H. B. Gray, *Inorg. Chem.* **2011**, *50*, 9741-9751.
- [10] a) A. Volbeda, M. H. Charon, C. Piras, E. C. Hatchikian, M. Frey, J. C. Fontecilla-Camps, *Nature* **1995**, *373*, 580-587; b) D. Shimizu, A. Osuka, *Chem. Sci.* **2018**, *9*, 1408-1423.
- [11] a) K. P. Jensen, B. O. Roos, U. Ryde, *J. Inorg. Biochem.* **2005**, *99*, 45-54; b) R. Garcia-Serres, R. M. Davydov, T. Matsui, M. Ikeda-Saito, B. M. Hoffman, B. H. Huynh, *J. Am. Chem. Soc.* **2007**, *129*, 1402-1412.
- [12] a) F. Murad, *Angew. Chem. Int. Ed.* **1999**, *38*, 1856-1868; b) J. A. McCleverty, *Chem. Rev.* **2004**, *104*, 403-418.
- [13] a) P. Chaudhuri, M. Hess, J. Müller, K. Hildenbrand, E. Bill, T. Weyhermüller, K. Wieghardt, *J. Am. Chem. Soc.* **1999**, *121*, 9599-9610; b) D. L. Broere, R. Plessius, J. I.

- van der Vlugt, *Chem. Soc. Rev.* **2015**, *44*, 6886-6915; c) J. Jacquet, P. Chaumont, G. Gontard, M. Orio, H. Vezin, S. Blanchard, M. Desage-El Murr, L. Fensterbank, *Angew. Chem. Int. Ed.* **2016**, *55*, 10712-10716; d) H. Nishiyama, H. Ikeda, T. Saito, B. Kriegel, H. Tsurugi, J. Arnold, K. Mashima, *J. Am. Chem. Soc.* **2017**, *139*, 6494-6505.
- [14] R. Chauhan, M. Moreno, D. M. Banda, F. P. Zamborini, C. A. Grapperhaus, *RSC Advances* **2014**, *4*, 46787-46790.
- [15] X. M. Ren, H. Okudera, R. K. Kremer, Y. Song, C. He, Q. J. Meng, P. H. Wu, *Inorg. Chem.* **2004**, *43*, 2569-2576.
- [16] H. Bois, N. G. Connelly, J. G. Crossley, J.-C. Guillorit, G. R. Lewis, A. G. Orpen, P. Thornton, *J. Chem. Soc., Dalton Trans.* **1998**, 2833-2838.
- [17] M. Urbani, M. Gratzel, M. K. Nazeeruddin, T. Torres, *Chem. Rev.* **2014**, *114*, 12330-12396.
- [18] a) N. Kitajima, K. Whang, Y. Moro-oka, A. Uchida, Y. Sasada, *J. Chem. Soc., Chem. Commun.* **1986**, 1504-1505; b) D. Sellmann, J. Sutter, *Acc. Chem. Res.* **1997**, *30*, 460-469; c) P. Chaudhuri, M. Hess, U. Flörke, K. Wieghardt, *Angew. Chem. Int. Ed.* **1998**, *37*, 2217-2220; d) I. Dance, *Dalton Trans.* **2010**, *39*, 2972-2983; e) E. P. Broering, S. Dillon, E. M. Gale, R. A. Steiner, J. Telsler, T. C. Brunold, T. C. Harrop, *Inorg. Chem.* **2015**, *54*, 3815-3828; f) S. Hirota, Y. W. Lin, *J. Biol. Inorg. Chem.* **2018**, *23*, 7-25.
- [19] a) A. Vlcek, Editor, *Coord. Chem. Rev.* **2010**, *254*, 1357-1588; b) P. J. Chirik, Editor, *Inorg. Chem.* **2011**, *50*, 9737-10516; c) J. R. E. Winkler, Editor, *Coord. Chem. Rev.* **2011**, *255*, 617-990; d) K. E. Hindson, B. E. de Bruin, Editors, *Eur. J. Inorg. Chem.* **2012**, *2012*, 340-580; e) T. E. Storr, R. E. Mukherjee, Editors, *Inorg. Chem.* **2018**, *57*, 9577-10480.
- [20] C. K. Jørgensen, *Coord. Chem. Rev.* **1966**, *1*, 164-178.
- [21] a) R. K. Szilagyi, B. S. Lim, T. Glaser, R. H. Holm, B. Hedman, K. O. Hodgson, E. I. Solomon, *J. Am. Chem. Soc.* **2003**, *125*, 9158-9169; b) K. Ray, S. Debeer George, E. I. Solomon, K. Wieghardt, F. Neese, *Chemistry* **2007**, *13*, 2783-2797; c) K. Ray, T. Petrenko, K. Wieghardt, F. Neese, *Dalton Trans.* **2007**, 1552-1566; d) S. Sproules, K. Wieghardt, *Coord. Chem. Rev.* **2011**, *255*, 837-860.
- [22] M. D. Ward, J. A. McCleverty, *J. Chem. Soc., Dalton Trans.* **2002**, 275-288.
- [23] a) C. G. Pierpont, R. M. Buchanan, *Coord. Chem. Rev.* **1981**, *38*, 45-87; b) C. G. Pierpont, *Coord. Chem. Rev.* **2001**, *216-217*, 99-125; c) P. Chaudhuri, K. Wieghardt, in *Prog. Inorg. Chem., Vol. 50*, **2002**, pp. 151-216; d) J. J. Loughrey, S. Sproules, E. J. McInnes, M. J. Hardie, M. A. Halcrow, *Chemistry* **2014**, *20*, 6272-6276.
- [24] a) N. A. Ketterer, H. Fan, K. J. Blackmore, X. Yang, J. W. Ziller, M. H. Baik, A. F. Heyduk, *J. Am. Chem. Soc.* **2008**, *130*, 4364-4374; b) M. M. Khusniyarov, K. Harms, O. Burghaus, J. Sundermeyer, B. Sarkar, W. Kaim, J. van Slageren, C. Duboc, J. Fiedler, *Dalton Trans.* **2008**, 1355-1365.
- [25] a) P. Chaudhuri, C. N. Verani, E. Bill, E. Bothe, T. Weyhermüller, K. Wieghardt, *J. Am. Chem. Soc.* **2001**, *123*, 2213-2223; b) X. Sun, H. Chun, K. Hildenbrand, E. Bothe, T. Weyhermüller, F. Neese, K. Wieghardt, *Inorg. Chem.* **2002**, *41*, 4295-4303; c) D. Herebian, E. Bothe, F. Neese, T. Weyhermüller, K. Wieghardt, *J. Am. Chem. Soc.* **2003**, *125*, 9116-9128; d) S. Kokatam, T. Weyhermüller, E. Bothe, P. Chaudhuri, K. Wieghardt, *Inorg. Chem.* **2005**, *44*, 3709-3717; e) S. L. Kokatam, P. Chaudhuri, T. Weyhermüller, K. Wieghardt, *Dalton Trans.* **2007**, 373-378.
- [26] a) Y. Shimazaki, T. D. Stack, T. Storr, *Inorg. Chem.* **2009**, *48*, 8383-8392; b) F. Thomas, *Dalton Trans.* **2016**, *45*, 10866-10877; c) R. M. Clarke, K. Herasymchuk, T. Storr, *Coord. Chem. Rev.* **2017**, *352*, 67-82.
- [27] a) R. H. Holm, A. L. Balch, A. Davison, A. H. Maki, T. E. Berry, *J. Am. Chem. Soc.* **1967**, *89*, 2866-2874; b) C. E. Forbes, A. Gold, R. H. Holm, *Inorg. Chem.* **1971**, *10*,

- 2479-2485; c) D. Herebian, E. Bothe, E. Bill, T. Weyhermüller, K. Wieghardt, *J. Am. Chem. Soc.* **2001**, *123*, 10012-10023; d) P. Ghosh, A. Begum, D. Herebian, E. Bothe, K. Hildenbrand, T. Weyhermüller, K. Wieghardt, *Angew. Chem. Int. Ed.* **2003**, *42*, 563-567.
- [28] J. A. McCleverty, in *Prog. Inorg. Chem.*, **2007**, pp. 49-221.
- [29] A. Falceto, D. Casanova, P. Alemany, S. Alvarez, *Chemistry* **2014**, *20*, 14674-14689.
- [30] W. Kaim, *Inorg. Chem.* **2011**, *50*, 9752-9765.
- [31] M. W. Lynch, D. N. Hendrickson, B. J. Fitzgerald, C. G. Pierpont, *J. Am. Chem. Soc.* **1984**, *106*, 2041-2049.
- [32] a) D. G. Brown, J. T. Reinprecht, G. C. Vogel, *Inorg. Nucl. Chem. Lett.* **1976**, *12*, 399-404; b) G. A. Razuvaev, V. K. Cherkasov, G. A. Abakumov, *J. Organomet. Chem.* **1978**, *160*, 361-371; c) J. Rall, W. Kaim, *J. Chem. Soc., Faraday Trans.* **1994**, *90*, 2905-2908.
- [33] C. Chatgililoglu, C. Ferreri, M. Guerra, A. Samadi, V. W. Bowry, *J. Am. Chem. Soc.* **2017**, *139*, 4704-4714.
- [34] K. D. Demadis, C. M. Hartshorn, T. J. Meyer, *Chem. Rev.* **2001**, *101*, 2655-2686.
- [35] a) Y. Shimazaki, T. Yajima, F. Tani, S. Karasawa, K. Fukui, Y. Naruta, O. Yamauchi, *J. Am. Chem. Soc.* **2007**, *129*, 2559-2568; b) Y. Shimazaki, N. Arai, T. J. Dunn, T. Yajima, F. Tani, C. F. Ramogida, T. Storr, *Dalton Trans.* **2011**, *40*, 2469-2479.
- [36] B. S. Brunschwig, C. Creutz, N. Sutin, *Chem. Soc. Rev.* **2002**, *31*, 168-184.
- [37] M. B. Robin, P. Day, *Adv. Inorg. Chem. Radiochem.* **1968**, *10*, 247-422.
- [38] N. S. Hush, *Coord. Chem. Rev.* **1985**, *64*, 135-157.
- [39] S. Kimura, E. Bill, E. Bothe, T. Weyhermüller, K. Wieghardt, *J. Am. Chem. Soc.* **2001**, *123*, 6025-6039.
- [40] M. Kaupp, *J. Comput. Chem.* **2007**, *28*, 320-325.
- [41] D. Enright, S. Gambarotta, G. P. A. Yap, P. H. M. Budzelaar, *Angew. Chem. Int. Ed.* **2002**, *41*, 3873-3876.
- [42] a) R. Williams, E. Billig, J. H. Waters, H. B. Gray, *J. Am. Chem. Soc.* **1966**, *88*, 43-50; b) W. B. Connick, H. B. Gray, *J. Am. Chem. Soc.* **1997**, *119*, 11620-11627; c) J. S. Pap, F. L. Benedito, E. Bothe, E. Bill, S. D. George, T. Weyhermüller, K. Wieghardt, *Inorg. Chem.* **2007**, *46*, 4187-4196; d) S. Poturovic, M. S. Mashuta, C. A. Grapperhaus, *Angew. Chem. Int. Ed. Engl.* **2005**, *44*, 1883-1887.
- [43] a) H. B. Gray, R. Williams, I. Bernal, E. Billig, *J. Am. Chem. Soc.* **1962**, *84*, 3596-3597; b) M. J. Baker-Hawkes, E. Billig, H. B. Gray, *J. Am. Chem. Soc.* **1966**, *88*, 4870-4875.
- [44] A. Davison, N. Edelstein, R. H. Holm, A. H. Maki, *J. Am. Chem. Soc.* **1964**, *86*, 2799-2805.
- [45] G. N. Schrauzer, V. Mayweg, *J. Am. Chem. Soc.* **1962**, *84*, 3221-3221.
- [46] a) T. Kurahashi, H. Fujii, *J. Am. Chem. Soc.* **2011**, *133*, 8307-8316; b) L. Chiang, A. Kochem, O. Jarjays, T. J. Dunn, H. Vezin, M. Sakaguchi, T. Ogura, M. Orio, Y. Shimazaki, F. Thomas, T. Storr, *Chemistry* **2012**, *18*, 14117-14127; c) L. Chiang, K. Herasymchuk, F. Thomas, T. Storr, *Inorg. Chem.* **2015**, *54*, 5970-5980.
- [47] V. Bachler, G. Olbrich, F. Neese, K. Wieghardt, *Inorg. Chem.* **2002**, *41*, 4179-4193.
- [48] T. J. Morsing, S. N. MacMillan, J. W. Uebler, T. Brock-Nannestad, J. Bendix, K. M. Lancaster, *Inorg. Chem.* **2015**, *54*, 3660-3669.
- [49] N. M. Mews, A. Berkefeld, unpublizierte Ergebnisse
- [50] N. M. Mews, A. Berkefeld, G. Hörner, H. Schubert, *J. Am. Chem. Soc.* **2017**, *139*, 2808-2815.
- [51] L. Malatesta, F. Bonati, *Isocyanide Complexes of Metals*, Wiley-Interscience Publication, London, **1969**.
- [52] F. Koch, H. Schubert, P. Sirsch, A. Berkefeld, *Dalton Trans.* **2015**, *44*, 13315-13324.

[53] N. M. Mews, G. Hörner, H. Schubert, A. Berkefeld, *Inorg. Chem.* **2018**, *57*, 9670-9682.

Publikationen I-III

Publikation I

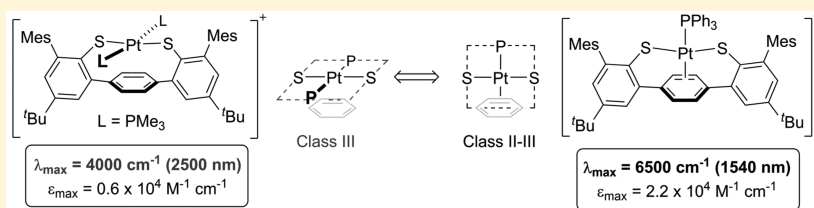
Controlling Near-Infrared Chromophore Electronic Properties through Metal–Ligand Orbital Alignment

Nicole M. Mews,[†] Andreas Berkefeld,^{*,†,‡} Gerald Hörner,^{*,‡} and Hartmut Schubert[†]

[†]Institut für Anorganische Chemie, Eberhard Karls Universität Tübingen, Auf der Morgenstelle 18, 72076 Tübingen, Germany

[‡]Institut für Chemie, Bioanorganische Chemie, TU Berlin, Straße des 17. Juni 135, 10623 Berlin, Germany

Supporting Information



ABSTRACT: Transition-metal complexes of radical ligands can exhibit low-energy electronic transitions in the near-infrared (NIR) spectral region. NIR band energy and intensity sensitively depend on the degree of electronic coupling of the chromophore. Using the example of open-shell complexes derived from platinum and a 1,4-terphenyldithiophenol, we present a novel approach toward spectroscopically distinct NIR dyes for which the degree of electronic coupling correlates with the relative orientation of radical ligand and metal orbitals. Ligand/metal orbital alignment is modulated by auxiliary phosphine donors and selectively results in electron localized Class II–III or delocalized Class III structures that display distinct NIR transitions at 6500 and 4000 cm^{-1} .

INTRODUCTION

The systematic search for defined mixed-valent electronic structures is of high interest from a scientific and technological point of view. At the molecular level, mixed-valency can give rise to intense electronic transitions in the low-energy near-infrared (NIR) spectral range, depending on the respective degree of charge delocalization.¹ With regard to application, for instance, controlling NIR absorptivity is relevant for glass optical fiber technology to modulate signal transduction in the 1300 and 1550 nm spectral ranges. Transition energy, intensity, and spectral width of an NIR band are determined by the respective type of charge-transfer (CT) mechanism.² Examples include π – π^* type interligand (LL) and metal-to-ligand (ML) CT in ligand radical ion complexes of bipyridine^{1a,b,2a,3} or aminiumpolypyridine,⁴ and metal centered interconfigurational transitions in complexes of Os^{III}.^{2a} Alternatively, electronic coupling of coplanar, π -conjugated mixed-valent ligands at a planar (d^8 -)metal site can give rise to intense ligand based intervalence (LLIV) CT or charge-resonance (CR) transitions, again depending on the degree of charge delocalization.^{1a,5} Prominent examples of ligand systems are benzenedi-⁶ and tetrathiophenols,⁷ catechols^{1c,8} and amino derivatives thereof,⁹ dithiolenes,¹⁰ salens¹¹ and thiosalens.¹²

Modification of chromophore systems has previously been achieved through variation of a number of parameters such as the conformational flexibility and substitution pattern of ligand(s), and the choice and number of metal bridges. A notable example is the family of transition-metal complexes of salen ligands schematized on the bottom left of Figure 1. In

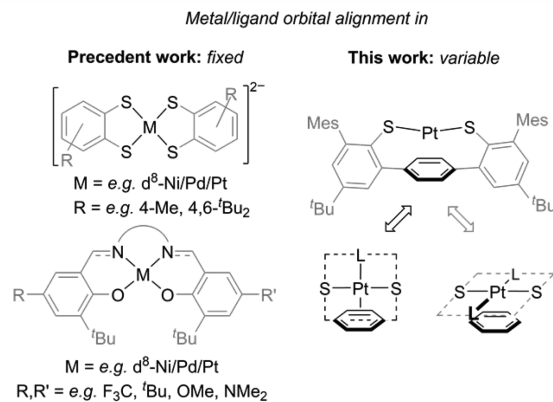


Figure 1. Left: Fixed alignment of the coordination plane of group 10 d^8 -metal ions of 1,2-benzenedithiol and salen ligands; Right: 1,4-terphenyldithiophenol complexes of d^8 -Pt with variable alignment of metal coordination plane and ligand.

solution of a weakly coordinating solvent such as CH_2Cl_2 , the one-electron oxidized complexes exist in the form of valence tautomers (thio)phenoxy/(thio)phenolato- M^{n+} and di(thio)phenolato- $M^{(n+1)+}$, depending on temperature.^{11c,13} The d -electron configuration of the metal bridge does not determine the character of the radical ligand orbitals but their relative contribution to the highest singly occupied MO (SOMO), and

Received: December 20, 2016

Published: February 10, 2017

so determines the strength of electronic coupling of the (thio)phenoxy and (thio)phenolato sites.^{11d,12,14}

Transition energy and intensity of the NIR bands correlate with the strength of electronic coupling along the metal bridge. For a given metal bridge, e.g., Ni, the electronic structure of the SOMO can be varied between delocalized Class III and electron localized Class II structures by changing the electronic properties of the *para*-substituents at the phenol moiety, cf. Figure 1, from, e.g., ^tBu with $\nu_{\max} = 4700 \text{ cm}^{-1}$ ($\epsilon_{\max} = 2.6 \times 10^4 \text{ M}^{-1} \text{ cm}^{-1}$, $\Delta\nu_{1/2} = 660 \text{ cm}^{-1}$, Class III)¹⁵ to NMe₂ with $\nu_{\max} = 8500 \text{ cm}^{-1}$ ($\epsilon_{\max} = 0.4 \times 10^4 \text{ M}^{-1} \text{ cm}^{-1}$, $\Delta\nu_{1/2} = 6650 \text{ cm}^{-1}$, Class II).^{11d,16} Expansion of the ligand field at Ni through coordination by axial pyridine donors^{11c,12,17} or solvent^{13a} shifts the valence tautomer equilibrium in favor of the bis(thio)phenolato-Ni(III) form. For a given ligand system, e.g., R, R' = ^tBu, the strength of electronic coupling of the phenoxy/phenolato moieties increases in the series Pd (Class II–III) < Ni (Class III) < Pt (Class III) and is associated with a blue-shift of ν_{\max} and an increase of ϵ_{\max} ($10^4 \text{ M}^{-1} \text{ cm}^{-1}$) in the same order 4100 (1.6) < 4700 (2.6) < 5450 (3.3) cm^{-1} .^{15b} Neese and Wieghardt had also substantiated the correlation of increasing superexchange efficiency and a blue-shift of low-energy transitions ν_{\max} for Class III 1,2-dithiosemiquinonato/dithiolato complexes $[(S_2^{2-})M^{II}(S_2^{\bullet-})]$, $S_2^{2-} = 4,6\text{-}^t\text{Bu}_2\text{-1,2-C}_6\text{H}_2\text{S}_2$ (cf. top left of Figure 1), which follow the order $M^{II} = \text{Pd}$ ($\nu_{\max} = 8800 \text{ cm}^{-1}$ [$\epsilon_{\max} = 2.5 \times 10^4/\text{M}^{-1} \text{ cm}^{-1}$]) < Pt (11100 [1.9×10^4]) < Ni (11200 [1.5×10^4]).^{6b,c} Herein, we report on a novel approach that uses the relative orientation of radical ligand and metal bridge orbitals as the key element to control the electronic and spectroscopic properties of a metal complex NIR chromophore.

RESULTS AND DISCUSSION

As summarized in Figures 1 and 2, open-shell complexes of Pt of a 1,4-terphenyldithiophenol have been prepared, and whose

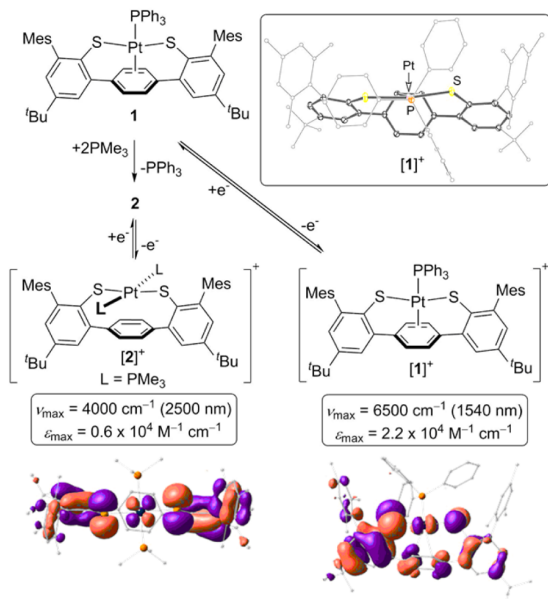


Figure 2. Preparation, structure, and key NIR absorption bands of complex cations $[2]^+$ and $[1]^+$. Bottom: Respective SOMOs (α -HOMOs) at the BLYP-35/TZVP/ZORA level; Inset: Molecular structure of $[1]^+$.

distinct NIR absorption profiles correlate with the parallel, $[1]^+$, or orthogonal, $[2]^+$, orientation of the metal coordination plane relative to the coplanar aryl-S π -systems. Auxiliary phosphine ligands aid in modulating the alignment of the metal coordination plane which determines the electronic character of the $[\text{ArS-Pt-S}^{\text{Ar}}]^{\bullet+}$ core structure and is responsible for the distinct NIR absorptivity of $[1]^+$ and $[2]^+$. Highest energy singly occupied molecular orbitals (SOMO; cf. bottom of Figure 2) are characterized by an intraligand electronic coupling via out-of-plane and in-plane metal d-orbitals in $[1]^+$ and $[2]^+$, respectively.

Parent complex **1** has been prepared by salt metathesis from *trans*-Pt(py)₂Cl₂,¹⁸ py = pyridine, ligand dipotassium salt, and PPh₃ in toluene solution, and is isolable as a light green crystalline solid in 49% yield. Exchange of PPh₃ for two PMe₃ affords yellow **2** quantitatively. Single crystal structure and solution NMR data provided in the Supporting Information (Figures S13 and S14, and Table S6, SI) support the parallel and orthogonal structural alignment of the metal coordination plane and S-aryl π -systems in neutral **1** and **2**, respectively.

One-electron oxidation using the 1,1'-diacetylferrocene cation yields the intensely colored ions $[1]^+$ and $[2]^+$ quantitatively. Cation $[1]^+$ is isolable as the $\text{N}(\text{SO}_2\text{CF}_3)_2^-$, NTf_2^- , salt in the form of maroon microcrystals in 77% yield, and displays a constant $\mu_{\text{eff}}([1]^+) = 2.3$ in CD_2Cl_2 solution over a 213–313 K range as expected for a $S = 1/2$ system. In clear contrast, $[2]\text{NTf}_2$ seems to be a kinetic reaction product and is metastable at $T \leq 253 \text{ K}$. Dark blue-purple solutions deteriorate noticeably if warmed to $T \geq 273 \text{ K}$ as the result of a redox reaction that involves thermally induced dissociation of one PMe₃ ligand from Pt. Variable temperature (VT) ¹H and ³¹P NMR spectroscopic monitoring indicates the partial reformation of **2** along with ill-defined diamagnetic products. Notably, addition of one equivalent of PMe₃ or, alternatively, $(\text{H}_5\text{C}_5)_2\text{Co}$ to $[2]\text{NTf}_2$ at $T = 203 \text{ K}$ instantaneously results in the almost quantitative ($\geq 95\%$) reduction back to **2**, as evidenced by ¹H and ³¹P NMR spectroscopy (cf. Figures S2 and S3, SI), proving the reaction stoichiometry correct. Accordingly, the susceptibility of a CD_2Cl_2 solution of an in situ prepared sample correlates with a constant $\mu_{\text{eff}}([2]^+) = 2.3$ at temperatures 193–233 K, identical to the value $\mu_{\text{eff}}([1]^+)$ obtained for the thermally robust $[1]^+$.

Chemical oxidation is consistent with the results of cyclic voltammetry at a Pt disc electrode in 0.1 M nBu₄NPF₆ CH_2Cl_2 solution at 290 K. Anodic potential sweeps relative to the $[\text{Fc}]^+/\text{Fc}$ couple, Fc = ferrocene, showed oxidation events at formal potentials of 60 and 727 mV in case of **1** and 117, 618, and 719 mV for **2**. All redox events are electrochemically reversible for **1**, whereas in case of **2** the second oxidation wave at 618 mV is not; cf. Figures S4–S5 and Tables S1–S4, SI. The redox couple **2**/ $[2]^+$ at 117 mV displays Nernstian behavior if the potential sweep direction is reversed at $E \leq 400 \text{ mV}$ but becomes chemically partially irreversible, $i_{\text{p,red}}/i_{\text{p,ox}} < 1$, otherwise. On the basis of this observation, the electrochemically reversible event at 719 mV is assigned to the $[2]^+/[2]^{2+}$ couple. Potential differences $\Delta E_{1/2}$ equal to 667 mV and 602 mV between the first and second redox couple of **1** and **2**, respectively, indicate that electronic stabilization of both monocations is sizable, and points to an extensive electronic coupling of redox-sites across Pt in both cases.

The molecular structure of $[1]^+$ shown in Figure 2 has been determined by X-ray crystallography.¹⁹ The general structural features indicate a contraction of the ligand-sphere upon

oxidation of **1**; Pt- π -arene, Pt-S, and C-S distances decrease by 0.02, 0.05, and 0.02 Å, respectively, whereas the Pt-P bond is elongated by 0.04 Å. These geometric changes reflect the overall π^* -character of the β -LUMO of $[1]^+$ (see Figure S*a*) that is characterized by significant Pt-S, Pt-C_{arene}, and S-C_{S-arene} interactions. Notably, Neese and Wieghardt also reported on the reduction of Pt-S and S-C_{arene} bond lengths for the one- and two-electron oxidized forms $[(S_2^{2-})Ni^{II}(S_2^{*-})]^-$ and $[Ni^{II}(S_2^{*-})_2]$ of the parent complex $[(4,6-(tBu)_2-1,2-C_6H_3S_2)_2Ni^{II}]^{2-}$.^{6b} In comparison to **1**, the square planar ligand environment at Pt is less distorted in $[1]^+$, and is indicated by an increase of the *trans*-P-Pt-(C=C) angle by 13° to 175°.

The quality of the diffraction data allowed for a highly accurate elucidation of the bond lengths, which are within ± 0.009 Å (3σ) for $[1]^+$ as compared to ± 0.021 Å for **1**. In particular, it renders the observed anisotropy in the Pt-S bond lengths ($\Delta d(\text{Pt-S}) = 1.4$ pm) a significant feature. DFT-derived (BP86-D3/TZVP/ZORA) structural metrics of $[1]^+$ confirm the experimentally observed dissymmetry about the S-Pt-S moiety ($\Delta d(\text{Pt-S}) = 3.1$ pm) and also indicate a dissymmetry of the electronic structure of the $[ArS-Pt-S^{Ar}]$ core in $[1]^+$. The close consistency of computed and experimental metrics, obtained in an experimentally calibrated DFT study of **1**, **2**, $[1]^+$ (Table S*5*, S*1*) and a related reference system $[(S_2^{2-})Pt(S_2^{*-})]^-$, $S_2^{2-} = 4\text{-Me-1,2-C}_6\text{H}_2\text{S}_2$, reported by Gray and co-workers^{6a} validates the optimized structure of elusive $[2]^+$. As seen for **1** and $[1]^+$, the structural features of $[2]^+$ greatly echo those of neutral **2**, particularly with respect to mutual orientation of the aryl-S π -systems and the coordination plane at Pt. The computed Pt-S bond contraction is slightly more pronounced in case of $[2]^+$ as compared to $[1]^+$; importantly, however, the contracted S-Pt-S vector is clearly isotropic in the case of $[2]^+$. These qualitative differences in the geometric structures of $[1]^+$ and $[2]^+$ persist in their electronic structures, as suggested by DFT results and clearly pointed out by EPR and UV/vis/NIR spectroscopy. Analysis of spin densities ρ computed at the BLYP-35-D3/TZVP/ZORA²⁰ level of theory identifies both cations as being predominantly ligand-centered radicals (cf. Table S*8*, S*1*). For both ions $[1]^+$ and $[2]^+$ > 99% of one spin integrate within the $[ArS-Pt-S^{Ar}]$ moiety but only ~11% localize at Pt. On the basis of the data, we suggest partial localization of spin on one ArS -moiety of $[ArS-Pt-S^{Ar}]^{*+}$ ($\rho(ArS)/\rho(Ar'S') \approx 1.91$) in the case of $[1]^+$, whereas a fully delocalized spin of a Class III $[ArS-Pt-S^{Ar}]^{*+}$ system prevails for $[2]^+$ ($\rho(ArS)/\rho(Ar'S') \approx 0.99$).

CW X-Band EPR spectral properties of isolated $[1]NTf_2$ and in situ generated $[2]NTf_2$ in an 1:1 CH_2Cl_2 /toluene solvent mixture corroborate the theoretical analysis and further substantiate the qualitative differences in their electronic structures as indicated by diverging sizes of g -anisotropy (Δg) and hyperfine coupling (hfc). In particular, while stronger g -anisotropy prevails for $[1]^+$, cation $[2]^+$ displays stronger overall hfc to naturally abundant ¹⁹⁵Pt ($I = 1/2$, 34%). Pertinent data are collected in Table 1. Although no further couplings are resolved in the rhombic derivative spectra, the decrease of line-widths observed for $[1]^+$ along $\Delta\nu_{1/2,1} = 76 > \Delta\nu_{1/2,2} = 43 > \Delta\nu_{1/2,3} = 13$ MHz with increasing magnetic field suggests a weak contribution of ³¹P- hfc . Both cations reveal moderate anisotropies in their g -values, reflecting the involvement of metal orbitals in the SOMO. This is corroborated by the clear distinction in g -anisotropies between $[2]^+$ ($\Delta g = 0.078$) and semiquinonate complexes of Pt^{II} ($\Delta g = 0.022$) reported by

Table 1. X-Band EPR Spectral Data of $[1]^+$ and $[2]^+$.^{a,b}

	g_1	g_2	g_3	Δg	A_1	A_2	A_3
$[1]^+$	2.174	2.082	2.005	0.169	175	184	239
$[2]^+$	2.124	2.063	2.046	0.078	325	490	291

^a NTf_2 -salts, CH_2Cl_2/C_7H_8 glass, 77 K; $A(^{195}Pt(I = 1/2, 34\%))$ in MHz. ^b $[1]^+$, 293 K: $g_{iso} = 2.089$, $A_{iso}(^{195}Pt) = 191$.

Halcrow,²¹ in which the radical is essentially ligand-localized. On the other hand, significant g -anisotropies reported for mixed-valent complexes $[(S_2^{2-})Pt(S_2^{*-})]^-$ ($S_2^{2-} = 4\text{-Me-1,2-benzenedithiolato}$, $\Delta g = 0.419$, by Gray;^{6a} $S_2^{2-} = 3,5\text{-}t\text{-Bu}_2\text{-1,2-benzenedithiolato}$, $\Delta g = 0.38$ (21% calculated spin density at Pt) by Neese and Wieghardt^{6b}) were correlated to an increase of Pt-character in the SOMO according to computational data. Similarly, observed $\Delta\Delta g([1]^+ - [2]^+) = 0.092$ and overall larger $A(^{195}Pt)$ for $[2]^+$ may be attributed to different relative contributions of ligand and metal orbitals to the SOMOs. However, computed spin-densities amount to ~11% at Pt for both compounds and contradict this picture, indicating that additional factors are active here. For instance, mixing of a metal-centered excited state to the ground state of $[1]^+$ by spin-orbit coupling may be significant. Note that combining dipolar and orbital terms may compensate the contribution of the Fermi contact term to $A(^{195}Pt)$.^{6b}

The difference of the electronic structures of the $[ArS-Pt-S^{Ar}]^{*+}$ cores between $[1]^+$ and $[2]^+$ is substantiated by the observation of distinctly different NIR absorption bands. The neutral complexes are optically transparent in the NIR spectral region, with the lowest-energy transitions λ_{max} ($\epsilon_{max}/M^{-1}cm^{-1}$) being observed at 578 nm (200, in 1,2- $C_6F_2H_4$) for **1** and 318 nm (1.4×10^4 , in CH_2Cl_2) for **2**. Upon oxidation of **1** and **2**, intense absorption bands develop across the visible range and in the NIR region. Table 2 summarizes the position, intensity,

Table 2. Band Shape Parameters and Solvent Dependence for Low-Energy NIR Transitions of $[1]^+$ and $[2]^+$.^{a,b}

	solvent	ϵ_{solv}^c	ν_{max} (cm^{-1})	ϵ_{max}^c ($M^{-1}cm^{-1}$)	$\Delta\nu_{1/2}$ (cm^{-1})
$[1]^+$	C_7H_8	2.39	6570	15000	1570
$[1]^+$	CH_2Cl_2	8.93	6470	22000	1470
$[1]^+$	1,2- $C_6F_2H_4$	13.4	6500	17000	1510
$[1]^+$	$C_6H_6O_3$	66	6580	16000	1680
$[2]^+$	C_7D_8	~2.4 ^c	4050	4000	2000
$[2]^+$	CH_2Cl_2	8.93	4000	6000	1700

^a NTf_2 -salts; $[2]NTf_2$ generated in situ at 213 K. ^bMeasurement $T = 296$ K for $[1]NTf_2$ and 203 K for $[2]NTf_2$. ^cSolvent dielectric constants taken from literature,²² estimate for $\epsilon_{solv}(C_7D_8) \approx \epsilon_{solv}(C_7H_8)$.

line-width at half height, and solvent dependence of ν_{max} for the NIR bands of $[1]NTf_2$ and $[2]NTf_2$. Compound $[1]NTf_2$ features an intense, narrow, slightly asymmetric transition at 6500 cm^{-1} (1540 nm, $\epsilon_{max} = 1.7 \times 10^4\text{ M}^{-1}\text{ cm}^{-1}$, $\Delta\nu_{1/2} = 1550\text{ cm}^{-1}$) in 1,2- $C_6F_2H_4$ solution. As depicted in Figure 3, the dependence of ν_{max} , ϵ_{max} , and $\Delta\nu_{1/2}$ on solvent relative permittivity is small for a range of solvents that spans in polarity from toluene to propylene carbonate ($\Delta\epsilon_{solv} \sim 63$, cf. Table 2). There is no clear correlation of the transition intensity with solvent polarity. The largest intensity is recorded in moderately polar CH_2Cl_2 , whereas the data in toluene, 1,2- $C_6F_2H_4$ and propylene carbonate are close to identical, despite their distinct permittivities (cf. Table 2; similar observations

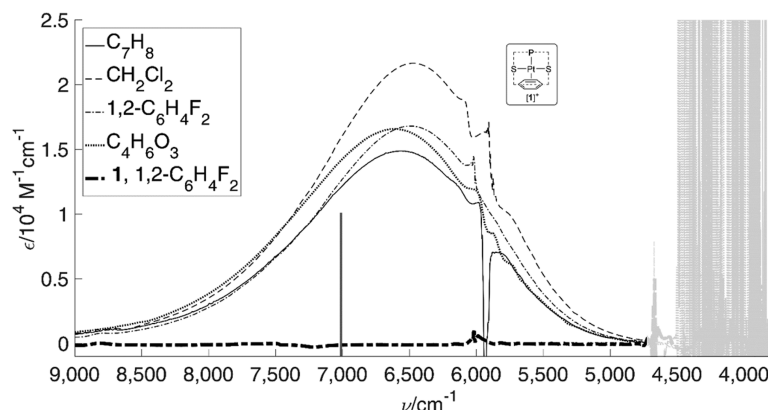


Figure 3. NIR absorption profiles of $[1]NTf_2$ in solvents of different relative permittivity²² (ϵ_{solv}) taken at $T = 296$ K: C_7H_8 (2.39), CH_2Cl_2 (8.93), $1,2-C_6F_4H_2$ (13.4), and $C_4H_6O_3$ (66) (cf. Figure S9 for spectra in $40000\text{--}4500\text{ cm}^{-1}$ range); Spectra of **1** were taken in $1,2-C_6F_4H_2$. Solid gray bar: TD-DFT derived $\nu_{\text{max}}(\text{TD-DFT}) = 7007\text{ cm}^{-1}$ ($f_{\text{osc}}(\text{TD-DFT}) = 0.20$). Strong solvent background absorption at $\nu_{\text{max}} < 4500\text{ cm}^{-1}$ attenuated (light gray) for clarity.

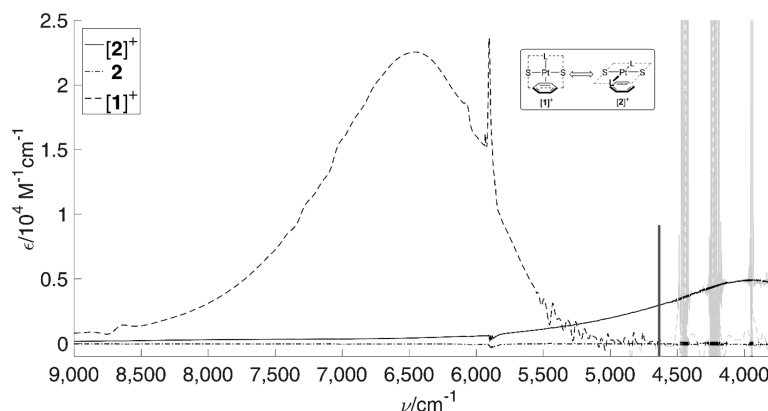


Figure 4. NIR absorption profiles of in situ generated $[2]NTf_2$, **2** and $[1]NTf_2$ in CH_2Cl_2 at $T = 203$ K; $\epsilon_{\text{solv}}(CH_2Cl_2) = 8.93$,²² Solid gray bar: TD-DFT derived $\nu_{\text{max}}(\text{TD-DFT}) = 4562\text{ cm}^{-1}$ ($f_{\text{osc}}(\text{TD-DFT}) = 0.19$); Solvent background absorption at $\nu_{\text{max}} < 4500\text{ cm}^{-1}$ attenuated (light gray) for clarity.

seem to hold for $[2]^+$ also). In line with EPR spectroscopic and structural data of $[1]^+$, a metal mediated LLIVCT type transition in a solvent averaged Class II–III system is proposed.² Note that both ν_{max} and ϵ_{max} of $[1]NTf_2$ proved to be nearly independent of temperature, as was probed in CH_2Cl_2 solution in the range of $203\text{--}298$ K (cf. Table 2 and Figure 4). Spectral changes are largely dominated by the temperature dependent change of solvent density, cf. Figure S10, SI.

Intriguingly, VT absorption spectra of $[2]NTf_2$ generated in situ in CH_2Cl_2 solution at 203 K display a clearly less intense but substantially red-shifted NIR band centered at $\nu_{\text{max}} = 4000\text{ cm}^{-1}$ (2500 nm , $\epsilon_{\text{max}} = 0.6 \times 10^4\text{ M}^{-1}\text{ cm}^{-1}$, $\Delta\nu_{1/2} \sim 1700\text{ cm}^{-1}$) as shown in Figure 4. The spectral features have been reproduced in a toluene- d_8 solution (cf. Figure S11, SI) as summarized in Table 2. On the basis of theoretical data, the lowest-energy transition of $[2]NTf_2$ is attributed to a CR transition within a Class III system. Solvent background absorption is strong in the $\leq 4500\text{ cm}^{-1}$ spectral region, so the complete NIR profile of $[2]^+$ could not be recorded. For this reason, the reported band widths rely on Gaussian curve fitting, and any asymmetry in the profile cannot be accounted for.

Electronic structure and TD-DFT calculations at the BLYP-35-D3/TZVP/ZORA level of theory fully support the Class II–III and Class III classifications and predict NIR transitions at 7000 and 4600 cm^{-1} for $[1]^+$ and $[2]^+$, respectively, and which are included as gray bars in Figures 3 and 4. Note that TD-DFT derived transitions generally match experimental data very well; cf. Table S9 and Figure S18, SI. Again, we find the relative orientation of the metal coordination plane to be decisive for the chromophore properties: While the $\beta\text{-HOMO} \rightarrow \beta\text{-LUMO}$ transition in $[1]^+$ is identified as a metal mediated LLIVCT along the S–Pt–S vector (Figure 5a; a detailed MO diagram is provided in Figure S16, SI), the low-energy $\beta\text{-HOMO} \rightarrow \beta\text{-LUMO}$ transition in $[2]^+$ is best described as a P–Pt LMCT augmented by a CR contribution from the electron delocalized thiophenoxyl/thiophenolato structure (Figure 5b; detailed MO diagram provided in Figure S17, SI).

The observation of a substantial decrease of $\epsilon_{\text{max}}([2]^+)$ as compared to $\epsilon_{\text{max}}([1]^+)$ is unexpected, both with respect to established models of CT band position and intensity of mixed-valent systems² and the outcomes of our TD-DFT studies. Despite that TD-DFT data indicate a change of the electronic character of the transition from LLIVCT in case of $[1]^+$ to a combined MLCT/CR for $[2]^+$, predicted transition probabilities are conserved, and computed oscillator strengths f_{osc} do

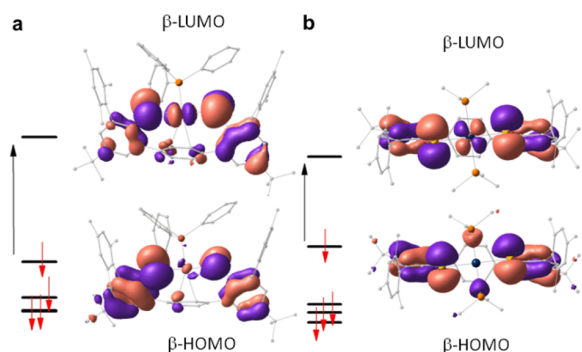


Figure 5. Kohn–Sham MOs and energy diagrams for $[1]^+$ (a) and $[2]^+$ (b) from a spin-unrestricted ZORA-BLYP-35 DFT calculations. TD-DFT derived lowest-energy transitions (β -HOMO \rightarrow β -LUMO): $\nu_{\max}(\text{TD-DFT}) = 7007 \text{ cm}^{-1}$ for $[1]^+$ and 4562 cm^{-1} for $[2]^+$.

not differ significantly for $[1]^+$ and $[2]^+$. Since the stoichiometry of the redox chemistry of the couple $2/[2]^+$ has been proven correct (vide supra), the small values of $\epsilon_{\max}([2]^+)$ cannot be attributed to trivial concentration effects; rather the diminished value of ϵ_{\max} is a property inherent to $[2]^+$.

Comparison with literature data does not provide a congruent picture at present. For instance, in the case of the well-studied complexes of mixed-valence salen ligands, spectral positions of the NIR bands become increasingly blue-shifted and gain intensity along the series Pd < Ni < Pt. This trend has been rationalized in terms of an enhancement of electronic coupling in the same direction.^{15b} In clear contrast, the intensities (f_{osc} and ϵ_{\max}) of the NIR bands of mixed-valence bis-benzene-1,2-dithiolato d⁸-metalate complexes systematically and substantially decrease with increasing coupling strength, clearly opposing the trend observed for their spectral positions, ν_{\max} .^{6b} Obviously, the substitution of oxygen donors for sulfur results in a significant change of electronic structures, pointing to a lack of generality of the current knowledge and the scope of the conclusions made.²³

CONCLUSIONS

The design of (electro-switchable) mixed-valent structures that allow the strength of electron coupling to be varied in a systematic fashion is a vibrant field of research. In this context, delineation of characteristic structural parameters that control electronic delocalization and associated optical properties is of pivotal importance. As a novel approach, control of the relative orientation of ligand and metal orbitals of an open-shell complex has been shown to result in spectroscopically distinct electronic structures, presenting a novel approach toward the design of NIR chromophores. The concept relies on the use of a *trans*-coordinating, redox noninnocent dithiophenol ligand of variable denticity. In general, complexes of metal-coupled mixed-valent thiol/thiolato ligands display optical properties that are similar to, for instance, those of the well-studied family of salen-derived mixed-valent coordination compounds. On the other hand, substituting oxygen for sulfur does result in electronic structures whose properties clearly oppose general trends, and which mandates further studies to understand their electronic origin. As one approach, studies on structures with metals other than precious platinum are currently underway.

EXPERIMENTAL SECTION

All manipulations of air and moisture sensitive compounds were carried out under a dry argon atmosphere using standard Schlenk or glovebox techniques (MBraun, MB 150-GI). 1,4-terphenyldithiophenol²⁴ and *trans*-Pt(py)₂Cl₂¹⁸ were prepared following literature procedures. AgClO₄, high purity ferrocene (Fc) were obtained from Alfa Aesar, and Fc was sublimed once prior to use. 1,1'-Diacetylferrocene (Fc'') was used as received from TCI. Benzoquinone was recrystallized 3 times from ethanol, sublimed twice (r.t., 10⁻³ mbar, static vacuum), and stored under argon. Bis(trifluoromethanesulfonyl)amine (HNTf₂, 99%, Acros Organics) was sublimed once before use. Solvents were purified and dried prior to use. 1,1,2,2-C₂H₂Cl₄ was dried over and distilled from P₂O₅, degassed, and saturated with Ar. Hexane was dried over Grubbs columns of an MBraun solvent purification system (SPS). Diethyl ether, pentane, and toluene were predried over activated 3 Å molecular sieves and distilled from sodium benzophenone ketyl under argon. Methanol was dried by percolation through a column of activated neutral alumina. Stabilizer free dichloromethane (Fisher Scientific) was first distilled from P₂O₅, then from K₂CO₃, and finally stored over activated basic alumina. Acetonitrile (MeCN) for use in electrochemical experiments was sequentially dried over and distilled from CaH₂ and P₂O₅, and finally percolated through activated neutral alumina. 1,2-Difluorobenzene (1,2-C₆F₂H₄; obtained from ABCR) was dried and purified by percolation through a column of activated neutral alumina, and distilled onto activated neutral alumina prior to use. C₆D₆ was dried over and distilled from NaK alloy whereas C₇D₈, CDCl₃ and CD₂Cl₂ were dried over and vacuum transferred from 3 Å molecular sieves. In general, solvents were stored over 3 Å molecular sieves under argon. Molecular sieves and alumina were activated by heating under dynamic vacuum (10⁻³ mbar) at 523 K for 24–48 h.

NMR data were recorded on a Bruker Avance II 400 and an AVII +500 spectrometer (VT NMR studies). δ values are given in ppm, J values in Hz. ¹H and ¹³C{¹H}-NMR chemical shifts are referenced to the residual proton and naturally abundant carbon resonances of the solvents: 7.16/128.06 (C₆H₆-d₆), 5.32/53.84 (CH₂Cl₂-d₂), and 7.26/77.16 (CHCl₃-d) ppm. ³¹P NMR chemical shifts are referenced to an external standard sample of 85% H₃PO₄ set to 0 ppm.

EPR spectra were collected using 4 mm O.D. Wilmad quartz (CFQ) EPR tubes on a continuous wave X-band Bruker ESP 300E spectrometer, and are referenced to the Bruker Strong Pitch standard $g_{\text{iso}} = 2.0028$. EPR simulations were done with EasySpin (version 5.0.21)²⁵ and MATLAB and Statistic Toolbox Release R2016a (The MathWorks, Inc., Natick, Massachusetts, United States). Fitting of EPR spectra was carried out with the easyfit tool included in EasySpin package, using either pepper for solid state or garlic for solution EPR data.

Electronic spectra were recorded on PerkinElmer Lambda 1050 UV/vis/NIR and Lambda 35 UV/vis spectrometer. For VT experiments, a CoolSpeK UV USP-203-B cryostat from UNISOKU and a four-side transparent cell with screw cap and septum were used. In general, sample concentrations were corrected for temperature dependent changes of solvent density δ by using a modified form of the Rackett equation,²⁶ and $\delta(\text{C}_7\text{D}_8, 213 \text{ K})$ was estimated from $\delta(\text{C}_7\text{D}_8, 298 \text{ K}) \times \delta(\text{C}_7\text{H}_8, 213 \text{ K})/\delta(\text{C}_7\text{H}_8, 298 \text{ K})$, assuming $\delta(T)$ of C₇D₈ and C₇H₈ be equal in the temperature range studied.

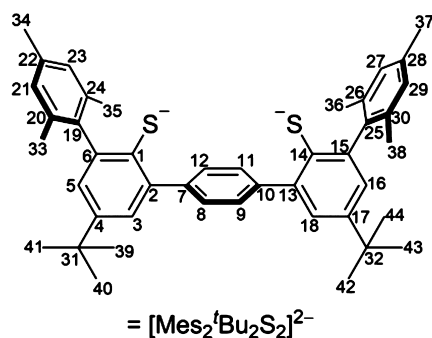
Evan's method²⁷ was employed to determine μ_{eff} in solution using a coaxial insert for 5 mm NMR sample tubes, $\chi_{\text{M}}^{\text{dia}} = -0.5 \times M$, M = dimensionless molecular weight of the sample, $\chi_{\text{M}}^{\text{dia}}(\text{CH}_2\text{Cl}_2) = -4.66 \times 10^{-5} \text{ cm}^3 \text{ mol}^{-1}$ and $\chi_{\text{M}}^{\text{dia}}(\text{THF}) = -5.3 \times 10^{-5} \text{ cm}^3 \text{ mol}^{-1}$ were used to correct for diamagnetic susceptibilities of sample and solvent.²⁸

X-ray diffraction data were collected on a Bruker Smart APEXII diffractometer with graphite-monochromated MoK α radiation. The programs used were Bruker's APEX2 v2011.8–0, including SADABS for absorption correction and SAINT for structure solution, the WinGX suite of programs version 2013.3,²⁹ SHELXS and SHELXL for structure solution and refinement,³⁰ PLATON,³¹ and Ortep.³² Crystals were, unless otherwise noted, coated in a perfluorinated polyether oil and mounted on a 100 μm MiTeGen MicroMounts loop

that was placed on the goniometer head under a stream of dry nitrogen at 100 K.

Cyclic voltammetry (CV) measurements were performed at 290 K under argon atmosphere with a BASI CV-50W in a gastight, full-glass, three-electrode cell setup. *n*Bu₄NPF₆ electrolyte (Alfa Aesar) was recrystallized 3 times from acetone/water and employed as a 0.1 M solution in CH₂Cl₂ and MeCN. A Pt disc electrode (Deutsche Metrohm GmbH & Co. KG, electro-active area = 0.080 ± 0.003 cm²) and a 1 mm coiled Pt-wire were employed as working and counter electrodes. The Ag/Ag⁺ redox couple, in the form of a 0.5 mm Ag wire in a 0.01 M AgClO₄/0.1 M *n*Bu₄NPF₆ MeCN solution, served as a reference electrode. Voltammograms were corrected for capacitive currents of electrolyte solutions and overall cell resistance, and potentials are reported relative to Fc/[Fc]⁺ in CH₂Cl₂, with $E_{1/2}(\text{Fc}/[\text{Fc}]^+)/0.1 \text{ M } n\text{Bu}_4\text{NPF}_6/\text{CH}_2\text{Cl}_2, 290 \text{ K}) = 0.212 \pm 0.001 \text{ V}$. The electro-active area of the Pt disc electrode was calculated from Fc/[Fc]⁺ measurements in 0.1 M *n*Bu₄NPF₆ solution in CH₂Cl₂ at various concentrations and potential sweep rates at 295 K, using $D(\text{Fc}/\text{CH}_2\text{Cl}_2, 295 \text{ K}) = 2.2 \times 10^{-5} \text{ cm}^2 \text{ s}^{-1}$.³³ The working electrode was rinsed with acetone, polished very gently with a paste of 0.3 μm alumina (Deutsche Metrohm GmbH & Co. KG) in deionized water, rinsed thoroughly with plenty of deionized water, and finally acetone after each use. Periodic Fc/[Fc]⁺ reference measurements verified the electro-active surface area of the Pt electrode, and the stability of the potential of the Ag/Ag⁺ reference electrode.

Numeration scheme used for 1,4-terphenyldithiophenolato ligand in coordination compounds.



Preparation of 1,1'-Diacetylferrocenium Bis(trifluoromethylsulfonyl)imide [Fc'']NTf₂. To a solution of 4-benzoquinone (62 mg, 0.576 mmol) in 8 mL Et₂O was added dropwise a solution of HNTf₂ (340 mg, 1.296 mmol) in 8 mL Et₂O at r.t., followed by a solution of Fc'' (259 mg, 0.96 mmol) in 0.5 mL CH₂Cl₂. Within 10 min a blue-green crystalline solid separated from the stirred solution, was filtered off, washed with Et₂O until the washings were colorless, and finally dried under dynamic vacuum overnight at r.t. Yield: 441 mg (0.8 mmol, 78%).

UV/vis (1,1,2,2-C₂H₂Cl₄, 293 K): λ (ε/M⁻¹ cm⁻¹) = 650 (420), 483 (252) nm. Elemental analysis calcd. (%) for C₁₆H₁₄F₆FeNO₆S₂: C, 34.93; H, 2.56; N, 2.55; S, 11.65; found: C, 35.29; H, 2.56; N, 2.71; S, 11.71; μ_{eff} (THF/1,1,2,2-C₂H₂Cl₄, 274–283 K) = 2.7(1).

Details on the molecular structure of [Fc'']NTf₂ are collected in Figure S12 and Table S7, SI.

Preparation of 1. Ligand Mes₂'Bu₂(SH)₂ (530 mg, 0.83 mmol) and benzyl potassium (215 mg, 1.65 mmol) were reacted in 36 g of toluene at r.t. to afford a clear yellow solution, to which PPh₃ (216 mg, 0.83 mmol) and *trans*-Pt(py)₂Cl₂ (350 mg, 0.83 mmol) were added and stirring was continued overnight. The dark green solution was filtered from KCl, the solvent removed under vacuum, and the dark green residual solid washed with pentane, redissolved in toluene, and finally crystallized by slow diffusion of pentane vapor at r.t. to yield dark green needles of **1** × 0.5C₇H₈. Yield 462 mg (0.4 mmol, 49%).

¹H NMR (500 MHz, CD₂Cl₂, 298 K): δ = 7.623 (d, ³J(H,P) = 2 Hz, ²J(H,Pt) = 15 Hz, 4H, H-8,9,11,12), 7.32 (d, ⁴J(H-H) = 2.3 Hz, 2H, H-3,18), 7.26 (m, 6H, PPh₃-H_{ortho}, ²J(C,P) = 10 Hz), 7.23 (m, 3H, PPh₃-H_{para}, ⁴J(C,P) = 3 Hz), 7.09 (m, 6H, PPh₃-H_{meta}, ³J(C,P) =

12 Hz), 6.79 (d, ⁴J(H,H) = 2.3 Hz, 2H, H-5,16), 6.60 (m, 4H, H-21,23,27,29), 2.28 (s, 6H, H-34,37), 1.709 (s, 12H, H-33,35,36,38), 1.309 (s, 18H, H-39–44) ppm. ¹³C{¹H}-NMR (126 MHz, CD₂Cl₂, 298 K): δ = 145.91 (C-4,17), 140.74 (C-6,15), 140.32 (d, ²J(C,P) = ~1 Hz, C-7,10), 139.72 (C-19,25), 138.04 (C-2,13), 136.61 (d, ²J(C,Pt) = 6 Hz, C-1,14), 135.93 (C-20,24,26,30), 135.34 (d, ²J(C,P) = 10 Hz, PPh₃-C_{ortho}), 135.3 (C-22,28), 130.74 (d, ⁴J(C,P) = 3 Hz, PPh₃-C_{para}), 127.73 (C-21,23,27,29), 127.68 (C-5,16), 127.44 (d, ³J(C,P) = 12 Hz, PPh₃-C_{meta}), 126.44 (d, ¹J(C,P) = 69 Hz, PPh₃-C_{ipso}), 122.17 (C-3,18), 114.7 (broad, ν_{1/2} ~53 Hz, C-8,9,11,12), 34.42 (C-31,32), 31.51 (C-39–44), 21.15 (C-34,37), 20.35 (C-33,35,36,38) ppm. ³¹P{¹H}-NMR (202 MHz, CD₂Cl₂, 298 K): δ = 33.9 (¹J(P-Pt) = 4770 Hz) ppm. ¹H-¹⁹⁵Pt-HSQC-NMR (500 MHz, CDCl₃, 298 K): δ_{Pt} = -4811 ppm. UV/vis (1,2-C₆F₂H₄, 293 K): λ (ε/M⁻¹ cm⁻¹) = 329 (22000), 360 (16000), 430 (1100), 578 (200) nm. Elemental analysis calcd. (%) for C₆₂H₆₃PtS₂: C, 68.74; H, 5.90; S, 5.60; found: C, 68.40; H, 5.58; S, 5.36.

Preparation of [1]NTf₂. Complex **1** (100 mg, 0.087 mmol) was dissolved in 6 mL of CH₂Cl₂ to which a solution of [FcAc₂]NTf₂ (50 mg, 0.091 mmol) in 2 mL CH₂Cl₂ was added dropwise at r.t. The resulting dark red solution was cannula-transferred into 100 mL of vigorously stirred pentane. Dark maroon needles separated at 245 K. The mother liquor was decanted and the crystals washed with pentane. Yield: 93 mg (0.067 mmol, 77%).

UV/vis/NIR (293 K): (a) C₇H₈, λ (ε/M⁻¹ cm⁻¹) = 348 (13700), 374 (14000), 483 (2300), 514 (2400), 612 (1000), 762 (400), 1003 (600), 1523 (15400) nm; (b) CH₂Cl₂, 277 (50000), 351 (17700), 381 (20200), 502 (3600), 621 (1500), 775 (700), 1000 (800), 1547 (22000) nm; (c) 1,2-C₆F₂H₄, 352 (14000), 378 (15500), 500 (3000), 610 (1200), 767 (500), 1002 (600), 1540 (17000) nm; (d) C₄H₆O₃, 270 (41300), 349 (15300), 377 (16000), 521 (2700), 615 (1200), 776 (500), 1520 (16200) nm. μ_{eff} = 2.3 (213–313 K, CD₂Cl₂ containing 1,1,2,2-C₂H₂Cl₄). Elemental analysis calcd. (%) for C₆₄H₆₃F₆NO₆PtS₄: C, 55.76; H, 4.61; N, 1.02; S, 9.30; found: C, 53.97; H, 4.09; N, 1.17; S, 8.88. Elemental analysis of different batches of [1]NTf₂ have consistently yielded lower than expected values for C, H, and S. Especially, determination of H and S composition is biased in some of the samples due to difficulties desorbing H₂O and SO₂ properly separated from the device column. For this reason, the chemical identity of [1]NTf₂ has been analyzed by high resolution ESI-MS from a THF solution of the compound. [M]⁺ calculated: 1097.37512; found: 1097.37753, deviation: 1.75 ppm; cf. to Figure S1, SI, for details.

Preparation of 2. To a suspension of **1** (100 mg, 0.087 mmol) in 4 mL of hexane were added 0.95 mL 0.2 M PMe₃ in toluene at r.t. A clear yellow solution formed, from which the solvent was removed under vacuum. Crystallization from C₆H₆/methanol afforded yellow needles of **2** × 2MeOH. Yield 67 mg (0.06 mmol, 73%). Methanol is removed by coevaporation of a C₆H₆ solution of **2** × 2MeOH. For this reason, samples of **2** usually contain ~0.17 equiv of residual C₆H₆.

¹H NMR (400 MHz, CDCl₃, 298 K): δ = 7.38 (s, 4H, H-8,9,11,12), 7.347 (d, ⁴J(H,H) = 2.5 Hz, 2H, H-3,18), 6.909 (m, 4H, H-21,23,27,29), 6.855 (d, ⁴J(H,H) = 2.5 Hz, H-5,16), 2.32 (s, 6H, H-34,37), 2.069 (s, 12H, H-33,35,36,38), 1.325 (s, 18H, H-39–44), 1.268 (N-line pattern, ¹²⁺⁴J(H,P) = 7 Hz, 18H, ³J(H,Pt) = 25 Hz, *trans*-PMe₃) ppm. ¹³C{¹H} NMR (101 MHz, CDCl₃, 298 K): δ = 143.79 (C-4,17), 141.69 (C-6,15), 141.09 (C-19,25), 140.26 (C-7,10), 140.09 (C-2,13), 137.14 (C-1,14), 136.22 (C-20,24,26,30), 135.46 (C-22,28), 127.85 (C-21,23,27,29), 127.8 (C-8,9,11,12), 126.31 (C-5,16), 123.91 (C-3,18), 34.06 (C-31,32), 31.46 (C-39–44), 21.29 (C-34,37), 20.49 (C-33,35,36,38), 12.64 (N-line pattern, ¹¹⁺³¹J(C,P) = 37 Hz, *trans*-PMe₃) ppm. ³¹P{¹H} NMR (162 MHz, CDCl₃, 298 K): δ = -20.9 (¹J(P,Pt) = 2870 Hz) ppm. ¹H-¹⁹⁵Pt-HSQC-NMR (500 MHz, CDCl₃, 298 K): δ_{Pt} = -4220 ppm. UV/vis/NIR (1,2-C₆F₂H₄, 293 K): λ (ε/M⁻¹ cm⁻¹) = 318 (14000) nm. Elemental analysis calcd. (%) for C₅₀H₆₆P₂PS₂: C, 60.77; H, 6.73; S, 6.49; found: C, 60.12; H, 6.30; S, 6.14.

UV/Vis/NIR Measurements. One mM stock solutions of **1**, [1]NTf₂, and **2** in 1,2-C₆F₂H₄ and of [Fc'']NTf₂ in 1,1,2,2-tetrachloroethane were prepared and spectra with concentrations

between 0.2 mM and 5 μ M were recorded to determine extinction coefficients.

UV/vis/NIR electronic absorption data of [2]NTf₂ were collected from an in situ prepared sample. Stock solutions of **2** (1.7 mM), [Fc^o]NTf₂ (2.4 mM), and Fc^o (0.8 mM) were prepared in CH₂Cl₂ and reference spectra were obtained at different temperatures. 2.8 mL CH₂Cl₂ was filled in a four-side transparent cell with screw cap and septum. After cooling to 203 K, 0.195 mL stock solution of **2** (0.33 μ mol) were added. Under stirring 0.25 equiv of [Fc^o]NTf₂ were added and a spectrum was recorded. This procedure was repeated three times. Spectra of CH₂Cl₂ were collected at the same temperature and subtracted for background correction.

UV/vis/NIR of [2]NTf₂ (203 K): (a) CH₂Cl₂, λ (ϵ /M⁻¹ cm⁻¹) = 510 (2600), 632 (2000), 870 (500), 1340 (400), 2500 (6000) nm; (b) C₇D₈, 513 (2700), 640 (1900), 866 (600), 2470 (4000) nm.

Computational Details. All DFT calculations were performed using ORCA2.9.1.³⁴ TZVP basis sets³⁵ were used throughout. The presence of platinum was accounted for with van Wüllen's zero order regular approximation (ZORA),³⁶ implying TZV-ZORA auxiliary basis sets.^{36b} Geometric structure optimizations were performed with the GGA functional BP86³⁷ starting from the experimental atom positions of **1**, [1]NTf₂, and **2**. Dispersion contributions were approximated using Grimme's DFT-D3 atom-pairwise dispersion corrections.³⁸ Numerical frequency calculations for [2]⁺ gave no imaginary modes and revealed the optimized structures to be a stationary point on the energy surface. It is noted that the frequency calculation of [1]⁺ gave one low-frequency imaginary mode due to methyl-group rotation. Computed Mulliken spin densities are tabulated in Table S8, SI. UV/vis/NIR spectroscopic properties were extracted from single-point TD-DFT calculations (BP86, B3LYP³⁹ and BLYP-35²⁰) in the BP86-optimized atomic positions. The computational methodology was validated by respective calculations on the platinate(II) complex [Pt(tdt)₂]⁻, tdt = 4-Me-1,2-benzenedithiophenol, reported by Gray et al.,^{6a} and was found to reproduce the original experimental data (cf. Figure S15, SI). The MO diagram fully reproduces the previous DFT analysis of the *tert*-butyl substituted congener by Neese and Wieghardt et al.^{6b}

■ ASSOCIATED CONTENT

Supporting Information

The Supporting Information is available free of charge on the ACS Publications website at DOI: 10.1021/jacs.6b13085.

Experimental procedures, spectra, crystallographic details, calculated structures, and TD-DFT data (PDF)
Crystal data (CIF)
Crystal data (CIF)

■ AUTHOR INFORMATION

Corresponding Authors

*andreas.berkefeld@anorg.uni-tuebingen.de

*gerald.hoerner@tu-berlin.de

ORCID

Andreas Berkefeld: 0000-0002-2757-7841

Notes

The authors declare no competing financial interest.

■ ACKNOWLEDGMENTS

A.B. and N.M.M. are grateful to the Fonds der Chemischen Industrie and the Baden-Württemberg Foundation for financial support. G.H. thanks the Deutsche Forschungsgemeinschaft DFG for financial support (SFB 658, Elementary processes in molecular switches on surfaces). G.H. and A.B. thank Prof. Andreas Grohmann (TU Berlin) for providing computational resources and Prof. Martin Kaupp (TU Berlin) for valuable

computational advice. A.B. acknowledges Umicore, Hanau, Germany for generous donation of (tBu₃P)₂Pd.

■ REFERENCES

- (1) (a) Kaim, W. *Coord. Chem. Rev.* **2011**, *255*, 2503–2513. (b) Mortimer, R. J. *Annu. Rev. Mater. Res.* **2011**, *41*, 28. (c) Ward, M. D. *J. Solid State Electrochem.* **2005**, *9*, 778–787.
- (2) (a) Demadis, K. D.; Hartshorn, C. M.; Meyer, T. J. *Chem. Rev.* **2001**, *101*, 2655–2686. (b) D'Alessandro, D. M.; Keene, F. R. *Chem. Rev.* **2006**, *106*, 2270–2298.
- (3) König, E.; Kremer, S. *Chem. Phys. Lett.* **1970**, *5*, 87–90.
- (4) Tang, J.-H.; Yao, C.-J.; Cui, B.-B.; Zhong, Y.-W. *Chem. Rec.* **2016**, *16*, 754–767.
- (5) Deibel, N.; Schweinfurth, D.; Fiedler, J.; Zalis, S.; Sarkar, B. *Dalton Trans.* **2011**, *40*, 9925–9934.
- (6) (a) Williams, R.; Billig, E.; Waters, J. H.; Gray, H. B. *J. Am. Chem. Soc.* **1966**, *88*, 43–50. (b) Ray, K.; Weyhermüller, T.; Neese, F.; Wieghardt, K. *Inorg. Chem.* **2005**, *44*, 5345–5360. (c) Ray, K.; Petrenko, T.; Wieghardt, K.; Neese, F. *Dalton Trans.* **2007**, 1552–1566. (d) Maiti, B. K.; Maia, L. B.; Pal, K.; Pakhira, B.; Avilés, T.; Moura, I.; Pauleta, S. R.; Nuñez, J. L.; Rizzi, A. C.; Brondino, C. D.; Sarkar, S.; Moura, J. J. G. *Inorg. Chem.* **2014**, *53*, 12799–12808. (e) Machata, P.; Herich, P.; Lušpai, K.; Bucinsky, L.; Šoralová, S.; Breza, M.; Kozisek, J.; Rapta, P. *Organometallics* **2014**, *33*, 4846–4859.
- (7) Arumugam, K.; Shaw, M. C.; Chandrasekaran, P.; Villagrán, D.; Gray, T. G.; Mague, J. T.; Donahue, J. P. *Inorg. Chem.* **2009**, *48*, 10591–10607.
- (8) (a) Kramer, W. W.; Cameron, L. A.; Zarkesh, R. A.; Ziller, J. W.; Heyduk, A. F. *Inorg. Chem.* **2014**, *53*, 8825–8837. (b) Zanella, P.; Corsini, M. *Coord. Chem. Rev.* **2006**, *250*, 2000–2022. (c) Pierpont, C. G. *Coord. Chem. Rev.* **2001**, *216–217*, 99–125. (d) Haga, M.; Dodsworth, E. S.; Lever, A. B. P. *Inorg. Chem.* **1986**, *25*, 447–453.
- (9) Sarkar, B.; Schweinfurth, D.; Deibel, N.; Weisser, F. *Coord. Chem. Rev.* **2015**, *293–294*, 250–262.
- (10) (a) Eisenberg, R.; Gray, H. B. *Inorg. Chem.* **2011**, *50*, 9741–9751. (b) Garreau-de Bonneval, B.; Moineau-Chane Ching, K. I.; Alary, F.; Bui, T.-T.; Valade, L. *Coord. Chem. Rev.* **2010**, *254*, 1457–1467. (c) Aragoni, M. C.; Arca, M.; Cassano, T.; Denotti, C.; Devillanova; Francesco, A.; Frau, R.; Isaia, F.; Lelj, F.; Lippolis, V.; Nitti, L.; Romaniello, P.; Tommasi, R.; Verani, G. *Eur. J. Inorg. Chem.* **2003**, *2003*, 1939–1947.
- (11) (a) Leung, W.-H.; Chan, E. Y. Y.; Chow, E. K. F.; Williams, I. D.; Peng, S.-M. *J. Chem. Soc., Dalton Trans.* **1996**, 1229–1236. (b) Pratt, R. C.; Stack, T. D. P. *J. Am. Chem. Soc.* **2003**, *125*, 8716–8717. (c) Shimazaki, Y.; Tani, F.; Fukui, K.; Naruta, Y.; Yamauchi, O. *J. Am. Chem. Soc.* **2003**, *125*, 10512–10513. (d) Thomas, F. *Dalton Trans.* **2016**, *45*, 10866–10877. (e) Kurahashi, T.; Fujii, H. *J. Am. Chem. Soc.* **2011**, *133*, 8307–8316.
- (12) Stenson, P. A.; Board, A.; Marin-Becerra, A.; Blake, A. J.; Davies, E. S.; Wilson, C.; McMaster, J.; Schröder, M. *Chem. - Eur. J.* **2008**, *14*, 2564–2576.
- (13) (a) Shimazaki, Y.; Yajima, T.; Tani, F.; Karasawa, S.; Fukui, K.; Naruta, Y.; Yamauchi, O. *J. Am. Chem. Soc.* **2007**, *129*, 2559–2568. (b) Storr, T.; Verma, P.; Pratt, R. C.; Wasinger, E. C.; Shimazaki, Y.; Stack, T. D. P. *J. Am. Chem. Soc.* **2008**, *130*, 15448–15459.
- (14) Orio, M.; Jarjays, O.; Kanso, H.; Philouze, C.; Neese, F.; Thomas, F. *Angew. Chem., Int. Ed.* **2010**, *49*, 4989–4992.
- (15) (a) Storr, T.; Wasinger, E. C.; Pratt, R. C.; Stack, T. D. P. *Angew. Chem., Int. Ed.* **2007**, *46*, 5198–5201. (b) Shimazaki, Y.; Stack, T. D. P.; Storr, T. *Inorg. Chem.* **2009**, *48*, 8383–8392.
- (16) (a) Rotthaus, O.; Jarjays, O.; Perez Del Valle, C.; Philouze, C.; Thomas, F. *Chem. Commun.* **2007**, 4462–4464. (b) Kochem, A.; Orio, M.; Jarjays, O.; Neese, F.; Thomas, F. *Chem. Commun.* **2010**, *46*, 6765–6767. (c) Chiang, L.; Kochem, A.; Jarjays, O.; Dunn, T. J.; Vezin, H.; Sakaguchi, M.; Ogura, T.; Orio, M.; Shimazaki, Y.; Thomas, F.; Storr, T. *Chem. - Eur. J.* **2012**, *18*, 14117–14127.
- (17) Rotthaus, O.; Thomas, F.; Jarjays, O.; Philouze, C.; Saint-Aman, E.; Pierre, J.-L. *Chem. - Eur. J.* **2006**, *12*, 6953–6962.

(18) Kauffman, G. B.; Cowan, D. O.; Slusarczuk, G.; Kirschner, S., In *Inorg. Synth.*; Kleinberg, J., Ed.; John Wiley & Sons, Inc.: Hoboken, NJ, 1963; Vol. 7, pp 239–245.

(19) CCDC 1511080–1511083 contain the crystallographic data for this paper. These data are provided free of charge by The Cambridge Crystallographic Data Centre. See Tables S6–S7, S1, for details.

(20) Parthey, M.; Kaupp, M. *Chem. Soc. Rev.* **2014**, *43*, 5067–5088.

(21) Loughrey, J. J.; Sproules, S.; McInnes, E. J. L.; Hardie, M. J.; Halcrow, M. A. *Chem. - Eur. J.* **2014**, *20*, 6272–6276.

(22) Speight, J. G.; Lange, N. A. *Lange's Handbook of Chemistry*, 16th ed.; McGraw-Hill: New York, 2004.

(23) Solomon, E. I.; Xie, X.; Dey, A. *Chem. Soc. Rev.* **2008**, *37*, 623–638.

(24) Koch, F.; Schubert, H.; Sirsch, P.; Berkefeld, A. *Dalton Trans.* **2015**, *44*, 13315–13324.

(25) Stoll, S.; Schweiger, A. *J. Magn. Reson.* **2006**, *178*, 42–55.

(26) Yaws, C. L. *Chemical Properties Handbook: Physical, Thermodynamic, Environmental, Transport, Safety, and Health Related Properties for Organic and Inorganic Chemicals*; McGraw-Hill: New York, 1999; pp VII, 779.

(27) Evans, D. F. *J. Chem. Soc.* **1959**, 2003–2005.

(28) Bain, G. A.; Berry, J. F. *J. Chem. Educ.* **2008**, *85*, 532.

(29) Farrugia, L. *J. Appl. Crystallogr.* **1999**, *32*, 837–838.

(30) (a) Hubschle, C. B.; Sheldrick, G. M.; Dittrich, B. *J. Appl. Crystallogr.* **2011**, *44*, 1281–1284. (b) Sheldrick, G. *Acta Crystallogr., Sect. A: Found. Crystallogr.* **2008**, *64*, 112–122.

(31) Spek, A. *Acta Crystallogr., Sect. D: Biol. Crystallogr.* **2009**, *65*, 148–155.

(32) Farrugia, L. *J. Appl. Crystallogr.* **2012**, *45*, 849–854.

(33) Janisch, J.; Ruff, A.; Speiser, B.; Wolff, C.; Zigelli, J.; Benthin, S.; Feldmann, V.; Mayer, H. A. *J. Solid State Electrochem.* **2011**, *15*, 2083–2094.

(34) Neese, F. *WIREs Comput. Mol. Sci.* **2012**, *2*, 73–78.

(35) Schäfer, A.; Horn, H.; Ahlrichs, R. *J. Chem. Phys.* **1992**, *97*, 2571–2577.

(36) (a) van Wüllen, C. *J. Chem. Phys.* **1998**, *109*, 392–399.

(b) Pantazis, D. A.; Chen, X.-Y.; Landis, C. R.; Neese, F. *J. Chem. Theory Comput.* **2008**, *4*, 908–919.

(37) Becke, A. D. *Phys. Rev. A: At., Mol., Opt. Phys.* **1988**, *38*, 3098–3100.

(38) (a) Grimme, S. *J. Comput. Chem.* **2006**, *27*, 1787–1799.

(b) Grimme, S.; Ehrlich, S.; Goerigk, L. *J. Comput. Chem.* **2011**, *32*, 1456–1465.

(39) (a) Becke, A. D. *J. Chem. Phys.* **1993**, *98*, 5648–5652. (b) Lee, C.; Yang, W.; Parr, R. G. *Phys. Rev. B: Condens. Matter Mater. Phys.* **1988**, *37*, 785–789.

Controlling Near-Infrared Chromophore Electronic Properties through Metal–Ligand Orbital Alignment

Nicole M. Mews, Andreas Berkefeld, Gerald Hörner, and Hartmut Schubert

Table of Contents

1	High Resolution ESI-MS Data of [1]NTf ₂	2
2	Additional NMR Spectroscopic Data for In Situ Generated [2]NTf ₂	3
3	Cyclic Voltammetry Data.....	4
4	EPR Data.....	7
5	Additional Information on UV/Vis/NIR Data.....	8
6	Additional Crystallographic Information.....	10
6.1	Structural details of [Fc ^{''}]NTf ₂	10
6.2	Structural details of 1 ×2C ₇ H ₈	10
6.3	Structural details of [1]NTf ₂	11
6.4	Structural details of 2	11
7	Additional Information on Computational Data.....	15
8	References.....	25
	Table S1. ΔE _p [V] of the First Oxidation Step of 1 in 0.1 M nBu ₄ NPF ₆ /CH ₂ Cl ₂	5
	Table S2. i _p ^{red} /i _p ^{ox} of the First Oxidation Step of 1 in 0.1 M nBu ₄ NPF ₆ /CH ₂ Cl ₂	5
	Table S3. ΔE _p [V] of the First Oxidation of 2 in 0.1 M nBu ₄ NPF ₆ /CH ₂ Cl ₂	6
	Table S4. i _p ^{red} /i _p ^{ox} of the First Oxidation Step of 2 in 0.1 M nBu ₄ NPF ₆ /CH ₂ Cl ₂	6
	Table S5. Selected Bond Lengths [Å] and Angles [°] in the Solid-State Structures of Parent Complexes and Derived Cations; Metrical Data from DFT Optimizations in Parentheses ^a	12
	Table S6. General Crystallographic Information of 1 , [1]NTf ₂ , and 2	13
	Table S7. General Crystallographic Information on 1,1'-Diacetylferrocenium Bis(trifluoromethylsulfonyl)imide.....	14
	Table S8. Computed Mulliken Spin Densities of [1] ⁺ and [2] ⁺	15
	Table S9. TD-DFT Computed Energies and Intensities of Electronic Transitions of [1] ⁺ and [2] ⁺	18
	Table S10. TD-DFT Computed Energies and Intensities of Electronic Transitions of Reference Compound [(tdt) ₂ Pt] ^{•+} , tdt = 4-Me-1,2-Benzenedithiophenol.....	20
	Table S11. Cartesian Coordinates of Optimized [1] ⁺	21
	Table S12. Cartesian Coordinates of Optimized [2] ⁺	23
	Table S13. Cartesian Coordinates of the Optimized Reference Compound [(tdt) ₂ Pt] ^{•+} , tdt = 4-Me-1,2-Benzenedithiophenol.....	25

1 High Resolution ESI-MS Data of [1]NTf₂

High resolution ESI-MS of [1]NTf₂ have been obtained from a THF solution of the isolated compound.

[M]⁺ calcd.: 1097.37512; found: 1097.37753, deviation: 1.75 ppm.

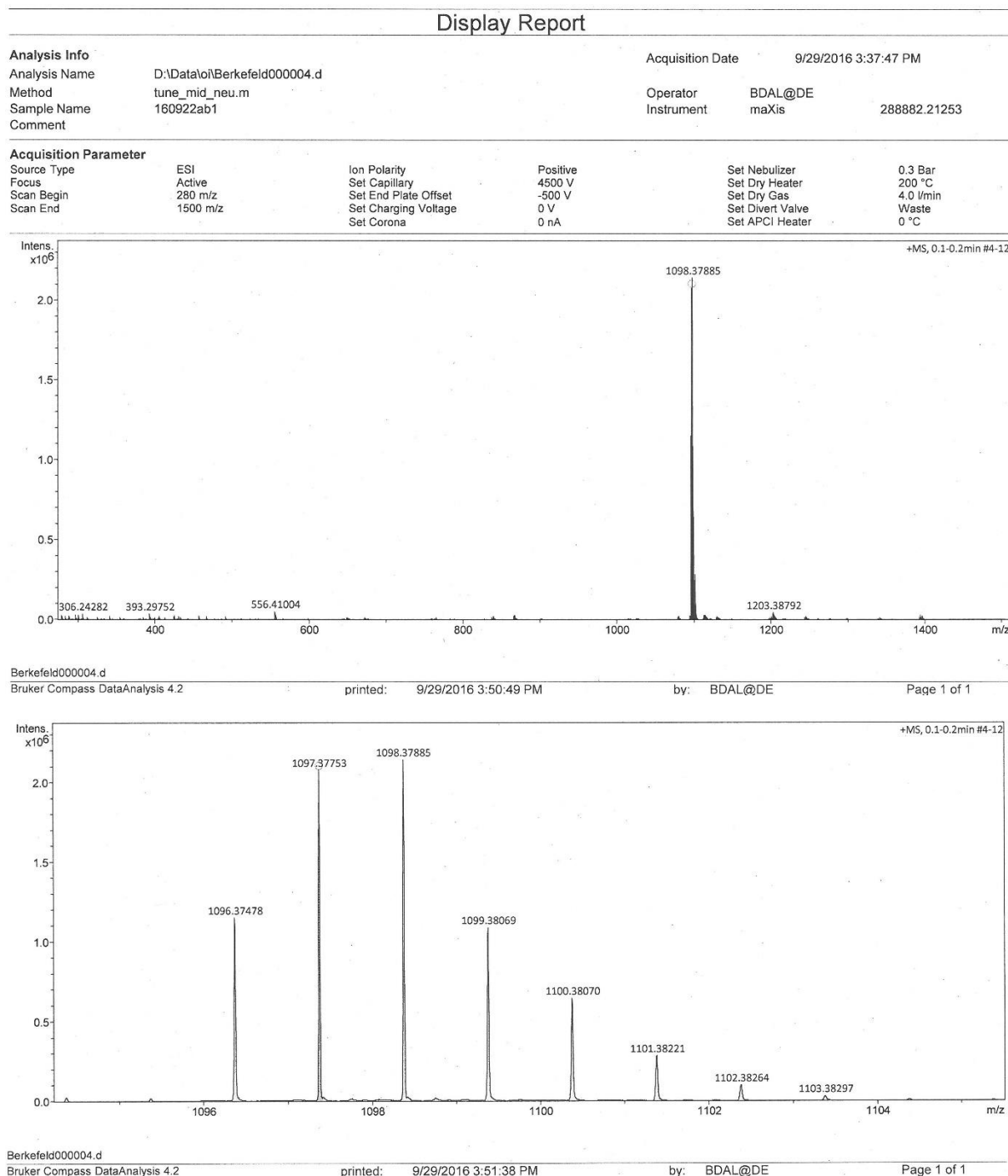


Figure S1. Results of high resolution ESI-MS data for [1]NTf₂ in THF: (top) overview; (bottom) isotopic distribution.

2 Additional NMR Spectroscopic Data for In Situ Generated [2]NTf₂

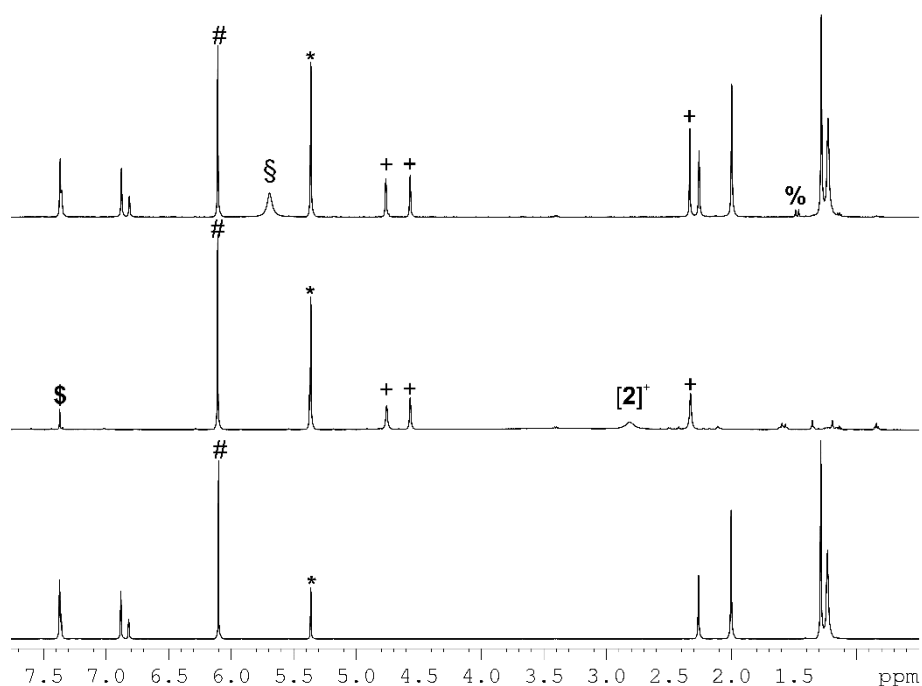


Figure S2. 500 MHz ¹H-NMR spectra, CD₂Cl₂ (*), 203 K: (bottom) neutral **2** (contains 0.17 equiv. of residual C₆H₆ (§) from synthesis) and 1,1,2,2-C₂H₂Cl₄ (#) internal standard; (centre) after addition of [Fc''']NTf₂ oxidant at 293 K (resonances of [2]⁺ other than that at lowest field at 2.82 ppm are severely broadened), 1,1,2,2-C₂H₂Cl₄ (#) internal standard, Fc'' by-product (+); (top) after addition of 1 equiv. of (H₅C₅)Co to [2]NTf₂ at 193 K, 1,1,2,2-C₂H₂Cl₄ (#) internal standard, Fc'' (+) and [(H₅C₅)Co]NTf₂ (§) by-products, degree of sample deterioration based on phosphine resonance(s) centered at 2.47 ppm (%): < 5 %.

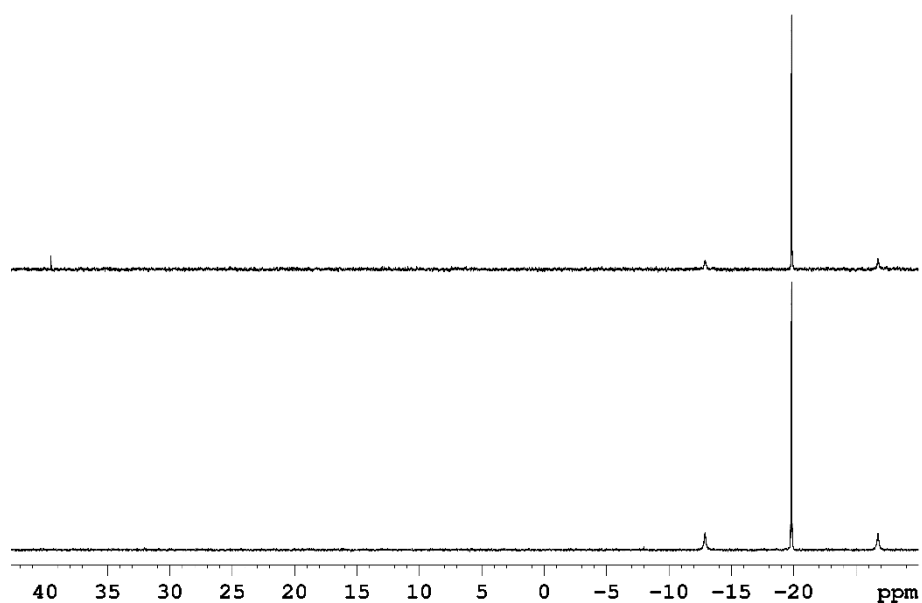


Figure S3. 202 MHz ³¹P{¹H}-NMR spectra, CD₂Cl₂, 203 K: (bottom) neutral **2**, ¹J(P,Pt) = 2800 Hz; (top) after addition of 1 equiv. of (H₅C₅)Co to [2]NTf₂ at 193 K, resonance at 40 ppm results from partial sample deterioration (< 5 % of total P).

3 Cyclic Voltammetry Data

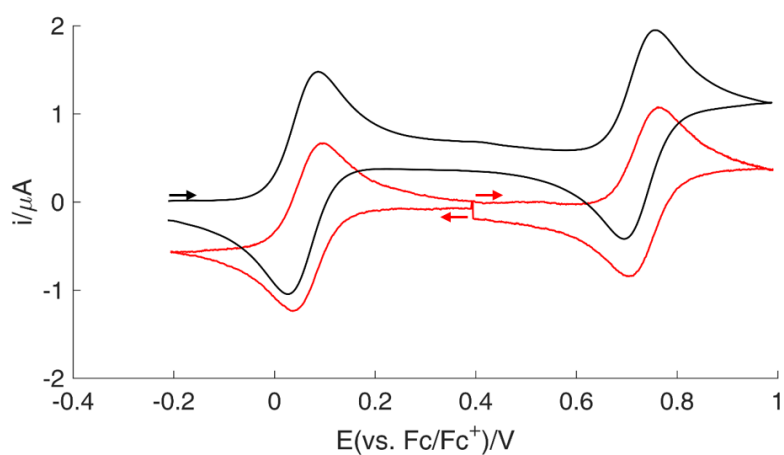


Figure S4. CV data in 0.1 M $n\text{Bu}_4\text{NPF}_6/\text{CH}_2\text{Cl}_2$, 50 mV s^{-1} , 290 K: (black) $114 \mu\text{M}$ **1**; (red) $101 \mu\text{M}$ **[1]NTf₂**, independent sweeps were performed in direction of cathodic and anodic potentials as indicated by red arrows.

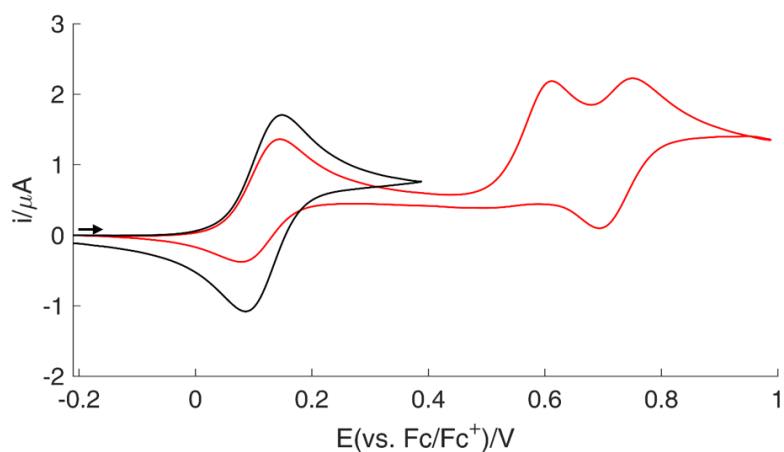


Figure S5. CV data in 0.1 M $n\text{Bu}_4\text{NPF}_6/\text{CH}_2\text{Cl}_2$, 50 mV s^{-1} , 290 K: (black) $115 \mu\text{M}$ **2**, potential sweep direction reversed at $\sim 0.4 \text{ V}$; (red) $94 \mu\text{M}$ **2**, full anodic potential sweep.

Table S1. ΔE_p [V] of the First Oxidation Step of **1** in 0.1 M $n\text{Bu}_4\text{NPF}_6/\text{CH}_2\text{Cl}_2$

$v/\text{V s}^{-1}$	$c(\mathbf{1})/\text{mmol L}^{-1}$			
	0.0404	0.0676	0.0928	0.119
0.02	0.061	0.061	0.061	0.062
0.05	0.061	0.059	0.060	0.061
0.10	0.062	0.062	0.064	0.062
0.20	0.067	0.067	0.068	0.068
0.50	0.063	0.066	0.070	0.072
1.00	0.067	0.071	0.076	0.078
2.00	0.070	0.077	0.084	0.086
5.00	0.090	0.093	0.102	0.110
10.00	0.102	0.113	0.126	0.134
20.00	0.132	0.146	0.156	0.162
40.00	0.186	0.198	0.213	0.228
50.00	0.196	0.224	0.244	0.248

Table S2. $i_p^{\text{red}}/i_p^{\text{ox}}$ of the First Oxidation Step of **1** in 0.1 M $n\text{Bu}_4\text{NPF}_6/\text{CH}_2\text{Cl}_2$

$v/\text{V s}^{-1}$	$c(\mathbf{1})/\text{mmol L}^{-1}$			
	0.0404	0.0676	0.0928	0.119
0.02	0.87	0.87	0.87	0.85
0.05	0.97	0.97	0.98	0.95
0.10	1.02	1.01	1.01	1.01
0.20	1.03	1.03	1.03	1.03
0.50	0.98	1.04	1.01	1.01
1.00	1.01	1.04	1.03	1.03
2.00	0.96	0.99	1.01	1.01
5.00	1.05	1.01	1.02	1.01
10.00	1.01	1.01	0.97	1.00
20.00	0.97	1.00	1.01	1.02
40.00	0.95	0.97	1.02	1.06
50.00	0.91	0.99	1.04	1.03

Table S3. ΔE_p [V] of the First Oxidation of **2** in 0.1 M $n\text{Bu}_4\text{NPF}_6/\text{CH}_2\text{Cl}_2$

$v/\text{V s}^{-1}$	$c(\mathbf{2})/\text{mmol L}^{-1}$			
	0.0308	0.0608	0.0899	0.115
0.02	0.060	0.062	0.061	0.062
0.05	0.059	0.061	0.060	0.062
0.10	0.063	0.063	0.063	0.064
0.20	0.067	0.067	0.070	0.070
0.50	0.061	0.062	0.063	0.069
1.00	0.062	0.068	0.065	0.075
2.00	0.063	0.075	0.068	0.083
5.00	0.083	0.079	0.083	0.101
10.00	0.080	0.091	0.080	0.125
20.00	0.128	0.094	0.100	0.148
40.00	0.168	0.117	0.129	0.201
50.00	0.188	0.204	0.212	0.220

Table S4. $i_p^{\text{red}}/i_p^{\text{ox}}$ of the First Oxidation Step of **2** in 0.1 M $n\text{Bu}_4\text{NPF}_6/\text{CH}_2\text{Cl}_2$

$v/\text{V s}^{-1}$	$c(\mathbf{2})/\text{mmol L}^{-1}$			
	0.0308	0.0608	0.0899	0.115
0.02	0.84	0.84	0.84	0.85
0.05	0.90	0.94	0.93	0.94
0.10	0.96	0.96	0.96	0.97
0.20	0.97	0.97	0.98	0.98
0.50	0.86	0.93	0.91	0.96
1.00	0.93	0.95	0.99	0.99
2.00	0.89	0.97	0.97	0.97
5.00	0.88	0.93	0.97	0.99
10.00	0.80	0.95	0.93	0.99
20.00	0.85	0.90	0.98	0.95
40.00	0.83	0.84	0.98	0.99
50.00	0.85	0.99	0.93	0.95

4 EPR Data

Samples of [1]NTf₂ (2 mM) were prepared in a 1:1 toluene/CH₂Cl₂ solution.

Complex [2]NTf₂ was generated *in situ* for EPR measurements. For that, a solution of **2** (10 mg, 0.01 mmol) in 1 mL 1:1 toluene/ CH₂Cl₂ was cannula-transferred into a solution of [Fc²⁺]⁺NTf₂⁻ (5.5 mg, 0.01 mmol) in 4 mL of the same solvent mixture precooled at 193 K in a dry ice/acetone bath. The instantaneously formed dark blue-purple solution was cannula-transferred into a precooled (193 K, dry ice/acetone bath) EPR tube.

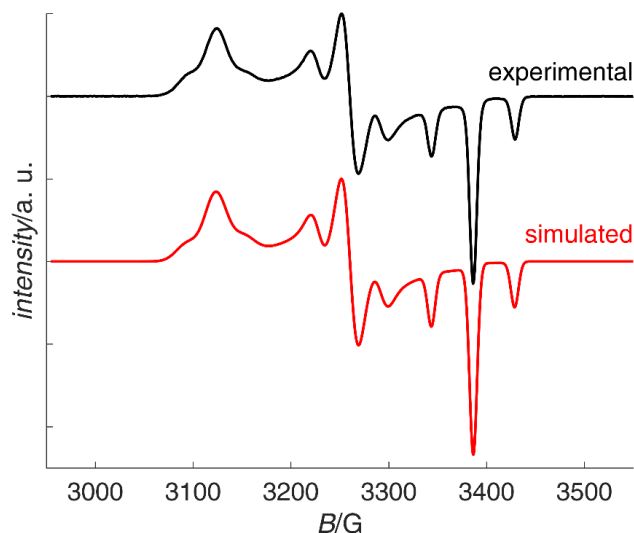


Figure S6. X-Band EPR spectrum (1:1 toluene/CH₂Cl₂, 77 K) of [1]NTf₂: microwave frequency 9.5009617 GHz, microwave power 2.01 mW, modulation amplitude 2.680 G. Simulated parameters: $g_x = 2.005$, $g_y = 2.082$, $g_z = 2.174$, $A_x = 239$; $A_y = 184$, $A_z = 175$ MHz; full line width at half maximum $lw = 0.784$ mT. H Strain = [12.69; 42.46; 76.36] MHz.

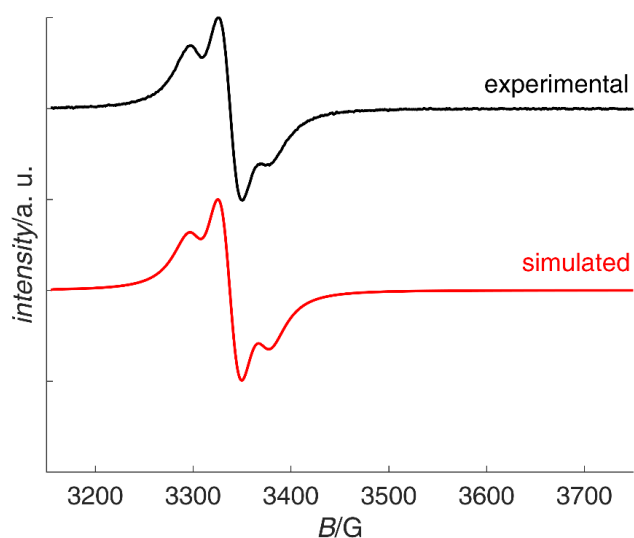


Figure S7. X-Band EPR spectrum (1:1 toluene/CH₂Cl₂, 298 K) of [1]NTf₂: microwave frequency 9.7577363 GHz, microwave power 2.01 mW, modulation amplitude 2.680 G. Simulated parameters: $g_{iso} = 2.089$, $A_{iso} = 191$ MHz, full line width at half maximum $lw = [0.816; 4.339]$ mT.

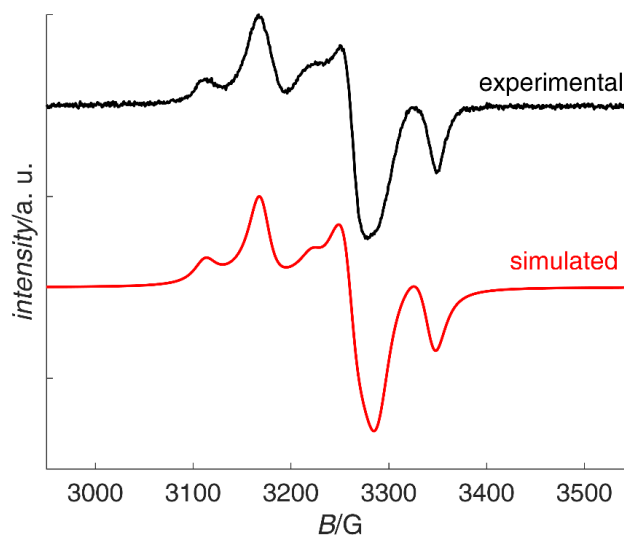


Figure S8. X-Band EPR spectrum (1:1 toluene/ CH_2Cl_2 , 105 K) of $[\mathbf{2}]\text{NTf}_2$: microwave frequency 9.4174098 GHz, microwave power 2.01 mW, modulation amplitude 1.898 G. Simulated parameters: $g_x = 2.124$, $g_y = 2.063$, $g_z = 2.046$, $A_x = 325$; $A_y = 490$, $A_z = 291$ MHz; full line width at half height $lw = [0.587; 2.55276]$ mT. A Strain = $[0; 9.55; 0]$ MHz. H Strain = $[0.49; 0; 0.17]$ MHz.

5 Additional Information on UV/Vis/NIR Data

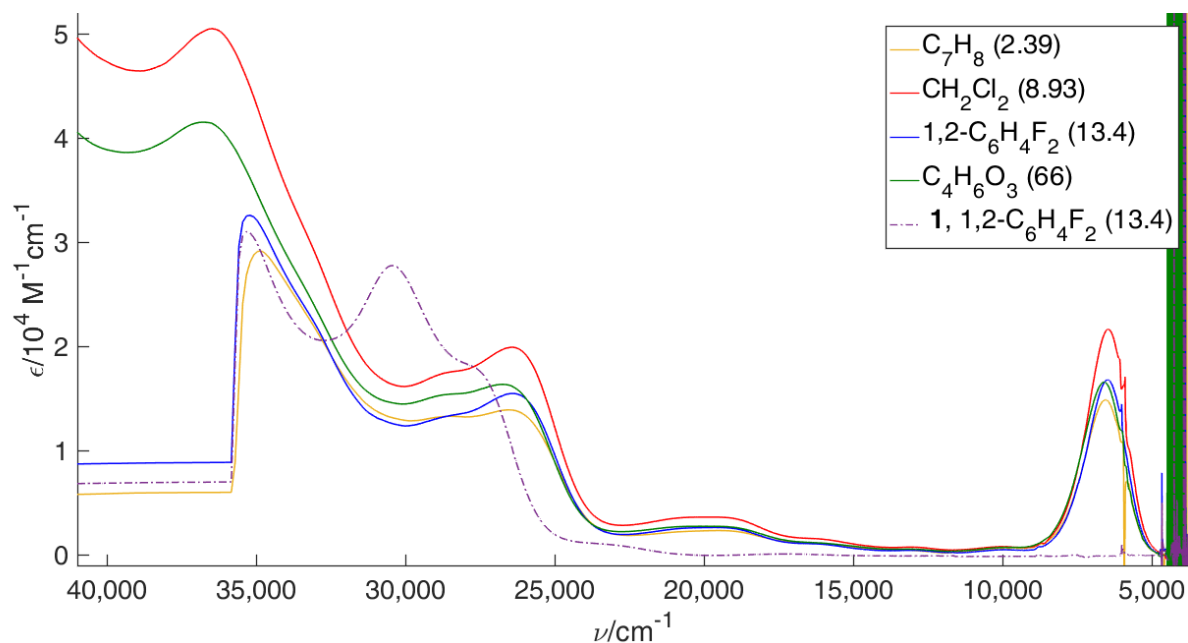


Figure S9. Dependence of electronic absorption spectra of $\mathbf{1}$ and $[\mathbf{1}]\text{NTf}_2$ on solvent polarity; spectra taken at 296 K, solvent relative permittivity is provided in parentheses and was taken from literature.¹

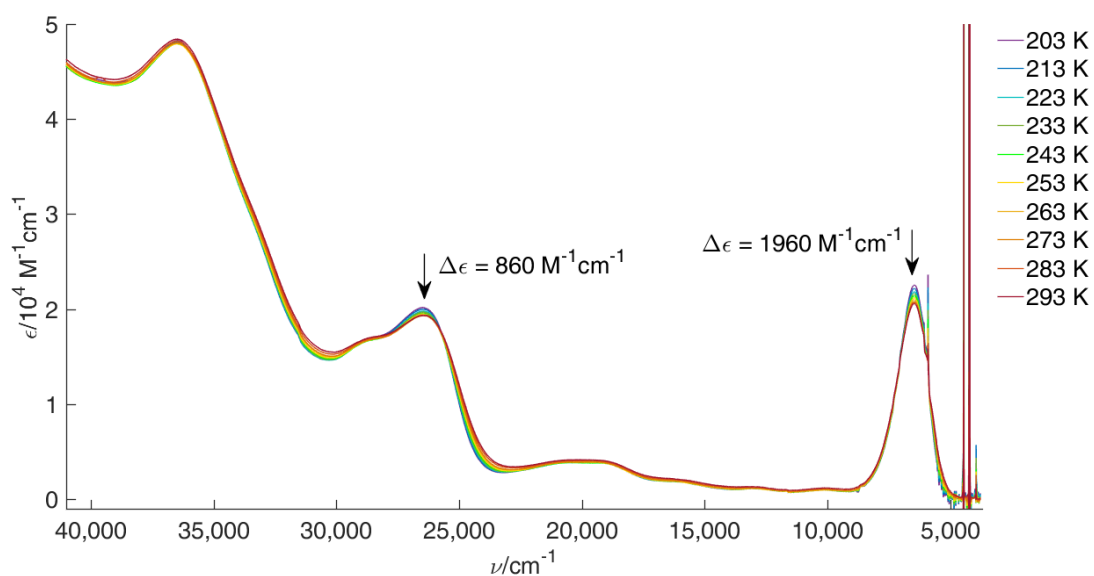


Figure S10. UV/vis/NIR spectra of [1]NTf₂ in CH₂Cl₂, temperature range 203-293 K.

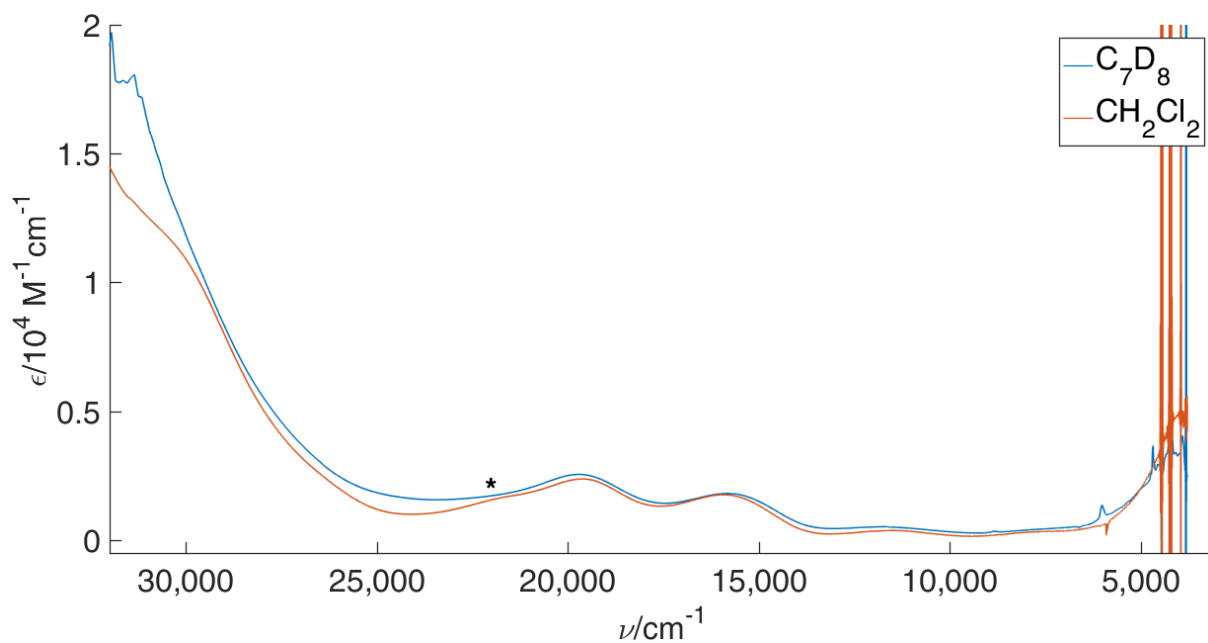


Figure S11. Electronic spectra of **2** and *in situ* generated [2]NTf₂ in C₇D₈ at 203 K. Shoulder highlighted with an asterisk (*) originates from 1,1'-Diacetylferrocene by-product.

6 Additional Crystallographic Information

Generally applied colour code:

C, black; H, light blue; O, red; metal, plum; P, orange; S, yellow; N, blue; F, green.

6.1 Structural details of $[Fc'']NTf_2$

Single crystalline samples suitable for XRD analysis were obtained by slow diffusion of hexane into a saturated solution of $[Fc'']NTf_2$ in 1,2- $C_6F_2H_4$ at r.t. The anion is disordered at an inversion centre.

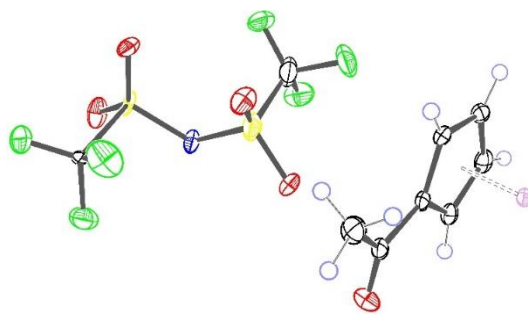


Figure S12. ORTEP representation of the asymmetric unit of $[Fc'']NTf_2$: 50% thermal probability ellipsoids. Site occupancy factor of atoms of the NTf_2 -anion displayed set to 0.5.

6.2 Structural details of $1 \times 2C_7H_8$.

Single crystalline samples suitable for XRD analysis were obtained by slow diffusion of hexane into a saturated solution of **1** in toluene at r.t., which produced **1** with 2 eq toluene. The unit cell contains two additional formula units of toluene, one on cell edge and another at the cell corner. The latter is disordered about the inversion centre. Both toluene units including the disorder could not be satisfactorily refined without additional restraints ('flat') and some of the ellipsoids were of poor quality. For this reason the program SQUEEZE implemented as the SQUEEZE option in PLATON was employed to remove the electron density attributable to the lattice solvent from a total potential solvent accessible void volume of 713.4 cubic angstroms. SQUEEZE results are collected at the end of the cif file.

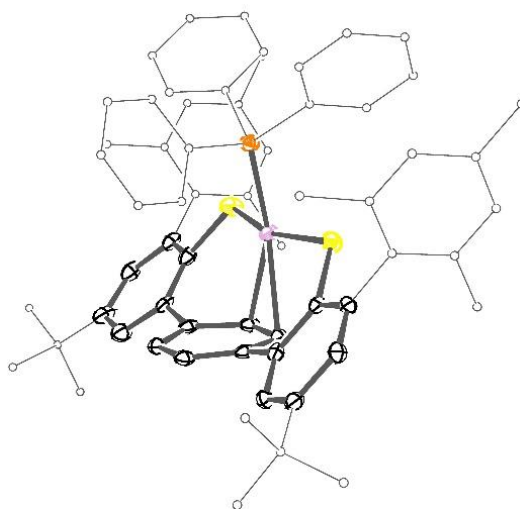


Figure S13. ORTEP representation of **1**, thermal displacement ellipsoids at 50% probability level, H-atoms omitted for clarity.

6.3 Structural details of $[1]NTf_2$

Slow diffusion of pentane into a saturated solution of $[1]NTf_2$ in 1,1,2,2- $C_2H_2Cl_4$ at r.t. produced maroon single crystals of $[1]NTf_2 \times 2(C_2H_2Cl_4)$.

6.4 Structural details of **2**.

Layering a saturated benzene solution of **2** with methanol (1:10) at r.t. produces yellow single crystals of $2 \times 2(CH_3OH)$.

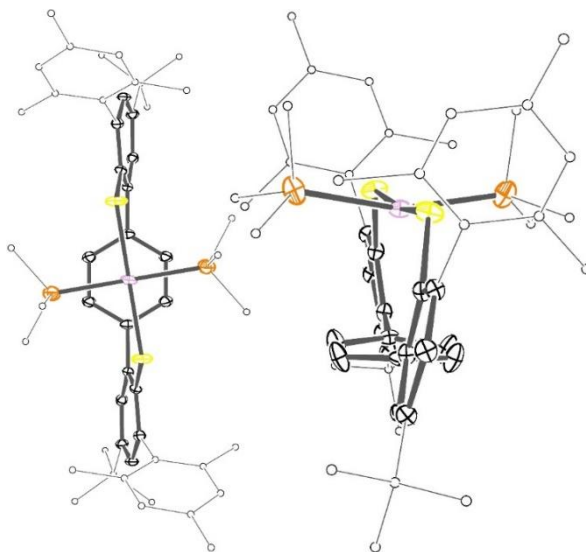


Figure S14. ORTEP representation of **2**: left, view from top, right, view along long molecular axis; 50% thermal probability ellipsoids, H-atoms and methanol lattice solvent omitted for clarity.

Table S5. Selected Bond Lengths [Å] and Angles [°] in the Solid-State Structures of Parent Complexes and Derived Cations; Metrical Data from DFT Optimizations in Parentheses^a

bond lengths	1	[1]NTf ₂	2	[2] ⁺
Pt-P	2.234(1) (2.257)	2.2694(7) (2.283)	2.3095(7) (2.316)	(2.348)
Pt-S1	2.347(1) (2.364)	2.3012(9) (2.324)	2.3415(6) (2.375)	(2.325)
Pt-S2	2.359(1) (2.403)	2.3149(9) (2.355)	2.3415(6) (2.375)	(2.325)
Pt-C11	2.416(4) (2.358)	2.375(2) (2.385)	>3.3 (3.305)	(3.307)
Pt-C12	2.390(4) (2.328)	2.373(2) (2.386)	>3.3 (3.341)	(3.333)
S1-C1	1.782(4) (1.790)	1.760(2) (1.775)	1.776(2) (1.796)	(1.785)
S2-C14	1.773(4) (1.786)	1.760(2) (1.780)	1.776(2) (1.796)	(1.785)
C1-C2	1.402(6) (1.415)	1.411(3) (1.422)	1.409(3) (1.418)	(1.418)
C14-C13	1.409(5) (1.418)	1.412(3) (1.419)	1.409(3) (1.418)	(1.418)
C2-C3	1.399(5) (1.396)	1.393(3) (1.395)	1.401(3) (1.404)	(1.399)
C13-C18	1.400(6) (1.408)	1.399(3) (1.404)	1.401(3) (1.404)	(1.399)
bond angles				
S1-Pt-S2	162.68(4) (164.4)	166.59(3) (163.9)	171.47(3) (172.9)	(168.9)
P-Pt-P			162.73(4) (164.6)	(162.9)
P-Pt-C11	152.9(1) (150.9)	158.14(6) (153.7)		
S1-Pt-P	90.28(4) (87.8)	88.19(3) (88.1)	88.85(3) (89.3)	(90.6)
C1-S1-Pt	116.9(1) (116.9)	119.01(8) (117.6)	118.02(8) (113.3)	(117.0)
C14-S2-Pt	115.6(1) (110.3)	117.24(8) (113.5)	118.02(8) (113.3)	(117.0)
torsion angle				
C14-C13-C10-C11	43.8(5) (35.5)	37.4(3) (36.9)	76.2(3) (63.9)	(77.1)

^a Full optimization on the BP86-D3/TZVP/ZORA level of theory.

Table S6. General Crystallographic Information of **1**, [1]NTf₂, and **2**

compound	1	[1]NTf ₂	2
Empirical formula	C ₆₂ H ₆₃ PPtS ₂ , 2(C ₇ H ₈)	C ₆₄ H ₆₃ F ₆ NO ₄ PPtS ₄ , 1.5(C ₂ H ₂ Cl ₄)	C ₅₀ H ₆₆ P ₂ PtS ₂ , 2(CH ₄ O)
<i>M_r</i> / g mol ⁻¹	1282.52	1630.20	1052.26
Source	Mo K _α , 0.71073 Å	Mo K _α , 0.71073 Å	Mo K _α , 0.71073 Å
Temperature/ K	100(2)	100(2)	100(2)
Crystal system	monoclinic	orthorhombic	monoclinic
Space group	P 21/n	P b c a	C 2/c
<i>Z</i>	4	8	4
<i>a</i> [Å]	9.4324(4)	25.0138(4)	13.6444(4)
<i>b</i> [Å]	34.7348(14)	18.0829(3)	12.1522(3)
<i>c</i> [Å]	17.2141(7)	30.6048(5)	30.1567(8)
α [°]	90	90	90
β [°]	91.9970(10)	90	92.7950
γ [°]	90	90	90
<i>V</i> [Å ³]	5636.5(4)	13843.2(4)	4994.3(2)
Density ρ_{diffn} / g cm ⁻³	1.511	1.564	1.399
Abs. coeff. μ / mm ⁻¹	2.640	2.466	2.995
<i>F</i> (000)	2640	6560	2168
Crystal size/ mm ³			
Theta range [°]	2.4545-20.1564	2.35-30.49	5.7713-28.2511
Unique reflections	12366	21152	5708
Absorption correction	multi-scan	multi-scan	multi-scan
Parameters/ restraints	607 / 0	830 / 3	278 / 0
<i>R</i> ₁ , ωR ₂ >2 σ (I)	0.0416 / 0.0754	0.0305 / 0.0683	0.0229 / 0.0557
<i>R</i> ₁ , ωR ₂ all data	0.0562 / 0.0803	0.0378 / 0.0726	0.0270 / 0.0644
Goodness-of-fit on <i>F</i> ²	1.136	1.072	1.191
Largest diff. peak/hole/ e ⁻ Å ⁻³	3.765 / -3.281	1.591 / -2.707	0.645 / -1.053
CCDC	1511081	1511082	1511080

Table S7. General Crystallographic Information on 1,1'-Diacetylferrocenium Bis(trifluoromethylsulfonyl)imide

compound	[Fc ⁺⁺]NTf ₂
Empirical formula	C ₁₆ H ₁₄ F ₆ FeNO ₆ S ₂
<i>M_r</i> / g mol ⁻¹	550.26
Source	Mo K _α , 0.71073 Å
Temperature/ K	100(2)
Crystal system	monoclinic
Space group	P 21/c
<i>Z</i>	4
<i>a</i> [Å]	10.6185(2)
<i>b</i> [Å]	13.6870(3)
<i>c</i> [Å]	7.4015(2)
<i>α</i> [°]	90
<i>β</i> [°]	108.1900(10)
<i>γ</i> [°]	90
<i>V</i> [Å ³]	1021.94
Density ρ_{diffn} / g cm ⁻³	1.788
Abs. coeff. μ / mm ⁻¹	1.031
<i>F</i> (000)	554
Crystal size/ mm	
Theta range [°]	2.51-27.49
Unique reflections	2348
Absorption correction	Multi-scan
Parameters/ restraints	215/12
R ₁ , wR ₂ >2sigma(I)	0.0276/0.0641
R ₁ , wR ₂ all data	0.0280/0.0642
Goodness-of-fit on <i>F</i> ²	1.252
Largest diff. peak/ hole/ e·Å ⁻³	0.382 / -0.256
CCDC	1511083

7 Additional Information on Computational Data

Table S8. Computed Mulliken Spin Densities of [1]⁺ and [2]⁺

	[1] ⁺			[2] ⁺		
<i>vacuum</i>	<i>BP86</i>	<i>B3LYP</i>	<i>BLYP-35</i>	<i>BP86</i>	<i>B3LYP</i>	<i>BLYP-35</i>
Pt	0.129	0.124	0.113	0.113	0.113	0.110
S	0.294	0.334	0.406	0.284	0.307	0.324
Ar	0.162	0.155	0.158	0.164	0.146	0.137
S'	0.253	0.255	0.223	0.284	0.308	0.330
Ar'	0.115	0.098	0.072	0.164	0.146	0.137

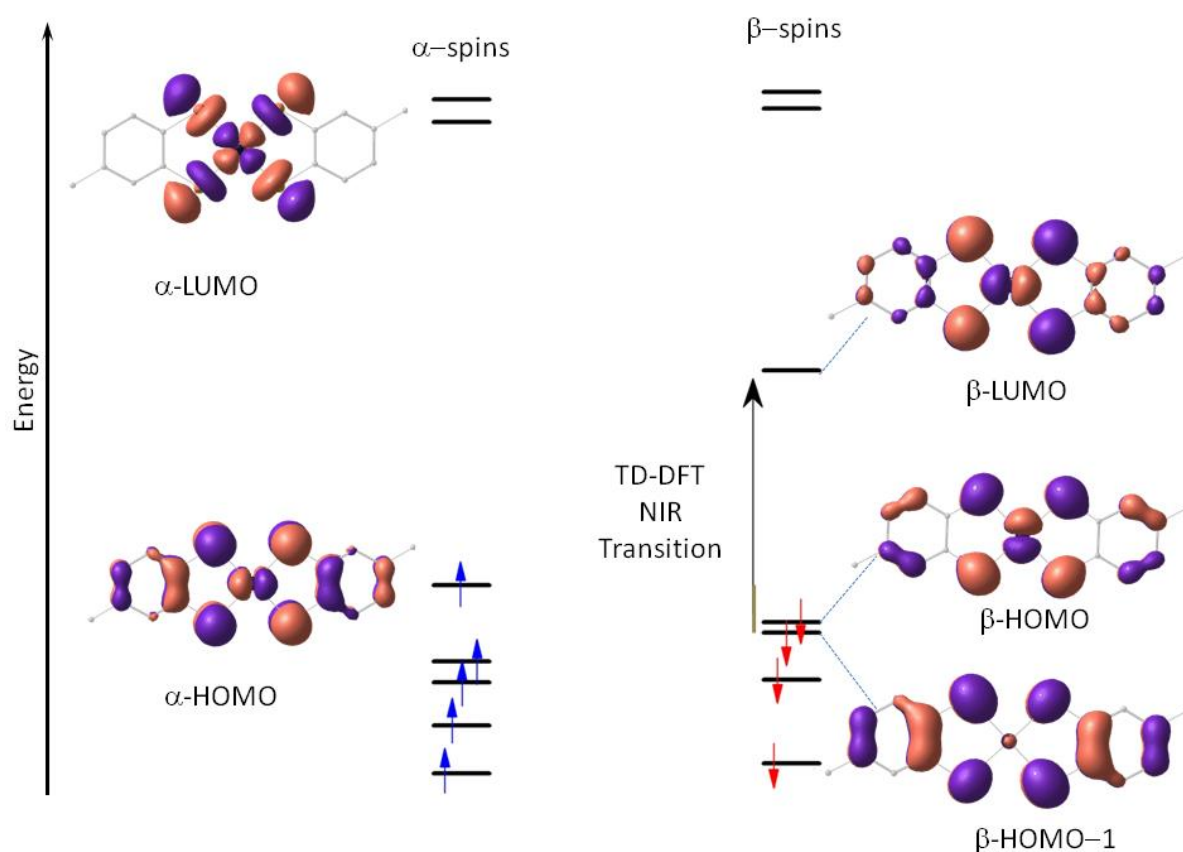


Figure S15. Kohn-Sham MOs and energy diagram for the reference platinate(II) complex $[(\text{tdt})_2\text{Pt}]^{\bullet-}$, $\text{tdt} = 4\text{-Me-}1,2\text{-benzenedithiophenol}$,² from a spin-unrestricted ZORA-BLYP-35 DFT calculation. TD-DFT derived lowest-energy transition (β -HOMO-1 \rightarrow β -LUMO) $\lambda_{\text{max}}(\text{computed}) = 12,590 \text{ cm}^{-1}$ (795 nm), $\lambda_{\text{max}}(\text{exp.}) = 11,220 \text{ cm}^{-1}$ (891 nm).

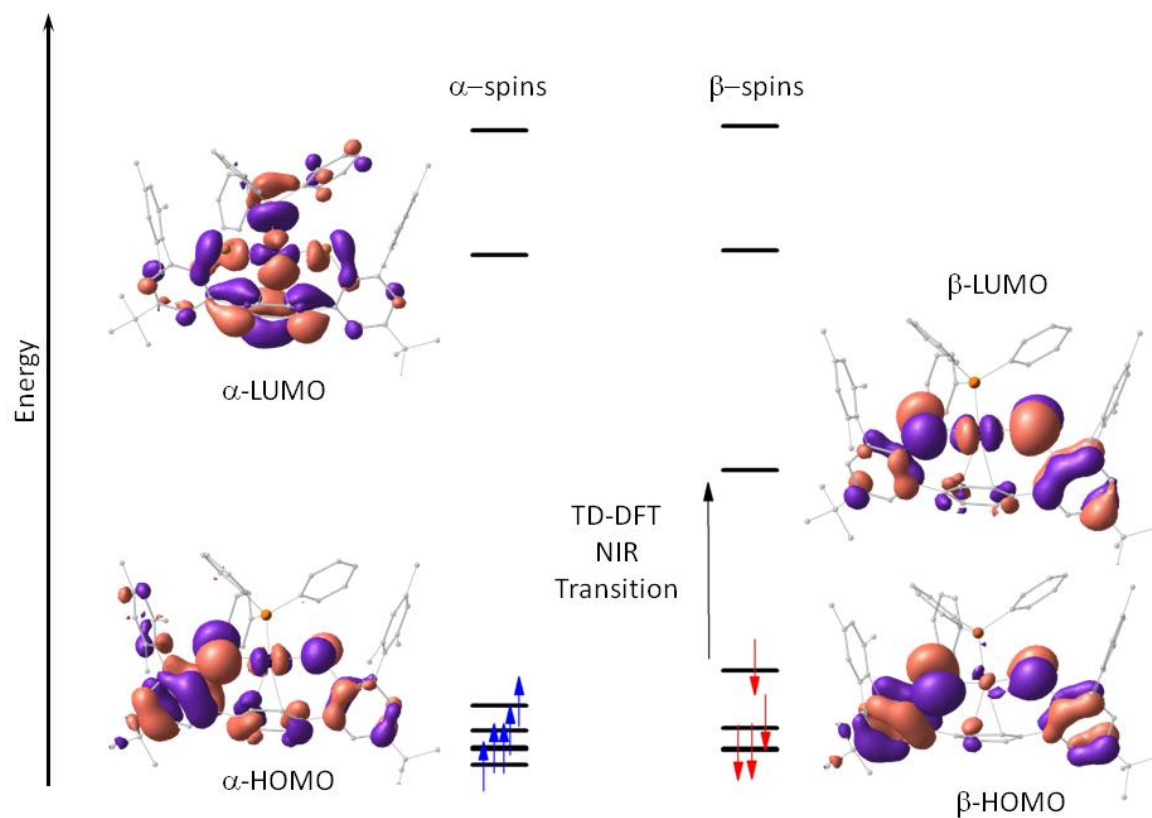


Figure S16. Kohn-Sham MOs and energy diagram for $[1]^+$ from a spin-unrestricted ZORA-BLYP-35 DFT calculation. TD-DFT derived lowest-energy transition (β -HOMO \rightarrow β -LUMO): $\lambda_{\max}(\text{computed}) = 7,007 \text{ cm}^{-1}$ (1427 nm).

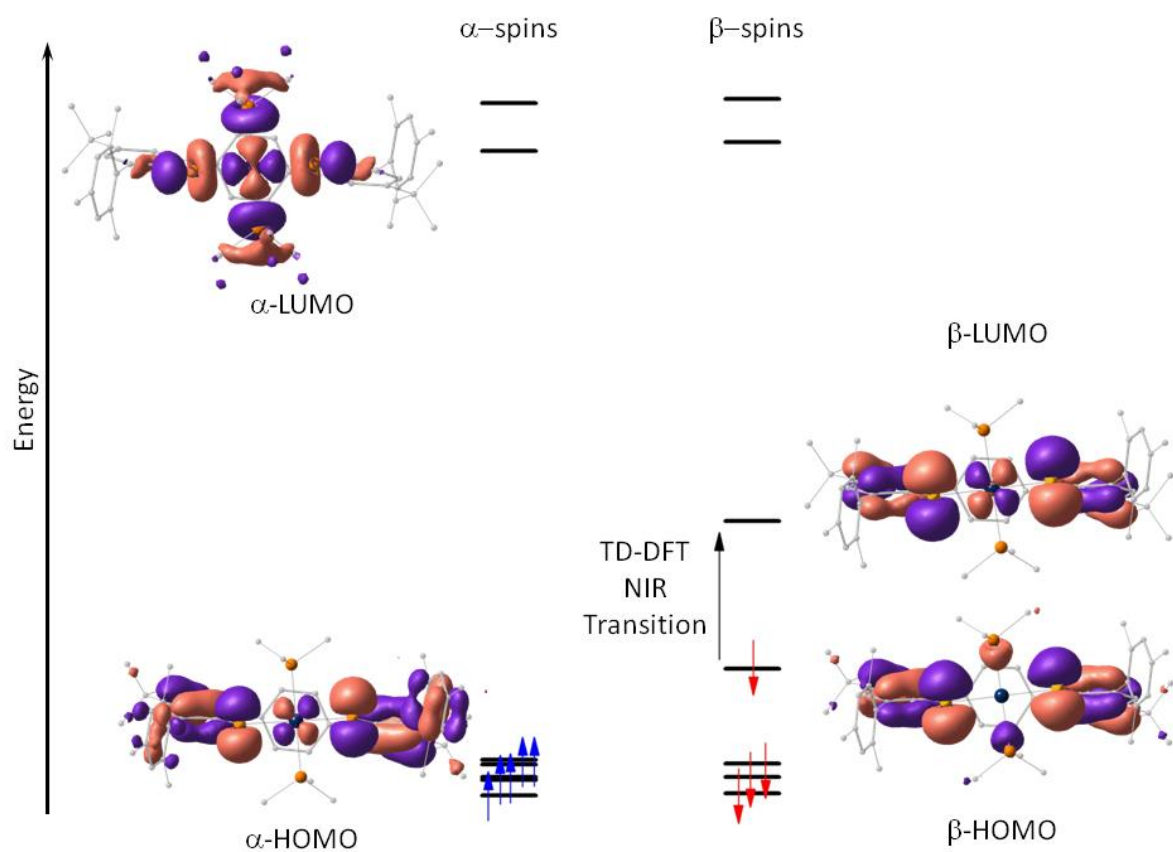


Figure S17. Kohn-Sham MOs and energy diagram for $[2]^+$ from a spin-unrestricted ZORA-BLYP-35 DFT calculation. TD-DFT derived lowest-energy transition (β -HOMO \rightarrow β -LUMO): $\lambda_{\max}(\text{computed}) = 4,562 \text{ cm}^{-1}$ (2192 nm).

Table S9. TD-DFT Computed Energies and Intensities of Electronic Transitions of [1]⁺ and [2]⁺

transition	[1] ⁺			[2] ⁺		
	$\tilde{\nu} / \text{cm}^{-1}$	λ / nm	f_{osc}	$\tilde{\nu} / \text{cm}^{-1}$	λ / nm	f_{osc}
1	7007.2	1427.1	0.19589	4562.1	2192	0.18621
2	9570.9	1044.8	0.00201	8266.4	1209.7	0.00343
3	12103.8	826.2	0.00201	10504	952	0.00147
4	12719.2	786.2	0.00762	12526.9	798.3	0.00338
5	13600.6	735.3	0.00134	12735.2	785.2	0.00219
6	13736.1	728	4.2×10^{-4}	12742	784.8	0.0016
7	16513.1	605.6	0.00473	13617.9	734.3	0.00143
8	17205.3	581.2	0.00358	14341	697.3	0.02646
9	18510.3	540.2	0.00303	15677.7	637.8	0.00176
10	18622.3	537	0.00188	16382.6	610.4	0.00768
11	19233.2	519.9	0.0056	16513.8	605.6	0.00253
12	19793.8	505.2	0.06145	19493.4	513	0.06462
13	20133.1	496.7	0.00414	20364.6	491	0.08252
14	20574.8	486	0.02738	22707.3	440.4	0.00184
15	21093.6	474.1	0.00457	24437.3	409.2	0.01153
16	21809.7	458.5	0.00157	25184	397.1	0.00695
17	22185.1	450.8	0.01304	27680.7	361.3	0.00147
18	22224.3	450	5.1×10^{-4}	28257.1	353.9	6.2×10^{-4}
19	22854.1	437.6	0.01504	28745	347.9	0.0018
20	23712.1	421.7	0.00115	29150.9	343	4.3×10^{-4}
21	-	-	0.19589	29786.2	335.7	0.00839
22	-	-	0.00201	29886.1	334.6	0.00207
23	-	-	0.00201	29983.9	333.5	0.00271
24	-	-	0.00762	30003.5	333.3	8.0×10^{-4}
25	-	-	0.00134	31422.5	318.2	0.00261

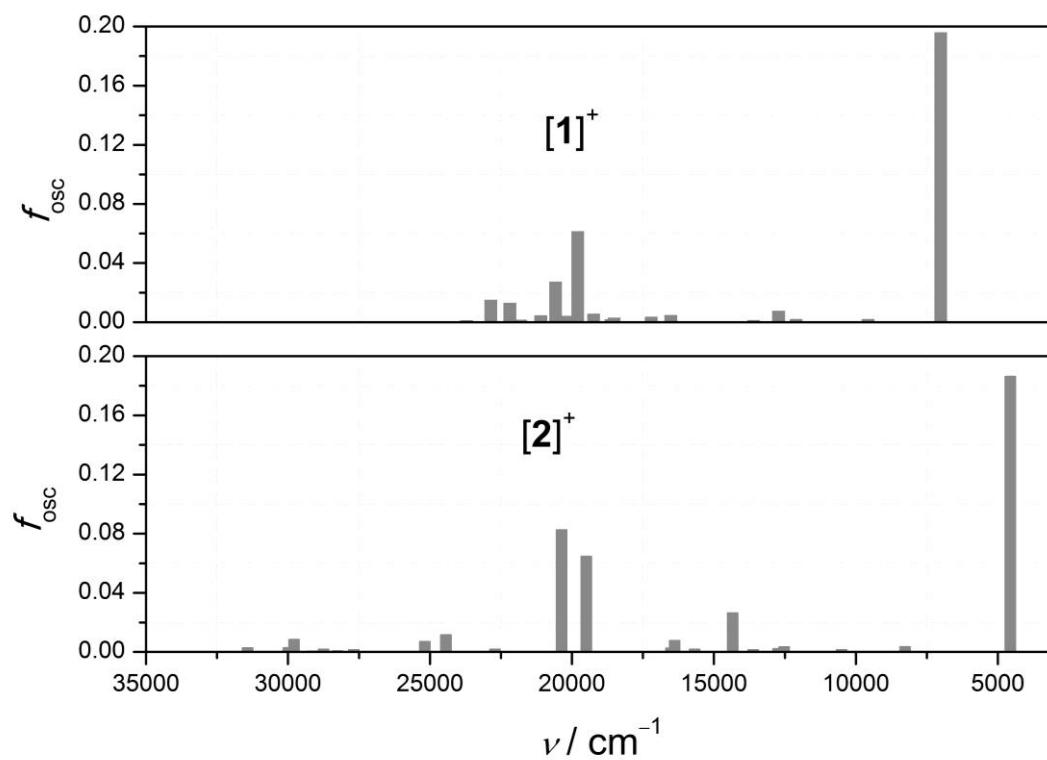


Figure S18. Computed line spectrum of $[1]^+$ (top) and $[2]^+$ (bottom).

Table S10. TD-DFT Computed Energies and Intensities of Electronic Transitions of Reference Compound [(tdt)₂Pt]^{•-}, tdt = 4-Me-1,2-Benzenedithiophenol

transition	$\tilde{\nu} / \text{cm}^{-1}$	λ / nm	f_{osc}
1	7330.8	1364.1	1.4×10^{-8}
2	12586.8	794.5	0.28352
3	13417.5	745.3	7.5×10^{-6}
4	15094.6	662.5	0.03449
5	18925.7	528.4	3.5×10^{-6}
6	21629.4	462.3	1.3×10^{-6}
7	21958.7	455.4	3.4×10^{-6}
8	22472.2	445	0.00162
9	23063.8	433.6	2.0×10^{-9}
10	24542	407.5	5.7×10^{-7}
11	24668.3	405.4	2×10^{-8}
12	28351.1	352.7	1.7×10^{-4}
13	28444.6	351.6	2.3×10^{-6}
14	28813.8	347.1	1.6×10^{-7}
15	30401	328.9	0.01231
16	30724.4	325.5	1.8×10^{-5}
17	31538.6	317.1	0.00355
18	31100.1	321.5	1.5×10^{-6}
19	31427.1	318.2	1.1×10^{-6}
20	33068.3	302.4	0.04865

Table S11. Cartesian Coordinates of Optimized [1]⁺

Pt	2.331028	4.385335	1.993982
S	1.842275	3.082346	3.848034
S	2.378550	5.291083	-0.176060
P	0.090709	4.716959	1.717761
C	3.066452	2.990545	5.131147
C	4.192047	3.850310	5.256203
C	4.951592	3.828662	6.426777
H	5.809171	4.500085	6.492043
C	4.667391	2.943975	7.479852
C	3.573837	2.077059	7.321307
H	3.318736	1.368216	8.108428
C	2.766001	2.088022	6.180311
C	4.503312	4.748540	4.142719
C	4.556508	4.177805	2.831215
H	4.731378	3.106286	2.725416
C	4.615709	5.015364	1.709499
H	4.851851	4.594318	0.733140
C	4.554885	6.438165	1.864616
C	4.641030	6.964326	3.151053
H	4.611585	8.045757	3.294310
C	4.630029	6.125076	4.282926
H	4.601211	6.570284	5.278421
C	4.271396	7.253512	0.683124
C	3.367581	6.765688	-0.296056
C	3.093294	7.549482	-1.445457
C	3.686359	8.801907	-1.569239
H	3.450580	9.387581	-2.459709
C	4.551432	9.329545	-0.589414
C	4.830437	8.532545	0.523024
H	5.524936	8.882309	1.286500
C	1.575289	1.194877	6.096595
C	1.619117	0.022247	5.311045
C	0.478936	-0.785414	5.241858
H	0.509953	-1.690681	4.629198
C	-0.695526	-0.466521	5.938141
C	-0.707579	0.694253	6.718188
H	-1.615216	0.962868	7.263555
C	0.406115	1.538427	6.804704
C	2.151321	7.045232	-2.487254
C	2.605356	6.129940	-3.460126
C	1.696011	5.647225	-4.409372
H	2.044068	4.928362	-5.156484
C	0.357099	6.057337	-4.423538
C	-0.066071	6.972470	-3.451665
H	-1.110592	7.294250	-3.436770
C	0.805051	7.468603	-2.476320
C	5.547834	2.942849	8.732123
C	5.146328	10.726504	-0.779404
C	2.862819	-0.346410	4.542579
H	2.771267	-1.350785	4.109282
H	3.755911	-0.323942	5.184185
H	3.041602	0.363559	3.719906
C	-1.914843	-1.347815	5.837489
H	-2.769735	-0.906484	6.366722
H	-1.727313	-2.342795	6.270474
H	-2.205207	-1.504789	4.787553
C	0.332719	2.816232	7.600782
H	0.564157	3.685234	6.966014
H	1.054610	2.825620	8.430893
H	-0.671674	2.956193	8.020454
C	4.034127	5.647682	-3.459404
H	4.257224	5.081707	-4.373469
H	4.225313	4.987253	-2.598197
H	4.743859	6.483944	-3.383977
C	-0.600592	5.539037	-5.465281
H	-0.325986	4.526542	-5.791533
H	-0.600720	6.183159	-6.359646

H	-1.630837	5.513414	-5.083177
C	0.298684	8.392054	-1.400159
H	0.827733	9.356310	-1.401244
H	0.455680	7.950830	-0.405909
H	-0.774380	8.588117	-1.522197
C	5.058807	1.936952	9.786514
H	4.036127	2.163115	10.122572
H	5.716984	1.982558	10.665908
H	5.079656	0.904584	9.407113
C	5.535291	4.357099	9.356771
H	5.926726	5.112346	8.660591
H	6.163511	4.371461	10.259614
H	4.514262	4.649920	9.641163
C	6.994172	2.573414	8.329865
H	7.409167	3.290870	7.607139
H	7.030089	1.571675	7.876839
H	7.640843	2.574584	9.219858
C	3.991279	11.747482	-0.888458
H	4.397829	12.760332	-1.028517
H	3.380605	11.744828	0.026833
H	3.332547	11.526499	-1.739966
C	5.979085	10.749407	-2.081035
H	6.405766	11.751404	-2.235501
H	5.365317	10.503950	-2.959166
H	6.806228	10.025945	-2.028727
C	6.053480	11.137333	0.391199
H	6.448633	12.146771	0.208242
H	6.910721	10.457550	0.501729
H	5.503425	11.161555	1.343639
C	-0.449356	4.157738	0.060460
C	0.041754	2.921025	-0.393338
H	0.741169	2.351546	0.222460
C	-0.341824	2.439461	-1.645136
H	0.044705	1.482648	-1.997223
C	-1.209187	3.189092	-2.446797
H	-1.502514	2.817297	-3.428991
C	-1.688595	4.421364	-1.995830
H	-2.352669	5.013991	-2.625354
C	-1.308845	4.913161	-0.745549
H	-1.660568	5.890125	-0.419246
C	-0.261335	6.500362	1.926187
C	0.510439	8.765875	2.306698
H	1.328871	9.465272	2.480694
C	-0.807587	9.226375	2.230120
H	-1.022077	10.290118	2.342526
C	-1.855048	8.321963	2.022367
H	-2.885337	8.677165	1.976546
C	-1.589027	6.958608	1.880483
H	-2.413492	6.256426	1.751234
C	-1.000572	3.883279	2.925131
C	-1.240336	4.496895	4.165936
H	-0.808443	5.472866	4.389029
C	-2.047479	3.858669	5.106807
H	-2.245982	4.341390	6.064094
C	-2.592702	2.601984	4.826238
H	-3.222338	2.105850	5.564726
C	-2.330051	1.979480	3.602995
H	-2.747461	0.995997	3.386921
C	-1.535871	2.617165	2.648651
H	-1.345585	2.134279	1.689694
C	0.784961	7.406364	2.151645
H	1.810655	7.041266	2.212642

Table S12. Cartesian Coordinates of Optimized [2]⁺

Pt	13.290774	11.361392	7.524839
S	12.081244	11.587108	5.551693
P	15.235805	11.732717	6.263101
C	15.213555	13.525395	5.839930
H	15.166975	14.110488	6.766542
H	14.315691	13.734228	5.243772
H	16.110423	13.803835	5.269433
C	15.451399	10.901130	4.631158
H	14.478953	10.780206	4.140563
H	15.904903	9.915042	4.776482
H	16.112691	11.506605	3.997330
C	16.857128	11.483229	7.097288
H	16.969411	10.424612	7.361350
H	16.889313	12.074296	8.019864
H	17.674937	11.784215	6.428812
C	11.820101	10.109802	4.583908
C	11.175988	10.367478	3.338602
C	11.022936	9.333120	2.421063
H	10.529364	9.567995	1.476830
C	11.460694	8.022278	2.680685
C	12.037089	7.776364	3.934805
H	12.352720	6.768856	4.203429
C	12.209288	8.781613	4.891893
C	12.763131	8.447059	6.225606
C	14.144788	8.331578	6.428750
H	14.807735	8.303436	5.565193
C	11.907677	8.319862	7.329957
H	10.828741	8.300360	7.166982
C	11.272863	6.931720	1.624744
C	11.800050	5.566498	2.095602
H	11.651574	4.823271	1.299661
H	11.266449	5.205943	2.986888
H	12.875805	5.599539	2.321865
C	12.037718	7.341223	0.345176
H	13.112896	7.452450	0.548654
H	11.667581	8.291973	-0.062759
H	11.912319	6.571100	-0.430509
C	9.766831	6.794575	1.303120
H	9.346330	7.729954	0.910116
H	9.197576	6.514968	2.201509
H	9.615623	6.012884	0.543902
C	10.619729	11.719700	3.046237
C	11.382800	12.681657	2.354397
C	10.825238	13.942229	2.117828
H	11.418538	14.690162	1.585083
C	9.531428	14.270554	2.545134
C	8.941459	15.625226	2.248950
H	8.550847	15.665708	1.219817
H	9.694121	16.420968	2.341449
H	8.108817	15.857842	2.926049
C	8.793695	13.296637	3.228148
H	7.782093	13.533275	3.567365
C	9.312241	12.021986	3.482072
C	8.478907	10.986421	4.194913
H	7.573664	11.436122	4.622185
H	9.042985	10.499128	5.003686
H	8.164791	10.185656	3.507912
C	12.793267	12.377230	1.921208
H	13.450885	12.266873	2.798740
H	13.199436	13.184740	1.297787

H	12.855560	11.437563	1.354227
S	14.499474	11.585238	9.498062
C	14.743881	10.109285	10.472120
C	15.378580	10.366742	11.722201
C	15.518530	9.333848	12.643491
H	16.005398	9.568465	13.591263
C	15.075866	8.024713	12.383468
C	14.509377	7.778537	11.124949
H	14.191601	6.771827	10.855855
C	14.351131	8.782144	10.163673
C	13.807007	8.447185	8.826367
C	12.429467	8.290937	8.621471
H	11.767717	8.230763	9.484391
C	14.665735	8.360569	7.720623
H	15.744814	8.373408	7.883496
C	15.248609	6.935911	13.443793
C	14.717871	5.572427	12.971904
H	14.855236	4.830479	13.771033
H	15.257171	5.206553	12.086227
H	13.644324	5.610883	12.736215
C	14.474986	7.353069	14.715591
H	13.402255	7.469792	14.502506
H	14.846933	8.302784	15.124255
H	14.589258	6.584287	15.494336
C	16.750973	6.791190	13.778936
H	17.173229	7.725227	14.173245
H	17.326495	6.506085	12.886294
H	16.891138	6.010630	14.541455
C	15.939089	11.716850	12.016092
C	15.177353	12.681834	12.705148
C	15.739424	13.939857	12.944619
H	15.147230	14.690102	13.475335
C	17.036328	14.262755	12.522697
C	17.631146	15.614554	12.822299
H	18.018061	15.652406	13.852920
H	16.882353	16.413690	12.727676
H	18.467357	15.844084	12.148559
C	17.772337	13.286163	11.841622
H	18.786147	13.518730	11.506179
C	17.249266	12.013959	11.584789
C	18.080245	10.975955	10.872742
H	18.990010	11.421965	10.451287
H	17.517334	10.494697	10.059525
H	18.386524	10.171207	11.558623
C	13.763709	12.383513	13.132233
H	13.109245	12.276629	12.251905
H	13.358543	13.192528	13.754347
H	13.694741	11.443865	13.698478
P	11.338843	11.688095	8.786717
C	11.320067	13.482512	9.202493
H	11.352897	14.064691	8.273482
H	12.213053	13.714460	9.797414
H	10.417182	13.742479	9.772223
C	11.142531	10.859060	10.422204
H	12.116873	10.765483	10.914888
H	10.715217	9.860934	10.280882
H	10.464762	11.450381	11.051950
C	9.723612	11.399099	7.953695
H	9.636326	10.337806	7.691284
H	9.677510	11.988122	7.030414
H	8.899256	11.682003	8.622010

Table S13. Cartesian Coordinates of the Optimized Reference Compound $[(\text{tdt})_2\text{Pt}]^{\bullet-}$, tdt = 4-Me-1,2-Benzenedithiophenol

Pt	18.07847	-1.05653	-0.29145
S	19.64488	-2.67005	-0.80740
S	16.61498	-2.72512	0.34510
C	18.83878	-4.18934	-0.42595
C	17.51541	-4.21430	0.07791
C	16.91260	-5.45706	0.36966
H	15.89022	-5.45936	0.75813
C	17.58224	-6.66278	0.17546
C	18.90203	-6.62407	-0.32825
H	19.44735	-7.55817	-0.48847
C	19.51384	-5.41258	-0.62254
C	16.92193	-7.98117	0.49770
H	15.89270	-7.83159	0.85468
H	17.47159	-8.52815	1.28187
H	16.87827	-8.63941	-0.38557
S	19.54277	0.61247	-0.92524
H	20.27408	3.34775	-1.31956
C	19.25143	3.34526	-0.93174
C	18.64556	2.10199	-0.64885
H	20.29624	5.72625	-1.33925
H	19.22447	6.55388	-0.18606
S	16.51287	0.55686	0.22722
C	18.58461	4.55123	-0.72914
C	17.32211	2.07672	-0.14509
C	19.24508	5.86981	-1.05005
C	17.26505	4.51219	-0.22507
C	16.65015	3.30013	0.06044
H	18.73748	6.38496	-1.88301
H	16.72263	5.44658	-0.05683
H	20.53478	-5.39102	-1.01101
H	15.62972	3.27840	0.45024

8 References

1. Speight, J. G.; Lange, N. A., *Lange's handbook of chemistry*. 16. ed.; McGraw-Hill: New York, 2004.
2. Williams, R.; Billig, E.; Waters, J. H.; Gray, H. B., *J. Am. Chem. Soc.* **1966**, *88*, 43-50.

Publikation II

Tuning of Thiyl/Thiolate Complex Near-Infrared Chromophores of Platinum through Geometrical Constraints

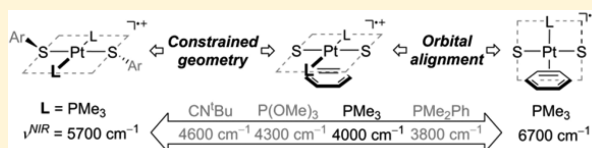
Nicole M. Mews,[†] Gerald Hörner,[‡] Hartmut Schubert,[†] and Andreas Berkefeld^{*,†,§}

[†]Institut für Anorganische Chemie, Eberhard Karls Universität Tübingen, Auf der Morgenstelle 18, 72076 Tübingen, Germany

[‡]Institut für Chemie, Quantenchemie und Bioanorganische Chemie, Technische Universität (TU) Berlin, Straße des 17 Juni 135, 10623 Berlin, Germany

Supporting Information

ABSTRACT: The chemistry of radical-ligand complexes of the transition metals has developed into a vibrant field of research that spans from fundamental studies on the relationship between the chemical and electronic structures to applications in catalysis and functional materials chemistry. In general, fine-tuning of the relevant properties relies on an increasingly diversifying pool of radical-proligand structures. Surprisingly, the variability of the conformational freedom and the number of distinct bonding modes supported by many radical proligands is limited. This work reports on the angular constraints and relative geometric alignment of metal and ligand orbitals as key parameters that render a series of chemically similar thiyl/thiolate complexes of platinum(II) electronically and spectroscopically distinct. The use of conformationally flexible thiophenols as primary ligand scaffolds is essential to establishing a defined radical-ligand $[(^{\text{arene}}\text{S})_2\text{Pt}^{\text{II}}]^{\bullet+}$ core whose electronic structure is modulated by a series of auxiliary coligands at platinum.

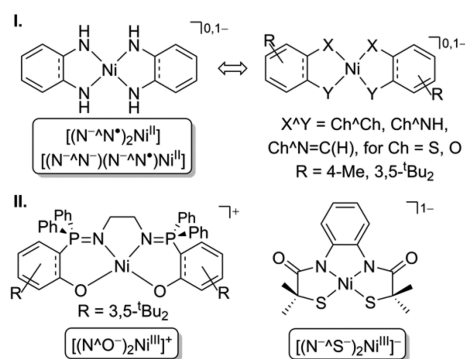


INTRODUCTION

Ligand participation in the redox chemistry of coordination compounds of the transition metals was evoked as early as 1927 when Feigl and Fürth reported on an “odd” coordination compound of nickel and *o*-phenylenediamine whose composition matched the formula $[(\text{H}_4\text{C}_6(\text{NH})_2)_2\text{Ni}]$.¹ The assignment as a bis(*o*-diiminobenzosemiquinonato)nickel(II)² complex, $[(\text{N}^{\wedge}\text{N}^{\bullet-})_2\text{Ni}^{\text{II}}]$, was considered but discarded in favor of a formulation as $[(\text{N}^{\wedge}\text{N}^{2-})_2\text{Ni}^{\text{IV}}]$, involving high-valent nickel. In a paper entitled “The Myth of Nickel(III) and Nickel(IV) in Planar Complexes” published in 1965, Gray and co-workers provided experimental and theoretical data in support of a “metal-stabilized radical-ligand” description.³ The involvement of high-valent nickel was generally refuted because electrochemical and electron paramagnetic resonance (EPR) data corroborated the assignment of equivalent electronic structures to a series of planar complexes of nickel that differ chemically with regard to the total charge and types of ligands, as shown in Chart 1, part I. Despite the fact that nickel(III) has been substantiated in the form of planar complexes^{4–9} such as those in Chart 1, part II, realization of this distinct electronic structure required specific types of ligand scaffolds. This ambivalence of the electronic structure adds support to the conclusion of the 1965 paper by Gray that the locus of oxidation of complexes of a given metal depends on the type(s) of redox ambivalent ligand(s).

Substantial progress in the theoretical treatment of the electronic structure and associated properties that can be probed experimentally revealed that it is the relative energetic order of the frontier orbitals at the metal and ligand that determines their relative contributions to (un)occupied

Chart 1. Effect of the Ligand Type on the Electronic Structures of Planar Complexes of Nickel^{3,5,9}



molecular orbitals (MOs) of the metal–ligand system. Knowledge of the frontier MO composition thus provides a description of the locus of charge depletion or accumulation during a redox process. The development of computational methods has not only aided in the identification of relevant intrinsic parameters such as metal effective core charge, *d*-electron count, and configuration but complements the systematic search for structure–property relationships in general.¹⁰ In this context, coordination compounds are

Special Issue: Applications of Metal Complexes with Ligand-Centered Radicals

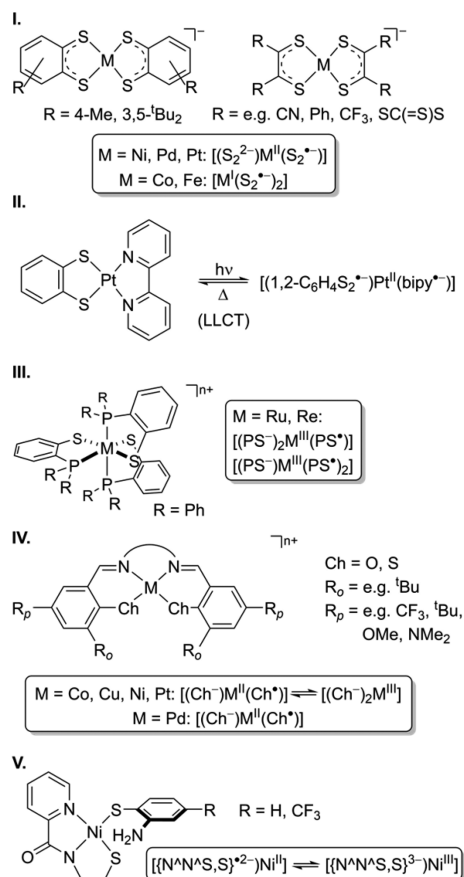
Received: January 12, 2018

Published: March 21, 2018

particularly suited for systematic studies because the compositions and energies of frontier orbitals can be varied to a greater extent than those in purely (in)organic materials.

The spectrum of redox-noninnocent/ambivalent ligands subdivides into two categories, namely, electron acceptors and donors. The group of electron acceptors comprises ligands that interconvert between a neutral and a radical-anionic form. Suitable candidates are ligands with energetically accessible π^* orbitals, such as (heterocyclic) arenes,^{11–17} conjugated N_4 -macrocycles,¹¹ azo-1,2-dicarbonyl compounds,¹¹ (conjugated) N derivatives of (di)carbonyls,^{11,18–21} and small (inorganic) molecules such as CO_2 , O_2 , or NO .²² The second category includes electron-donor ligands that establish an isomorphous series of distinct valence states that include closed-shell and (bi)radical forms. A prominent example of this class of ligands is the catecholato (1,2- $C_6H_4(O^-)_2 = cat^{2-}$)/semiquinonato (1,2- $C_6H_4(O^\bullet)(O^-) = sq^{\bullet-}$)/quinone (1,2- $C_6H_4(O)_2 = q$) redox triad.¹¹ It further includes dithiolenes^{23–26} and 1,2-dithiophenols^{3,10,26–28} (Chart 2, part I/II), tetrathiophenols,²⁹

Chart 2. Selected Representative Examples of Metal Complexes Containing Sulfur-Derived Redox-Ambivalent Ligands and Their Electronic Structures



o-phenylenediamines^{2,30} and their mixed 1,2-chalcogen/amino derivatives,^{10,31,32} 2-phosphinothiophenols^{33–36} (Chart 2, part III), (thio)salens^{37,38} (Chart 2, part IV), bi- and terpyridines with pendant diarylamine,³⁹ and, more recently, bis(phenols) that feature an N-heterocyclic carbene linker.⁴⁰

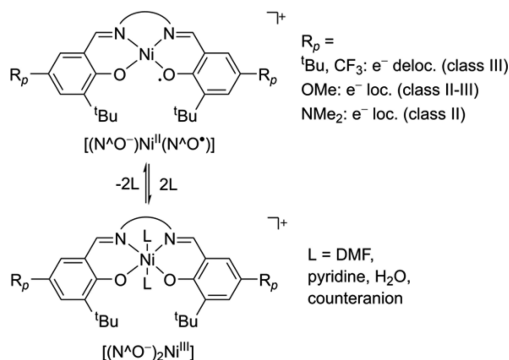
Metal complexes of redox-ambivalent ligands can be further differentiated according to the type and dynamic behavior of

their electronic ground states. The first class includes complexes that feature distinct valence tautomeric forms of the general type $[(L^{n-})M^{(m+1)+}]$ and $[(L^{\bullet(n-1)-})M^{m+}]$, which coexist in temperature-dependent equilibria. Representative examples include oxidized salen complexes (Chart 2, part IV) of cobalt,³⁸ copper,⁴¹ nickel,^{42,43} and platinum,⁴³ mixed alkyl/arylthiolate complexes of nickel⁴⁴ (Chart 2, part V), and octahedral complexes of cobalt from the aforementioned { $cat^{2-}/sq^{\bullet-}/q$ } dioxolene ligand triad as in the mixture of $[(bipy)Co^{III}(cat^{2-})(sq^{\bullet-})]$ and $[(bipy)Co^{II}(sq^{\bullet-})_2]$ (*bipy* = bipyridine).⁴⁵ Intramolecular electron transfer between a metal and its ligand(s) in isostructural complexes can result in a discrete change of the spin multiplicity. In contrast, the second class comprises systems that adopt an energetically distinct electronic ground state with a defined spin multiplicity. Reported examples include complexes of radical-anionic dithiolenes/dithiophenol ligands shown in Chart 2, part I,¹⁰ radical-salen complexes of palladium⁴³ (Chart 2, part IV), and octahedral thiol-radical complexes of ruthenium^{33,34} and rhenium^{35,36} from 2-phosphinothiophenol (Chart 2, part III). Special cases are complexes that support light-induced ligand-to-ligand or metal-to-ligand charge transfer (CT). For example, the electronically excited state of the planar mixed donor-acceptor ligand complex of platinum(II) shown in Chart 2, part II, is formulated as $[(1,2-C_6H_4S_2^{\bullet-})Pt^{II}(bipy^{\bullet-})]$.⁴⁶ Depending on a particular combination of metal and ligand, unambiguous assignment of the valence states may prove difficult or even pointless under the circumstance in which metal and ligand orbitals contribute equally to occupied frontier orbitals. The effective core charge of the metal is a significant parameter that determines the energies of metal valence orbitals relative to those of the ligand system. If the energies of the metal orbitals fall below those of the ligand system, a significant admixture of orbitals from ligand atoms dominates the highest occupied molecular orbital (HOMO) of the complex. This situation of metal complexes with essentially ligand-centered frontier orbitals is coined as the *inverted bonding scheme*.²³ Single-electron oxidation results in the formation of a formally metal-stabilized radical-ligand complex, with diminished spin density at the metal, $\rho(M) \ll 0.5$.^{24,27} This electronic situation applies to the late-3d metals nickel and copper and their 4d and 5d congeners.

The role that a metal site plays in complexes of redox-ambivalent ligands is twofold. On the one hand, the metal acts as a reactive site for the coordination, activation, and turnover of a substrate, but electrons are drawn from the manifold of redox-active ligands. This concept adapts well to stoichiometric and catalytic reactions,^{47–50} circumventing high-energy intermediates such as low- or high-valent metal species. On the other hand, the metal assists in the formation and stabilization of a reactive main-group-element radical that promotes chemical reactivity. The catalytic turnover of nitrene radicals formed in the coordination sphere of a cobalt(II) porphyrin complex is a recent example.⁵¹ In fact, hydrogen-atom transfer (HAT) from a C–H bond to a metal–(heteroatom radical) fragment is a kinetically and thermodynamically favorable process and provides a selective mechanism for functional group (inter)conversion. One prominent example for metal-assisted free-radical chemistry of an organic radical ligand is HAT to a four-coordinate copper(II) phenoxyl site in fungal galactose oxidase, which is the key step in the selective aerobic oxidation of primary alcohols to aldehydes.⁵² Among many reports on functional model systems of copper and other

metals that mediate mechanistically related free-radical-type chemical transformations,^{53–60} the oxidized metal salen complexes shown in Chart 2, part IV, and Scheme 1 stand out because of their variable spectrum of electronic structures.^{37,38}

Scheme 1. Effect of Electron-Withdrawing/Releasing Substituents and Additional Coligands on the Electronic Structure of Nickel Salen Complexes^{37,38,61}



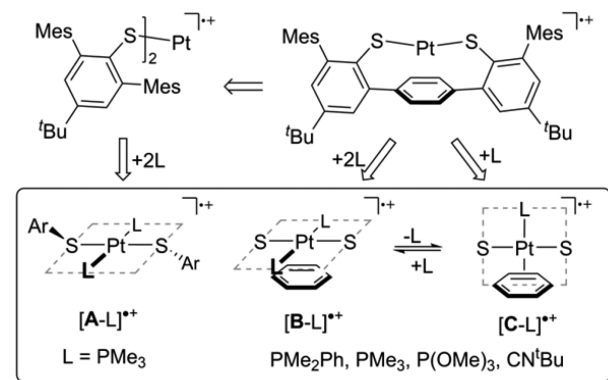
First, the admixture of ligand orbitals to the HOMO depends on the substituents in the 4-position. As a result, the electronic structures vary as indicated in Scheme 1 between electron-localized classes II and II–III and delocalized class III,^{37,38,61} according to a modified Robin and Day classification scheme.⁶² Second, as mentioned above, the effective core charge, d-electron count, and configuration of the metal determine the relative contributions of metal and ligand orbitals to the singly occupied molecular orbital (SOMO) of the complex but do not change the character of the radical ligand.^{37,55,63,64} Third, expansion of the coordination sphere at nickel to an octahedron through external donors favors the formation of a high-valent nickel(III) form.^{37,38}

Various analytic techniques are commonly employed that probe electron-spin distributions at different experimental time scales, namely, X-ray absorption, vibrational spectroscopy (IR and resonance Raman), electron- and nuclear-spin magnetic resonance (EPR and NMR) spectroscopy, and electrochemistry. Single-crystal X-ray diffraction (XRD) adds valuable insight from the analysis of structural metrics. If lattice effects are not dominant and structural resolution is sufficient, metal and intraligand bond lengths and angles are diagnostic of the valence states of the ligand and metal. In addition, low-energy electronic transitions in the near-infrared (NIR) spectral range are characteristic for intervalence charge transfer (IVCT) in open-shell metal–ligand systems. The spectral position, shape, intensity, and width of an NIR band depend on the nature of the optical transition, which, in turn, reflect the electronic structure.^{10,37,38,62} Comprehensive theoretical studies of mixed-valent radical-ligand complexes $[(S_2^{2-})Ni/Pd/Pt^{II}(S_2^{\bullet-})]$ from 1,2-dithiophenols formulated a correlation of the NIR transition energy and strength of electronic coupling.¹⁰ Stronger metal-assisted coupling of mixed-valent ligands results in a shift of the NIR transition to higher energy. The correlation also applies to the analogous series of oxidized metal salen complexes.⁶⁴ According to the *inverse bonding scheme*, the strength of electronic coupling is associated with the degree of metal orbital admixture to the lowest unoccupied molecular orbital (LUMO). Owing to symmetry consider-

ations, the LUMO is metal–ligand antibonding and increasingly destabilized by an enhanced metal orbital admixture, which causes the observed shift of NIR transitions to higher energy. For a series of structurally related complexes, the energy of the NIR transitions is a sensitive spectroscopic marker of the strength of metal-mediated electronic coupling of redox-amбивalent ligands.

Systematic studies of the relationship of chemical and electronic structures are not only of fundamental scientific interest. The search for smart optoelectronic molecular building blocks such as electrochromic metal complex NIR chromophores whose electronic structures can be fine-tuned and absorptivity controlled by external electrochemical stimuli gives a major impetus to ongoing synthetic diversification.^{65–67} Despite the fact that a diverse pool of radical proligands is available, the mode of coordination to a metal is generally invariant, which becomes evident by structures shown in Charts 1 and 2. As a consequence, modification of remote substituent effects at the ligand(s) and variation of the coordination numbers through additional coligands remain as options for tuning the electronic structures of radical-ligand complexes. As an alternative, 1,4-terphenyldithiophenol is a unique ligand scaffold that provides two topologically different bonding modes for four-coordinate metal sites such as nickel⁶⁸ and platinum,⁶⁹ as indicated in Scheme 2.

Scheme 2. Comparison of Coordination Modes of Mono- and Bidentate Terphenyl(di)thiophenols to Platinum(II) Augmented by Auxiliary Coligands L and Their Effect on the Electronic Properties of Radical-Ligand Complex Cations^a



^aThe preparation and properties of $[C-L]^{0/+}$ and $[B-PMe_3]^{0/+}$ were reported in ref 69.

Variation of the steric properties of coligand L allows for discrimination between two bonding modes. A structure of type C-L forms from the coordination of a sterically demanding coligand $L = PR_3$, where $R = Ph$ (Pt^{69}), C_6H_{11} (Cy ; Ni^{68}), which causes η^2 bonding of the central π system of the ligand backbone to the metal. Alternatively, changing the alignment of the metal coordination plane relative to the ligand through bonding of two coligands L results in structure B-L. One-electron oxidation of platinum(II) complexes B- PMe_3 and C- PPh_3 selectively affords mixed-valent thyl/thiolate cores $[(^{Ar}S^-)Pt^{II}(^{Ar}S^{\bullet})]^+$ whose chemical structures are similar but differ in their electronic structures, reflecting the different coordination modes depicted in Scheme 2. In terms of the extended Robin and Day classification scheme, the resulting mixed-valence radical-ligand complexes are characterized by the

energy, shape, and nature of diagnostic NIR transitions. The low-energy electronic transitions are invariant to changes of the solvent polarity and temperature for both types of structures but differ in energy, $\nu^{\text{NIR}}([\text{C-PPh}_3]^{*\dagger}) = 6500 \text{ cm}^{-1}$ ($2.2 \times 10^4 \text{ M}^{-1} \text{ cm}^{-1}$; $\Delta\nu_{1/2} = 1300 \text{ cm}^{-1}$) and $\nu^{\text{NIR}}([\text{B-PMe}_3]^{*\dagger}) = 4000 \text{ cm}^{-1}$ ($0.6 \times 10^4 \text{ M}^{-1} \text{ cm}^{-1}$; $\Delta\nu_{1/2} = \sim 1600 \text{ cm}^{-1}$). Theoretical analysis supported the assignment as thiol-to-thiolate IVCT for $[\text{C-PPh}_3]^{*\dagger}$. By contrast, time-dependent density functional theory (TD-DFT) assigns the single NIR electronic transition observed for $[\text{B-PMe}_3]^{*\dagger}$ as a combination of a Me_3P -to-Pt CT and a charge-resonance (CR)-type transition that refers to a CT between donor and acceptor MOs that are delocalized over the entire $[\text{ArS}^-\text{Pt}-\text{S}^{\text{Ar}}]^{*\dagger}$ chromophore. Therefore, at $T \geq 110 \text{ K}$, an electron-localized class II–III structure prevails for $[\text{C-PPh}_3]^{*\dagger}$, whereas $[\text{B-PMe}_3]^{*\dagger}$ is better described as a delocalized class III system.⁶⁹

This report aims at validating and extending the previous finding that the electronic structure and associated spectroscopic properties of a $[\text{ArS}^-\text{Pt}^{\text{II}}-\text{S}^{\text{Ar}}]^{*\dagger}$ chromophore depend on the relative geometric orientation of the metal coordination plane and radical ligand. Accordingly, structure C supports an out-of-plane coupling of Pt 5d and S 3p orbitals, whereas type B features unique in-plane coupling. This dichotomy is sketched in graphical form by the dashed squares shown in Scheme 2. For the present work, two aspects are of major importance. First, the effect of metal–ligand topology on the radical-ligand complex chromophore has been studied by a comparison of structures A–C. Second, the effect of the electronic and steric properties of auxiliary coligands L on the chromophore properties has been examined. More precisely, the σ -donor/ π -acceptor strengths of coligands L were varied by substituting PMe_3 for PMe_2Ph , $\text{P}(\text{OMe})_3$, and CN^tBu . As a result, the size of the dihedral angle Θ defined by the $\{\text{Pt}-\text{S}-\text{C}_{\text{arene}}\}\{\text{S}-(\text{C}-\text{C})_{\text{arene}}\}$ moieties (cf. Figure 1 for definition) has

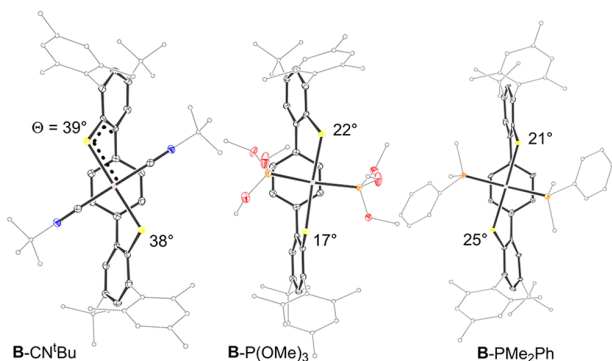


Figure 1. Molecular structures of complexes **B-L** for $L = \text{CN}^t\text{Bu}$ (left), $\text{P}(\text{OMe})_3$ (center), and PMe_2Ph (right). Thermal displacement ellipsoids are at the 50% probability level. Hydrogen atoms and the lattice solvent are not shown for clarity. Color code: C, black; N, blue; O, red; S, yellow; Pt, plum.⁷⁰ Dihedral angles Θ are defined by $\text{Pt}-\text{S}-\{\text{C}-\text{C}\}_{\text{arene}}$ linkages, as indicated by dashed lines.

been identified as a key parameter that determines the electronic structure of the $[(\text{ArS}^-)\text{Pt}^{\text{II}}(\text{ArS}^\bullet)]^{*\dagger}$ chromophore. Small dihedral angles favor the overlap of in-plane orbitals of the $[\text{ArS}^-\text{Pt}-\text{S}^{\text{Ar}}]^{*\dagger}$ core and out-of-plane π^* orbitals of appended arene rings, which determines the degree of delocalization of the unpaired spin density across the chromophore system. It varies with the structural flexibility of the primary thiophenolate ligand(s) and is further governed by

the steric requirements of coligands L. In the case of the 1,4-terphenyldithiophenol scaffold, Θ can adopt distinct values at the trans-oriented $\text{Pt}-\text{S}-(\text{C}-\text{C})_{\text{arene}}$ linkages, which determines the electronic structure of the $[(\text{ArS}^-)\text{Pt}^{\text{II}}(\text{ArS}^\bullet)]^{*\dagger}$ chromophore.

RESULTS AND DISCUSSION

Synthesis and Characterization of Closed-Shell and Radical-Ligand Complexes.

As indicated in Scheme 2, substitution of a bidentate dithiophenol in **B-PMe**₃ for individual thiophenols in **A-PMe**₃ changes the dihedral angles Θ enclosed by the $\text{Pt}-\text{S}-(\text{C}-\text{C})_{\text{arene}}$ moieties but does not change the chemical character of the radical proligand and auxiliary coligand. Complex **A-PMe**₃ forms in a salt metathesis starting from in situ prepared *trans*-(Me_3P)₂PtCl₂ and 2 equiv of a potassium thiolate ligand salt in the presence of ≥ 2 equiv of additional PMe_3 in a toluene solution at room temperature and is isolated as a yellow microcrystalline solid in 46% yield. N-line resonance patterns in ¹H and ¹³C{¹H} NMR spectra and ¹J_{P-Pt} = 2720 Hz indicate a trans disposition of coligands $L = \text{PMe}_3$. The structural metrics in the single-crystalline state⁷⁰ confirm a C_2 -symmetric coordination environment at planar platinum(II), as shown in Figure S1. The overall structural metrics of **A-PMe**₃ are similar to those of geometrically constrained **B-PMe**₃ with respect to most of the bond lengths and angles, and pertinent structure data are summarized in Table S1. Only the Pt–S bond lengths in **B-PMe**₃ are shorter by 3 pm, a difference that is not reproduced in DFT modeling at the BP86-D/TZVP/ZORA (for computational details see the Experimental Section) level of theory, although the overall performance of DFT optimization is fully satisfactory otherwise. This deviation may reflect the presence of several supramolecular interactions between the methyl groups of the ^tBu and mesityl substituents and PMe_3 coligands that dominate the packing of formula units of **B-PMe**₃ in the single-crystalline state. In addition, hydrogen bonding of each sulfur atom to cocrystallized methanol may also affect the Pt–S distances.⁶⁹ The structural linkage of the thiophenol donors in **B-PMe**₃ clearly affects the trans angles across the metal coordination plane. Whereas the P–Pt–P and S–Pt–S angles are close to 180° in **A-PMe**₃, the respective values in **B-PMe**₃ deviate significantly by 17 and 9° and indicate a minor pyramidalization at platinum. Because of thiophenolate/ PMe_3 interligand interactions in **A-PMe**₃, the torsion angles that are enclosed by the $\{\text{Pt}-\text{S}-\text{C}_{\text{arene}}\}$ and $\{\text{S}-(\text{C}-\text{C})_{\text{arene}}\}$ units increased from 6° in **B-PMe**₃ to 58°. As a consequence, the higher torsion about the $\text{Pt}-\text{S}-(\text{C}-\text{C})_{\text{arene}}$ linkage reduces the overlap of the $\{\text{S}-\text{Pt}-\text{S}\}$ and $\{\text{S}-(\text{C}-\text{C})_{\text{arene}}\}$ orbital manifolds in **A-PMe**₃, compared to **B-PMe**₃.

In order to study the effect of coligand L on the physical and chemical properties of $[\text{B-L}]^{*\dagger}$, the series of complexes **B-L** shown in Scheme 2 was prepared. Pertinent data with respect to electrochemistry, electron spectroscopy, and EPR spectroscopy are summarized in Table 1. In general, the addition of ≥ 2 equiv of the respective coligand L to a suspension of **C-PPh**₃⁶⁹ in hexanes affords products **B-L** in the form of yellow microcrystalline solids in yields $\geq 71\%$. N-line resonance patterns in the ¹H and ¹³C{¹H} NMR spectra and ⁿJ_{Pt-X} to two equivalent ³¹P ($n = 1$) and ¹⁴N ($n = 2$, 93 Hz) nuclei corroborate the planar and symmetrical bonding environment about platinum of **B-L** in solution. In agreement with a local D_{2h} symmetry, Raman and IR spectra taken from crystalline

Table 1. Summary of Electrochemical, Spectroscopic, and Computational Data of Radical-Ligand Complex Cations [A/B/C-L]^{•+}

[A/B/C-L] ^{•+}	E^0 / mV ^a	$\nu^{\text{NIR}}/\text{cm}^{-1}$ ($\epsilon^{\text{NIR}}/\text{M}^{-1}\text{cm}^{-1}$) ^b	g_1 (A_1) ^c	g_2 (A_2) ^c	g_3 (A_3) ^c
A-PMe ₃	231 (ir)	5700 (8000)	2.288 (291)	2.134 (223)	1.996 (420)
B-PMe ₂ Ph	121	3840 (7200)	2.117 (288)	2.067 (449)	2.047 (292)
B-P(OMe) ₃	253 (qr)	4290 (6000)	2.103 (305)	2.044 (343)	2.016 (202)
B-CN ^t Bu	318	4570 (8000)	2.149 (180)	2.085 (147)	1.989 (215)
C-PMe ₂ Ph		6700 (10000)	2.186 (210)	2.084 (192)	2.007 (249)
C-PMe ₃		6660 (4000)			

^a E^0 versus ferrocene/[ferrocene]⁺; qr/ir = electrochemically quasi-reversible/irreversible. ^b $T \leq -80$ °C; CH₂Cl₂ solution. ^cX-band cw-EPR, 1:1 CH₂Cl₂/C₇H₈ glass, 110 K, A[¹⁹⁵Pt($I = 1/2$, 34%)] in MHz.

samples of B-CN^tBu each show an intense band due to the symmetric (A_1 , 2230 cm⁻¹) and dissymmetric (B_{3u} , 2197 cm⁻¹) C≡N stretching modes that closely match the DFT-derived modes at 2232 and 2191 cm⁻¹, respectively. The increase of $\nu_{\text{C}\equiv\text{N}}$ by +87 cm⁻¹ (A_1) and +54 cm⁻¹ (B_{3u}) as a consequence of coordination to platinum indicates very little d(Pt)– π^* (CN) back-donation⁷¹ and is consistent with the almost linear 'Bu–N≡C bond angles of 175 and 177° in the single-crystal molecular structure that is shown on the left-hand side of Figure 1. As is also depicted, a planar bonding about platinum generally prevails for complexes B-L, and pertinent metrical data are provided in Table S1.

In addition, the entire series of complexes B-L was modeled using DFT methods at the ZORA/BP86-D/TZVP level of theory. Experimental and computationally optimized metrics are in excellent agreement, which includes the slight pyramidalization at platinum for L = P(OMe)₃ and PMe₂Ph and the almost linear trans angles in B-CN^tBu. Compared to B-PMe₃, variation of L results in an isotropic elongation of the Pt–S bond distances between 2 and 3 pm (cf. Table S1 for details). The spatial proximity of the mesityl groups at the main ligand and coligands L likely affects the torsion angles enclosed by the {Pt–S–C_{arene}} and {S–(C–C)_{arene}} units. Compared to B-PMe₃, these increase to 17/22° (36/36°; DFT) in the case of L = P(OMe)₃, 21/25° for PMe₂Ph, and 37/39° (36/37°; DFT) for CN^tBu. Interligand interactions generally feature very prominently in the molecular structures because of the coligands that fill the cleft enclosed by the mesityl substituents to a high degree. This becomes most evident for B-P(OMe)₃, in which the platinum atom locates close to one of the C–C edges of the bridging π system, rendering the Pt–S bond lengths unsymmetrical by 3 pm (cf. Figure 1).

Different from the parent B-PMe₃, the electrochemical oxidation of A-PMe₃ at a platinum-disk working electrode in a 0.1 M ⁿBu₄NPF₆/CH₂Cl₂ solution at 290 K is not reversible because of a consecutive chemical reaction. The peak potential is recorded at $E_{p,\text{ox}}(\text{A-PMe}_3/[\text{A-PMe}_3]^{\bullet+}, \nu = 200 \text{ mV s}^{-1}) = 231 \text{ mV}$ versus Fc/[Fc]⁺, where Fc = ferrocene. The observed difference in the ligand topology translates into an anodic shift of +114 mV compared to $E^0(\text{B-PMe}_3/[\text{B-PMe}_3]^{\bullet+})$ and points to a diminished stabilization of the positive charge in [A-PMe₃]^{•+}. Chemical one-electron oxidation of yellow A-PMe₃ using the 1,1-diacetylferrocene cation, [Fc'⁺]⁺, at $T \leq 193 \text{ K}$ yields intensely blue-purple-colored [A-PMe₃]^{•+}. The suscept-

ibility of a CD₂Cl₂ solution of an in situ prepared sample yielded $\mu_{\text{eff}}([\text{A-PMe}_3]^{\bullet+}) = 2.4$, in agreement with the formation of a $S = 1/2$ system. Solutions of A-PMe₃ feature no low-energy transitions [$\lambda^{\text{max}}(\epsilon^{\text{max}}/10^4 \text{ M}^{-1} \text{ cm}^{-1}) = 349 \text{ nm}$ (2.1, CH₂Cl₂)] similar to B-PMe₃,⁶⁹ as do yellow congeners B-L [$\lambda^{\text{max}}(>1 \times 10^3 \text{ M}^{-1} \text{ cm}^{-1}, \text{CH}_2\text{Cl}_2)$] = 475, 398, and 355/400 nm for L = PMe₂Ph, P(OMe)₃, and CN^tBu, respectively. Concomitant with the stepwise addition of an oxidant, intense low-energy transitions at $\nu = 9670$ ($4 \times 10^3 \text{ M}^{-1} \text{ cm}^{-1}$, $\Delta\nu_{1/2} = 1900 \text{ cm}^{-1}$) and 5700 cm⁻¹ ($8 \times 10^3 \text{ M}^{-1} \text{ cm}^{-1}$, $\Delta\nu_{1/2} = 2400 \text{ cm}^{-1}$) develop in the NIR spectral region, which are depicted as the blue curve in Figure 2.

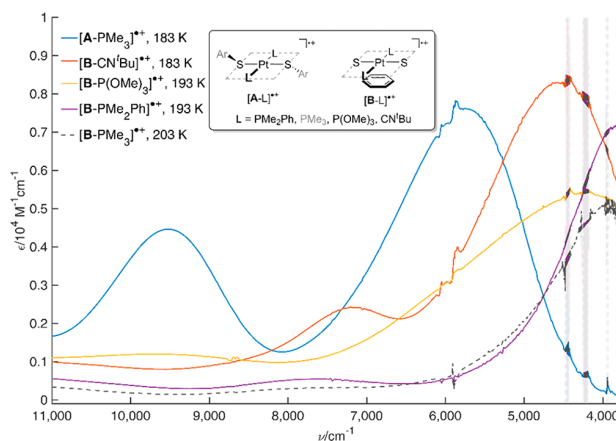
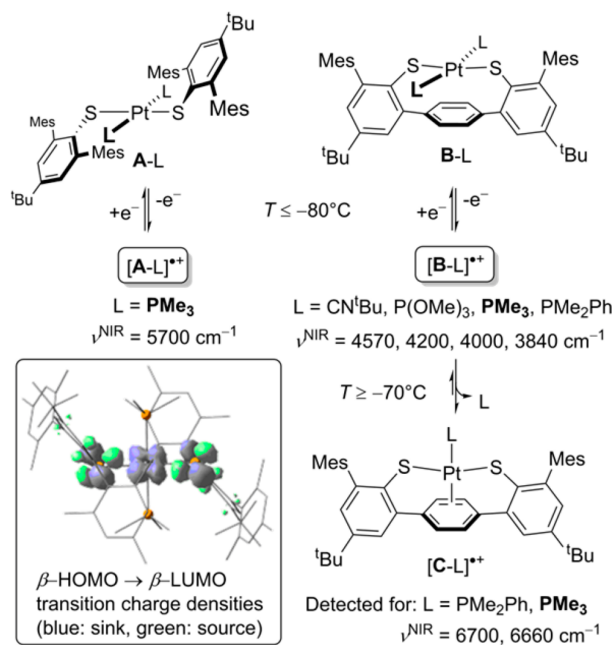


Figure 2. Overview of characteristic NIR electronic transitions of thiol/thiolate radical cations [A-PMe₃]^{•+} and [B-L]^{•+} observed in a CH₂Cl₂ solution at 183 K ≤ T ≤ 203 K. Noncorrectable residual absorption bands of the solvent at $\nu \leq 4500 \text{ cm}^{-1}$ are attenuated (light gray) for clarity. The spectral data of [B-PMe₃]^{•+} (broken black)⁶⁹ are included for comparison.

Whereas the intensity ϵ^{NIR} and bandwidth $\Delta\nu_{1/2} = 2400 \text{ cm}^{-1}$ are similar, the energy difference $\Delta\nu^{\text{NIR}}([\text{A-PMe}_3]^{\bullet+} - [\text{B-PMe}_3]^{\bullet+}) = 1700 \text{ cm}^{-1}$ between the lowest-energy transitions is significant. According to the *inverse bonding scheme*, the shift of ν^{NIR} to higher energy is associated with a higher admixture of platinum to (un)occupied frontier orbitals of [A-PMe₃]^{•+}. This hypothesis is supported by X-band continuous-wave (cw)-EPR data recorded from a frozen 1:1 CH₂Cl₂/C₇H₈ solution at 110 K. The spectrum is of rhombic appearance and shows a significant g anisotropy of 0.292, which should be compared to $\Delta g = 0.078$ for [B-PMe₃]^{•+}. No other hyperfine coupling (hfc) than to naturally abundant ¹⁹⁵Pt($I = 1/2$, 34%) is resolved, but absolute principal values of $A(^{195}\text{Pt})$ in the 223–420 MHz range (cf. Table 1) are similar to those reported for [B-PMe₃]^{•+}.⁶⁹ Notably, $\Delta g = 0.292$ of [A-PMe₃]^{•+} approaches the g anisotropies of 0.419 and 0.38 of related thiol/thiolate radical-anion complexes [(S₂²⁻)Pt^{II}(S₂^{•-})], for S₂²⁻ = 4-Me and 3,5-^tBu₂-substituted 1,2-benzenedithiolates,^{26,72} for which $\rho(\text{Pt}) = 0.21$ was calculated. Indeed, DFT analysis at the ZORA/BLYP35-D/TZVP level of theory provided $\rho(\text{Pt}) = 0.18$ for [A-PMe₃]^{•+} (cf. Scheme 3) compared to 0.11 for [B-PMe₃]^{•+}.⁶⁹ In addition to the redox properties, the difference in the ligand topology also results in diverging numbers and energies of NIR transitions and a greater g anisotropy, which indicates a significant difference between the electronic structures of [A-PMe₃]^{•+} and [B-PMe₃]^{•+}.

Scheme 3. Molecular Structures of the Starting Materials A/B-L and Conditions of Chemical Oxidation to Thiyl/Thiolate Radical Cations [A/B-L]^{•+}



^aDetails on $[\text{B-PMe}_3]^{0/+}$ are reported in ref 69. Inset: TD-DFT-derived character of diagnostic ν^{NIR} of $[\text{A-PMe}_3]^{•+}$ at the ZORA/BLYP35-D3/TZVP level of theory (blue, sink; green, source).

Qualitatively similar observations result for the series of one-electron-oxidized cations $[\text{B-L}]^{•+}$. Redox events are electrochemically reversible in the case of coligands $L = \text{PMe}_2\text{Ph}$ and CN^tBu , whereas electrochemical quasireversibility is observed for $\text{B-P}(\text{OMe})_3$ (cf. Figures S4–S7). As a consequence of substituting $L = \text{PMe}_3$ for $\text{P}(\text{OMe})_3$ and CN^tBu , the potentials for the $\text{B-L}/[\text{B-L}]^{•+}$ redox couple increase by ~ 136 and 201 mV to 253 mV ($\nu = 200 \text{ mV s}^{-1}$) for $L = \text{P}(\text{OMe})_3$ and 318 mV in the case of CN^tBu . The anodic shifts again indicate diminished stabilization of the positive charge but do not correlate with the σ -donor/ π -acceptor capabilities of the coligands. In fact, aliphatic isonitriles have been recognized to act even as π donors to a metal if symmetry permits.⁷³ In principle, the coordination of two CN^tBu coligands can stabilize an electron-deficient platinum site better than $\text{P}(\text{OMe})_3$, but formal potentials point to the opposite. By contrast, the very small increase of $E^0(\text{B-L}/[\text{B-L}]^{•+})$ by 4 mV to 121 mV for $L = \text{PMe}_2\text{Ph}$ indicates equivalent electronic structures for radical cations $[\text{B-PMe}_{3-n}\text{Ph}_n]^{•+}$, where $n = 0$ and 1 .

According to Scheme 3, the radical-ligand character of $[\text{B-L}]^{•+}$ was established unambiguously by monitoring the chemical oxidation of B-L by $[\text{Fc}^{•+}]^+$ at $T \leq 188$ K in solution by UV/vis/NIR, X-band cw-EPR, and IR spectroscopy. The stepwise addition of an oxidant results in the appearance of intense bands in the visible and NIR region in all cases, akin to the behavior of B-PMe_3 . The following discussion emphasizes the diagnostic NIR transitions; a summary of the experimental and computed transitions in the visible spectral region is given in Table S6. As shown in Figure 2, a single sharp band at $\nu^{\text{NIR}} = 3840$ ($7 \times 10^3 \text{ M}^{-1} \text{ cm}^{-1}$; $\Delta\nu_{1/2} = \sim 1400 \text{ cm}^{-1}$; CH_2Cl_2) corroborates the formation of $[\text{B-PMe}_2\text{Ph}]^{•+}$. The oxidation of $\text{B-P}(\text{OMe})_3$ results in a broad asymmetrical band centered at

4300 cm^{-1} , which is depicted in Figure 2. The susceptibility of a bright-raspberry-red-colored CD_2Cl_2 solution of $[\text{B-P}(\text{OMe})_3]^{•+}$ prepared in situ in an NMR tube at $T \leq 203$ K correlates with $\mu_{\text{eff}}([\text{B-P}(\text{OMe})_3]^{•+}) = 2.6$. The subsequent addition of $(\text{H}_3\text{C}_5)_2\text{Co}$ recovered the starting material in $>95\%$ ^1H NMR spectroscopic yield, which proves the overall stoichiometry to be correct and rules out the irreversible formation of side products. Intriguingly, contributions from two distinct low-energy electronic transitions at $\nu^{\text{NIR}} = 5000$ and 4200 cm^{-1} with similar intensities (cf. Figure S16) may be read from UV/vis/NIR spectra recorded after the stepwise addition of substoichiometric amounts of oxidant. Finally, the oxidation of $\text{B-CN}^t\text{Bu}$ results in the appearance of an intense and sharp band at $\nu^{\text{NIR}} = 4570 \text{ cm}^{-1}$ ($8 \times 10^3 \text{ M}^{-1} \text{ cm}^{-1}$; $\Delta\nu_{1/2} = 2300 \text{ cm}^{-1}$); cf. the orange trace in Figure 2. Complementary IR data taken at $T < 193$ K in CH_2Cl_2 and CD_2Cl_2 solutions show a single $\nu_{\text{C}\equiv\text{N}}$ mode at 2225 cm^{-1} of the radical-cation product, as depicted in Figure 3, which matches $\nu_{\text{C}\equiv\text{N}} = 2215 \text{ cm}^{-1}$

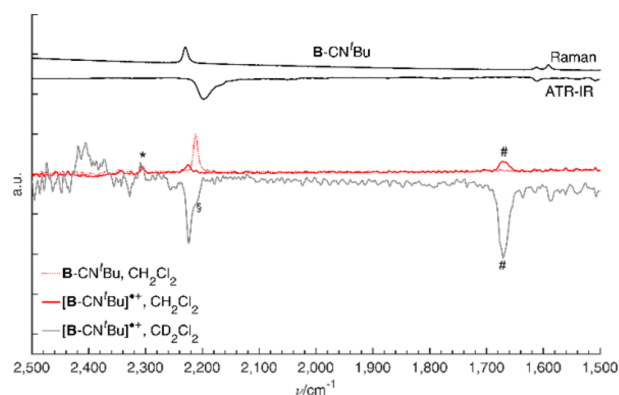


Figure 3. Top: Normalized traces of linear Raman microscopy and ATR-IR data taken from a single-crystalline sample of $\text{B-CN}^t\text{Bu}$. Bottom: Normalized solution IR spectra of neutral $\text{B-CN}^t\text{Bu}$ (dotted red) and oxidized $[\text{B-CN}^t\text{Bu}]^{•+}$ in CH_2Cl_2 (solid red) and CD_2Cl_2 (solid gray, inverted) at $T \leq -85^\circ\text{C}$; § = residual $\text{B-CN}^t\text{Bu}$ due to the substoichiometric addition of $[\text{Fc}^{•+}]^+$ oxidant; # = $\nu_{\text{C}=\text{O}}$, 1,1-diacetylferrocene coproduct; * = residual uncompensated IR band of the CH_2Cl_2 solvent.

calculated for DFT-optimized $[\text{B-CN}^t\text{Bu}]^{•+}$. The observation of a single IR band supports the preservation of local D_{2h} symmetry, and $\Delta\nu_{\text{C}\equiv\text{N}} = +13 \text{ cm}^{-1}$ suggests a conserved oxidation state at platinum in agreement with the formulation of a thiyl/thiolate radical-ligand complex.

Experimental IR data are corroborated by both calculated $\rho(\text{Pt})$ (cf. Table 2) and a g anisotropy of 0.160 of the three

Table 2. Mulliken Spin Densities Computed at the ZORA/BLYP35-D3/TZVP Level of Theory

	$[\text{A-L}]^{•+}$		$[\text{B-L}]^{•+}$	
	PMe_3	$\text{P}(\text{OMe})_3^a$	CN^tBu	PMe_3^b
$\rho(\text{Pt})$	0.18	0.09/0.08	0.07	0.11
$\rho(\text{S})$	0.36	0.49/0.62	0.41	0.28
$\rho(\text{Ar})$	0.03	0.20/0.27	0.20	0.16
$\rho(\text{S}')$	0.36	0.13/0.03	0.24	0.28
$\rho(\text{Ar}')$	0.03	0.06/0.01	0.08	0.16

^aData refer to DFT-optimized local/global minimum structures, respectively. ^bData taken from ref 69 for comparison.

principal resonances that are observed in X-band cw-EPR spectra of $[\text{B-CN}^t\text{Bu}]^{*\bullet}$ in a 1:1 $\text{CH}_2\text{Cl}_2/\text{C}_7\text{H}_8$ glass at 110 K (cf. Table 1). No hfc to $^{14}\text{N}(I = 1)$ is resolved, whereas principal values of $A(^{195}\text{Pt})$ are in the 204–319 MHz range. Rhombic spectra also result for the other members $[\text{B-L}]^{*\bullet}$ of the series with $\text{L} = \text{PMe}_2\text{Ph}$ and $\text{P}(\text{OMe})_3$ (cf. Figures S8 and S10). Simulation of the spectra provided $\Delta g = 0.087$ for $\text{L} = \text{P}(\text{OMe})_3$ and 0.07 in the case of $\text{L} = \text{PMe}_2\text{Ph}$, and principal values of $A(^{195}\text{Pt})$ indicate an electronic structure equivalent to that for $[\text{B-PMe}_3]^{*\bullet}$.

DFT Modeling and TD-DFT Data. As originally reported for $[\text{B-PMe}_3]^{*\bullet}$, thiy/thiolate cations $[\text{A/B-L}]^{*\bullet}$ generally are metastable at $T \leq 213$ K, which renders their isolation in pure form impossible in some of the cases. Although $[\text{B-PMe}_3]^{*\bullet}$ is isolable in the form of purple needles at low temperature, poor crystal quality has obviated the determination of its molecular structure. For this reason, structural and electronic properties were modeled computationally. The DFT method was calibrated through a comparison of experimentally established and DFT-optimized molecular structures of the starting materials A/B-L . As mentioned before, such a comparison is fully convincing (cf. Table S1), rendering the structure prediction of the respective cations reliable. Cation structures were fully optimized starting from optimized geometries of neutral compounds at the BP86-D3/TZVP level of theory, applying the ZORA^{74,75} to account for platinum. Because generalized gradient approximation (GGA)-type functionals such as BP86 greatly overestimate delocalization and therefore are not capable of describing the electronic structure of mixed-valence systems properly, the spectroscopic properties and underlying details of the electronic structure, that is, MOs and spin densities, were addressed through single-point calculations on the ZORA/BLYP35-D3/TZVP level of theory. Systematic work by Kaupp and co-workers has identified the hybrid functional BLYP35 as a valuable and reliable tool,^{76,77} which previously also accounted adequately for the effect of varied orientation of the metal–ligand orbital alignment on the electronic structures of $[\text{B-PMe}_3]^{*\bullet}$ and $[\text{C-PPh}_3]^{*\bullet}$.⁶⁹ For all optimized structures, spin expectation values very close to the ideal value of $\langle S \rangle^2 = 0.75$ are found, ruling out significant spin contamination. It is noted that BP86-optimized cation structures most probably suffer from overemphasized delocalization as a result of an artificially favored symmetry. This deficiency is necessarily only partly compensated by the BLYP35 functional.

Analogous to B-PMe_3 , the cation formation from A-PMe_3 is largely a structure-conserving process, as shown in Figure 4. While the overall appearance and metrics are similar in both forms, changes to the Pt–P and Pt–S bond lengths are most diagnostic of the oxidation event. Whereas the former expand, the Pt–S bond lengths both contract by 7 pm. Similarly, contraction of the coordination sphere in radical-salen complexes of nickel/palladium/platinum has been discussed in terms of the *inverse bonding scheme*. Pt–S bond contraction indicates that withdrawal of the electron (density) occurs from essentially metal–ligand antibonding orbitals. Different from A-L , oxidation of the other members of the B-L series significantly affects the overall structure, going far beyond Pt–S/Pt–P bond contractions/expansions, as shown in Figure 4. In particular, the mutual orientation of the $[\text{S}_2\text{PtL}_2]$ plane and the bridging arene varies with oxidation. Compared to neutral B-L , the platinum atom is shifted toward one of the C–C bonds of the bridging arene, which renders the overall structure of the

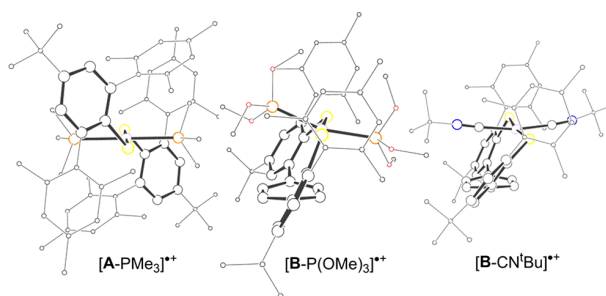


Figure 4. Side views of the DFT-derived molecular structures of thiy/thiolate cations $[\text{A-PMe}_3]^{*\bullet}$ (left), $[\text{B-P}(\text{OMe})_3]^{*\bullet}$ (global minimum structure; center), and $[\text{B-CN}^t\text{Bu}]^{*\bullet}$ (right) at the ZORA/BP86-D3/TZVP level of theory.

cations $[\text{B-L}]^{*\bullet}$ [$\text{L} = \text{P}(\text{OMe})_3$, PMe_2Ph , and CN^tBu] very similar to that of single-crystalline $\text{B-P}(\text{OMe})_3$ (cf. Figure 2). Although interaction of the metal and π system is not yet bonding in nature, the nonbonded Pt–C distances are clearly shorter than the sum of the van der Waals radii. Notably, the corresponding arrangement in $[\text{B-PMe}_3]^{*\bullet}$ resides just 12 kJ mol^{-1} above of the global minimum structure; quite probably, a tilted structure akin to the other series members is accessible also for $[\text{B-PMe}_3]^{*\bullet}$.

On the basis of the DFT-derived structural data, the dithiolate ligand scaffold must be considered to be conformationally flexible, allowing for variable conformations at low energy costs. This notion is corroborated by the above-mentioned observations made during the optimization of $[\text{B-P}(\text{OMe})_3]^{*\bullet}$. Depending on the input geometry (XRD data of $\text{B-P}(\text{OMe})_3$ vs modified XRD data of B-PMe_3), two minima are obtained that differ in energy by ≈ 10 kJ mol^{-1} . The structure of the global minimum is shown in Figure 4, and that of the local minimum is provided in Figure S2. Both structures differ markedly with respect to both the metrics of the metal coordination plane and the overall appearance. Most strikingly, the P–Pt–P angle in the local minimum structure is reduced to only 149° , reflecting severe signs of pyramidalization at platinum. Interestingly, if no dispersion correction is included both structures are essentially degenerate in energy. Dispersion effects feature prominently and may even be decisive for the overall structure.

According to electronic structure calculations at the ZORA/BLYP35-D3/TZVP level of theory, the unpaired spin accumulates to $>90\%$ at the central $[\text{Ar}'\text{S}'\text{-Pt-S}^{\text{Ar}}]$ core for all cations, which is in agreement with the formulation as thiy/thiolate complexes with only minor spin density located at platinum, as summarized in Table 2. This is further corroborated by analysis of the MO diagrams of $[\text{A-PMe}_3]^{*\bullet}$ (Figure 5) and $[\text{B-L}]^{*\bullet}$ in Figures S23 and S24. Overall, the spin-carrying α -SOMO is best described as a ligand-centered orbital of π^* symmetry in all cases, revealing only minor contributions from the metal. More precisely, within the series of complexes, subtle structural effects on the spin distribution prevail, ranging from symmetric, fully delocalized class III behavior ($[\text{B-PMe}_3]^{*\bullet}$ and $[\text{A-PMe}_3]^{*\bullet}$) to localized descriptions ($[\text{B-P}(\text{OMe})_3]^{*\bullet}$).

Most significant is the close-to-complete accumulation of the spin density within the S–Pt–S group in $[\text{A-PMe}_3]^{*\bullet}$. More precisely, the β -SOMO of $[\text{A-PMe}_3]^{*\bullet}$ is dominated by contributions from sulfur (57%) and platinum (24%) atomic orbitals. A compilation of the frontier MO composition is given

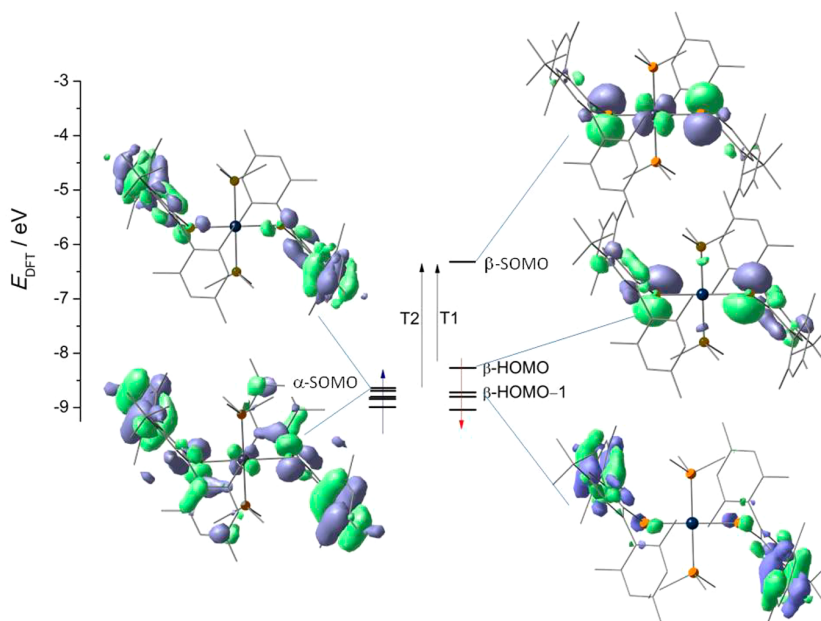


Figure 5. Kohn–Sham MOs and energy diagram for $[\text{A-PMe}_3]^{\bullet+}$ at the ZORA/BLYP35-D3/TZVP level of theory.

in Table S7. A similar result holds for $[\text{B-PMe}_3]^{\bullet+}$, in which the sulfur atoms contribute about 50% but the platinum contribution of 15% in the β -SOMO is significantly smaller than that of $[\text{A-PMe}_3]^{\bullet+}$. The minor spin export to the adjacent π systems in the case of $[\text{A-PMe}_3]^{\bullet+}$ is supported by the substantial dihedral angles Θ adopted by the two trans-oriented Pt–S–(C–C)_{arene} linkages. The large dihedral angles $\Theta = 56^\circ$ in DFT-optimized $[\text{A-PMe}_3]^{\bullet+}$ limit the spin density at each of the flanking π systems to 3% compared to 14% in $[\text{B-PMe}_3]^{\bullet+}$.⁶⁹ While 72% of the total computed spin density in $[\text{A-PMe}_3]^{\bullet+}$ distribute equally to both sulfur atoms, $\rho(\text{S},\text{S}') = 0.36$, platinum retains $\rho(\text{Pt}) = 0.18$, which indicates predominant platinum(II) character. Variation of the ligand-sphere topology from $[\text{B-PMe}_3]^{\bullet+}$ to $[\text{A-PMe}_3]^{\bullet+}$ increases the spin densities at platinum and each sulfur significantly from 0.11 to 0.18 and from 0.28 to 0.36, respectively, which is reflected by the substantial contributions of sulfur and platinum atomic orbitals to the frontier orbital composition. Overall, the computational data are in agreement with the above discussion of the g anisotropies in EPR spectra, $\Delta g([\text{A-PMe}_3]^{\bullet+}) = 0.29$ compared to $\Delta g([\text{B-PMe}_3]^{\bullet+}) = 0.078$. It is further corroborated by the divergence of the NIR transition energies [$\Delta\nu^{\text{NIR}}([\text{A-PMe}_3]^{\bullet+} - [\text{B-PMe}_3]^{\bullet+}) = 1700 \text{ cm}^{-1}$]. The NIR band pattern and transition energies of both $[\text{B-PMe}_3]^{\bullet+}$ and $[\text{A-PMe}_3]^{\bullet+}$ could be modeled convincingly by TD-DFT methods. For the transitions at lowest energies, TD-DFT predicts only slightly blue-shifted bands ($\Delta\nu^{\text{NIR}} \approx 500 \text{ cm}^{-1}$) in both cases. Notably, theory correctly predicts the presence of a second NIR transition in $[\text{A-PMe}_3]^{\bullet+}$ at higher energy and slightly lower intensity. The two low-energy transitions at $\nu = 9570 \text{ cm}^{-1}$ (T2; 67% β -HOMO-1 \rightarrow β -LUMO; $f_{\text{osc,calc}} = 0.06$) and 6370 cm^{-1} (T1; 79% β -HOMO \rightarrow β -LUMO; $f_{\text{osc,calc}} = 0.10$) are interpreted as CR transitions of a class III electron-delocalized radical ligand. While T1 has dominant sulfur-borne donor components (cf. the inset of Scheme 3), charge shifts from both mesityl groups feature prominently in T2 (see Figure S25).

TD-DFT also models the NIR transitions within the $[\text{B-L}]^{\bullet+}$ series very well, albeit the nature of the transitions is interpreted differently. The above-mentioned slight overestimation of the transition energies persists throughout the series, indicating a systematic error of the method (see Table 3). The origin of the

Table 3. Computed Energies (cm^{-1}), Intensities, and Character of the Low-Energy Transitions^a

		$[\text{B-L}]^{\bullet+}$		$[\text{A-L}]^{\bullet+}$
		$\text{P}(\text{OMe})_3^b$	CN^tBu	PMe_3
ν^{NIR}	DFT	5040/6480	5100	6370/9570
	exptl	4300/5000	4600	5700/9670
f_{osc}		0.13/0.06	0.19	0.10/0.06
	purity (%) ^c	94/97	91	79/67 ^d

^aSingle-point ZORA/BLYP35-D3/TZVP. ^bDFT data for two minimum structures. ^cPercentage of the β -HOMO \rightarrow β -LUMO contribution to the transition. ^d β -HOMO-1 \rightarrow β -LUMO transition.

increased line width of ν^{NIR} of $[\text{B-P}(\text{OMe})_3]^{\bullet+}$ observed at $T = 193 \text{ K}$ cannot be decided at present. On the one hand, the observed line width and computed spin-density distribution (Table 2) are indicative of a class II type electron-localized structure. In agreement with this notion, chemical reduction cleanly returns $\text{B-P}(\text{OMe})_3$ close to the quantitative yield, which rules out decomposition, and the EPR data support the formation of a single oxidation product. On the other hand, UV/vis/NIR data obtained from the stepwise addition of oxidant at $T = 183 \text{ K}$ showing two strongly overlapping narrow bands may be associated with the presence of isomers. TD-DFT calculations provided distinct but energetically similar intense transitions for the two geometric isomers of $[\text{B-P}(\text{OMe})_3]^{\bullet+}$ (Table 3). Consequently, interpretation in terms of interconverting isomers that is rapid on the EPR time scale equally fits the observations.

Different from the above discussion of $[\text{A-PMe}_3]^{\bullet+}$ and $[\text{B-PMe}_3]^{\bullet+}$, DFT predicts electron-localized structures for the other members of the $[\text{B-L}]^{\bullet+}$ series (Table 2 and MO

diagrams in Figures S24 and S25). This detail of the electronic structure features prominently in some of the geometries of $[\text{B-L}]^{\bullet+}$. The metrical structures become more dissymmetric with increasing spin localization. An instructive example is $[\text{B-CN}^t\text{Bu}]^{\bullet+}$, where significant spin localization at one ArS moiety is reflected by a small dihedral angle Θ of 6° . By contrast, diminished π overlap in the opposite $\text{Ar}'\text{S}'$ ($\Theta' = 31^\circ$) allows only minor spin localization. Similar reasoning applies for $[\text{B-PMe}_3]^{\bullet+}$ and $[\text{B-P(OMe)}_3]^{\bullet+}$. In general, $\rho(\text{Pt})$ are small and show little effect of coligand variation. This is in full agreement with the small g anisotropies in EPR, $\Delta g < 0.1$, akin to $[\text{B-PMe}_3]^{\bullet+}$. With regard to the narrow line widths observed experimentally, a borderline class II–III classification of electron-localized solvent-averaged radical ligands is proposed. Taken together, confinement of the spin density to the thyl/thiolate metal core in $[(\text{ArS}^-)\text{Pt}^{\text{II}}(\text{ArS}^{\bullet})]^+$ is the result of limiting the overlap of the orbitals of the $[\text{S-Pt-S}]$ core and arene sulfur moieties, which renders the chromophores spectroscopically distinct.

Thermal Stability of Radical-Ligand Cations. In agreement with the cyclic voltammetry data, blue-purple $[\text{A-PMe}_3]^{\bullet+}$ is metastable at $T \leq 233$ K and converts irreversibly to a green species that is characterized by $\nu = 9300$ cm^{-1} ($\sim 2 \times 10^3$ M^{-1} cm^{-1} ; $\Delta\nu_{1/2} = \sim 4000$ cm^{-1} ; CH_2Cl_2). As shown in Figure S18, a series of electronic absorption spectra that were collected at variable temperature (VT) to monitor the conversion of $[\text{A-PMe}_3]^{\bullet+}$ into the green product lack defined isosbestic points. X-band cw-EPR spectral data corroborate conversion into an $S = 1/2$ product that is characterized by a rhombic, ^{195}Pt -coupled spectrum (cf. Figure S13). In general, the intensely colored CH_2Cl_2 solutions of radical-ligand complex cations $[\text{B-L}]^{\bullet+}$ are subject to a color change if warmed to $T > 203$ K, whereas no intermediates were detected spectroscopically when the samples of $[\text{B-L}]^{\bullet+}$ with $\text{L} = \text{P(OMe)}_3$ and CN^tBu were gradually warmed to room temperature. As shown in Figures S19 and S21, sample deterioration finally results in the complete loss of NIR bands and rhombic EPR resonances. By contrast, gradual warming of a 0.12 mM solution of $[\text{B-PMe}_3]^{\bullet+}$ to $T \geq 273$ K produces a distinct band at $\nu^{\text{NIR}} = 6660$ ($\sim 4 \times 10^3$ M^{-1} cm^{-1} ; $\Delta\nu_{1/2} = 1600$ cm^{-1} ; CH_2Cl_2) cm^{-1} . The position and shape of this transition compare well to $\nu^{\text{NIR}} = 6410$ cm^{-1} of the chemically robust class II–III thyl/thiolate radical cation $[\text{C-PPh}_3]^{\bullet+}$,⁶⁹ suggesting the formation of $[\text{C-PMe}_3]^{\bullet+}$, as formulated in Scheme 3. The formation of the thyl/thiolate complex cation $[\text{C-PMe}_3]^{\bullet+}$ could not be proven independently by EPR spectroscopy owing to rapid deterioration of the sample at higher concentrations as discussed below. In the case of $[\text{B-PMe}_2\text{Ph}]^{\bullet+}$, however, the formation of $[\text{C-PMe}_2\text{Ph}]^{\bullet+}$ is evident from its distinct rhombic EPR spectrum shown in Figure S9. Spectral simulation provided principal values of the g and $A(^{195}\text{Pt})$ tensors that are 2.186/210, 2.084/192, and 2.007/249 MHz, which match those reported for $[\text{C-PPh}_3]^{\bullet+}$ (2.174/175, 2.082/184, and 2.005/239 MHz).⁶⁹ As observed for $[\text{B-PMe}_3]^{\bullet+}$, gradual conversion of $[\text{B-PMe}_2\text{Ph}]^{\bullet+}$ to $[\text{C-PMe}_2\text{Ph}]^{\bullet+}$ is accompanied by the appearance of a new NIR transition centered at $\nu^{\text{NIR}} = 6700$ cm^{-1} ($\sim 1 \times 10^4$ M^{-1} cm^{-1} ; $\Delta\nu_{1/2} = 1800$ cm^{-1}), which is depicted in Figure 6. The assignments are corroborated by TD-DFT modeling of BP86-optimized structures of $[\text{C-L}]^{\bullet+}$ for $\text{L} = \text{PMe}_3$ and PMe_2Ph , as shown in Figure S3. A single intense NIR transition is calculated at $\nu^{\text{NIR}} = 7500$ cm^{-1} (PMe_3) and 6990 cm^{-1} (PMe_2Ph). Akin to $[\text{C-PPh}_3]^{\bullet+}$ ($\Delta\nu^{\text{NIR}} = 590$ cm^{-1}), TD-DFT only slightly overestimates the NIR transition

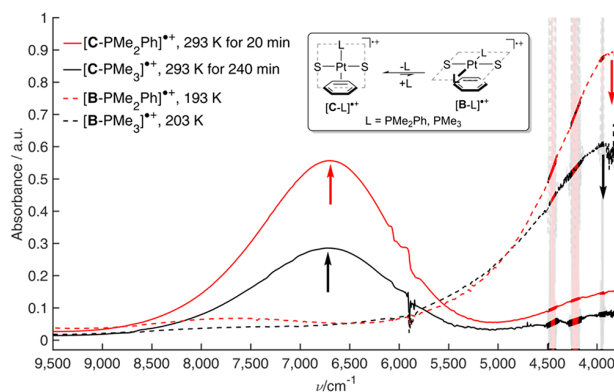


Figure 6. Evolution of distinct NIR transitions that reflect thermally induced conversion of radical-ligand cations $[\text{B-L}]^{\bullet+}$ into $[\text{C-L}]^{\bullet+}$ through the dissociation of 1 equiv of coligand $\text{L} = \text{PMe}_2\text{Ph}$ and PMe_3 . Spectra were taken in CH_2Cl_2 , the noncorrectable residual solvent background at $\nu \leq 4500$ cm^{-1} was attenuated for clarity, and the spectral data of $[\text{B-PMe}_3]^{\bullet+}$ are included for comparison and are equivalent to those reported in ref 69.

energy. According to the dissymmetric spin-density distribution and narrow NIR band widths, corroborated by the solvent indifference of ν^{NIR} in $[\text{C-PPh}_3]^{\bullet+}$,⁶⁹ $[\text{C-L}]^{\bullet+}$ is best formulated as an electron-localized solvent-averaged radical ligand. In this respect, the electronic structures of $[\text{C-L}]^{\bullet+}$ and the series $[\text{B-L}]^{\bullet+}$ are similar, but NIR transition energies differ substantially. The large differences $\Delta\nu^{\text{NIR}}([\text{C-L}]^{\bullet+} - [\text{B-L}]^{\bullet+})$ of 2700 and 2900 cm^{-1} for $\text{L} = \text{PMe}_3$ and PMe_2Ph , respectively, reflect the different relative alignments of platinum and ligand orbitals in $[\text{C-L}]^{\bullet+}$ and $[\text{B-L}]^{\bullet+}$.

Radical-ligand cations $[\text{C-L}]^{\bullet+}$ gradually decompose within hours at room temperature, a process that involves the irreversible oxidation of dissociated L .⁶⁹ The higher redox stability of PMe_2Ph compared to PMe_3 renders bimolecular decomposition mechanisms less facile such that $[\text{C-PMe}_2\text{Ph}]^{\bullet+}$ is metastable even in higher concentrated samples that are typically employed for EPR and NMR studies, whereas $[\text{C-PMe}_3]^{\bullet+}$ obviously does not.

CONCLUSIONS

Radical-ligand complexes of the transition metals are an outstanding class of compounds in view of their intriguing electronic structures and associated chemical and physical properties. The increasing spectrum of their applications spans from stoichiometric and catalytic reactivity to electrochromic NIR dyes and magnetic materials. Correlating the chemical and electronic structures is fundamentally important for the formulation of structure–property relationships, which aid in the future development of the field. A considerable body of mono- and multinuclear complexes exists in which the radical ligand adopts a terminal or bridging position. In general, the electronic structure of any radical-ligand complex depends on the particular combination of a metal and radical proligand. More precisely, the key parameter is the relative admixture of metal and ligand atom orbitals to the (un)occupied frontier MOs. For this reason, tuning of the electronic structure and associated physicochemical properties commonly involves varying the type(s) of metal(s) and the electronic properties of the ligand(s), e.g., through the prudent screening of substitution patterns.

As an alternative, this work reports that the geometrical constraints and relative alignment of the metal and ligand orbitals determine the electronic structure and spectroscopic properties of a chromophore system $[(\text{ArS}^-)\text{Pt}^{\text{II}}(\text{S}^{\text{Ar}})]^+$ whose chemical composition has not been changed. The choice of a structurally flexible coordination environment that supports distinct bonding modes in this context. Starting from a 1,4-terphenyldithiophenolate–metal fragment, varying the number of auxiliary coligands at the metal aids in the discrimination between spectroscopically distinct bonding modes B-L and C-L, as indicated in Scheme 2. Dissociation of one PMe_2Ph ligand converts $[\text{B-PMe}_2\text{Ph}]^{*+}$ to thermodynamically favored $[\text{C-PMe}_2\text{Ph}]^{*+}$ and causes a shift of ν^{NIR} by 2900 cm^{-1} to higher energy, which equals an energy difference of 34 kJ mol^{-1} . Computational and experimental data indicate that the auxiliary coligand does not contribute to the spectroscopically active frontier orbitals directly but affects the distribution of the unpaired spin density through modulation of the relative alignment of metal thiy/thiolate ligand orbitals. In fact, whereas the electronic and steric properties of coligands $\text{L} = \text{PMe}_3, \text{PMe}_2\text{Ph},$ and PPh_3 are certainly different, the spectroscopic properties of the platinum(II) arylthiy/thiolate chromophores in $[\text{C-L}]^{*+}$ are conserved, albeit their kinetic stabilities differ.

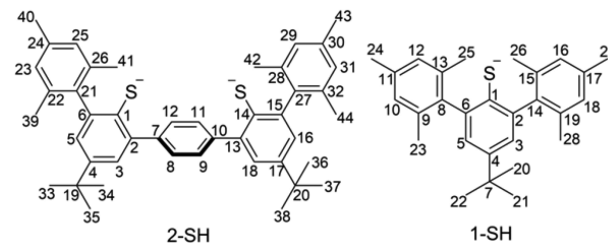
For a given type of metal ligand alignment, torsion affects the degree of delocalization of the unpaired spin density within the platinum(II) arylthiy/thiolate MO manifold. Despite the fact that chromophore systems $[\text{A-PMe}_3]^{*+}$ and $[\text{B-PMe}_3]^{*+}$ are chemically identical, they are spectroscopically distinct because of different distributions of the spin density. This extends to the series of thiy/thiolate radical cations $[\text{B-L}]^{*+}$, whose spectroscopic properties depend on the steric rather than electronic properties of coligands L. Interligand interactions have a subtle effect on the structural properties of neutral and radical-ligand complexes, but the electronic structures are significantly different. Albeit the effect is small within the series of complexes $[\text{B-L}]^{*+}$ ($\Delta\nu^{\text{NIR}} = 730\text{ cm}^{-1}$ for $\text{L} = \text{CN}^t\text{Bu}$ and PMe_2Ph equals an energy difference of 9 kJ mol^{-1}), it is significantly pronounced for $[\text{A-L}]^{*+}$ and geometrically constrained for $[\text{B-L}]^{*+}$, whose transition energies differ by 20 kJ mol^{-1} for $\text{L} = \text{PMe}_3$.

Taken together, studying the relationship of the chemical and electronic structures is of fundamental importance to understand and make use of the chemical and physical properties of radical-ligand complexes. Options for modulating the electronic structures are diverse and aid in broadening the scope of applications of radical-ligand complexes in the future.

EXPERIMENTAL SECTION

General Information. All manipulations of air- and moisture-sensitive compounds were carried out under an atmosphere of dry argon using standard Schlenk or glovebox techniques. Literature procedures were followed for the preparation of S',S''' -di-*tert*-butyl-2,2''',4,4''',6,6'''-hexamethyl-[1,1':3',1''':4'',1''':3''',1''''-quinquephenyl]-2',2''-dithiol (2-SH),⁶⁸ S' -(*tert*-butyl)-2,2'',4,4'',6,6''-hexamethyl-[1,1':3',1''-terphenyl]-2'-thiol (1-SH),⁷⁸ *trans*-(py)₂PtCl₂ (py = pyridine),⁷⁹ C-PPh₃, and 1,1-diacetylferrocenium bis-(trifluoromethanesulfonyl)imide.⁶⁹ General information on the purification of additional starting materials, solvents and reagents, cyclic voltammetry, X-band cw-EPR spectroscopic and XRD data, computational details, and DFT-optimized structures is provided in the Supporting Information. ¹H and ¹³C{¹H} NMR chemical shifts (δ) are referenced to residual ¹H and naturally abundant ¹³C NMR resonances of the solvents (cf. the Supporting Information). VT

electronic spectra were recorded on PerkinElmer Lambda 1050 and Cary 5000 UV/vis/NIR photospectrometers equipped with a Unisoku CoolSpeK UV USP-203-B cryostat ($\text{Pt-100 Class B}, -150\text{ }^\circ\text{C} \leq T \leq 100\text{ }^\circ\text{C}$), using 1 cm quartz cells with septum screw caps. UV/vis/NIR spectra were recorded in the 200–2650 nm range because of the strong background absorption of the solvent at longer wavelengths. Deviating from IUPAC recommendations, the following numeration applies:



Preparation of A-PMe₃. Benzylpotassium (32 mg, 0.248 mmol) was added to a solution of ligand 1-SH (100 mg, 0.248 mmol) in toluene (6 mL) at room temperature. The mixture was stirred for ~30 min, during which time the base was consumed and a white precipitate separated. A yellow suspension of *trans*-(py)₂PtCl₂ (53 mg, 0.124 mmol) in toluene (6 mL) was combined with 1.24 mL of a 0.2 M solution of PMe_3 (0.248 mmol) in toluene and the mixture stirred at room temperature until a white suspension formed (~1 h). The suspension of the ligand potassium salt was added dropwise to the platinum precursor and the flask rinsed with 3 mL of toluene. Stirring for 0.5 h at room temperature afforded an orange solution, after which an additional 1.24 mL of a 0.2 M PMe_3 solution was added. After stirring overnight, the solvent was removed under vacuum, the yellow residue dissolved in toluene, and the solution filtered and finally concentrated until a crystalline material separated. Rectangular yellow crystals separated upon cooling the solution at $5\text{ }^\circ\text{C}$ overnight. The mother liquor was filtered off, and the crystals were dried. Yield: 71 mg (46%) of A-PMe₃-C₇H₈. Vapor diffusion of pentane into a concentrated solution in toluene at room temperature afforded a single-crystalline material suitable for XRD analysis. Unit cell parameters: $a = 8.7771(4)\text{ \AA}$, $b = 13.0930(5)\text{ \AA}$, $c = 13.2600(5)\text{ \AA}$, $P\bar{1}$, CCDC 1816320. ¹H NMR (500 MHz, CD₂Cl₂, 298 K): δ 6.81 (s, 4H, H-3,5), 6.78 (m, 8H, H-10,13,16,18), 2.27 (s, 12H, H-24,27), 2.06 (s, 24H, H-23,25,26,28), 1.21 (s, 18H, H-20,21,22), 0.71 (N-line pattern, 18H, ¹²⁺⁴J_{H,P} = 3.8 Hz, *trans*-PMe₃). UV/vis/NIR [183 K, CH₂Cl₂; λ , nm (ϵ , $\times 10^3\text{ M}^{-1}\text{ cm}^{-1}$)] = 300 (35), 349 (21). Elem. anal. Calcd for C₆₂H₈₄P₂PtS₂: C, 64.74; H, 7.36; S, 5.57. Found: C, 64.76; H, 7.37; S, 5.37.

Representative Procedure for the Preparation of B-L. To a suspension of C-PPh₃ (100 mg, 0.088 mmol) in 6 mL of hexanes coligand L (PMe_2Ph ; 60 μL , 0.420 mmol) was added dropwise under stirring at room temperature. The initially green suspension quickly turned into a yellow solution from which the product separated as a yellow solid. Within 0.5 h, the supernatant solution became pale yellow after which the product was filtered off, washed three times with 3 mL of pentane, and finally dried under dynamic vacuum. Yield: 85 mg (95%) of B-PMe₂Ph. Vapor diffusion of pentane into a concentrated solution of B-PMe₂Ph in toluene at room temperature yielded single-crystalline material suitable for XRD analysis. Unit cell parameters: $a = 9.2794(5)\text{ \AA}$, $b = 9.4421(5)\text{ \AA}$, $c = 29.9667(16)\text{ \AA}$, $P\bar{1}$, CCDC 1816318. ¹H NMR (600 MHz, C₆D₆, 298 K): δ 7.67 (d, 2H, ³J_{H,H} = 2.5 Hz, H-3,18), 7.31 (s, 4H, H-8,9,11,12), 7.30 (m, 4H, *ortho*-H, PMe_2Ph), 7.14 (d, 2H, ³J_{H,H} = 2.5 Hz, H-5,16), 6.97 (s, 4H, H-23,25,29,31), 6.81 (m, 6H, *meta/para*-H, PMe_2Ph), 2.39 (s, 12H, H-39,41,42,44), 2.21 (s, 6H, H-40,43), 1.37 (N-line pattern, 12H, ¹²⁺⁴J_{H,P} = 3.6 Hz, *trans*-PMe₂Ph), 1.33 (s, 18H, H-33,34,35,36,37,38). UV/vis/NIR [193 K, CH₂Cl₂; λ , nm (ϵ , $\times 10^3\text{ M}^{-1}\text{ cm}^{-1}$)] = 475 (>10). Elem. anal. Calcd for C₆₀H₇₀P₂PtS₂: C, 64.79; H, 6.34; S, 5.76. Found: C, 64.81; H, 6.22; S, 5.38.}}}

$\text{L} = \text{P}(\text{OMe})_3$. A total of 5 equiv of freshly distilled $\text{P}(\text{OMe})_3$ was added. Yield: 62 mg (71%) of B-P(OMe)₃ as a yellow solid. Vapor diffusion of hexamethyldisiloxane into a concentrated solution of B-

P(OMe)₃ in toluene at room temperature yielded a single-crystalline material suitable for XRD analysis. Unit cell parameters: $a = 9.8965(3)$ Å, $b = 30.6248(10)$ Å, $c = 16.1666(5)$ Å, $P21/c$, CCDC 1816321. ¹H NMR (600 MHz, C₆D₆, 298 K): δ 7.75 (s, 4H, H-8,9,11,12), 7.72 (d, 2H, $^3J_{\text{H,H}} = 2.5$ Hz, H-5,16), 7.11 (d, $^3J_{\text{H,H}} = 2.5$ Hz, H-3,18), 6.99 (s, 4H, H-23,25,29,31), 3.29 (N-line pattern, 18H, $^{13+51}J_{\text{H,P}} = 5.6$ Hz, *trans*-P(OMe)₃), 2.34 (s, 12H, H-39,41,42,44), 2.22 (s, 6H, H-40,43), 1.33 (s, 18H, H-33,34,35,36,37,38). UV/vis/NIR [193 K, CH₂Cl₂; λ , nm (ϵ , $\times 10^3$ M⁻¹ cm⁻¹): 398 (2.8). Elem. anal. Calcd for C₅₀H₆₆O₆P₂PtS₂: C, 55.39; H, 6.14; S, 5.91. Found: C, 54.94; H, 6.16; S, 5.58.

$L = \text{CN}^t\text{Bu}$. Ligand exchange was carried out in a toluene solution by the addition of 8 equiv of distilled CN^tBu. Yield: 85 mg (87%) of B-CN^tBu as a yellow solid. Vapor diffusion of pentane into a concentrated solution of B-CN^tBu in toluene at room temperature yielded a single-crystalline material suitable for XRD analysis. Unit cell parameters: $a = 19.4796(4)$ Å, $b = 9.4067(2)$ Å, $c = 28.7470(6)$ Å, $P21/n$, CCDC 1816319. ¹H NMR (600 MHz, C₆D₆, 298 K): δ 7.86 (s, 4H, H-8,9,11,12), 7.76 (d, 2H, $^3J_{\text{H,H}} = 2.4$ Hz, H-3,18), 7.14 (d, 2H, $^3J_{\text{H,H}} = 2.4$ Hz, H-5,16), 6.99 (s, 4H, H-23,25,29,31), 2.35 (s, 12H, H-39,41,42,44), 2.26 (s, 6H, H-40,43), 1.30 (s, 18H, H-33,34,35,36,37,38), 0.66 (s, 18H, CN^tBu). UV/vis/NIR [183 K, CH₂Cl₂; λ , nm (ϵ , $\times 10^3$ M⁻¹ cm⁻¹): 355 (5.2), 400 (2.7). Elem. anal. Calcd for C₅₄H₆₆N₂PtS₂: C, 64.71; H, 6.64; N, 2.79; S, 6.40. Found: C, 64.51; H, 6.65; N, 2.95; S, 6.08.

Generation and VT UV/Vis/NIR Data of [A/B-L]⁺. Radical-ligand cations [A/B-L]⁺ were generated in situ at $T \leq 193$ K. Stock solutions (1.7 mM) of A/B-L and [Fc⁺]NTf₂ were prepared in CH₂Cl₂. A total of 2.8 mL of CH₂Cl₂ was transferred to a four-sided transparent cell with a screw cap and septum, and background spectra were recorded at $183 \text{ K} \leq T \leq 293 \text{ K}$ at 10 K steps. A total of 0.3 μmol of A/B-L was transferred by syringe to the cuvette at $T \leq 183 \text{ K}$, and a reference spectrum was recorded. Aliquots of 0.25 equiv of [Fc⁺]NTf₂ were added by syringe, and spectra were recorded after the addition. Finally, reaction mixtures were gradually warmed to 293 K in steps of 10 K, and spectra were acquired at each temperature. Spectra were corrected by subtraction of the respective background of neat CH₂Cl₂.

[A-PMe₃]⁺. UV/vis/NIR [183 K, CH₂Cl₂; λ , nm (ϵ , $\times 10^3$ M⁻¹ cm⁻¹): 497 (4.4), 650 (1.8), 856 (1.9), 1056 (4.3; 9670 cm⁻¹, $\Delta\nu_{1/2} = 1900$ cm⁻¹), 1754 nm (7.5; 5700 cm⁻¹, $\Delta\nu_{1/2} = 2400$ cm⁻¹). μ_{eff} (188–213 K, CD₂Cl₂, 1,1,2,2-C₂H₄Cl₄ shift reference): 2.4. [B-PMe₂Ph]⁺. UV/vis/NIR [193 K; λ , nm (ϵ , $\times 10^3$ M⁻¹ cm⁻¹): 449 (2.2), 519 (2.8), 663 (2.3), 872 (0.6), 1300 (0.5), 2605 (7.2; 3840 cm⁻¹, $\Delta\nu_{1/2} \sim 1400$ cm⁻¹). [C-PMe₂Ph]⁺. UV/vis/NIR [293 K; λ , nm (ϵ , $\times 10^3$ M⁻¹ cm⁻¹): 1490 (9.6; 6700 cm⁻¹, $\Delta\nu_{1/2} = 1800$ cm⁻¹). [B-P(OMe)₃]⁺. UV/vis/NIR [193 K; λ , nm (ϵ , $\times 10^3$ M⁻¹ cm⁻¹): 527 (8.3), 833 (1.2), 1040 (1.3), 2330 (5.6; 4300 cm⁻¹). μ_{eff} (188 K, CD₂Cl₂, 1,1,2,2-C₂H₄Cl₄ shift reference): 2.6. [B-CN^tBu]⁺. UV/vis/NIR [183 K; λ , nm (ϵ , $\times 10^3$ M⁻¹ cm⁻¹): 445 (3.7), 460 (3.5), 561 (4.4), 1388 (2.4), 2330 (7.7; 4570 cm⁻¹, $\Delta\nu_{1/2} = 2300$ cm⁻¹). [C-PMe₃]⁺. UV/vis/NIR [293 K; λ , nm (ϵ , $\times 10^3$ M⁻¹ cm⁻¹): 1500 (3.8; 6660 cm⁻¹, $\Delta\nu_{1/2} = 1700$ cm⁻¹).

Computational Details. All DFT and TD-DFT calculations were performed using ORCA 2.9.1.⁸⁰ TZVP basis sets⁸¹ were used throughout. The presence of platinum was accounted for with van Willen's ZORA,^{74,75} implying TZV-ZORA auxiliary basis sets. Geometric structure optimizations with the BP86 functional⁸² started from the nuclear positions of the corresponding neutral complexes. Dispersion contributions were approximated using Grimme's DFT-D3 atom-pairwise dispersion corrections.^{83,84} Numerical frequency calculations of B-CN^tBu and [B-CN^tBu]⁺ proved the optimized structures to be stationary points. UV/vis/NIR spectroscopic properties, MOs, and spin densities were extracted from single-point TD-DFT calculations (BLYP35^{76,77}) in the BP86-optimized atomic positions.

■ ASSOCIATED CONTENT

Supporting Information

The Supporting Information is available free of charge on the ACS Publications website at DOI: 10.1021/acs.inorgchem.8b00122.

Additional experimental procedures, cyclic voltammetry, NMR, X-band cw-EPR, and UV/vis/NIR spectroscopic data, crystallographic details, DFT-optimized structures and Cartesian coordinates, and TD-DFT data (PDF)

Accession Codes

CCDC 1816318–1816321 contain the supplementary crystallographic data for this paper. These data can be obtained free of charge via www.ccdc.cam.ac.uk/data_request/cif, or by emailing data_request@ccdc.cam.ac.uk, or by contacting The Cambridge Crystallographic Data Centre, 12 Union Road, Cambridge CB2 1EZ, UK; fax: +44 1223 336033.

■ AUTHOR INFORMATION

Corresponding Author

*E-mail: andreas.berkefeld@anorg.uni-tuebingen.de.

ORCID

Andreas Berkefeld: 0000-0002-2757-7841

Author Contributions

The manuscript was written through contributions of all authors. All authors have given approval to the final version of the manuscript.

Notes

The authors declare no competing financial interest.

■ ACKNOWLEDGMENTS

A.B. and N.M.M. are grateful to the Fonds der Chemischen Industrie and the Baden-Württemberg Foundation for financial support and Andreas Früh and Prof. Thomas Chassé (Universität Tübingen) for assistance with the linear Raman microscope. G.H. thanks the Deutsche Forschungsgemeinschaft DFG (SFB 658, elementary processes in molecular switches on surfaces) and the Berlin FG cluster of excellence on "Unifying Concepts in Catalysis (UniCat)" for financial support. G.H. and A.B. thank Prof. Martin Kaupp (TU Berlin) for computational advice. A.B. acknowledges Umicore, Hanau, Germany, for the generous donation of (^tBu₃P)₂Pd.

■ REFERENCES

- Feigl, F.; Fürth, M. Über Verbindungen des Nickels mito-Phenylendiamin und 1, 3, 4-Toluyldiamin. *Monatsh. Chem.* **1927**, *48*, 445–450.
- Herebian, D.; Bothe, E.; Neese, F.; Weyhermüller, T.; Wieghardt, K. Molecular and Electronic Structures of Bis-(o-diiminobenzosemiquinonato)metal(II) Complexes (Ni, Pd, Pt), Their Monocations and -Anions, and of Dimeric Dications Containing Weak Metal–Metal Bonds. *J. Am. Chem. Soc.* **2003**, *125*, 9116–9128.
- Stiefel, E. I.; Waters, J. H.; Billig, E.; Gray, H. B. The Myth of Nickel(III) and Nickel(IV) in Planar Complexes I. *J. Am. Chem. Soc.* **1965**, *87*, 3016–3017.
- Collins, T. J.; Nichols, T. R.; Uffelman, E. S. A square-planar nickel(III) complex of an innocent ligand system. *J. Am. Chem. Soc.* **1991**, *113*, 4708–4709.
- Hanss, J.; Krüger, H.-J. First Isolation and Structural Characterization of a Nickel(III) Complex Containing Aliphatic Thiolate Donors. *Angew. Chem., Int. Ed.* **1998**, *37*, 360–363.
- Alonso, P. J.; Arauzo, A. B.; García-Monforte, M. A.; Martín, A.; Menjón, B.; Rillo, C.; Tomás, M. Homoleptic Organoderivatives of High-Valent Nickel(III). *Chem. - Eur. J.* **2009**, *15*, 11020–11030.

- (7) Iluc, V. M.; Miller, A. J. M.; Anderson, J. S.; Monreal, M. J.; Mehn, M. P.; Hillhouse, G. L. Synthesis and Characterization of Three-Coordinate Ni(III)-Imide Complexes. *J. Am. Chem. Soc.* **2011**, *133*, 13055–13063.
- (8) Lipschutz, M. I.; Yang, X.; Chatterjee, R.; Tilley, T. D. A Structurally Rigid Bis(amido) Ligand Framework in Low-Coordinate Ni(I), Ni(II), and Ni(III) Analogues Provides Access to a Ni(III) Methyl Complex via Oxidative Addition. *J. Am. Chem. Soc.* **2013**, *135*, 15298–15301.
- (9) Cao, T.-P.-A.; Nocton, G.; Ricard, L.; Le Goff, X. F.; Auffrant, A. A Tetracoordinated Phosphaalen Nickel(III) Complex. *Angew. Chem., Int. Ed.* **2014**, *53*, 1368–1372.
- (10) Ray, K.; Petrenko, T.; Wiegardt, K.; Neese, F. Joint spectroscopic and theoretical investigations of transition metal complexes involving non-innocent ligands. *Dalton Trans.* **2007**, 1552–1566.
- (11) Kaim, W. The transition metal coordination chemistry of anion radicals. *Coord. Chem. Rev.* **1987**, *76*, 187–235.
- (12) Falceto, A.; Casanova, D.; Alemany, P.; Alvarez, S. Distortions of π -Coordinated Arenes with Anionic Character. *Chem. - Eur. J.* **2014**, *20*, 14674–14689.
- (13) Wadepohl, H. Benzene and Its Derivatives as Bridging Ligands in Transition-Metal Complexes. *Angew. Chem., Int. Ed. Engl.* **1992**, *31*, 247–262.
- (14) Lee, S.; Lovelace, S. R.; Arford, D. J.; Geib, S. J.; Weber, S. G.; Cooper, N. J. Reductively Induced Dimerization of the Ligated Benzene in $[\text{Mn}(\eta^6\text{-C}_6\text{H}_6)(\text{CO})_3]^+$: Formation of the Initial C–C Bond by Anion/Cation Addition. *J. Am. Chem. Soc.* **1996**, *118*, 4190–4191.
- (15) Bach, I.; Pörschke, K.-R.; Goddard, R.; Kopske, C.; Krüger, C.; Ruffínska, A.; Seevogel, K. Synthesis, Structure, and Properties of $\{(\text{Bu}_2\text{PC}_2\text{H}_4\text{P}^+\text{Bu}_2)\text{Ni}\}_2(\mu\text{-}\eta^2\text{-}\eta^2\text{-C}_6\text{H}_6)$ and $(\text{Bu}_2\text{PC}_2\text{H}_4\text{P}^+\text{Bu}_2)\text{Ni}(\eta^2\text{-C}_6\text{F}_6)$. *Organometallics* **1996**, *15*, 4959–4966.
- (16) Bai, G.; Wei, P.; Stephan, D. W. A β -Diketiminato–Nickel(II) Synthon for Nickel(I) Complexes. *Organometallics* **2005**, *24*, 5901–5908.
- (17) Buss, J. A.; Agapie, T. Four-electron deoxygenative reductive coupling of carbon monoxide at a single metal site. *Nature* **2016**, *529*, 72–75.
- (18) Enright, D.; Gambarotta, S.; Yap, G. P. A.; Budzelaar, P. H. M. The Ability of the α,α' -Diiminopyridine Ligand System to Accept Negative Charge: Isolation of Paramagnetic and Diamagnetic Trianions. *Angew. Chem., Int. Ed.* **2002**, *41*, 3873–3876.
- (19) Chirik, P. J.; Wiegardt, K. Radical Ligands Confer Nobility on Base-Metal Catalysts. *Science* **2010**, *327*, 794.
- (20) Zhou, Y.-Y.; Hartline, D. R.; Steiman, T. J.; Fanwick, P. E.; Uyeda, C. Dinuclear Nickel Complexes in Five States of Oxidation Using a Redox-Active Ligand. *Inorg. Chem.* **2014**, *53*, 11770–11777.
- (21) Nishiyama, H.; Ikeda, H.; Saito, T.; Kriegel, B.; Tsurugi, H.; Arnold, J.; Mashima, K. Structural and Electronic Noninnocence of α -Diimine Ligands on Niobium for Reductive C–Cl Bond Activation and Catalytic Radical Addition Reactions. *J. Am. Chem. Soc.* **2017**, *139*, 6494–6505.
- (22) Kaim, W.; Schwederski, B. Non-innocent ligands in bioinorganic chemistry—An overview. *Coord. Chem. Rev.* **2010**, *254*, 1580–1588.
- (23) Deplano, P.; Pilia, L.; Espa, D.; Mercuri, M. L.; Serpe, A. Square-planar d8 metal mixed-ligand dithiolene complexes as second order nonlinear optical chromophores: Structure/property relationship. *Coord. Chem. Rev.* **2010**, *254*, 1434–1447.
- (24) Stiefel, E. I.; Karlin, K. D. *Dithiolene Chemistry. Synthesis, Properties, and Applications*, 1st ed.; John Wiley & Sons, Inc.: Hoboken, NJ, 2004; Vol. 52, p 738.
- (25) Eisenberg, R.; Gray, H. B. Noninnocence in Metal Complexes: A Dithiolene Dawn. *Inorg. Chem.* **2011**, *50*, 9741–9751.
- (26) Williams, R.; Billig, E.; Waters, J. H.; Gray, H. B. The Toluenedithiolate and Maleonitriledithiolate Square-Matrix Systems. *J. Am. Chem. Soc.* **1966**, *88*, 43–50.
- (27) Ray, K.; DeBeer George, S.; Solomon, E. I.; Wiegardt, K.; Neese, F. Description of the Ground-State Covalencies of the Bis(dithiolato) Transition-Metal Complexes from X-ray Absorption Spectroscopy and Time-Dependent Density-Functional Calculations. *Chem. - Eur. J.* **2007**, *13*, 2783–2797.
- (28) Baker-Hawkes, M. J.; Billig, E.; Gray, H. B. Characterization and Electronic Structures of Metal Complexes Containing Benzene-1,2-dithiolate and Related Ligands. *J. Am. Chem. Soc.* **1966**, *88*, 4870–4875.
- (29) Arumugam, K.; Shaw, M. C.; Chandrasekaran, P.; Villagrán, D.; Gray, T. G.; Mague, J. T.; Donahue, J. P. Synthesis, Structures, and Properties of 1,2,4,5-Benzenetetrathiolate Linked Group 10 Metal Complexes. *Inorg. Chem.* **2009**, *48*, 10591–10607.
- (30) Ketterer, N. A.; Fan, H.; Blackmore, K. J.; Yang, X.; Ziller, J. W.; Baik, M.-H.; Heyduk, A. F. $\pi\bullet\text{-}\pi\bullet$ Bonding Interactions Generated by Halogen Oxidation of Zirconium(IV) Redox-Active Ligand Complexes. *J. Am. Chem. Soc.* **2008**, *130*, 4364–4374.
- (31) Sarkar, B.; Schweinfurth, D.; Deibel, N.; Weisser, F. Functional metal complexes based on bridging “imino”-quinonoid ligands. *Coord. Chem. Rev.* **2015**, *293–294*, 250–262.
- (32) Ghosh, P.; Begum, A.; Herebian, D.; Bothe, E.; Hildenbrand, K.; Weyhermüller, T.; Wiegardt, K. Coordinated o-Dithio- and o-Iminothiobenzosemiquinonate(1 $^-$) π Radicals in $[\text{M}^{\text{I}}(\text{bpy})(\text{L}^{\bullet})](\text{PF}_6)$ Complexes. *Angew. Chem., Int. Ed.* **2003**, *42*, 563–567.
- (33) Poturovic, S.; Mashuta, M. S.; Grapperhaus, C. A. Carbon–Sulfur Bond Formation between a Ruthenium-Coordinated Thiyl Radical and Methyl Ketones. *Angew. Chem., Int. Ed.* **2005**, *44*, 1883–1887.
- (34) Tang, H.; Guan, J.; Hall, M. B. Understanding the Radical Nature of an Oxidized Ruthenium Tris(thiolate) Complex and Its Role in the Chemistry. *J. Am. Chem. Soc.* **2015**, *137*, 15616–15619.
- (35) Grapperhaus, C. A.; Ouch, K.; Mashuta, M. S. Redox-Regulated Ethylene Binding to a Rhenium-Thiolate Complex. *J. Am. Chem. Soc.* **2009**, *131*, 64–65.
- (36) Tang, H.; Brothers, E. N.; Hall, M. B. The Distinctive Electronic Structures of Rhenium Tris(thiolate) Complexes, an Unexpected Contrast to the Valence Isoelectronic Ruthenium Tris(thiolate) Complexes. *Inorg. Chem.* **2017**, *56*, 583–593.
- (37) Thomas, F. Ligand-centred oxidative chemistry in sterically hindered salen complexes: an interesting case with nickel. *Dalton Trans.* **2016**, *45*, 10866–10877.
- (38) Clarke, R. M.; Herasymchuk, K.; Storr, T. Electronic structure elucidation in oxidized metal–salen complexes. *Coord. Chem. Rev.* **2017**, *352*, 67–82.
- (39) Tang, J.-H.; Yao, C.-J.; Cui, B.-B.; Zhong, Y.-W. Ruthenium-Amine Conjugated Organometallic Materials for Multistate Near-IR Electrochromism and Information Storage. *Chem. Rec.* **2016**, *16*, 754–767.
- (40) Harris, C. F.; Bayless, M. B.; van Leest, N. P.; Bruch, Q. J.; Livesay, B. N.; Bacsá, J.; Hardcastle, K. I.; Shores, M. P.; de Bruin, B.; Soper, J. D. Redox-Active Bis(phenolate) N-Heterocyclic Carbene [OCO] Pincer Ligands Support Cobalt Electron Transfer Series Spanning Four Oxidation States. *Inorg. Chem.* **2017**, *56*, 12421–12435.
- (41) Storr, T.; Verma, P.; Pratt, R. C.; Wasinger, E. C.; Shimazaki, Y.; Stack, T. D. P. Defining the Electronic and Geometric Structure of One-Electron Oxidized Copper–Bis-phenoxide Complexes. *J. Am. Chem. Soc.* **2008**, *130*, 15448–15459.
- (42) Shimazaki, Y.; Tani, F.; Fukui, K.; Naruta, Y.; Yamauchi, O. One-Electron Oxidized Nickel(II)–(Disalicylidene)diamine Complex: Temperature-Dependent Tautomerism between Ni(III)–Phenolate and Ni(II)–Phenoxy Radical States. *J. Am. Chem. Soc.* **2003**, *125*, 10512–10513.
- (43) Shimazaki, Y.; Yajima, T.; Tani, F.; Karasawa, S.; Fukui, K.; Naruta, Y.; Yamauchi, O. Syntheses and Electronic Structures of One-Electron-Oxidized Group 10 Metal(II)–(Disalicylidene)diamine Complexes (Metal = Ni, Pd, Pt). *J. Am. Chem. Soc.* **2007**, *129*, 2559–2568.
- (44) Broering, E. P.; Dillon, S.; Gale, E. M.; Steiner, R. A.; Telser, J.; Brunold, T. C.; Harrop, T. C. Accessing Ni(III)-Thiolate Versus Ni(II)-Thiyl Bonding in a Family of Ni–N₂S₂ Synthetic Models of NiSOD. *Inorg. Chem.* **2015**, *54*, 3815–3828.

- (45) Pierpont, C. G. Studies on charge distribution and valence tautomerism in transition metal complexes of catecholate and semiquinonate ligands. *Coord. Chem. Rev.* **2001**, *216–217*, 99–125.
- (46) Connick, W. B.; Gray, H. B. Photooxidation of Platinum(II) Diimine Dithiolates. *J. Am. Chem. Soc.* **1997**, *119*, 11620–11627.
- (47) Lyaskovskyy, V.; de Bruin, B. Redox Non-Innocent Ligands: Versatile New Tools to Control Catalytic Reactions. *ACS Catal.* **2012**, *2*, 270–279.
- (48) Praneeth, V. K. K.; Ringenberg, M. R.; Ward, T. R. Redox-Active Ligands in Catalysis. *Angew. Chem., Int. Ed.* **2012**, *51*, 10228–10234.
- (49) Luca, O. R.; Crabtree, R. H. Redox-active ligands in catalysis. *Chem. Soc. Rev.* **2013**, *42*, 1440–1459.
- (50) Broere, D. L. J.; Plessius, R.; van der Vlugt, J. I. New avenues for ligand-mediated processes - expanding metal reactivity by the use of redox-active catechol, o-aminophenol and o-phenylenediamine ligands. *Chem. Soc. Rev.* **2015**, *44*, 6886–6915.
- (51) Kuijpers, P. F.; van der Vlugt, J. I.; Schneider, S.; de Bruin, B. Nitrene Radical Intermediates in Catalytic Synthesis. *Chem. - Eur. J.* **2017**, *23*, 13819–13829.
- (52) Whittaker, J. W. Free Radical Catalysis by Galactose Oxidase. *Chem. Soc. Rev.* **2003**, *103*, 2347–2364.
- (53) Chaudhuri, P.; Hess, M.; Flörke, U.; Wieghardt, K. From Structural Models of Galactose Oxidase to Homogeneous Catalysis: Efficient Aerobic Oxidation of Alcohols. *Angew. Chem., Int. Ed.* **1998**, *37*, 2217–2220.
- (54) Chaudhuri, P.; Hess, M.; Müller, J.; Hildenbrand, K.; Bill, E.; Weyhermüller, T.; Wieghardt, K. Aerobic Oxidation of Primary Alcohols (Including Methanol) by Copper(II)- and Zinc(II)-Phenoxyl Radical Catalysts. *J. Am. Chem. Soc.* **1999**, *121*, 9599–9610.
- (55) Orio, M.; Jarjays, O.; Kanso, H.; Philouze, C.; Neese, F.; Thomas, F. X-Ray Structures of Copper(II) and Nickel(II) Radical Salen Complexes: The Preference of Galactose Oxidase for Copper(II). *Angew. Chem., Int. Ed.* **2010**, *49*, 4989–4992.
- (56) Kochem, A.; Molloy, J. K.; Gellon, G.; Leconte, N.; Philouze, C.; Berthiol, F.; Jarjays, O.; Thomas, F. A Structurally Characterized Cu(II) Complex Supported by a Bis(anilido) Ligand and Its Oxidative Catalytic Activity. *Chem. - Eur. J.* **2017**, *23*, 13929–13940.
- (57) Jacquet, J.; Blanchard, S.; Derat, E.; Desage-El Murr, M.; Fensterbank, L. Redox-ligand sustains controlled generation of CF₃ radicals by well-defined copper complex. *Chem. Sci.* **2016**, *7*, 2030–2036.
- (58) Jacquet, J.; Chaumont, P.; Gontard, G.; Orio, M.; Vezin, H.; Blanchard, S.; Desage-El Murr, M.; Fensterbank, L. Desage-El Murr, M.; Fensterbank, L. C–N Bond Formation from a Masked High-Valent Copper Complex Stabilized by Redox Non-Innocent Ligands. *Angew. Chem., Int. Ed.* **2016**, *55*, 10712–10716.
- (59) Jacquet, J.; Cheaib, K.; Ren, Y.; Vezin, H.; Orio, M.; Blanchard, S.; Fensterbank, L.; Desage-El Murr, M. Desage-El Murr, M. Circumventing Intrinsic Metal Reactivity: Radical Generation with Redox-Active Ligands. *Chem. - Eur. J.* **2017**, *23*, 15030–15034.
- (60) Chaudhuri, P.; Wieghardt, K. *Progress in Inorganic Chemistry*; John Wiley & Sons, Inc., 2002; pp 151–216.
- (61) Chiang, L.; Kochem, A.; Jarjays, O.; Dunn, T. J.; Vezin, H.; Sakaguchi, M.; Ogura, T.; Orio, M.; Shimazaki, Y.; Thomas, F.; Storr, T. Radical Localization in a Series of Symmetric Ni(II) Complexes with Oxidized Salen Ligands. *Chem. - Eur. J.* **2012**, *18*, 14117–14127.
- (62) Demadis, K. D.; Hartshorn, C. M.; Meyer, T. J. The Localized-to-Delocalized Transition in Mixed-Valence Chemistry. *Chem. Rev.* **2001**, *101*, 2655–2686.
- (63) Stenson, P. A.; Board, A.; Marin-Becerra, A.; Blake, A. J.; Davies, E. S.; Wilson, C.; McMaster, J.; Schröder, M. Molecular and Electronic Structures of One-Electron Oxidized Ni^{II}-(Dithiosalicylidenediamine) Complexes: Ni^{III}-Thiolate versus Ni^{II}-Thiyl Radical States. *Chem. - Eur. J.* **2008**, *14*, 2564–2576.
- (64) Shimazaki, Y.; Stack, T. D. P.; Storr, T. Detailed Evaluation of the Geometric and Electronic Structures of One-Electron Oxidized Group 10 (Ni, Pd, and Pt) Metal(II)-(Disalicylidene)diamine Complexes. *Inorg. Chem.* **2009**, *48*, 8383–8392.
- (65) Kaim, W. Concepts for metal complex chromophores absorbing in the near infrared. *Coord. Chem. Rev.* **2011**, *255*, 2503–2513.
- (66) Mortimer, R. J. Electrochromic Materials. *Annu. Rev. Mater. Res.* **2011**, *41*, 241.
- (67) Ward, M. D. Near-infrared electrochromic materials for optical attenuation based on transition-metal coordination complexes. *J. Solid State Electrochem.* **2005**, *9*, 778–787.
- (68) Koch, F.; Schubert, H.; Sirsch, P.; Berkefeld, A. Binuclear complexes of Ni(I) from 4-terphenyldithiophenol. *Dalton Trans* **2015**, *44*, 13315–24.
- (69) Mews, N. M.; Berkefeld, A.; Hörner, G.; Schubert, H. Controlling Near-Infrared Chromophore Electronic Properties through Metal–Ligand Orbital Alignment. *J. Am. Chem. Soc.* **2017**, *139*, 2808–2815.
- (70) CCDC 1816318–1816321 contain the crystallographic data for this paper. These data are provided free of charge by The Cambridge Crystallographic Data Centre.
- (71) Malatesta, L.; Bonati, F. *Isocyanide complexes of metals*; Wiley: London, 1969; p VII, 199.
- (72) Ray, K.; Weyhermüller, T.; Neese, F.; Wieghardt, K. Electronic Structure of Square Planar Bis(benzene-1,2-dithiolato)metal Complexes [M(L)₂]^z (z = 2–, 1–, 0; M = Ni, Pd, Pt, Cu, Au): An Experimental, Density Functional, and Correlated ab Initio Study. *Inorg. Chem.* **2005**, *44*, 5345–5360.
- (73) Csonka, I. P.; Szepes, L.; Modelli, A. Donor–acceptor properties of isonitriles studied by photoelectron spectroscopy and electron transmission spectroscopy. *J. Mass Spectrom.* **2004**, *39*, 1456–1466.
- (74) van Wüllen, C. Molecular density functional calculations in the regular relativistic approximation: Method, application to coinage metal diatomics, hydrides, fluorides and chlorides, and comparison with first-order relativistic calculations. *J. Chem. Phys.* **1998**, *109*, 392–399.
- (75) Pantazis, D. A.; Chen, X.-Y.; Landis, C. R.; Neese, F. All-Electron Scalar Relativistic Basis Sets for Third-Row Transition Metal Atoms. *J. Chem. Theory Comput.* **2008**, *4*, 908–919.
- (76) Parthey, M.; Kaupp, M. Quantum-chemical insights into mixed-valence systems: within and beyond the Robin-Day scheme. *Chem. Soc. Rev.* **2014**, *43*, 5067–5088.
- (77) Parthey, M.; Vincent, K. B.; Renz, M.; Schauer, P. A.; Yufit, D. S.; Howard, J. A. K.; Kaupp, M.; Low, P. J. A Combined Computational and Spectroelectrochemical Study of Platinum-Bridged Bis-Triarylamine Systems. *Inorg. Chem.* **2014**, *53*, 1544–1554.
- (78) Koch, F.; Berkefeld, A.; Speiser, B.; Schubert, H. Mechanistic Aspects of Redox-Induced Assembly and Disassembly of S-Bridged [2M–2S] Structures. *Chem. - Eur. J.* **2017**, *23*, 16681–16690.
- (79) Kauffman, G. B.; Cowan, D. O.; Slusarczuk, G.; Kirschner, S.. In *Inorganic Synthesis*; Kleinberg, J., Ed.; John Wiley & Sons, Inc.: Hoboken, NJ, 1963; Vol. 7, pp 239–245.
- (80) Neese, F. The ORCA program system. *WIREs Comput. Mol. Sci.* **2012**, *2*, 73–78.
- (81) Schäfer, A.; Horn, H.; Ahlrichs, R. Fully optimized contracted Gaussian basis sets for atoms Li to Kr. *J. Chem. Phys.* **1992**, *97*, 2571–2577.
- (82) Becke, A. D. Density-functional exchange-energy approximation with correct asymptotic behavior. *Phys. Rev. A: At., Mol., Opt. Phys.* **1988**, *38*, 3098–3100.
- (83) Grimme, S. Semiempirical GGA-type density functional constructed with a long-range dispersion correction. *J. Comput. Chem.* **2006**, *27*, 1787–1799.
- (84) Grimme, S.; Ehrlich, S.; Goerigk, L. Effect of the damping function in dispersion corrected density functional theory. *J. Comput. Chem.* **2011**, *32*, 1456–1465.

Tuning of Thiol/Thiolate Complex Near-Infrared Chromophores of Platinum through Geometrical Constraints

Nicole M. Mews, Gerald Hörner, Hartmut Schubert, and Andreas Berkefeld

Table of Contents

1	General Information.....	2
2	Additional Analytical Data for Starting Materials A/B-L	4
3	Additional Structural Information	5
4	Cyclic Voltammetry Data	8
5	EPR Data.....	10
6	Additional UV/vis/NIR Data.....	14
7	Additional Computational Data.....	20
7.1	Cartesian coordinates of DFT-optimized structures (ZORA-BP86-D3/TZVP)	23
8	References	34

1 General Information

AgClO₄ (Alfa Aesar) and 1,1-diacetylferrocene (TCI) were used as received. PMe₂Ph, P(OMe)₃, and CN^tBu (Aldrich) were purified by distillation whereas high purity ferrocene (99.5%; TCI) was sublimed, and stored under argon. 0.2 M PMe₃ in toluene was prepared from commercially available 1 M PMe₃ in toluene (Aldrich). In general, solvents were purified and dried prior to use. 1,1,2,2-C₂H₂Cl₄ was dried over and distilled from P₂O₅, degassed, and saturated with Ar. Hexane was dried over Grubbs columns of an MBraun solvent purification system (SPS). Pentane and toluene were pre-dried over activated 3 Å molecular sieves (MS) and distilled from sodium benzophenone ketyl under argon. Dichloromethane stabilized with EtOH (CHEMSOLUTE, Th. Geyer) was first distilled from P₂O₅, then from K₂CO₃, and finally stored over activated basic alumina. Acetonitrile (MeCN) for use in electrochemical experiments was sequentially dried over and distilled from CaH₂ and P₂O₅, and finally percolated through activated neutral alumina. 1,2-Difluorobenzene (1,2-C₆F₂H₄; ABCR) was dried and purified by percolation through a column of activated neutral alumina, and distilled onto activated neutral alumina prior to use. C₆D₆ was dried over and distilled from NaK alloy, and CD₂Cl₂ was dried over and vacuum transferred from 3 Å MS. Hexamethyldisiloxane was dried over and distilled from 3 Å MS. In general, solvents were stored over 3 Å MS under argon. Molecular sieves and alumina were activated by heating under dynamic vacuum (10⁻³ mbar) at $T \leq 200^\circ\text{C}$ for 24-48 h.

NMR data were acquired on a Bruker Avance III HDX 600 and an AVII+500 spectrometer (VT NMR studies). ¹H and ¹³C{¹H}-NMR chemical shifts are referenced to the residual proton and naturally abundant carbon resonances of the solvents: 7.16/128.06 (C₆D₆), 5.32/53.84 (CD₂Cl₂). ³¹P NMR chemical shifts are referenced to an external standard sample of 85% H₃PO₄ set to 0 ppm. ¹⁹⁵Pt NMR chemical shifts are referenced to an external standard sample of 1.2 M hexachloroplatinate(IV) in D₂O set to 0 ppm.

EPR spectra were collected using 4 mm O.D. Wilmad quartz (CFQ) EPR tubes on a continuous wave X-band Bruker EMXmicro spectrometer, and are referenced to the Bruker Strong Pitch standard $g_{\text{iso}} = 2.0028$. EPR simulations were done with EasySpin (version 5.1.12)¹ and MATLAB and Statistic Toolbox Release R2016a (The MathWorks, Inc., Natick, Massachusetts, United States). X-band cw-EPR spectral data were fitted using the easyfit tool included in EasySpin package (pepper for solid state and garlic for solution data).

In general, the sample concentrations for electronic spectra were corrected for temperature dependent changes of solvent density ρ by using a modified form of the Rackett equation²

Evan's method³ was employed to determine μ_{eff} in solution using a coaxial insert for 5 mm NMR sample tubes, $\chi_{\text{M}}^{\text{dia}} = -0.5 \times M$, M = dimensionless molecular weight of the sample and $\chi_{\text{M}}^{\text{dia}}(\text{CD}_2\text{Cl}_2) = -4.66 \times 10^{-5} \text{ cm}^3 \text{ mol}^{-1}$ were used to correct for diamagnetic susceptibilities of sample and solvent.⁴

X-Ray diffraction data were collected on a Bruker Smart APEXII diffractometer with graphite-monochromated MoK_α radiation. The programs used were Bruker's APEX2 v2011.8-0, including SADABS for absorption correction and SAINT for structure solution, the WinGX suite of programs version 2013.3,⁵ SHELXS and SHELXL for structure solution and refinement,^{6,7} PLATON,⁸ and Ortep.⁹ Crystals were, unless otherwise noted, coated in a perfluorinated polyether oil and mounted on a 100 μm MiTeGen MicroMounts™ loop that was placed on the goniometer head under a stream of dry nitrogen at 100 K.

Cyclic voltammetry (CV) measurements were performed under argon at 17°C using a Julabo CF40 (resistance thermometer: Pt-100, temperature range: -40 to 50°C) and an ECI 200 potentiostat (Nordic Electrochemistry) in a gas-tight, full-glass, three-electrode cell setup. The potentiostat was controlled by using the EC4 DAQ (version 4.1.133.1, Nordic Electrochemistry) software, and data were treated with EC4 VIEW (version 1.2.55.1, Nordic Electrochemistry). $n\text{Bu}_4\text{NPF}_6$ electrolyte (Alfa Aesar) was recrystallized 3 times from

acetone/water and employed as a 0.1 M solution in CH₂Cl₂ and MeCN. A Pt disc electrode (Deutsche Metrohm GmbH & Co. KG, electro-active area = 0.080 ± 0.003 cm²) and a 1 mm coiled Pt-wire were employed as working and counter electrodes. The Ag/Ag⁺ redox couple, in the form of a 0.5 mm Ag wire in a 0.01 M AgClO₄/0.1 M *n*Bu₄NPF₆ MeCN solution, served as a reference electrode. Voltammograms were corrected for capacitive currents of electrolyte solutions and overall cell resistance, and potentials are reported relative to Fc/[Fc]⁺ in CH₂Cl₂, with $E_{1/2}(\text{Fc}/[\text{Fc}]^+ / 0.1 \text{ M } n\text{Bu}_4\text{NPF}_6 / \text{CH}_2\text{Cl}_2, 17^\circ\text{C}) = 0.212 \pm 0.001 \text{ V}$. The electro-active area of the Pt disc electrode was calculated from Fc/[Fc]⁺ measurements in 0.1 M *n*Bu₄NPF₆ solution in CH₂Cl₂ at various concentrations and potential sweep rates at 295 K, using $D(\text{Fc}/\text{CH}_2\text{Cl}_2, 295 \text{ K}) = 2.2 \times 10^{-5} \text{ cm}^2 \text{ s}^{-1}$.¹⁰ The working electrode was rinsed with acetone, polished very gently with a paste of 0.3 μm alumina (Deutsche Metrohm GmbH & Co. KG) in deionized water, rinsed thoroughly with plenty of deionized water, and finally acetone after each use. Periodic Fc/[Fc]⁺ reference measurements verified the electro-active surface area of the Pt electrode, and the stability of the potential of the Ag/Ag⁺ reference electrode.

FT-IR spectra in solution were recorded with a Mettler-Toledo ReactIR 15 (6.3 mm AgX, SiComp dip probe) under argon. FT-IR spectra in solids were recorded with a Bruker Vertex 70 spectrometer equipped with a Harrik MVP 2 Series ATR module.

Raman spectra were collected with a LabRAM HR800 joba yvon equipped with a 532 nm Nd-YAG laser.

2 Additional Analytical Data for Starting Materials A/B-L

A-PMe₃: ¹³C{¹H} NMR (125 MHz; CD₂Cl₂; 298 K): δ 147.18 (C4), 146.33 (C2,6), 141.89 (C8,14), 139.5 (t, ³J_{C,P} = 3.7 Hz, C1), 137.1 (C9,13,15,19), 135.7 (C11,17), 128.5 (C10,12,16,18), 127.2 (C3,5), 34.5 (C7), 31.5 (C20,21,22), 22.1 (C23,25,26,28), 21.0 (C24,27), 13.9 ppm (N-line pattern, ¹⁺³J_{C,P} = 19 Hz, *trans*-Pt(PMe₃)₂). ³¹P{¹H} NMR (202 MHz; CD₂Cl₂; 298 K): δ -20.5 ppm (¹J_{P,Pt} = 2720 Hz). ¹⁹⁵Pt NMR (129 MHz, C₆D₆, 298 K): δ -4375 ppm (t, ¹J_{Pt,P} = 2720 Hz).

B-PMe₂Ph: ¹³C{¹H} NMR (150 MHz, C₆D₆, 298 K): δ 144.4 (C4,17), 142.9 (C6,15), 141.1 (C2,13), 140.6 (C7,10), 138.5 (C1,14), 136.5 (PMe₂Ph-C_{ipso}), 136.2 (C24,30), 135.7 (C22,26,28,32), 130.8 (*para*-C, PMe₂Ph), 128.9 (*ortho*-C, PMe₂Ph), 128.4 (C23,25,29,31), 127.9 (*meta*-C, PMe₂Ph), 126.6 (C5,16), 124.4 (C3,18), 34.2 (C19,20), 31.7 (C33,34,35,36,37,38), 21.3 (C40,43), 21.16 (C39,41,42,44), 9.99 ppm (N-line pattern, 12H, ¹⁺³J_{C,P} = 19 Hz, *trans*-PMe₂Ph). ³¹P{¹H} NMR (242 MHz, C₆D₆, 298 K): δ -17.37 ppm (¹J_{Pt,P} = 2980 Hz). ¹⁹⁵Pt NMR (129 MHz, C₆D₆, 298 K): δ -4134 ppm (t, ¹J_{Pt,P} = 2980 Hz).

B-P(OMe)₃: ¹³C{¹H} NMR (150.9 MHz; C₆D₆; 298 K): δ 144.7 (C4,17), 143.2 (C2,6,13,15), 142.3 (C7,10), 138.9 (C1,14), 136.4 (C22,26,28,32), 135.6 (C24,30), 130.6 (C8,9,11,12), 128.3 (C23,25,29,31), 125.5 (C5,16), 124.1 (C3,18), 53.4 (P(OMe)₃), 34.3 (C4,17), 31.7 (C33,34,35,36,37,38), 21.3 ppm (C40,43), 20.9 (C39,41,42,44). ³¹P NMR (242.9 MHz; C₆D₆; 298 K): δ 88.4 ppm (m, ³J_{P,H} = 5.87 Hz, ¹J_{P,Pt} = 4910 Hz). ¹⁹⁵Pt NMR (129 MHz; C₆D₆; 298 K): δ -4161.9 ppm (t, J_{Pt,P} = 4910 Hz).

B-CN^tBu: ¹³C{¹H} NMR (150.9 MHz; C₆D₆; 298 K): δ 146.2 (C4,17), 145.2 (C6,15), 144.5 (C2,13), 144.4 (C7,10), 141.7 (C21,27), 141.1 (C1,14), 136.0 (C22,26,28,32), 135.6 (C24,30), 128.0 (CNC(CH₃)₃), 132.8 (C8,9,11,12), 128.4 (C23,25,29,31), 125.57 (C5,16), 123.57 (C3,18), 57.14 (CNC(CH₃)₃), 34.30 (C19,20), 31.69 (C33,34,35,36,37,38), 29.09 (CNC(CH₃)₃), 21.64 (C39,41,42,44), 21.32 ppm (C40,43). ¹⁹⁵Pt NMR (129 MHz; C₆D₆; 298 K): δ -4184 ppm (quint, ²J_{Pt,N} = 93 Hz).

3 Additional Structural Information

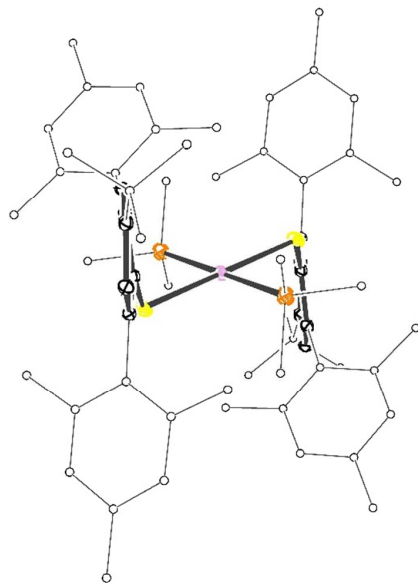


Figure S1. ORTEP representation of molecular structure of **A-PMe₃** (ellipsoids at 50 % probability, H-atoms omitted for clarity; Colour code: C, black; P, orange; S, yellow, Pt, plum).

Table S1. Selected bond lengths [\AA] and angles [$^\circ$] of neutral complexes **B-L** with L = PMe_3 , P(OMe)_3 , PMe_2Ph and CN^tBu ; **A-PMe**₃ denotes an open-chain congener of **B-L**, wherein the bridging arene (C7-C12) is replaced at C2 and C13 by mesityl groups; data in italics from DFT optimized structures (ZORA-BP86-D3/TZVP).

	B-PMe ₃	B-PMe ₂ Ph	B-P(OMe) ₃	B-CN ^t Bu	A-PMe ₃
Bond lengths					
Pt-P1	2.3094 <i>2.316</i>	2.312(2)	2.2942(7) <i>2.282</i>	1.954(2) <i>1.932</i>	2.315 <i>2.330</i>
Pt-P2	2.3094 <i>2.316</i>	2.310(2)	2.2696(8) <i>2.279</i>	1.956(2) <i>1.933</i>	2.315 <i>2.330</i>
Pt-S1	2.3414 <i>2.375</i>	2.374(2)	2.3723(9) <i>2.391</i>	2.3661(8) <i>2.395</i>	2.370 <i>2.380</i>
Pt-S2	2.3414 <i>2.375</i>	2.369(2)	2.3686(9) <i>2.397</i>	2.3591(8) <i>2.394</i>	2.370 <i>2.380</i>
S1-C1	1.776(2) <i>1.796</i>	1.792(8)	1.785(2) <i>1.796</i>	1.785(8) <i>1.802</i>	1.782(2) <i>1.789</i>
S2-C14	1.776(2) <i>1.796</i>	1.789(7)	1.785(2) <i>1.800</i>	1.789(3) <i>1.802</i>	1.782(2) <i>1.789</i>
C1-C2	1.409(3) <i>1.418</i>	1.41(1)	1.411(3) <i>1.414</i>	1.414(4) <i>1.424</i>	1.420(2) <i>1.421</i>
C14-C13	1.409(3) <i>1.418</i>	1.42(1)	1.416(3) <i>1.419</i>	1.415(4) <i>1.421</i>	1.418(2) <i>1.421</i>
Bond Angles					
S1-Pt-S2	171.47 <i>172.8</i>	174.25(7)	172.66(3) <i>177.5</i>	178.18(3) <i>178.3</i>	180.00 <i>180.0</i>
P-Pt-P	162.74 <i>164.6</i>	162.81(7)	164.91(3) <i>160.0</i>	179.6(1) <i>179.3</i>	180.00 <i>180.0</i>
S1-Pt-P	89.87 <i>89.7</i>	91.27(7)	88.82(3) <i>90.5</i>	90.99(8) <i>90.1</i>	90.48 <i>90.2</i>
S2-Pt-P	88.85 <i>89.6</i>	87.80(7)	92.43(3) <i>89.8</i>	89.71(8) <i>90.2</i>	89.52 <i>90.2</i>
C1-S1-Pt	118.03 <i>113.4</i>	115.6(3)	117.46(8) <i>112.5</i>	109.99(9) <i>108.7</i>	115.58 <i>111.6</i>
C14-S2-Pt	118.03 <i>113.4</i>	116.5(2)	115.92(8) <i>111.4</i>	111.84(9) <i>108.7</i>	115.58 <i>111.6</i>

Table S2. Selected bond lengths [\AA] and angles [$^\circ$] in the DFT-optimized structures of complex cations $[\mathbf{B-L}]^{\bullet+}$ with $L = \text{PMe}_3$, PPhMe_2 , P(OMe)_3 , CN^tBu ; $[\mathbf{A-PMe}_3]^{\bullet+}$ denotes an open-chain congener of $[\mathbf{B-PMe}_3]^{\bullet+}$, wherein the bridging arene (C7-C12) is replaced at C2 and C13 by mesityl groups.^a

	PMe_3^b	PMe_2Ph	P(OMe)_3^c	CN^tBu	$[\mathbf{A-PMe}_3]^{\bullet+}$	
bond length						
Pt-P ^d	2.348(1)	2.358(1)	2.309(3)	2.315(15)	1.954(3)	2.370(1)
Pt-S1	2.325	2.345	2.363	2.365	2.355	2.311
Pt-S2	2.325	2.322	2.363	2.339	2.370	2.311
S1-C1	1.785	1.786	1.781	1.790	1.789	1.790
S2-C14	1.785	1.777	1.730	1.774	1.781	1.790
C1-C2	1.418	1.421	1.422	1.419	1.422	1.418
C14-C13	1.418	1.423	1.422	1.429	1.422	1.418
bond angle						
S1-Pt-S2	168.9	170.5	171.3	169.9	171.3	179.9
P-Pt-P	162.9	161.5	148.8	163.9	169.8	180.0
S1-Pt-P	87.9/90.6	84.5/91.9	84.6/96.1	84.8/89.1	89.0/90.1	88.9/91.1
S2-Pt-P	87.7/90.6	87.4/94.2	89.8/87.1	93.1/90.5	82.1/96.3	88.9/91.1
C1-S1-Pt	117.0	118.5	118.4	115.6	113.3	112.3
C14-S2-Pt	117.0	117.5	115.5	116.9	117.6	112.4

^a Full optimization on the BP86-D3/TZVP/ZORA level of theory. ^b From Ref. 69 in manuscript. ^c Local minimum (left column) and global minimum (right column). ^d Averaged Pt-P bond length (deviation of individual Pt-P bond lengths from average).

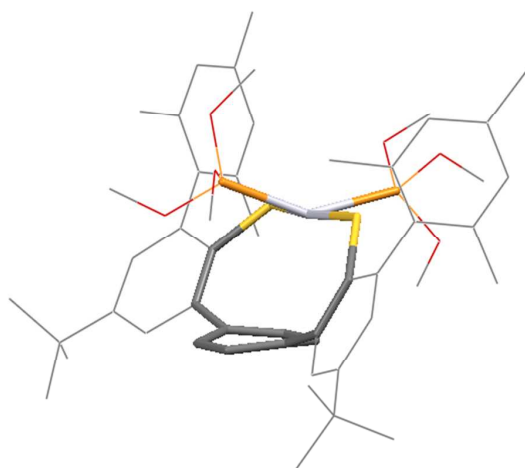


Figure S2. DFT-optimized structure of the local minimum of $[\mathbf{B-P(OMe)}_3]^{\bullet+}$.

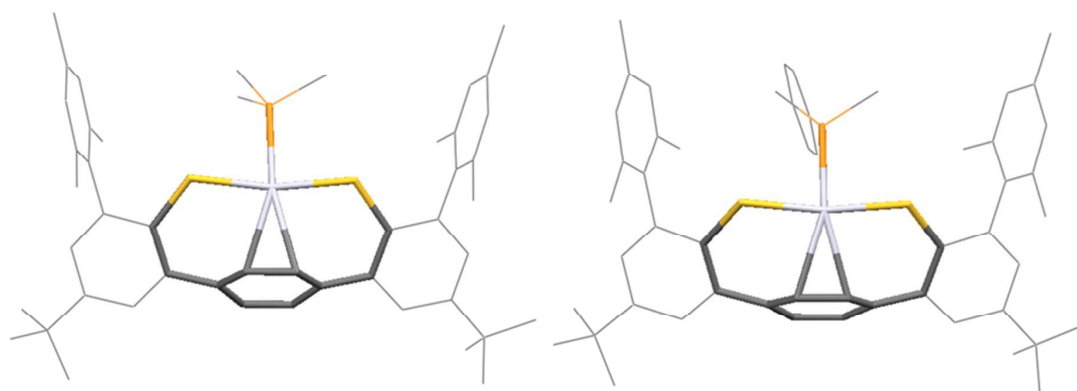


Figure S3. DFT-optimized structures of [C-PMe₃]⁺ (*left*) and [C-PMe₂Ph]⁺ (*right*).

4 Cyclic Voltammetry Data

For a collection of redox potentials of A/B-L in tabular form see Table S5 on page S19.

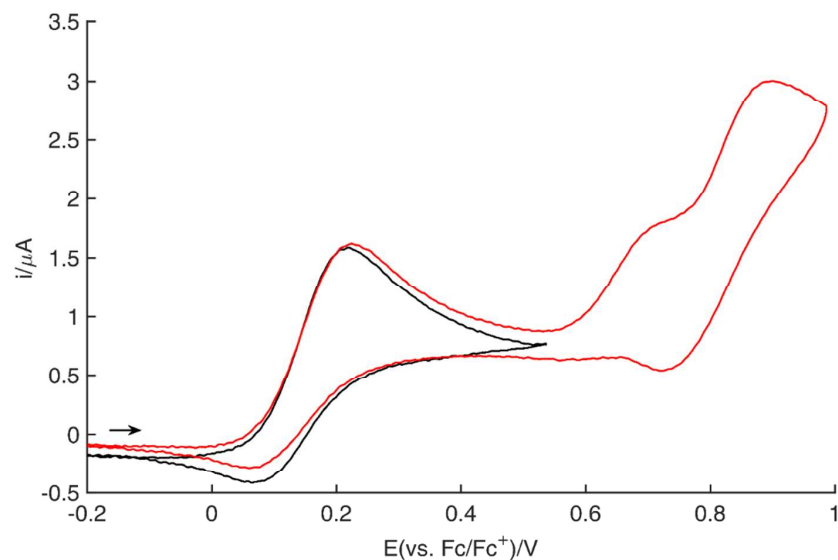


Figure S4. CV (0.1 M *n*Bu₄NPF₆/CH₂Cl₂, 50 mVs⁻¹, 290 K): 144 μM B-P(OMe)₃ (black, potential sweep direction reversed at 0.538 V).

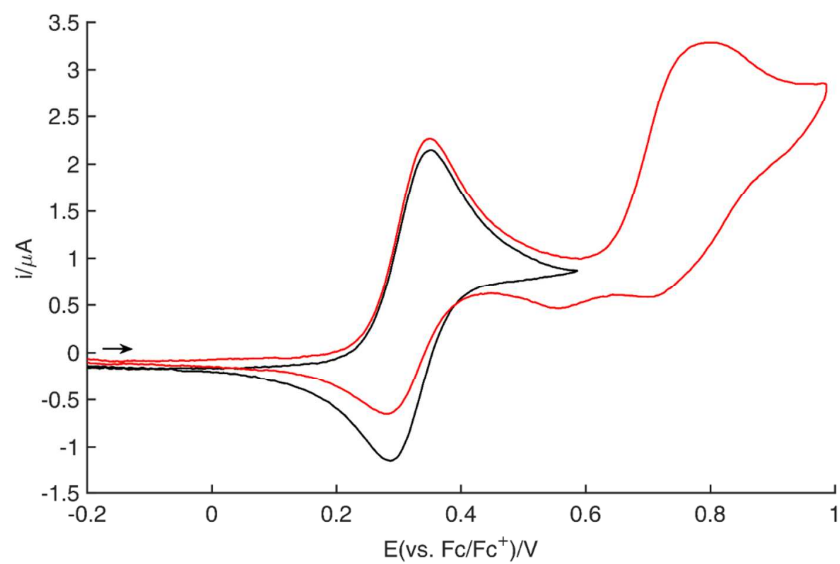


Figure S5. CV (0.1 M $n\text{Bu}_4\text{NPF}_6/\text{CH}_2\text{Cl}_2$, 50 mVs^{-1} , 290 K): $157 \mu\text{M}$ **B-CN^tBu**, (black, potential sweep direction reversed at 0.588 V).

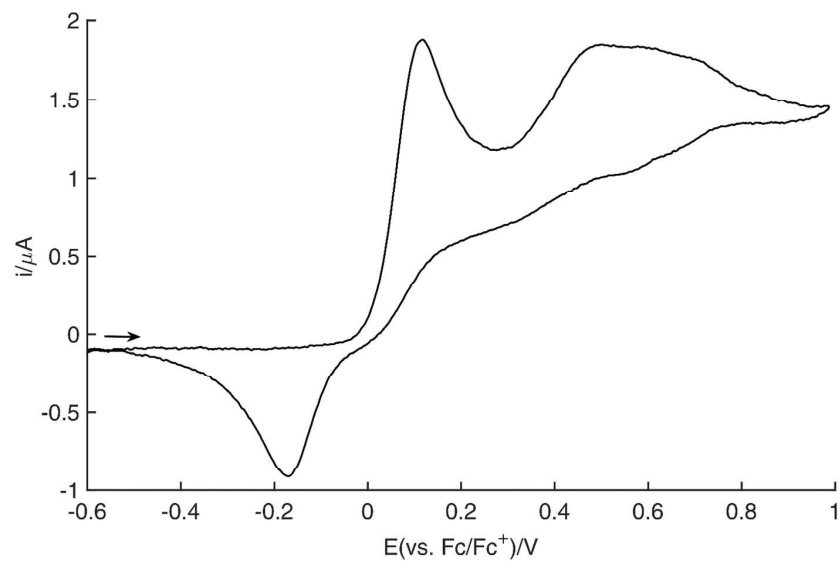


Figure S6. CV (0.1 M $n\text{Bu}_4\text{NPF}_6/\text{CH}_2\text{Cl}_2$, 50 mV s^{-1} , 290 K): $129 \mu\text{M}$ **A-PMe₃**.

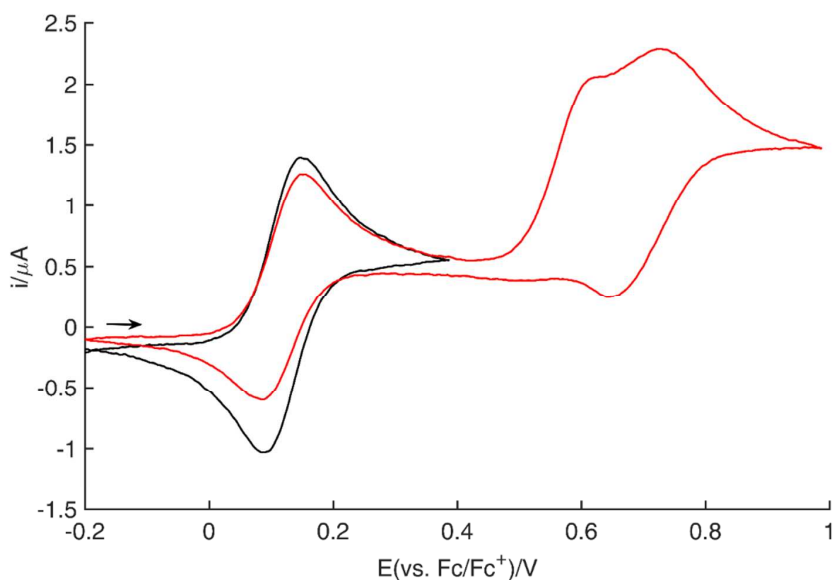


Figure S7. CV (0.1 M $n\text{Bu}_4\text{NPF}_6/\text{CH}_2\text{Cl}_2$, 50 mVs^{-1} , 290 K): 126 μM **B**-PMe₂Ph (black, potential sweep direction reversed at 0.388 V).

5 EPR Data

All samples were recorded at a concentration of 2 mM in a toluene/ CH_2Cl_2 (1:1) solution at 110 K.

All radical cationic complexes were generated *in situ* for EPR measurements. For that, 4 mM stock solutions of the neutral complexes in toluene and a 4 mM stock solution of $[\text{Fc}^{\bullet\bullet}]\text{NTf}_2$ in CH_2Cl_2 were prepared. These solutions were precooled at -80°C (dry ice/acetone). To 1.1 mL of neutral complex solution 1.1 mL of $[\text{Fc}^{\bullet\bullet}]\text{NTf}_2$ was transferred by cannula. The instantaneously formed dark solution was cannula-transferred into an EPR tube precooled at $T = -80^\circ\text{C}$ (dry ice/acetone).

For temperature sensitive samples, 250 μL of neutral complex stock solution was transferred into a precooled ($T = -80^\circ\text{C}$; dry ice/acetone) NMR tube, and 250 μL of precooled $[\text{Fc}^{\bullet\bullet}]\text{NTf}_2$ solution were added slowly. The sample tube was agitated carefully to mix the two phases.

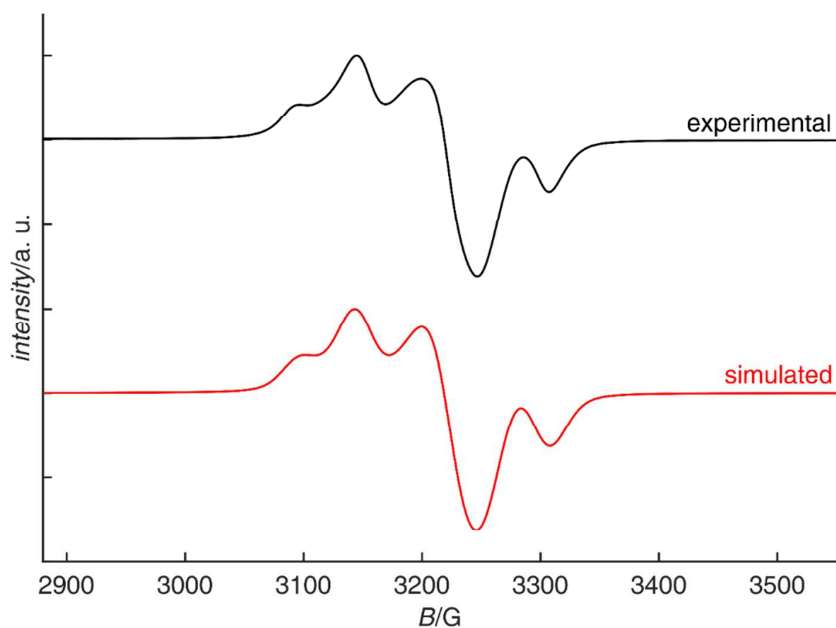


Figure S8. X-Band cw-EPR spectra (1:1 C₇H₈/CH₂Cl₂, 110 K): [B-PMe₂Ph]⁺⁺, microwave frequency = 9.318885 GHz, microwave power = 7.962 mW, modulation amplitude = 9.81 G. Simulated parameters: $g_x = 2.116$, $g_y = 2.067$, $g_z = 2.047$, $A_x = 288$; $A_y = 449$, $A_z = 293$ MHz; full line width at half maximum $lw = [0.098; 1.432]$ mT. $gStrain = [0.0176; 0.019; 0.0204]$.

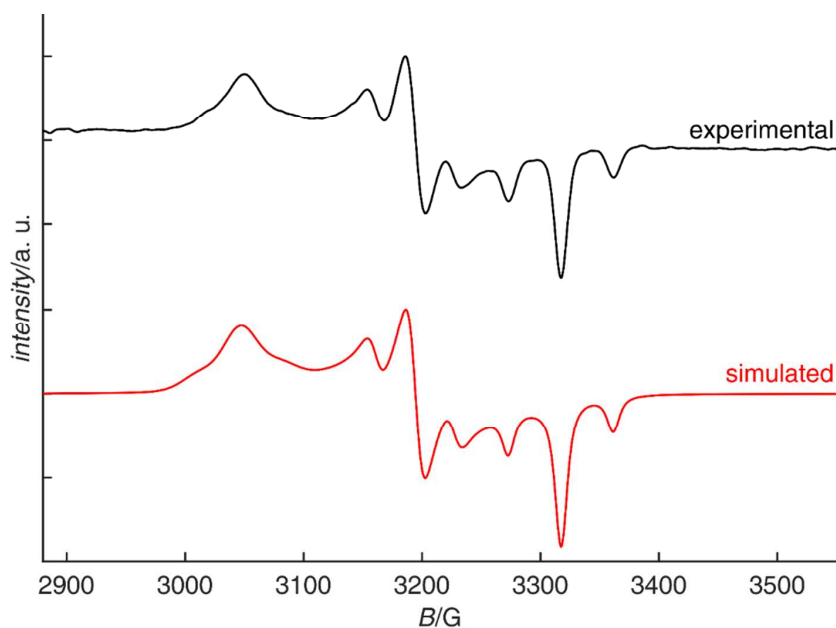


Figure S9. X-Band cw-EPR spectra (1:1 C₇H₈/CH₂Cl₂, 110 K): [C-PMe₂Ph]⁺⁺, microwave frequency = 9.318652 GHz, microwave power = 7.962 mW, modulation amplitude = 9.81 G. Simulated parameters: $g_x = 2.186$, $g_y = 2.084$, $g_z = 2.007$, $A_x = 210$; $A_y = 192$, $A_z = 249$ MHz; full line width at half maximum $lw = [0.479, 1.011]$ mT. $gStrain = [0.0209 0.0057 0.001]$

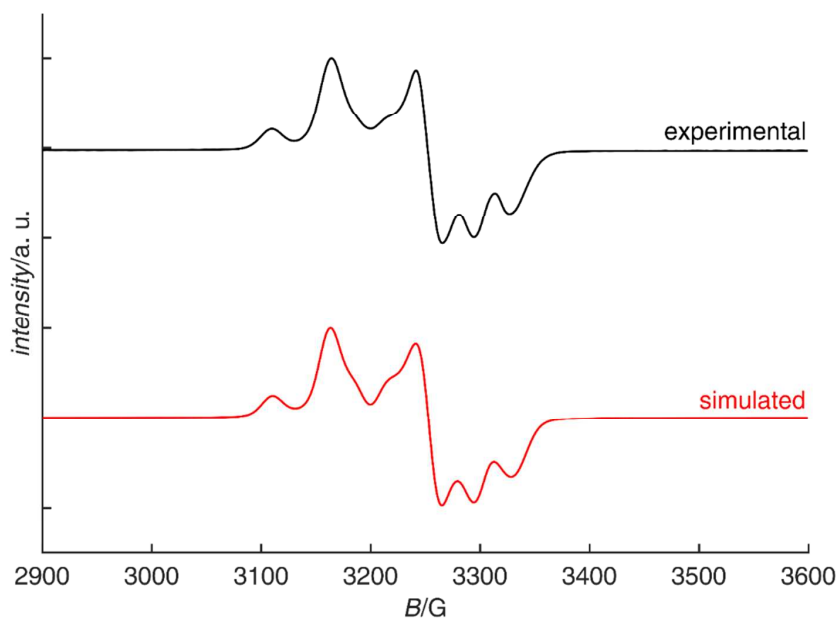


Figure S10. X-Band cw-EPR spectra (1:1 C₇H₈/CH₂Cl₂, 110 K): [B-P(OMe)₃]⁺⁺, microwave frequency = 9.305916 GHz, microwave power = 2 mW, modulation amplitude = 6.002 G. Simulated parameters: $g_x = 2.103$, $g_y = 2.044$, $g_z = 2.016$, $A_x = 305$; $A_y = 343$, $A_z = 202$ MHz; full line width at half maximum $lw = [1.822; 0.712]$ mT. $gStrain = [0.0031; 0.0004; 0.0087]$.

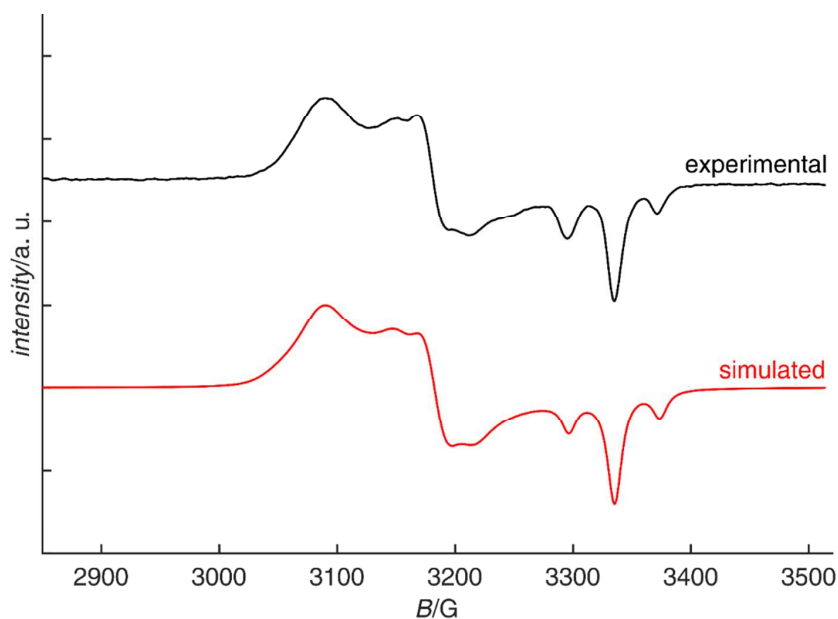


Figure S11. X-Band cw-EPR spectra (1:1 C₇H₈/CH₂Cl₂, 110 K): [B-CN^tBu]⁺⁺, microwave frequency = 9.288811 GHz, microwave power = 1.262 mW, modulation amplitude = 1.001 G. Simulated parameters: $g_x = 2.149$, $g_y = 2.085$, $g_z = 1.989$, $A_x = 181$; $A_y = 148$, $A_z = 215$ MHz; full line width at half maximum $lw = [0.373; 1.355]$ mT. $gStrain = [0.0226; 0.0118; 0.0004]$.

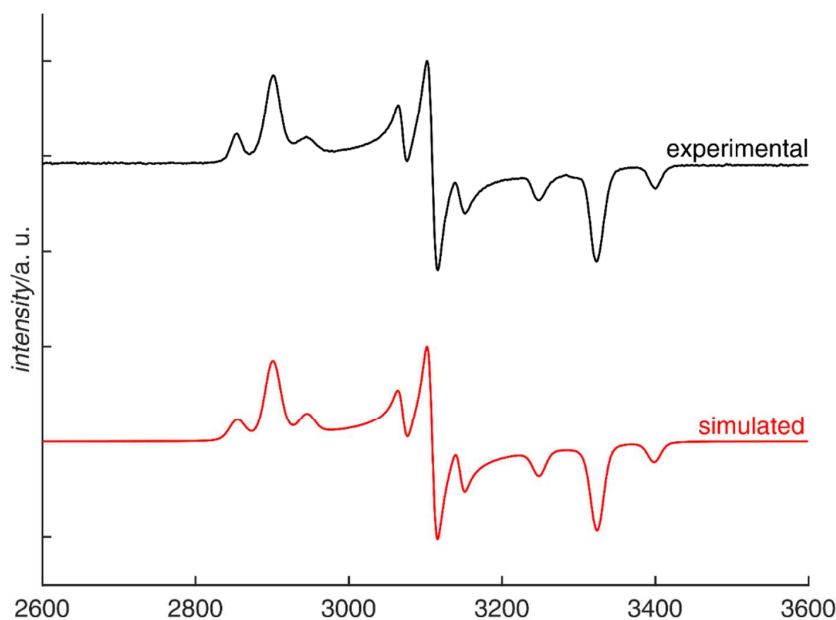


Figure S12. X-Band cw-EPR spectra (1:1 C_7H_8/CH_2Cl_2 , 110 K): $[A-PMe_3]^{+}$, microwave frequency = 9.28722 GHz, microwave power = 3.17 mW, modulation amplitude = 2.007 G. Simulated parameters: $g_x = 2.288$, $g_y = 2.134$, $g_z = 1.996$, $A_x = 291$; $A_y = 223$, $A_z = 420$ MHz; full line width at half maximum $lw = [0.926; 0.6707]$ mT. $gStrain = [0.0143; 0.000032; 0.0081]$.

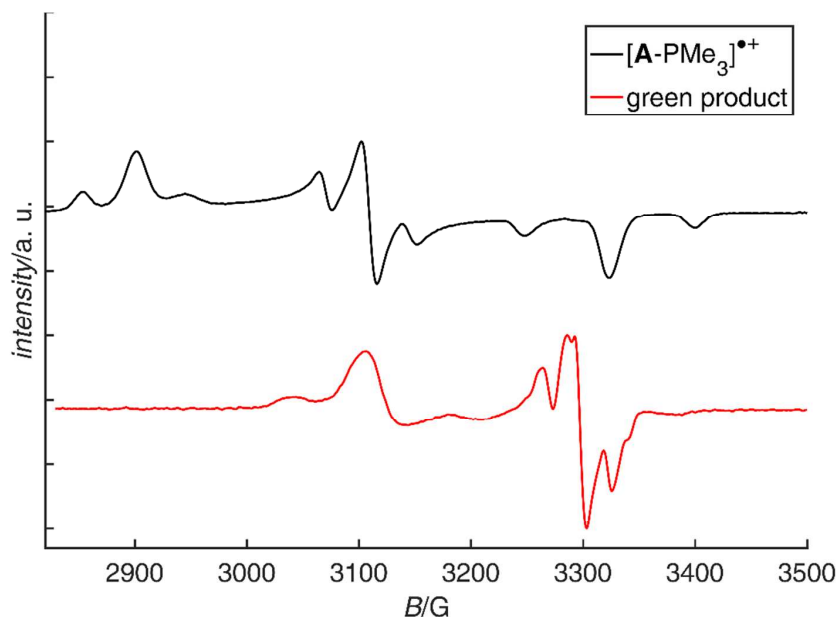


Figure S13. X-Band cw-EPR spectra (1:1 C_7H_8/CH_2Cl_2 , 110 K): Green product (red trace) formed from $[A-PMe_3]^{+}$ (black trace) after warming to $T \leq 233$ K; microwave frequency = 9.28722 GHz, microwave power = 3.17 mW, modulation amplitude = 2.007 G. Green product, microwave frequency = 9.287045 GHz, microwave power = 2.00 mW, modulation amplitude = 2.007 G.

6 Additional UV/vis/NIR Data

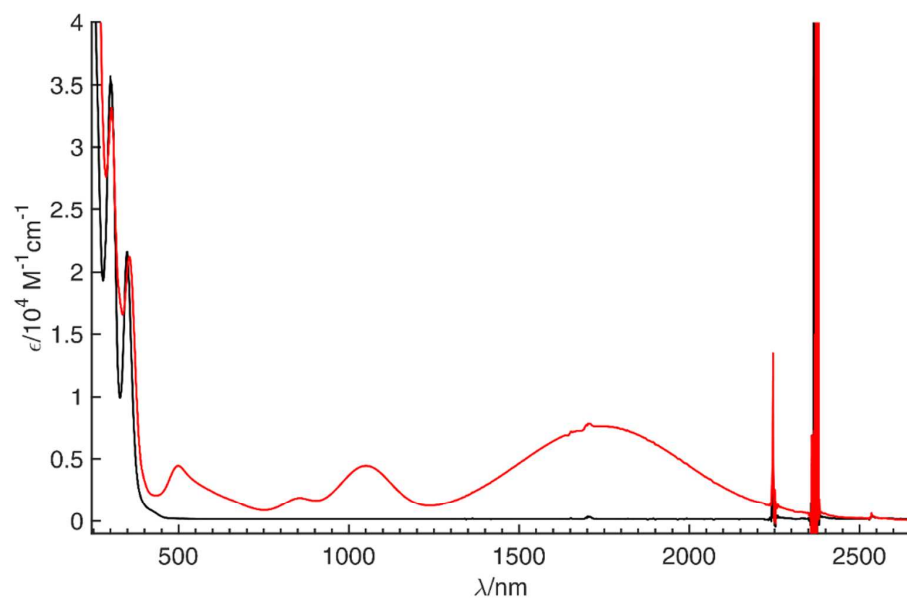


Figure S14. VT UV/vis/NIR spectra (-90°C , CH_2Cl_2): 124 μM A-PMe₃ (black), and 93 μM [A-PMe₃]⁺ (red).

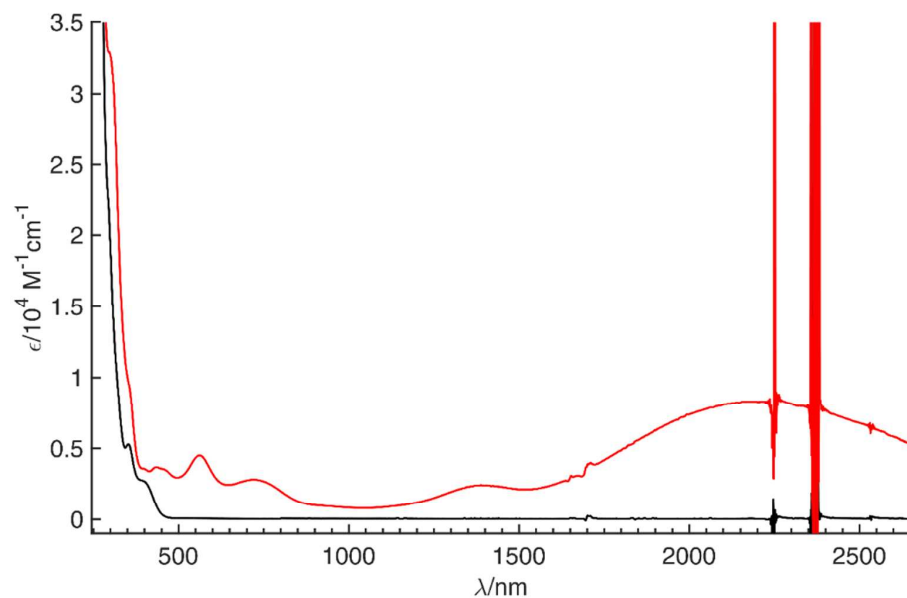


Figure S15. VT UV/vis/NIR spectra (-90°C , CH_2Cl_2): 130 μM B-CN^tBu (black) and 94 μM [B-CN^tBu]⁺ (red).

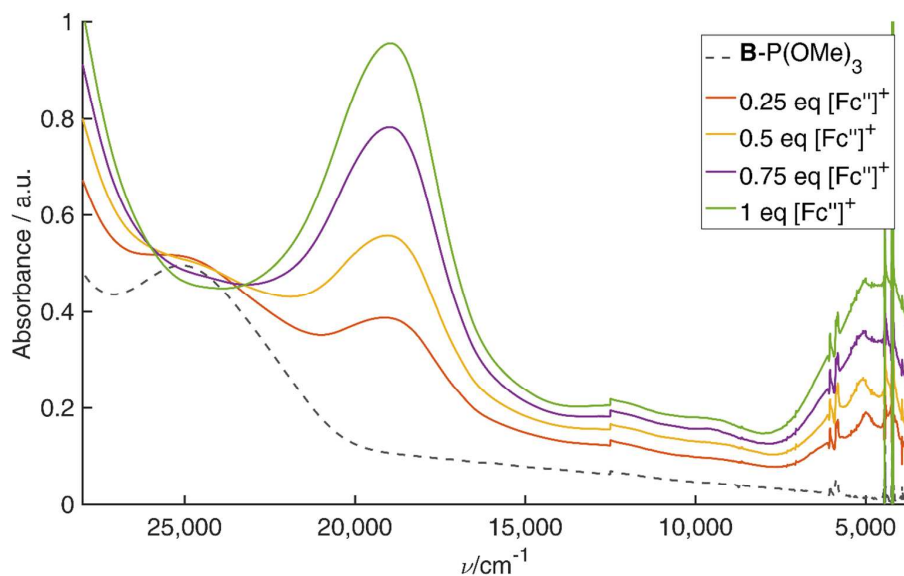


Figure S16. VT UV/vis/NIR spectra (-90°C , CH_2Cl_2): Conversion of $\mathbf{B-P(OMe)_3}$ ($131\ \mu\text{M}$; dashed) into $[\mathbf{B-P(OMe)_3}]^{++}$ through stepwise addition (series of solid lines) of $[\text{Fc}''']^+$.

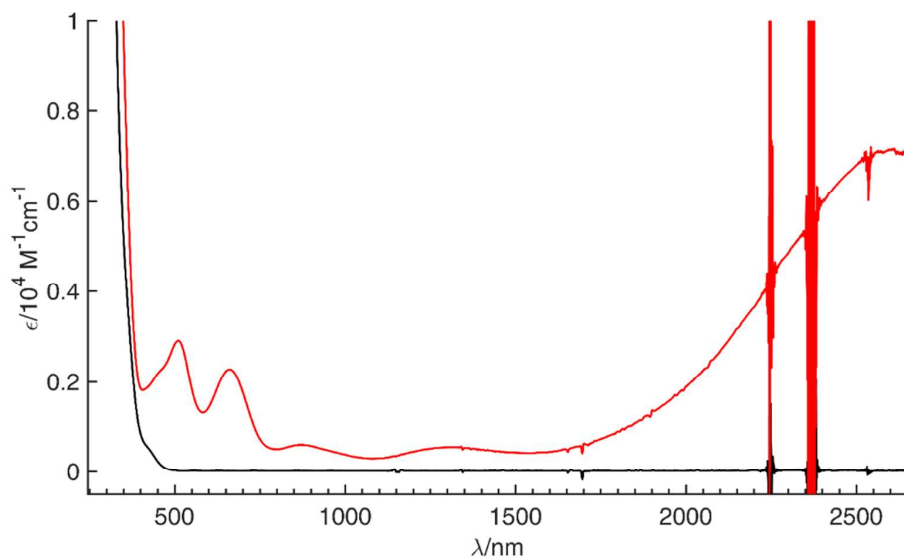


Figure S17. VT UV/vis/NIR spectra (-80°C , CH_2Cl_2): $131\ \mu\text{M}$ $\mathbf{B-PMe_2Ph}$ (black) and $125\ \mu\text{M}$ $[\mathbf{B-PMe_2Ph}]^{++}$ (red).

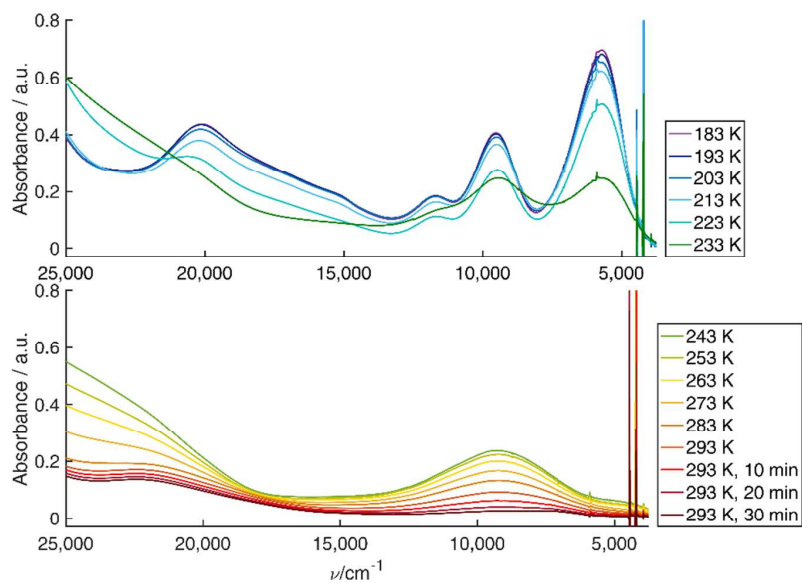


Figure S18. VT UV/vis/NIR spectra (-90°C to 20°C , CH_2Cl_2): Conversion of $[\text{A-PMe}_3]^{++}$ into green product.

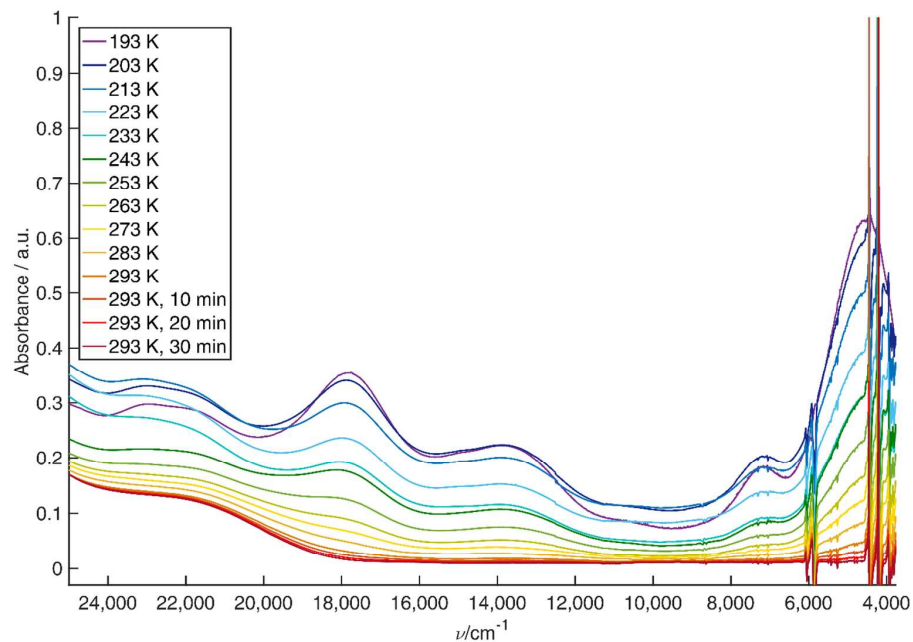


Figure S19. VT UV/vis/NIR spectra (-80°C to 20°C , CH_2Cl_2): Deterioration of a sample of $[\text{B-CN}^t\text{Bu}]^{++}$.

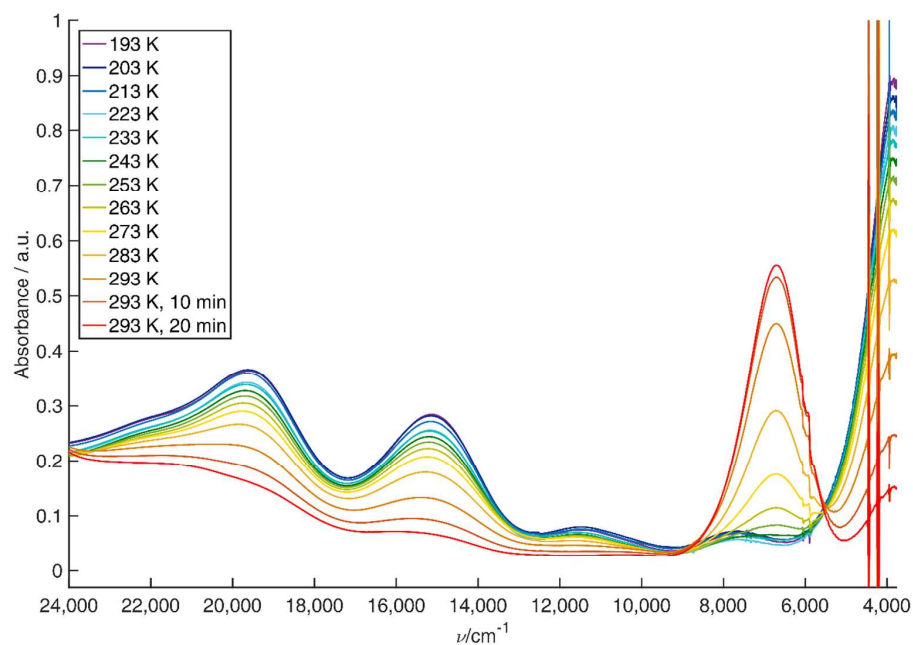


Figure S20. VT UV/vis/NIR spectra (-80 to 20°C , CH_2Cl_2): Conversion of $[\mathbf{B}\text{-PMe}_2\text{Ph}]^{++}$ into $[\mathbf{C}\text{-PMe}_2\text{Ph}]^{++}$.

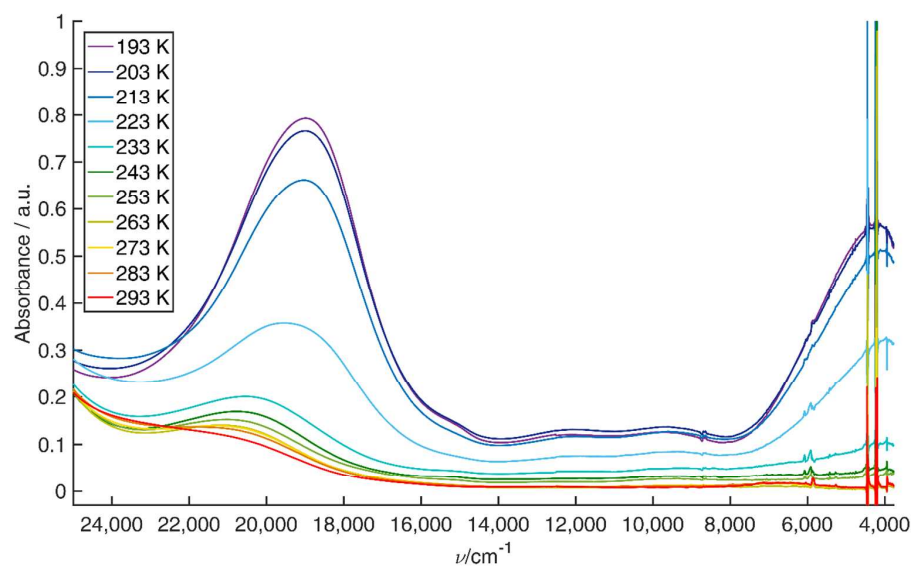


Figure S21. VT UV/vis/NIR spectra (-80°C to 20°C , CH_2Cl_2): Deterioration of a sample of $[\mathbf{B}\text{-P}(\text{OMe})_3]^{++}$.

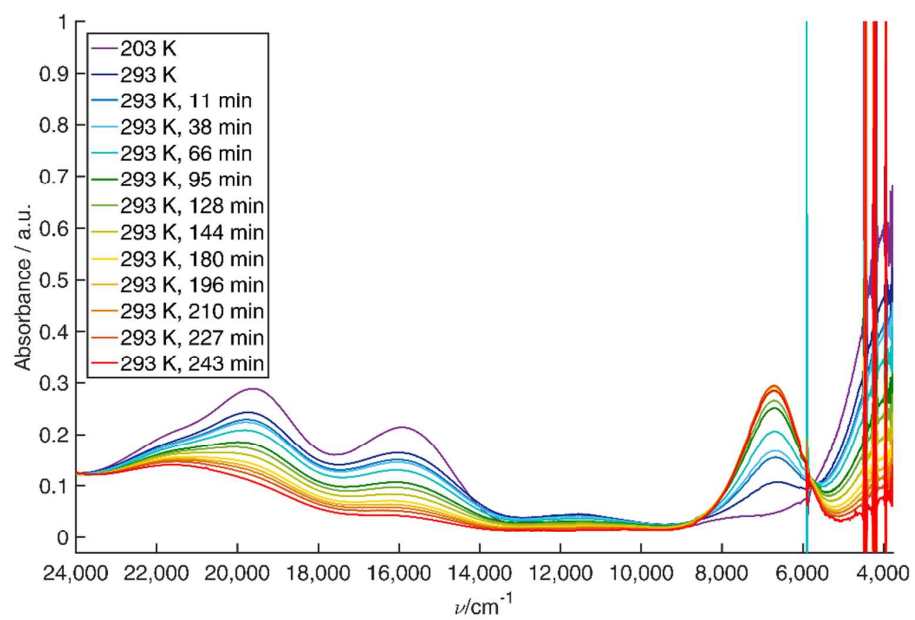


Figure S22. VT UV/vis/NIR spectra (-80°C to 20°C , CH_2Cl_2): Conversion of $[\mathbf{B-PMe}_3]^{++}$ into $[\mathbf{C-PMe}_3]^{++}$.

Table S3. Characteristic UV/vis/NIR transitions of complex radical-cations in CH₂Cl₂ solution.

chromophore	$\lambda^{\text{NIR}}/\text{nm}$	$\nu^{\text{NIR}}/\text{cm}^{-1}$	$\epsilon^{\text{NIR}}/\text{M}^{-1} \text{cm}^{-1}$	T/K
[A-PMe ₃] ⁺⁺	1754	5700	8000	183
[B-PMe ₃] ⁺⁺	2500	4000	5500	203
[C-PMe ₃] ⁺⁺	1502	6660	4000	293
[B-PMe ₂ Ph] ⁺⁺	2605	3840	7200	193
[C-PMe ₂ Ph] ⁺⁺	1493	6700	10000	273
[B-P(OMe) ₃] ⁺⁺	2330	4290	6000	193
[B-CN ^t Bu] ⁺⁺	2190	4570	8000	183

Table S4. Potentials of first redox events starting from neutral A/B-L.^a

	E^0/mV	$E_{\text{p,ox}}-E_{\text{p,red}}/\text{mV}^d$	$E_{\text{p,red}}/\text{mV}^e$	$E_{\text{p,ox}}/\text{mV}^e$
B-PMe ₂ Ph	121	78	-	-
B-P(OMe) ₃ ^b	-	-	43	253
B-CN ^t Bu	318	74	-	-
A-PMe ₃ ^c	-	-	-	231

^a Pt-disc working electrode, 0.1 M nBu₄NPF₆/CH₂Cl₂, 17°C, E vs. ferrocene/[ferrocene]⁺. ^b

Electrochemically quasireversible. ^c Chemically irreversible. ^d $20 \leq \nu \leq 2000 \text{ mV s}^{-1}$. ^e $\nu = 200 \text{ mV s}^{-1}$.

Table S5. Characteristic IR and Raman spectroscopic data of [B-CN^tBu]^{0/+}.

Local symmetry at Pt: D_{2h}	Solid state Raman (linear Raman microscope) $\nu_{\text{C}\equiv\text{N}}/\text{cm}^{-1}$	Solid state IR (ATR/KBr pellet) $\nu_{\text{C}\equiv\text{N}}/\text{cm}^{-1}$	Solution IR (Si dip probe) $\nu_{\text{C}\equiv\text{N}}/\text{cm}^{-1}$
B-CN ^t Bu	2230 (A ₁)	2197 (B _{3u})	2212
[B-CN ^t Bu] ⁺⁺	<i>not determined</i>	<i>not determined</i>	2225

7 Additional Computational Data

Table S6. Summary of experimental and computed vis/NIR transition energies and intensities.^a

transition	exp.		TD-DFT	
	λ / nm	ε [$M^{-1} \text{ cm}^{-1}$]	λ / nm	f_{osc}
[A-PMe_3]^{•+}				
1	497	4400	469	0.060 (P \rightarrow [S-Pt-S] CT)
2	650	1800	660	0.014 (Mes \rightarrow [S-Pt-S] CT)
3	856	1900	732	0.012 (Mes \rightarrow [S-Pt-S] CT)
4	1056	4300	1044	0.059 (CR)
5	1754	7500	1570	0.102 (CR)
[B-PMe_2Ph]^{•+}				
1	449	2200	-	-
2	519	2800	-	-
3	663	2300	-	-
4	872	600	-	-
5	1300	500	-	-
6	2600	7200	-	-
[B-$\text{P}(\text{OMe})_3$]^{•+b}				
1	527	8300	478/548	0.120/0.073
2	833	1200	817/792	0.005/0.022
3	1040	1300	1085/1221	0.002/0.004
4	2330	5600	1542/1983	0.065/0.128
5	1754	7500	1570	0.102
[B-CN^tBu]^{•+}				
1	445	3700	454	0.041
2	460	3500	475	0.077
3	561	4400	518	0.013
4	750	3000	832	0.019
5	2330	5600	1996	0.191

^a Computed at ZORA-BLYP35-D3/TZVP level of theory; ^b Computed data correspond to the structures of global minimum/local minimum.

Table S7. Energies and compositions (%) of frontier spin-down molecular orbitals.^a

MO	<i>E</i> (eV)	Pt	S1	S2	P1	P2
[A-PMe₃]^{•+}						
unoccupied						
β-LUMO	-3.1848	31.9	9.2	9.2	7.0	7.0
β-SOMO	-6.2377	24.4	28.4	28.4	0.0	0.0
occupied						
β-HOMO	-8.1959	3.7	24.7	24.7	1.7	1.7
β-HOMO-1	-8.6365	0.9	3.6	3.6	0.0	0.0
β-HOMO-1	-8.7201	1.0	0.4	0.4	0.0	0.0
[B-PMe₃]^{•+}						
unoccupied						
β-LUMO	-3.0560	41.3	10.4	10.4	9.0	9.0
β-SOMO	-6.4871	15.0	24.5	24.5	0.2	0.2
occupied						
β-HOMO	-7.8254	2.5	22.8	22.8	2.4	2.4
β-HOMO-1	-8.6855	1.2	4.0	4.0	0.0	0.0
β-HOMO-1	-8.8046	1.2	0.6	0.6	0.1	0.1

^a Computed at ZORA-BLYP35-D3/TZVP level of theory.

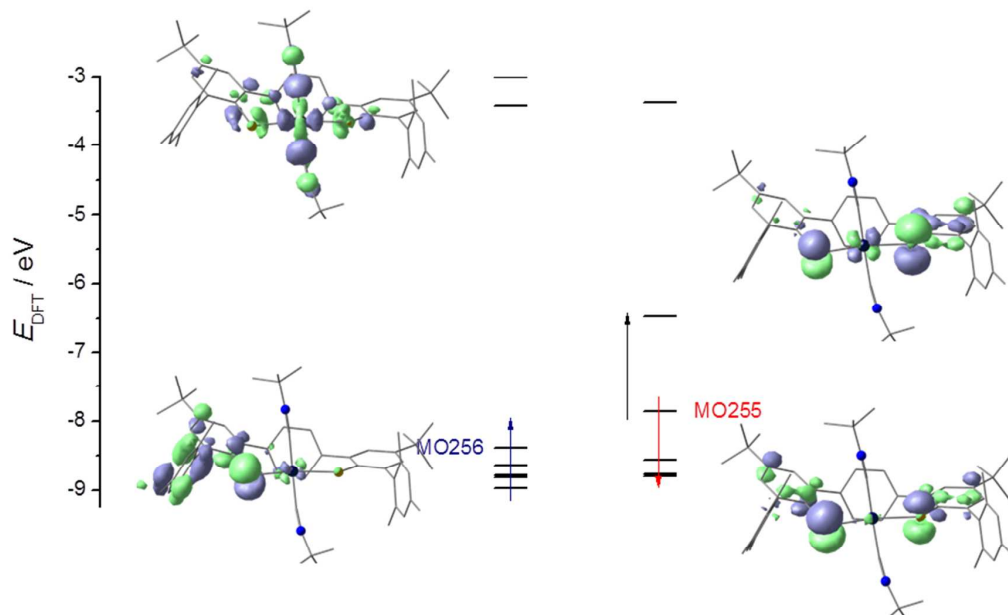


Figure S23. Kohn-Sham MOs and energy diagram for $[\mathbf{B}\text{-CN}^t\text{Bu}]^{\bullet+}$ from spin-unrestricted ZORA-BLYP35-D3/TZVP DFT calculations.

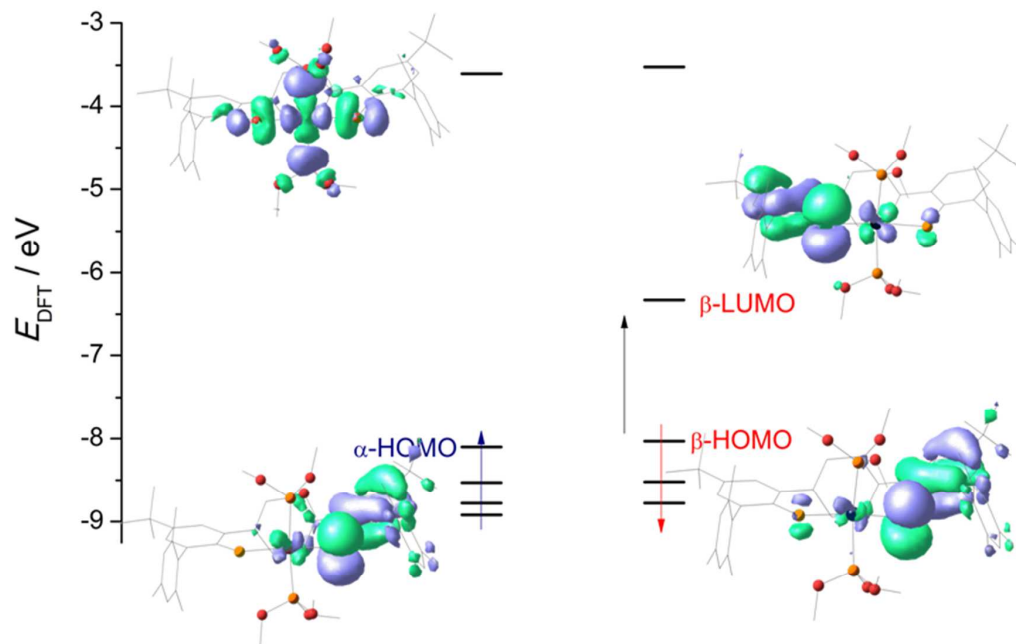


Figure S24. Kohn-Sham MOs and energy diagram for optimized $[\mathbf{B}\text{-P(OMe)}_3]^{\bullet+}$ from spin-unrestricted ZORA-BLYP35-D3/TZVP DFT calculations.

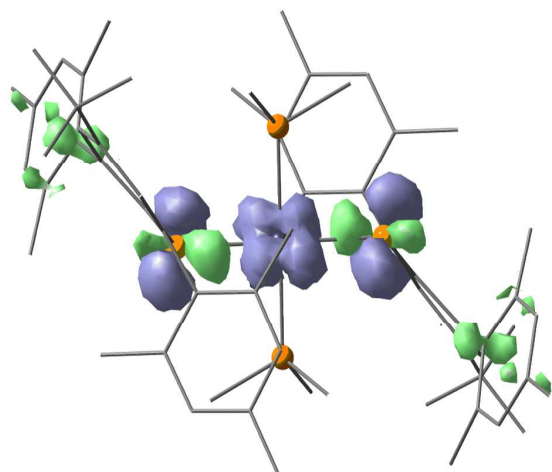


Figure S25. TD-DFT derived nature of the second NIR transition at $\nu = 9570 \text{ cm}^{-1}$ in $[\text{A-PMe}_3]^{\bullet+}$ (blue: sink; green: source).

7.1 Cartesian coordinates of DFT-optimized structures (ZORA-BP86-D3/TZVP)

A-PMe₃

151 atoms

Pt	7.966833	7.301511	6.368565	H	6.767281	4.451159	14.116646
S	9.073427	5.822543	7.868842	H	5.101334	4.735957	14.686747
P	6.188889	5.805302	6.192125	H	5.995454	6.030168	13.853004
C	7.786888	4.062052	9.605982	C	8.410247	2.91606	8.880235
C	9.175398	8.161094	10.760743	C	7.95209	7.860701	10.118268
C	8.04413	5.420791	9.275922	C	6.91221	3.763631	10.663997
C	7.100915	8.914512	9.721728	H	6.74223	2.711735	10.889766
C	6.609129	6.080764	11.129339	C	5.821874	8.646824	8.981539
H	6.204887	6.889764	11.741639	H	5.215972	9.55753	8.889821
C	6.267748	4.750582	11.412003	H	5.224387	7.863461	9.465325
C	9.815885	2.73469	8.903879	H	6.070699	8.297253	7.963081
C	7.508328	6.43178	10.11634	C	7.479833	10.237485	9.982561
C	10.383905	1.671574	8.196582	H	6.80857	11.043856	9.674137
H	11.471075	1.550049	8.218174	C	9.527504	9.499036	10.982187
C	5.262799	4.436658	12.525675	H	10.476027	9.717177	11.480586
C	10.715652	3.639759	9.704558	C	6.096961	1.999335	8.250331
H	11.671947	3.143444	9.918306	H	5.679055	1.554215	7.33692
H	10.250212	3.929774	10.655244	H	5.710143	3.017701	8.355341
H	10.928407	4.568967	9.1526	H	5.705679	1.419876	9.101925
C	7.606267	1.958937	8.217947	C	5.103418	5.542844	7.66471
C	10.091817	7.059096	11.219407	H	4.419636	4.707788	7.459954
H	10.962845	7.465734	11.750379	H	4.516498	6.452517	7.834164
H	10.446214	6.472345	10.359187	H	5.695758	5.331674	8.559195
H	9.569193	6.357892	11.887511	C	8.22008	0.916952	7.508229
C	5.815367	4.946374	13.87538	H	7.587468	0.204902	6.970326

C	8.690561	10.554774	10.60843	H	5.480903	8.137614	2.375798
C	3.929982	5.151854	12.213243	H	6.362693	8.2589	0.850797
H	4.061704	6.241213	12.152319	C	10.112592	9.666833	-1.138718
H	3.187655	4.941886	12.999043	H	9.160221	10.161639	-1.379032
H	3.521125	4.806984	11.251696	H	10.826126	9.87867	-1.950147
C	6.785791	4.130903	5.74966	H	9.933297	8.582878	-1.117586
H	5.947174	3.425078	5.685083	C	7.522634	11.689873	3.863226
H	7.51484	3.801822	6.498245	C	7.976152	6.748009	2.614439
H	7.288959	4.201351	4.778645	C	9.018135	10.845231	2.075984
C	4.912223	6.150022	4.912331	H	9.188076	11.8975	1.851936
H	5.387731	6.173493	3.927798	C	10.10447	5.957066	3.751125
H	4.449597	7.126069	5.100483	H	10.709732	5.045686	3.840448
H	4.148859	5.358653	4.942466	H	10.702337	6.741158	3.269022
C	10.2495	-0.368714	6.706183	H	9.856238	6.304497	4.770561
H	10.664902	-1.12657	7.389816	C	8.443324	4.370245	2.749168
H	11.078988	-0.008539	6.079195	H	9.112983	3.562361	3.057163
H	9.523645	-0.872789	6.052923	C	6.397849	5.113481	1.748614
C	9.607075	0.761943	7.46997	H	5.449129	4.897568	1.249625
C	9.096159	11.990433	10.824212	C	9.837042	12.605236	4.491063
H	9.843848	12.080452	11.624739	H	10.25642	13.049407	5.404264
H	8.232256	12.617726	11.086614	H	10.223626	11.586939	4.384402
H	9.538886	12.41545	9.907916	H	10.227045	13.185539	3.63946
C	4.988263	2.929295	12.647721	C	10.829088	9.059357	5.070493
H	4.585833	2.514178	11.711475	H	11.514142	9.893447	5.274954
H	4.246437	2.75024	13.440223	H	11.414709	8.149213	4.899034
H	5.897867	2.368951	12.910965	H	10.23544	9.272148	4.177239
S	6.859347	8.781053	4.869455	C	7.715239	13.686454	5.238569
P	9.745578	8.796627	6.544442	H	8.348785	14.397458	5.776758
C	8.144714	10.545068	3.134574	C	7.232115	4.055802	2.122806
C	6.752598	6.45057	1.971071	C	11.998818	9.460744	0.522376
C	7.887365	9.185765	3.462191	H	11.867673	8.371253	0.58222
C	8.825032	5.692296	3.010613	H	12.740705	9.671995	-0.263497
C	9.319832	8.528932	1.605605	H	12.407864	9.804812	1.484135
H	9.72297	7.72101	0.99115	C	9.150402	10.470803	6.989277
C	9.661373	9.859591	1.325238	H	9.989359	11.176277	7.05299
C	6.116991	11.871519	3.842058	H	8.420194	10.80081	6.242218
C	8.421626	8.17636	2.618883	H	8.648535	10.399906	7.960909
C	5.550238	12.933367	4.55225	C	11.023739	8.450221	7.822436
H	4.463056	13.055119	4.532532	H	10.549247	8.426956	8.807445
C	10.665404	10.17544	0.211289	H	11.485543	7.473967	7.633419
C	5.215872	10.968287	3.040825	H	11.787568	9.241115	7.791566
H	4.259563	11.465442	2.82907	C	5.687191	14.970638	6.046483
H	5.680093	10.679815	2.089069	H	5.268241	15.728516	5.365052
H	5.003374	10.038158	3.591324	H	4.860452	14.608808	6.676175
C	8.3278	12.645727	4.525925	H	6.414727	15.475092	6.697564
C	5.837968	7.554703	1.514015	C	6.328325	13.841505	5.279386
H	4.968462	7.150519	0.978674	C	6.823672	2.621051	1.906248

H	6.070704	2.533757	1.110393	H	11.342037	12.097464	1.026937
H	7.685181	1.993453	1.636629	H	11.679672	11.863553	-0.702415
H	6.386579	2.194224	2.824381	H	10.028544	12.243131	-0.170893
C	10.938828	11.683116	0.090687				

[A-PMe₃]^{•+}:

151 atoms

Pt	7.963773	7.305801	6.37035	C	6.10432	2.029723	8.209778
S	9.043665	5.847497	7.800767	H	5.645856	1.606257	7.30611
P	6.069406	5.884758	6.278398	H	5.694074	3.03087	8.378115
C	7.824252	4.083288	9.550657	H	5.779499	1.405615	9.057107
C	9.276541	8.178287	10.658638	C	5.049591	5.607689	7.78823
C	8.05558	5.446698	9.238227	H	4.347725	4.788301	7.583073
C	7.156086	8.947861	9.721685	H	4.482268	6.51812	8.008947
C	6.720768	6.096772	11.148161	H	5.672589	5.35766	8.650609
H	6.349977	6.894842	11.793519	C	8.211442	1.039997	7.305602
C	6.390691	4.76132	11.427231	H	7.56995	0.33643	6.768004
C	9.838427	2.81154	8.727649	C	8.802806	10.576554	10.522334
C	7.564858	6.46342	10.095515	C	4.093119	5.152884	12.327561
C	10.392284	1.799585	7.938122	H	4.217971	6.243465	12.272996
H	11.479995	1.687765	7.917348	H	3.38783	4.934306	13.142895
C	5.438002	4.435597	12.580522	H	3.640169	4.813518	11.383732
C	10.758405	3.668775	9.560205	C	6.60583	4.225509	5.732926
H	11.684171	3.125143	9.789989	H	5.741919	3.553399	5.65385
H	10.288428	3.967193	10.505275	H	7.337209	3.81916	6.440592
H	11.040937	4.591482	9.028751	H	7.086383	4.32872	4.753646
C	7.609765	2.030877	8.093048	C	4.773807	6.346563	5.059513
C	10.190389	7.073225	11.121116	H	5.211524	6.365818	4.056835
H	11.081225	7.482503	11.614007	H	4.363925	7.335927	5.295538
H	10.520255	6.443903	10.282834	H	3.969941	5.59794	5.097042
H	9.677902	6.407428	11.831839	C	10.225559	-0.166547	6.356537
C	6.052008	4.940143	13.906076	H	10.650147	-0.961018	6.990146
H	7.016539	4.449801	14.101771	H	11.046645	0.228168	5.740289
H	5.376707	4.714833	14.744506	H	9.48915	-0.633468	5.688746
H	6.219705	6.025983	13.890245	C	9.599508	0.91604	7.196963
C	8.429225	2.968798	8.764597	C	9.224757	12.00404	10.752505
C	8.018129	7.888656	10.074598	H	9.537088	12.164954	11.794735
C	6.993691	3.776549	10.638079	H	8.408287	12.703563	10.530092
H	6.82603	2.724148	10.860488	H	10.08127	12.272496	10.114397
C	5.823014	8.695677	9.074185	C	5.174124	2.926671	12.703913
H	5.219649	9.611359	9.04147	H	4.726156	2.514475	11.787268
H	5.255857	7.91582	9.598176	H	4.471118	2.741896	13.528499
H	5.978772	8.354884	8.036982	H	6.094754	2.366381	12.924326
C	7.561353	10.268957	9.957199	S	6.885106	8.763784	4.938603
H	6.881955	11.081129	9.686475	P	9.857496	8.727408	6.462508
C	9.650021	9.512212	10.85509	C	8.105739	10.5239	3.185967
H	10.618736	9.722923	11.315622	C	6.655323	6.425572	2.085999

C	7.874262	9.161045	3.500993	H	10.281282	13.003281	5.429768
C	8.777065	5.659191	3.022724	H	10.234148	11.578195	4.358378
C	9.210656	8.507452	1.59344	H	10.150388	13.203173	3.678469
H	9.581967	7.708152	0.949912	C	10.878476	9.003504	4.953266
C	9.540873	9.842332	1.311959	H	11.579765	9.823424	5.158277
C	6.090564	11.79792	4.003096	H	11.446415	8.093093	4.734071
C	8.365873	8.142674	2.646226	H	10.256201	9.252338	4.090027
C	5.535725	12.812219	4.788904	C	7.715736	13.572331	5.42366
H	4.448033	12.924625	4.807326	H	8.35658	14.277006	5.960579
C	10.49401	10.165779	0.158397	C	7.132458	4.028007	2.222849
C	5.171704	10.938782	3.171276	C	11.838232	9.447525	0.411995
H	4.246123	11.481752	2.939217	H	11.712503	8.357105	0.467712
H	5.642829	10.63834	2.227421	H	12.543604	9.664594	-0.403666
H	4.888667	10.01721	3.704439	H	12.291615	9.787511	1.355392
C	8.3184	12.579134	4.639873	C	9.320049	10.387136	7.006099
C	5.740654	7.529224	1.621698	H	10.183877	11.05929	7.085822
H	4.848227	7.118423	1.132971	H	8.589735	10.792827	6.296936
H	5.413651	8.162568	2.457996	H	8.83827	10.284649	7.984907
H	6.251602	8.191506	0.906545	C	11.152252	8.266692	7.682605
C	9.879335	9.660309	-1.166523	H	10.713756	8.247001	8.684943
H	8.91528	10.151405	-1.362661	H	11.562885	7.277576	7.446767
H	10.554765	9.883957	-2.005298	H	11.955745	9.015751	7.645807
H	9.71053	8.574666	-1.14931	C	5.700416	14.782622	6.365394
C	7.499788	11.639962	3.96912	H	5.277015	15.575259	5.728694
C	7.913537	6.717161	2.669482	H	4.878283	14.389941	6.981542
C	8.93722	10.828658	2.098739	H	6.435881	15.251384	7.032938
H	9.105119	11.880651	1.874559	C	6.327543	13.69736	5.529217
C	10.11007	5.913269	3.669674	C	6.712445	2.599879	1.993175
H	10.71479	4.998457	3.701845	H	6.399401	2.438416	0.951245
H	10.675819	6.694033	3.145533	H	7.530176	1.901622	2.214918
H	9.95446	6.253585	4.707028	H	5.856953	2.330208	2.632139
C	8.373575	4.337478	2.787702	C	10.759362	11.674314	0.033308
H	9.053956	3.526289	3.058894	H	11.207213	12.087171	0.94971
C	6.283601	5.091075	1.890151	H	11.46296	11.857434	-0.791146
H	5.315082	4.878858	1.429889	H	9.839394	12.23522	-0.188292
C	9.824047	12.579571	4.525599				

B-P(OMe)₃

127 atoms

Pt	6.337423	29.794081	12.224724	C	3.694184	30.503275	10.253577
S	5.968877	32.161346	12.13786	O	4.33965	30.489648	14.784068
S	6.601175	27.420272	12.324913	C	6.535948	24.816629	9.227304
P	7.594599	29.890573	10.326008	O	7.156056	28.844271	9.136595
P	5.792374	29.835581	14.440737	O	7.83281	31.314103	9.529068
O	5.664843	28.446075	15.311284	O	9.197268	29.618172	10.562761
C	7.715591	24.238491	12.414872	C	3.242014	30.534187	11.582571
O	6.886228	30.618948	15.398808	C	4.135808	28.129341	10.441918

C	3.022523	29.315288	12.243688	H	8.325744	31.144068	13.959066
C	4.115228	29.306138	9.678316	H	2.948549	31.17627	16.09639
C	3.490704	28.127093	11.689793	H	4.53964	30.82513	16.855931
C	6.088366	26.607409	10.808139	H	3.455693	29.470341	16.386108
C	8.785143	23.823271	13.216983	H	7.6894	27.729619	7.517414
C	5.47795	25.217709	8.397829	H	9.008448	28.787454	8.129253
C	4.701461	26.297311	8.833022	H	7.642895	29.500117	7.205197
C	9.312242	25.314308	10.912775	H	7.124873	32.739102	8.256929
C	10.111739	24.141621	12.903875	H	5.957226	32.235316	9.532327
C	4.968488	26.977787	10.027866	H	6.272606	31.16562	8.114765
C	7.982794	24.999138	11.257295	H	10.774067	28.954725	11.660465
C	6.852651	25.484915	10.412127	H	9.271741	27.980078	11.896354
C	10.354541	24.887498	11.74392	H	9.414979	29.594623	12.652711
C	6.298453	23.908974	12.808341	H	6.537974	26.718203	15.956364
C	11.250456	23.662446	13.769445	H	7.416841	28.218021	16.432283
C	9.603708	26.130441	9.681006	H	7.513231	27.59062	14.744282
C	4.944443	22.980631	7.383914	H	3.795329	31.441837	9.708199
C	4.001092	25.040279	6.328564	H	4.565654	29.300579	8.686102
C	5.211823	24.472092	7.085645	H	2.619426	29.326155	13.255193
C	6.455405	24.596466	6.177157	H	3.459042	27.204658	12.270098
C	1.712522	33.421536	13.52371	H	3.841683	26.628472	8.249877
C	4.126138	33.797845	13.315388	H	7.151804	23.956535	8.954127
C	2.853588	34.197113	13.748148	H	1.022264	31.603115	12.568371
C	4.285214	32.582507	12.614028	H	2.783594	35.142203	14.286702
C	-0.200564	32.709991	14.976831	H	4.757321	22.43068	6.448808
C	0.320505	33.814953	14.031069	H	4.065275	22.867064	8.035014
C	0.338209	35.143613	14.804051	H	5.799523	22.508941	7.887775
C	1.88435	32.23375	12.796152	H	6.298687	24.056959	5.230658
C	-0.641672	33.959111	12.832098	H	7.350087	24.179546	6.660313
C	3.128449	31.814477	12.319958	H	6.658483	25.651568	5.940832
C	7.932248	28.718722	7.922647	H	3.851422	24.478779	5.394836
C	3.794685	30.480896	16.125956	H	4.146897	26.097327	6.062962
C	9.684916	28.989671	11.775605	H	3.077077	24.957471	6.919995
C	7.870864	31.54529	14.874685	H	-0.285722	34.736921	12.140613
C	6.713669	31.890801	8.81518	H	-1.648547	34.238794	13.17871
C	6.870051	27.708476	15.627198	H	-0.726956	33.019707	12.268406
C	5.847415	34.666973	14.923243	H	0.675486	35.977342	14.171067
C	5.295375	34.672129	13.625956	H	0.994031	35.092995	15.685801
C	6.938825	36.317228	12.949235	H	-0.676197	35.380088	15.155913
C	5.840298	35.510503	12.631648	H	5.725304	23.51397	11.957068
C	7.514064	36.314357	14.225483	H	5.773772	24.814544	13.154094
C	6.952168	35.481413	15.200097	H	6.277222	23.169351	13.620419
C	8.682693	37.210608	14.551478	H	8.573265	23.239028	14.117257
C	5.271886	35.517463	11.235759	H	12.084856	24.378721	13.769305
C	5.273325	33.772149	15.99141	H	11.645957	22.700233	13.405921
H	8.623962	31.648118	15.665154	H	10.927859	23.511025	14.809034
H	7.412199	32.51325	14.643001	H	11.38334	25.149644	11.480239

H	10.655798	26.442218	9.649898	H	5.680677	36.350628	10.648286
H	8.972139	27.027408	9.655909	H	4.175277	35.597771	11.247996
H	9.384788	25.566282	8.761115	H	5.518269	34.577909	10.716167
H	-0.262266	31.738297	14.467775	H	7.362738	36.960291	12.172667
H	-1.205498	32.963503	15.348257	H	7.388789	35.459448	16.202851
H	0.467123	32.59607	15.843683	H	9.306602	37.394453	13.6654
H	5.111081	32.759823	15.601011	H	9.318213	36.771951	15.334338
H	4.294814	34.137359	16.339309	H	8.339573	38.190925	14.919757
H	5.942991	33.712086	16.859789				

[B-P(OMe)₃]^{•+} (global minimum):

127 atoms

Pt	6.34865	29.750607	12.602368	C	10.757888	25.784096	10.893009
S	5.892902	31.965834	13.197409	H	11.588219	26.29586	10.399328
S	7.153811	27.556767	12.23071	C	7.485842	23.751386	12.824351
P	7.070841	30.334835	10.498362	H	7.826212	23.230195	13.727953
P	6.258814	29.110653	14.840645	H	7.018323	23.010138	12.159153
O	5.27578	27.896834	15.327514	H	6.693061	24.459181	13.109705
C	8.628153	24.460404	12.143314	C	12.419283	24.798068	12.528389
O	7.677153	28.572345	15.474024	H	12.842068	23.842994	12.177801
C	3.181369	30.125666	10.501516	H	12.445417	24.779457	13.627482
H	2.900346	30.88566	9.771974	H	13.085718	25.599012	12.180351
O	5.73663	30.315865	15.799578	C	9.210969	26.816605	9.183676
C	6.4537	24.668545	9.560457	H	8.855796	26.225449	8.325653
H	7.07095	23.846929	9.193078	H	10.123057	27.345108	8.878077
O	6.486142	29.34644	9.336035	H	8.429981	27.558298	9.401559
O	6.885361	31.858433	9.917376	C	4.630583	22.483163	8.488056
O	8.690094	30.29223	10.29992	H	4.245207	21.797417	7.719081
C	3.243421	30.47193	11.862515	H	3.995164	22.391616	9.380485
C	4.107962	27.938696	10.998335	H	5.642975	22.150544	8.754765
C	3.499664	29.455858	12.800195	C	3.190854	24.293089	7.532024
H	3.404897	29.668289	13.866005	H	3.129568	25.306873	7.10903
C	3.615112	28.873955	10.072999	H	2.486766	24.223014	8.374462
H	3.697991	28.662143	9.006982	H	2.85043	23.592027	6.757395
C	3.919178	28.196744	12.36792	C	4.623958	23.933979	7.954934
H	4.151394	27.425457	13.098911	C	5.543441	24.03095	6.715277
C	6.238201	26.587622	11.036636	H	5.560019	25.057355	6.319713
C	9.935766	24.329556	12.62245	H	5.177896	23.363413	5.921398
H	10.117713	23.698656	13.496484	H	6.576233	23.740141	6.951177
C	5.161978	24.870785	9.03834	C	1.812525	33.946024	12.387746
C	4.427456	25.944084	9.549187	C	4.074583	33.903042	13.326728
H	3.414316	26.1289	9.19354	C	2.879917	34.56694	13.054668
C	9.464171	25.943902	10.384415	H	2.797596	35.602024	13.384002
C	11.015629	24.98297	12.012408	C	4.239148	32.546721	12.921603
C	4.922688	26.797844	10.547748	C	-0.656838	33.918588	12.790587
C	8.393727	25.284499	11.023439	H	-0.744373	32.877782	12.449581
C	7.001091	25.499827	10.530882	H	-1.611392	34.422509	12.579307

H	-0.506055	33.909237	13.879785	C	5.567684	32.341105	9.563542
C	0.49775	34.662434	12.080048	H	5.064985	31.646332	8.87706
C	0.506716	36.123993	12.553876	H	5.729862	33.302598	9.065804
H	0.63825	36.200775	13.64335	H	4.952528	32.487847	10.460015
H	-0.453886	36.595378	12.303746	C	5.638137	26.492837	15.231902
H	1.299799	36.70835	12.065614	H	6.660097	26.334389	15.594449
C	1.981962	32.601043	12.018426	H	5.559674	26.152268	14.191726
H	1.165654	32.06779	11.528297	H	4.918722	25.961443	15.863278
C	0.26276	34.639264	10.55218	C	5.237872	34.501247	15.459439
H	1.075155	35.15629	10.021495	C	5.168789	34.609887	14.052715
H	-0.682093	35.148249	10.311213	C	7.127813	36.024475	14.063351
H	0.19798	33.613371	10.163766	H	7.865126	36.61742	13.515845
C	3.145897	31.879793	12.287563	C	6.117444	35.372459	13.344855
C	6.975417	29.432097	7.969269	C	7.219155	35.936045	15.456358
H	6.578717	30.330417	7.477505	C	6.263147	35.166775	16.135831
H	6.60245	28.53221	7.46966	H	6.314101	35.090216	17.225991
H	8.071876	29.44892	7.95036	C	8.313473	36.644505	16.213074
C	5.641603	30.125402	17.241681	H	7.898345	37.301124	16.992466
H	6.58875	29.740894	17.640931	H	8.929091	37.260693	15.544374
H	4.8215	29.435431	17.473699	H	8.979201	35.926103	16.716802
H	5.435056	31.118432	17.651511	C	6.091896	35.437057	11.839327
C	9.606143	29.861341	11.336102	H	6.452637	34.487601	11.410511
H	9.338083	30.313356	12.2991	H	6.742479	36.238457	11.466681
H	10.591603	30.216378	11.016442	H	5.077267	35.605781	11.451836
H	9.598319	28.766481	11.421026	C	4.232902	33.665951	16.210809
C	8.9423	29.069645	14.966311	H	3.202171	34.003346	16.024732
H	9.193706	28.551561	14.032535	H	4.415382	33.71432	17.293138
H	9.684183	28.832691	15.73644	H	4.286379	32.612211	15.894999
H	8.909094	30.155686	14.803303				

[B-P(OMe)₃]⁺ (local minimum):

127 atoms

Pt	12.907867	11.306904	7.679506	C	12.280813	8.272201	6.461265
S	11.951713	11.426099	5.521974	C	13.487325	7.576901	6.649961
P	15.084749	11.037183	6.968306	H	13.976775	7.121191	5.788261
C	15.39792	13.691631	7.058065	C	11.612314	8.774135	7.593713
C	15.151907	9.788794	4.591287	H	10.608405	9.186156	7.483931
C	17.439092	9.880236	7.536327	C	10.858633	6.570876	1.917603
C	11.607212	9.903184	4.662004	C	11.162501	5.194389	2.529804
C	11.122426	10.128102	3.340153	H	10.963887	4.410613	1.785525
C	10.894126	9.045079	2.499826	H	10.529464	4.986554	3.4046
H	10.524753	9.258669	1.495639	H	12.216363	5.104056	2.831544
C	11.121759	7.713846	2.898899	C	11.7553	6.76721	0.673718
C	11.565889	7.508676	4.207987	H	12.819531	6.753075	0.951375
H	11.721583	6.496275	4.580166	H	11.548534	7.720055	0.166513
C	11.792071	8.564713	5.103931	H	11.577314	5.95721	-0.048926

C	9.372281	6.6056	1.494167	C	18.343267	7.331215	12.422856
H	9.110841	7.550944	0.999017	H	18.548463	8.309877	12.877882
H	8.713655	6.483603	2.366012	H	18.648136	7.375873	11.367114
H	9.163702	5.788383	0.788116	H	18.9721	6.585431	12.930494
C	10.815169	11.510342	2.866315	C	15.392986	11.747569	12.182181
C	11.818149	12.324451	2.302575	C	14.487638	12.168977	13.1792
C	11.479944	13.614092	1.876828	C	14.558973	13.48705	13.640575
H	12.257531	14.246039	1.439988	H	13.855157	13.816275	14.409909
C	10.177735	14.114292	1.994133	C	15.507562	14.392621	13.146166
C	9.829392	15.493092	1.495274	C	15.59282	15.795652	13.68953
H	9.505177	15.457148	0.443	H	16.252634	15.83358	14.571051
H	10.693139	16.170327	1.548449	H	14.607754	16.165698	14.004787
H	9.007163	15.934841	2.074681	H	16.001895	16.492165	12.944561
C	9.19844	13.284307	2.556809	C	16.39629	13.947788	12.159977
H	8.174913	13.655973	2.656508	H	17.1455	14.639032	11.764524
C	9.492989	11.987763	2.992826	C	16.357849	12.638953	11.667915
C	8.417988	11.123733	3.602648	C	17.306632	12.203916	10.582284
H	7.497512	11.698139	3.767977	H	18.09557	12.950401	10.424826
H	8.742027	10.699431	4.564887	H	16.768962	12.076368	9.629877
H	8.169871	10.270207	2.953699	H	17.78293	11.241906	10.822872
C	13.242367	11.843041	2.202955	C	13.443044	11.224236	13.715576
H	13.742658	11.921858	3.181653	H	12.775549	10.874503	12.911757
H	13.813169	12.445104	1.484594	H	12.827812	11.711882	14.482431
H	13.2938	10.789814	1.892867	H	13.89724	10.326668	14.160558
S	13.668024	11.477875	9.910675	P	11.186725	12.727637	8.28203
C	14.492347	10.036223	10.553913	C	11.046378	14.871568	9.891797
C	15.317073	10.346612	11.671087	C	9.775767	11.186302	9.94419
C	16.044463	9.336595	12.288674	C	9.483038	13.487026	6.29232
H	16.670931	9.613954	13.138397	O	10.624224	13.756359	7.158707
C	16.007054	8.000661	11.843386	O	15.447781	10.980658	5.360921
C	15.175627	7.710022	10.75783	O	9.751038	12.191968	8.899903
H	15.085321	6.684273	10.401524	O	11.821752	13.753285	9.374739
C	14.400955	8.686739	10.114724	O	15.941463	12.377219	7.349469
C	13.575376	8.315702	8.957162	O	15.989983	9.886358	7.678923
C	12.253888	8.787183	8.832419	H	11.614254	15.246137	10.748831
H	11.75516	9.201551	9.70722	H	10.050998	14.539043	10.21282
C	14.130566	7.60144	7.883185	H	10.955838	15.646561	9.120882
H	15.133073	7.186471	7.981008	H	8.899602	11.373894	10.574702
C	16.852515	6.940706	12.550105	H	10.689499	11.256926	10.552676
C	16.659324	5.540775	11.947249	H	9.697044	10.186646	9.497728
H	17.286927	4.818784	12.487458	H	9.810444	13.657223	5.261656
H	16.954926	5.506235	10.888075	H	8.685325	14.185565	6.573073
H	15.616664	5.199585	12.030202	H	9.129254	12.456332	6.40278
C	16.45992	6.892882	14.044058	H	15.558686	9.973239	3.592102
H	15.398032	6.632983	14.162431	H	14.070845	9.620927	4.52434
H	16.631716	7.856534	14.543323	H	15.640973	8.911663	5.03549
H	17.060105	6.133467	14.56558	H	17.875425	10.675635	8.150628

H	17.730131	10.014492	6.486517	H	14.393844	13.792746	7.493139
H	17.763713	8.89981	7.900197	H	15.361879	13.854091	5.972903
H	16.084307	14.403592	7.52577				

B-CN^tBu:

125 atoms

Pt	13.92245	7.418647	24.742071	C	10.469908	2.740075	26.075791
C	9.960179	4.689861	22.959419	C	9.962488	3.806928	26.824776
C	10.442621	5.955324	22.231027	H	8.984031	3.734993	27.299865
C	11.058364	5.609995	20.863937	C	10.349899	5.994444	29.279453
C	9.307364	6.981901	22.086124	C	9.783384	6.961011	30.117105
C	16.151038	4.904006	25.29935	C	8.968278	7.984683	29.617132
C	14.981385	4.42104	25.88076	C	8.345732	8.999098	30.543839
C	13.995078	4.199194	23.692434	C	8.737374	8.029248	28.238111
H	13.143125	3.935539	23.063557	C	11.258117	4.930821	29.843021
C	15.14262	4.738593	23.116162	C	16.804204	7.418762	22.895369
C	16.187198	5.206141	23.928552	C	21.058324	6.326878	23.07107
C	17.199635	6.152109	23.402647	C	21.307349	4.964781	23.739143
C	18.560991	5.817779	23.461795	C	21.805165	7.408497	23.882352
H	18.815761	4.838536	23.867689	C	21.628671	6.280422	21.636027
C	19.567042	6.676975	23.008592	C	12.398758	6.903008	23.670726
C	19.154941	7.898459	22.453919	C	15.449573	7.912898	25.818124
H	19.89251	8.597024	22.053015	C	17.47494	7.419795	28.461632
C	17.811151	8.275435	22.384704	C	17.599566	8.334242	27.230972
C	17.457338	9.557979	21.705647	C	18.78116	7.913607	26.342093
C	17.273427	9.560158	20.308798	C	17.711721	9.810722	27.643822
C	17.371045	8.277087	19.521878	S	12.758594	6.748049	26.725005
C	16.963834	10.765587	19.665645	S	15.113267	8.024757	22.755523
C	16.83163	11.965336	20.372142	N	11.482952	6.549464	23.033214
C	16.522322	13.258705	19.660008	N	16.393375	8.177178	26.457785
C	17.009683	11.936785	21.761474	H	16.131687	13.075028	18.649618
C	17.319409	10.753297	22.438016	H	17.425508	13.882335	19.557084
C	17.456499	10.739123	23.935827	H	15.77781	13.851826	20.211628
C	9.067268	7.181237	25.883992	H	21.683992	8.404994	23.435343
C	9.287521	7.080124	27.368798	H	22.882038	7.182468	23.922155
C	10.09267	6.05285	27.892979	H	21.424947	7.452799	24.913383
C	10.675062	5.00142	27.006097	H	21.10698	5.520217	21.037106
C	11.946795	5.169655	26.413512	H	22.701135	6.030848	21.656854
C	12.502449	4.070517	25.697984	H	21.515363	7.247571	21.126628
C	11.752766	2.902065	25.532698	H	20.830289	4.144671	23.182733
H	12.215061	2.085382	24.973435	H	20.930527	4.944378	24.772168
C	13.849445	4.17523	25.088369	H	22.38749	4.760746	23.772294
C	10.519206	0.266332	26.484491	H	17.172389	8.454216	18.45629
C	9.707409	1.426305	25.866235	H	16.644456	7.536783	19.891458
C	8.317964	1.453015	26.522834	H	18.366316	7.816885	19.617101
C	9.525773	1.17225	24.35428	H	17.297363	11.740291	24.35931

H	18.453462	10.38755	24.243755	H	8.581538	6.275442	25.488066
H	16.713939	10.053375	24.372685	H	10.034637	7.289419	25.369651
H	17.772335	10.455245	26.758517	H	8.438995	8.047016	25.633263
H	18.621092	9.950382	28.244518	H	7.985512	9.877676	29.990881
H	16.843731	10.11359	28.244906	H	9.06363	9.344789	31.302289
H	10.292466	5.146895	20.226554	H	7.484626	8.570881	31.082113
H	11.891039	4.903709	20.984235	H	12.2658	5.008174	29.40602
H	11.436051	6.513238	20.367049	H	10.891634	3.91956	29.611212
H	9.143555	4.232011	22.385142	H	11.346604	5.026482	30.933817
H	9.601606	4.927804	23.968261	H	18.818349	8.514742	25.426131
H	10.773885	3.961723	23.062112	H	18.694426	6.862561	26.042594
H	8.50786	6.552706	21.467062	H	19.718092	8.049959	26.900339
H	9.671747	7.899174	21.60528	H	17.360846	6.371852	28.152972
H	8.891864	7.239017	23.068393	H	16.604859	7.700796	29.06982
H	7.690447	2.257222	26.110728	H	18.382379	7.509247	29.074524
H	8.386007	1.593511	27.611431	H	15.184018	4.916795	22.041188
H	7.803455	0.498097	26.339668	H	14.896557	4.348761	26.965499
H	10.49168	1.125779	23.833143	H	16.991808	5.195782	25.931303
H	8.929795	1.973841	23.89456	H	8.119805	8.831718	27.824055
H	9.003981	0.217083	24.186157	H	16.892416	12.859906	22.336473
H	11.509868	0.17543	26.018226	H	16.812428	10.762902	18.582251
H	9.989631	-0.689425	26.346306	H	9.990353	6.916428	31.190564
H	10.667588	0.427534	27.562104				

[B-CN^tBu]^{•+}:

125 atoms

Pt	13.752005	11.381683	7.362459	H	11.486147	5.202974	2.862779
S	12.527505	11.593543	5.34486	C	10.93142	6.861217	0.730018
C	15.153398	12.217953	6.282922	H	12.008083	6.653921	0.811697
C	12.04813	10.095573	4.508736	H	10.80655	7.819183	0.206682
C	11.388069	10.366627	3.272405	H	10.475551	6.076708	0.108413
C	10.841613	9.321002	2.539817	C	8.759021	7.180653	1.977184
H	10.348738	9.570553	1.598869	H	8.58378	8.144679	1.479782
C	10.908932	7.981101	2.968832	H	8.265222	7.208957	2.959119
C	11.596133	7.727507	4.160594	H	8.277339	6.398644	1.372372
H	11.71611	6.703737	4.514359	C	11.318407	11.762929	2.751079
C	12.185808	8.743419	4.926092	C	12.396097	12.264228	1.990809
C	12.906734	8.388529	6.161675	C	12.337068	13.58136	1.523409
C	14.264383	8.71563	6.321846	H	13.168922	13.970292	0.929744
H	14.842283	9.044368	5.457219	C	11.239248	14.410099	1.790608
C	12.224719	7.811093	7.244094	C	11.180514	15.81565	1.249179
H	11.190774	7.489566	7.111674	H	10.680234	15.836007	0.26791
C	10.267785	6.878143	2.12639	H	12.185924	16.236414	1.11223
C	10.428669	5.488624	2.763115	H	10.615671	16.480521	1.916978
H	9.942858	4.735608	2.127347	C	10.183224	13.886884	2.547306
H	9.957777	5.437633	3.755542	H	9.320131	14.520017	2.769404

C	10.199881	12.573436	3.030152	H	16.588623	16.498532	12.763884
C	9.061361	12.047448	3.866701	H	18.250035	15.876482	12.604722
H	8.274873	12.804147	3.982697	C	17.592171	13.269081	12.42212
H	9.412366	11.762459	4.871005	H	18.672645	13.433757	12.452738
H	8.611044	11.149457	3.418802	C	17.112396	11.993367	12.108823
C	13.601066	11.402746	1.708459	C	18.068602	10.870141	11.79899
H	14.087373	11.085739	2.645168	H	19.109068	11.215317	11.850808
H	14.33816	11.943115	1.099746	H	17.892856	10.464406	10.790575
H	13.325987	10.482046	1.17281	H	17.951328	10.031661	12.501786
S	15.161071	11.446725	9.248419	C	13.337543	12.634916	12.259551
C	14.893749	10.086494	10.378825	H	13.039885	12.279305	11.260981
C	15.199199	10.426486	11.724646	H	12.79607	13.567009	12.466637
C	15.036729	9.479453	12.729916	H	13.008928	11.879789	12.990538
H	15.27122	9.783629	13.751668	C	12.237381	10.870064	8.48127
C	14.585329	8.172844	12.466322	N	11.371595	10.646234	9.230784
C	14.321018	7.845788	11.134699	C	10.354573	10.346172	10.21666
H	14.003292	6.835869	10.877317	C	11.045006	9.629122	11.389802
C	14.472756	8.761009	10.080007	C	9.30714	9.443043	9.54534
C	14.076016	8.361503	8.718457	C	9.737099	11.681196	10.665917
C	12.807639	7.792187	8.507099	H	11.495541	8.683757	11.065388
H	12.225578	7.455021	9.365616	H	10.298182	9.416054	12.165504
C	14.846707	8.699027	7.589591	H	11.836574	10.253349	11.822171
H	15.880847	9.01798	7.719618	H	10.498667	12.329982	11.116868
C	14.413938	7.179681	13.616966	H	8.959424	11.480267	11.414523
C	13.904537	5.811928	13.135649	H	9.279451	12.205793	9.816848
H	13.794297	5.137826	13.996404	H	9.763521	8.506733	9.200139
H	14.605515	5.337962	12.432319	H	8.845984	9.949361	8.687472
H	12.920728	5.889663	12.64891	H	8.522408	9.201375	10.274065
C	13.394929	7.757748	14.625271	H	16.419837	11.86884	3.101864
H	12.416635	7.914357	14.147222	H	17.700678	13.055408	2.746984
H	13.730516	8.71907	15.037468	C	17.188441	12.511078	3.551302
H	13.257599	7.061228	15.465084	H	17.924845	11.881614	4.068644
C	15.776601	6.979552	14.318675	H	14.677411	13.731298	3.409531
H	16.166565	7.921906	14.727538	H	15.938241	14.925329	2.991241
H	16.522559	6.577684	13.617848	C	15.474335	14.367369	3.815786
H	15.670146	6.270411	15.152934	C	16.555428	13.52547	4.516543
C	15.716966	11.786504	12.057253	N	15.881425	12.774419	5.559347
C	14.826876	12.848771	12.324455	H	18.128724	14.999634	4.4072
C	15.348638	14.106645	12.638923	H	15.02547	15.08568	4.514468
H	14.659152	14.929447	12.844758	C	17.620388	14.409247	5.181166
C	16.728902	14.338508	12.695794	H	18.370113	13.799316	5.702227
C	17.27143	15.693547	13.068784	H	17.162188	15.100126	5.901383
H	17.406783	15.773547	14.159442				

8 References

1. Stoll, S.; Schweiger, A. EasySpin, a comprehensive software package for spectral simulation and analysis in EPR. *J. Magn. Res.* **2006**, 178, 42-55.
2. Yaws, C. L. *Chemical properties handbook : physical, thermodynamic, environmental, transport, safety, and health related properties for organic and inorganic chemicals*. McGraw-Hill: New York, 1999; p VII, 779.
3. Evans, D. F. 400. The determination of the paramagnetic susceptibility of substances in solution by nuclear magnetic resonance. *J. Chem. Soc.* **1959**, 2003-2005.
4. Bain, G. A.; Berry, J. F. Diamagnetic Corrections and Pascal's Constants. *J. Chem. Educ.* **2008**, 85, 532.
5. Farrugia, L. WinGX suite for small-molecule single-crystal crystallography. *J. Appl. Cryst.* **1999**, 32, 837-838.
6. Hubschle, C. B.; Sheldrick, G. M.; Dittrich, B. ShelXle: a Qt graphical user interface for SHELXL. *J. Appl. Cryst.* **2011**, 44, 1281-1284.
7. Sheldrick, G. A short history of SHELX. *Acta Cryst., A* **2008**, 64, 112-122.
8. Spek, A. Structure validation in chemical crystallography. *Acta Cryst., D* **2009**, 65, 148-155.
9. Farrugia, L. WinGX and ORTEP for Windows: an update. *J. Appl. Cryst.* **2012**, 45, 849-854.
10. Janisch, J.; Ruff, A.; Speiser, B.; Wolff, C.; Zigelli, J.; Benthin, S.; Feldmann, V.; Mayer, H. A. Consistent diffusion coefficients of ferrocene in some non-aqueous solvents: electrochemical simultaneous determination together with electrode sizes and comparison to pulse-gradient spin-echo NMR results. *J. Solid State Electrochem.* **2011**, 15, 2083-2094.

Publikation III

Influencing Factors on the Electronic Structures of Complex Radical-Ligand Ions of the Group 10 Metal Triad

Nicole M. Mews,^[a] Marc Reimann,^[b] Gerald Hörner,^[c] Hartmut Schubert,^[a] and Andreas Berkefeld*^[a]

Abstract: A series of group 10 metal complexes of a $k^2S,S':\eta^2$ -thiolate-arene-thiolate ligand features sulphur-centred redox chemistry, affording thiyl-thiolate complex cations from oxidation. Combined experimental and DFT data correlate metal admixture to frontier molecular orbitals to three factors of general validity: a) the energies and radial size of nd vs. ligand orbitals, b) steric interactions between ligands affecting metal-ligand orbital alignment (spatial match), and c) type and number of negatively charged donor sites, which determine the degree of metal admixture. An electronic transition λ^{NIR} located in the near-infrared spectral region reflects relative metal character in the lowest unoccupied metal-ligand antibonding spin-orbital that is diagnostic of the electronic coupling of formally mixed-valence ligand hemispheres by the metal. Intensity and band shape of λ^{NIR} further reflect structural strain impaired by metal coordination. Subtle changes of interligand steric interactions augments fine-tuning of electronic structures, which have been addressed by DFT computations at PBE0-1/3-D3(BJ)/TZP/ZORA/COSMO(CH₂Cl₂) level of theory. As one major result of DFT analysis, the validity of calculated metal-centred spin density, often reported as a diagnostic parameter, varies widely depending on methodology and functional used for initial structure optimization, which strongly advises caution in correlating this parameter with experimental data. Overall, group 10 d^8 -ions provide an indispensable tool for understanding the effects that metal-ligand bonding and coordinative strain have on the structure-property relationship of radical-ligand compounds.

Introduction

Coordination compounds of the group 10 metal triad are of central importance to many areas of chemical research, among which the field of Pd and Ni mediated bond formation certainly is the most elaborate.^[1] Contrasting metal-centred redox chemistry that is prerequisite to key elementary reaction steps in chemical bond formation, the examples of group 10 metalate complexes shown at the top of Figure 1 are members of a series of four

redox isomers in which the 1,2-heteroatom functionalized benzene ligands adopt three distinct valence states, including the open-shell form shown. The relative contributions of ligand and metal orbitals to frontier molecular orbitals (MOs) are variable and Pd contributes least in keeping with the energetic order of nd orbitals that increase as $Pd < Pt \approx Ni$ owing to the combined effect of effective nuclear charge, nd radial nodes, and the relativistic effect.^[2] This energetic order results in properties such as the appearance of an electronic transition λ^{NIR} whose position in the near-infrared (NIR) spectral region and band shape have served as diagnostic features of the electronic structures of radical-ligand compounds of the group 10 metals as shown in Figure 1.^[2-3] Least metal admixture correlates with the largest redshift of λ^{NIR} and is observed for Pd compounds. In addition to nd orbital energy and radial expansion, frontier MO composition varies with the np orbital energy of the heteroatoms Y ,^[3b, 4] and the overall oxidation state as reflected by net charge.^[3b, 4b, 5] The steric properties of vicinal groups R can affect the spatial overlap of metal and ligand orbitals, including the π -systems.^[3b, 4c, 5-6]

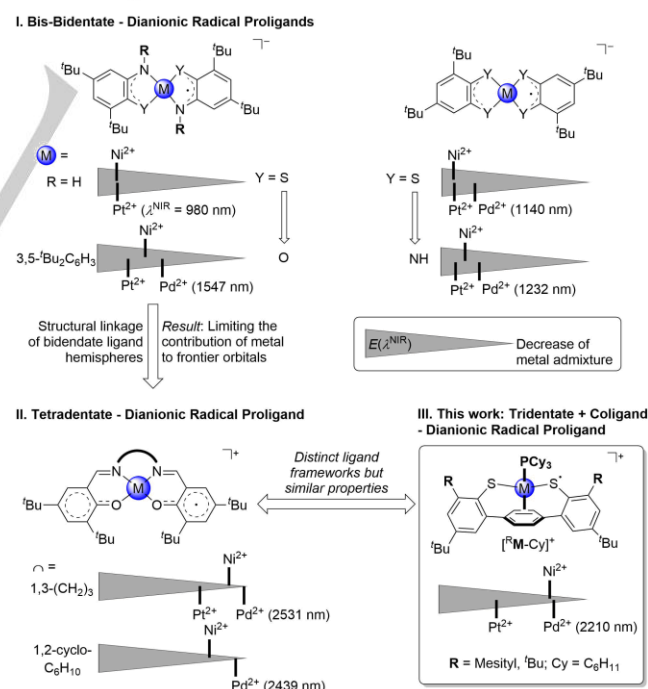


Figure 1. Correlation of spectroscopic signatures and relative metal admixture to spectroscopically relevant frontier orbitals of precedent and novel radical-ligand complexes of the group 10 metal triad; for additional details cf. Chart S1, SI.

[a] N.M. Mews, Dr. Hartmut Schubert, Privatdozent Dr. A. Berkefeld
Institut für Anorganische Chemie
Eberhard Karls Universität Tübingen
Auf der Morgenstelle 18, 72076 Tübingen, Germany
E-mail: andreas.berkefeld@anorg.uni-tuebingen.de

[b] M. Reimann
Institut für Chemie, Theoretical Chemistry – Quantum Chemistry
Technische Universität Berlin
Straße des 17. Juni 135, 10623 Berlin, Germany

[c] Dr. Gerald Hörner
Anorganische Chemie IV
Universität Bayreuth
Universitätsstraße 35, 95440 Bayreuth, Germany

within limits imposed by a specific combination of redox active and spectating donors of the ligand.^[2, 7] The noticeable similarity of thiol-radical ate complexes of Ni and Pt with regard to λ^{NIR} was attributed to similar energies of 3d and 5d with respect to S 3p orbitals,^[2] whereas the generally larger relative radical-ligand character for phenol type ligands relates to the resonance stabilization of the phenoxyl radical.^[8] Albeit radical-ligand ate and cationic salen complexes are similar in terms of their chemical structures, the organic linker of salen(-type) ligands constrains metal-ligand bond metrics and can impair a coplanar alignment of the donor hemispheres at the metal. The considerable redshift of λ^{NIR} by ~ 1000 nm and comparatively small deviations of g -factors from $g_e \approx 2.00$ both indicate a substantially lower metal admixture in radical-salen as compared to ate compounds; cf. Chart S1, and supporting information (SI) for additional details.^[3c, 3d, 9]

Even though a considerable number of influencing parameters has been ascertained, any discussion of the structure-property relationship of radical-ligand metal complexes relates to a specific ligand environment, rendering the search for a unified picture clearly worthwhile. One question of general importance concerns the correlation of redox active and spectator donors and their impact on electronic structure. This connects to another question of the variability of electronic structure for a given set of metal and ligand, and how this affects spectroscopic markers. Based on a combined experimental and computational study, which is based on the triad of 10 metal complex ions $[\text{R}^{\text{M}}\text{-Cy}]^+$ of the $\kappa^2\text{S}_2\text{S}^{\cdot-}\eta^2$ -coordinate thiol-arene-thiolate ligand shown at the bottom right of Figure 1, we herein provide detailed insight into how divergent preferences of the group 10 metal d^8 -ions with respect to ligand-bonding and coordinative strain reflect in EPR and UV/vis/NIR spectroscopic markers. An interchange of electron localized mixed-valence and delocalized descriptions can result from subtle changes of interligand interactions but may go unnoticed since spectroscopic markers are largely indifferent. In this regard, spin unrestricted DFT calculations that include exact exchange and scalar relativistic correction provide an indispensable tool to augment and correlate spectroscopic and structure data.

Results and Discussion

The terphenyl framework provides a geometrically flexible bonding pocket whose *trans*-disposed thiolate donors define the redox responsive $[\text{Ar}^{\text{S}}\text{-M-S}^{\text{Ar}}]$ core. The combination of η^2 -arene and κ -phosphine auxiliary ligands adopts to specific bonding preferences of d^8 -metal ions. The precursors $\text{R}^{\text{M}}\text{-Cy}$ to thiol-arene-thiolate cations shown at the bottom right of Figure 1, and reference compounds $\text{R}^{\text{M}}\text{-Ph}$, for Ph = PPh_3 , have been prepared using a salt metathesis protocol, reacting the ligand potassium salt with a mixture of *trans*- $[(\text{py})_2\text{MCl}_2]$ (M = Pd, Pt; py = pyridine) and PCy_3 (Cy = C_6H_{11}) or PPh_3 in toluene or 1,2- $\text{C}_6\text{H}_4\text{F}_2$ at room temperature. Bulk crystallization afforded $\text{R}^{\text{Pd}}\text{-Cy}$, R = Mes (58 %) and ^tBu (47 %), $^t\text{BuPt-Ph}$ (32 %) as light green, $^{\text{Mes}}\text{Pd-Cy}$ (40 %) and $^{\text{Mes}}\text{Pd-Ph}$ (61 %) as yellow-brown materials. $^{\text{Mes}}\text{Ni-Cy}$ forms dark purple crystalline needles as reported previously.^[10] Figure 2 compares pertinent solid-state structure

data of $^{\text{Mes}}\text{M-Cy}$ that reflect critical differences with regard to metal-ligand bonding, and respective data for $^t\text{BuPt-Cy}$, $^t\text{BuPt-Ph}$, and $^{\text{Mes}}\text{Pd-Ph}$ are provided in the SI. While a planar coordination is common to all precursors, the metal-donor bond metrics clearly mirror the discontinuous trend in electronic properties of the group 10 triad. Nickel forms the shortest bonds to the η^2 -arene moiety and *trans*-aligned thiolates. These contracted bonds associate the longest M-P bond in the series with repulsive interactions of mesityl and Cy groups. Most notably, bond anisotropy $\Delta d(\text{Ni-S}/\text{Ni-S}^{\cdot-}) = 0.037$ Å is a distinct feature ($3\sigma = 0.009$ Å) and associates with a difference between torsion angles along the two M-S-(C-C)_{arene} moieties of $\Delta\Theta = 9^\circ$, pointing out that coordination of Ni, as the smallest member of the triad, results in structural strain. As compared to $^{\text{Mes}}\text{Ni-Cy}$, M-donor bond lengths increase for the 4/5d congeners and torsion angles Θ in the range of 2–4° indicate unstrained spatial alignment of out-of-plane metal 4/5d, S 3p, and π -orbitals at flanking arenes. The 4/5d M-S bonds are equal within experimental accuracy but Pt forms somewhat shorter bonds to both η^2 -arene and PCy_3 auxiliary ligand. Substitution of R = Mes for ^tBu results in a substantial and, different from $^{\text{Mes}}\text{Ni-Cy}$, symmetrical increase of Θ to 15–20° in $^t\text{BuPt-Cy}$ and $^t\text{BuPt-Ph}$ as shown in Table S1, SI.

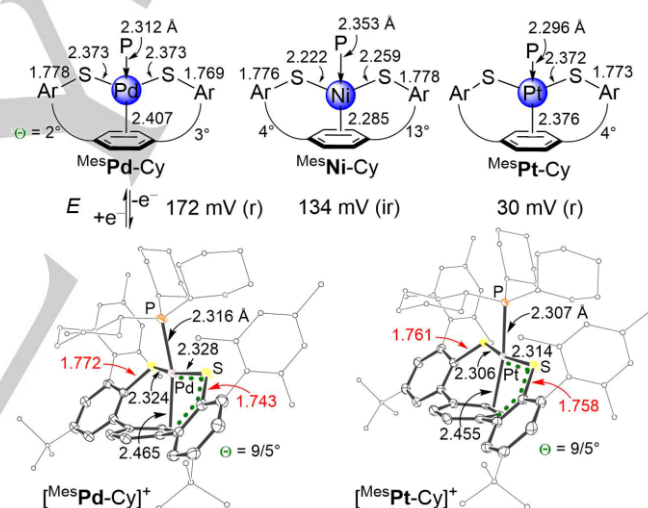


Figure 2. Pertinent molecular structure data of $^{\text{Mes}}\text{M-Cy}$ (top), and ORTEP representations of $[\text{MesM-Cy}]^+$ for M = Pd and Pt (bottom; torsion angle Θ along M-S-(C-C)_{arene} moieties as indicated by dotted green line); bond metrics of $^{\text{Mes}}\text{Ni-Cy}$ taken from ref. [10] for comparison; thermal displacement ellipsoids set at 50 % probability level, H atoms and counterions omitted for clarity, E vs. $\text{Fc}/[\text{Fc}]^+$, Fc = ferrocene, ir/r = electrochemically ir/reversible.

According to solid-state structure data, binding of Ni imposes greater geometric strain to the ligand as compared to Pd and Pt, which coordinate similarly in terms of overall metal-ligand geometry. Contrary to solid-state structure data, formal potentials of redox couples $\text{R}^{\text{M}}\text{-Cy}/[\text{R}^{\text{M}}\text{-Cy}]^+$ determined by cyclic voltammetry, CV, differ largely for Pd and Pt. As noted in Figure 2, $E(\text{R}^{\text{M}}\text{-Cy}/[\text{R}^{\text{M}}\text{-Cy}]^+)$ varies along the order Pt \ll Ni $<$ Pd. While $[\text{MesNi-Cy}]^+$ appears to deteriorate on the time scale of the CV experiment, redox processes are electrochemically reversible for the 4/5d metal congeners but the formal potential is 142 mV

more positive for Pd. The exchange of R = Mes for ^tBu in ^RPt-Cy has a marginal effect on E° , decreasing it by 10 mV, while replacing PCy₃ in ^RM-Cy for the weaker σ -donor PPh₃ increases E° by 50 mV for ^tBuPt-Ph and 20 mV for ^{Mes}Pd-Ph. The greater variation of E° for Pt points to a higher relative metal admixture to frontier MOs as compared to Pd.

Substituting ^tBuPt-Ph in electrochemical experiments for isolated [^tBuPt-Ph]⁺ fully reproduced CV data, substantiating the identity of electrochemically generated cations in general. Bulk oxidation of ^RM-Cy using either [Fc⁺]NTf₂, Fc⁺ = 1,1'-diacetylferrocene, NTf₂ = ⁻N(SO₂CF₃)₂, or [(4-BrC₆H₄)₃N]BAR^{F24}, BAR^{F24} = (3,5-(F₃C)₂C₆H₃)₄B⁻, afforded [^RM-Cy]⁺ salts of Pd (R = Mes, 68 %, BAR^{F24} salt) and Pt (R = Mes, 61 %, BAR^{F24} salt; ^tBu, 75 %, NTf₂ salt), and [^RPt-Ph]⁺ (^tBu, 48 %, BAR^{F24} salt) as maroon or dark reddish-purple crystalline solids. ¹H NMR spectra of crystalline [^{Mes}Pd-Cy]BAR^{F24} indicate the presence of a diamagnetic, yet ionic coproduct. The relative amount of coproduct increases from ~10 to >90 % by substituting PCy₃ for less sterically demanding PPh₃. Based on DOSY data, recorded from a sample of ^{Mes}Pd-Ph oxidized *in situ* using [Fc⁺]NTf₂, equilibrium formation of an S = 0 dimer is attributed to account for the coproduct. Different from Pd and Pt, isolation of [^{Mes}Ni-Cy]⁺ has been impaired by its instability even at -90 °C as implied by CV experiments, which necessitated *in situ* characterization as reported below.

The molecular structures derived from single crystalline samples of [^{Mes}M-Cy]BAR^{F24} of Pd and Pt are shown in Figure 2, and Table S2, SI, provides data of [^tBuPt-Ph]⁺. In all cases, ligand-centred oxidation reflects in a preserved square planar metal coordination and symmetrical contraction of the bonds along the S-M-S core that, in turn, likely contributes to the observed elongation of η^2 -M-arene and M-P bonds. Comparison of M- η^2 -arene distances and their relative increase upon oxidation corroborates the general picture that relativistic effects enhance σ and π components in Pt- η^2 -arene bonding.^[11] The increase of Θ by 4° implies a moderate increase of structural strain upon oxidation. A similar increase of Θ by 5° was found for [^tBuPt-Ph]⁺ but torsion angles of 17 and 20° are twice as large as for [^{Mes}Pt-Cy]⁺, pointing to a more strained structure. The combined effect contracted Pt-S bonds and significant torsion along the Pt-S-CC moieties likely results in the observed dislocation of Pt from the η^2 -arene centroid, with an bond anisotropy $\Delta d(\text{Pt-C}(\eta^2\text{-arene})) = 0.08$ Å, which indicates a dissymmetric [^{Ar}S-Pt-S^{Ar}]⁺ core in [^tBuPt-Ph]⁺ akin to previously reported [^{Mes}Pt-Ph]⁺.^[12] The structure data substantiate how subtle changes in the steric rather than electronic properties of the auxiliary coligand render the geometrical and electronic structures of chemically identical [^{Ar}S-M-S^{Ar}] cores distinct.

Constraining the spatial alignment of metal and ligand orbitals through interligand interactions is reminiscent of the effect that organic linkers have on radical-salen complexes.^[3c, 3d] While bond metrics point to a symmetric structure for [^{Mes}Pt-Cy]⁺, [^{Mes}Pd-Cy]⁺ features disparate peripheral S-Ar moieties based on the difference between S-Ar/S'-Ar' bond lengths of 0.029 Å ($3\sigma = 0.009$ Å). A related disparity between oxygen-arene bond lengths was reported for radical-salen complexes of Pd.^[9, 13] Albeit crystal packing effects cannot be ruled out to contribute to observed differences in bond lengths, $\Delta E^\circ = 142$ mV points

clearly to distinct electronic structures for [^{Mes}Pd-Cy]⁺ and [^{Mes}Pt-Cy]⁺.

X-Band cw-EPR data of radical-ligand cations corroborate the formation of S = 1/2 systems and substantiate the differences between electronic structures inferred from electrochemical and solid-state structure data. In all cases, spectra of frozen solutions are of rhombic appearance and display resolved hyperfine coupling (*hfc*) to ¹⁰⁵Pd ($I = 5/2$, 22 % abundance) and ¹⁹⁵Pt ($I = 1/2$, 34 %), while the field dependent broadening of resonance lines points to unresolved *hfc* to ³¹P. In accord with the electrochemical reversibility for ^RM-Cy/[^RM-Cy]⁺ of Pd and Pt, X-band cw-EPR spectra in liquid solution feature two sets of isotropic resonance lines owing to isotropic *hfc* to ¹⁰⁵Pd and ¹⁹⁵Pt; cf. SI for liquid solution EPR data. Isotropic g -factors exceed $g_e \approx 2.00$ but the deviations are generally small, in particular for Pd, cf. top and bottom entries in Table 1.

Table 1. Pertinent X-Band cw-EPR data of [^RM-L]⁺ recorded at $T = 107$ K.

[^R M-L] ⁺ [a]	g_{33} [b]	g_{iso} [c]	Δg [d]	$A_{11}, A_{22}, A_{33}; A_{iso}$ [e]
[^{Mes} Pd-Cy] ⁺	2.062	2.039	0.023	22, 7, 10; 17
[^{Mes} Ni-Cy] ⁺	2.131	2.076[e]	0.055	-
[^{Mes} Pt-Cy] ⁺	2.177	2.094	0.083	191, 186, 259; 192
[^t BuPt-Cy] ⁺ [e]	2.155	2.079	0.076	280, 189, 237; 214
	2.169	2.079	0.090	168, 173, 261; 214
[^t BuPt-Ph] ⁺	2.158	2.084	0.074	185, 175, 237; 195
[^{Mes} Pd-Ph] ⁺	2.058	2.035	0.023	31, 13, 12; 16

[a] 1:1 C₇H₈:CH₂Cl₂ glass; counterion = NTf₂; L = Cy (PCy₃) and Ph (PPh₃). [b] g -factor at lowest field. [c] g_{iso} and A_{iso} determined from spectra recorded at $T = 293$ K, $A(^{105}\text{Pd}, I = 5/2, 22\%)$ and $A(^{195}\text{Pt}, I = 1/2, 34\%)$ in MHz. [d] $\Delta g = g_{33} - g_{iso}$. [e] $g_{iso} = 1/3 \times (g_{11} + g_{22} + g_{33})$. [e] Data in frozen solution present a 1:2 mixture of two S = 1/2 species that coalesce at 293 K, cf. Figures S24 and S25, SI for details.

The impact of the different steric demands of groups R on the properties of cations [^RPt-Cy]⁺ manifests in the g -factors, whose deviations from g_e decrease noticeably upon substituting R = Mes for ^tBu, albeit $A_{iso}(^{195}\text{Pt})$ appears unchanged. Different from R = Mes, frozen solution data of [^tBuPt-Cy]⁺ are composed of two distinct S = 1/2 systems in 1:2 ratio that collapse into a single set of resonances at 293 K, adding support to structural strain inferred from solid-state structure data; cf. Figures S24-S25 for details. Oxidation of ^{Mes}Ni-Cy *in situ* affords a single S = 1/2 product whose EPR parameters vary with the choice of counterion. As presented in Figures S12-S13, [^{Mes}Ni-Cy]NTf₂ is characterized by a spectrum of rhombic appearance whereas for BAR^{F24} a spectrum of pseudo axial appearance results. The anisotropy of g -factors, provided in Table 1 as $\Delta g = g_{33} - g_{iso}$, are small and follow the order Pd < Ni < Pt that is reminiscent of the order of associated formal redox potentials. EPR data imply that admixture of metal orbitals to spectroscopically relevant frontier MOs increases along the order Pd < Ni < Pt but is

counterbalanced for each system by coordinative strain caused by peripheral groups, which is in line with increasing torsion angles Θ along the M-S-Arene moieties in solid-state structure data. The position of Pd 4d orbitals at lowest energy along the *nd* series renders the Pd-S bond character least covalent which reflects in distinct EPR parameters for $[\text{MesPd-L}]^+$, with L = PCy₃ and PPh₃, in agreement with previous S K-edge XAS data on one-electron oxidized bis-1,2-benzenedithiolato group 10 metal ate complexes.^[14]

Different from precursors $^{\text{R}}\text{M-Cy}$, dark maroon or reddish-purple colored solutions of radical-ligand complex ions $[\text{R}^{\text{M-Cy}}]^+$ feature additional diagnostic electronic transitions λ^{NIR} whose energies vary with the nature of the linking metal site as depicted in Figure 3. While the counterion has no discernible effect on the position and shape of the low-energy bands, the use of $\text{BAR}^{\text{F}24}$ increases the lifetime of *in situ* generated $[\text{MesNi-Cy}]^+$ noticeably as compared to NTf_2 , albeit samples of either counterion deteriorate noticeably on the timescale of ≤ 2 h at $T = -90$ °C. The same applies to $[\text{tBuPt-Ph}]^+$ that is stable if combined with $\text{BAR}^{\text{F}24}$ whereas the NTf_2 salt gradually deteriorates in CH_2Cl_2 solution at $T \geq 0$ °C. In line with electrochemical reversibility, UV/vis/NIR spectra of $[\text{MesM-Cy}]^+$ for Pd and Pt are preserved at ambient temperature. Full line-widths of the bands at half maximum are narrow, $1100 \leq \nu_{\text{whm}} \leq 1500$ cm^{-1} , and, as are their energies, invariant to changes of the solvent dielectric constant between 9 (CH_2Cl_2) and 66 (propylene carbonate, $\text{C}_3\text{H}_6\text{O}_3$; grey curves in Figure 3). Contrasting their similar band shapes, the redshift of λ^{NIR} (ν^{NIR} ; $\epsilon^{\text{NIR}}/\text{M}^{-1}\text{cm}^{-1}$) from 1530 nm (6540 cm^{-1} ; 2.4×10^4) for Pt to 2210 nm (4530 cm^{-1} ; $\geq 1.7 \times 10^4$) for Pd indicates a decrease of metal admixture to frontier MOs. Different from radical-ligand cations of Pd and Pt, *in situ* oxidation of $^{\text{Mes}}\text{Ni-Cy}$ results in the appearance of additional low-energy bands at 1098 and 1297 nm (9110 and 7710 cm^{-1}) that are of similar intensity as λ^{NIR} (ν^{NIR} ; $\epsilon^{\text{NIR}} = 2150\text{ nm}$ (4650 cm^{-1} ; $0.5 \times 10^4\text{ M}^{-1}\text{cm}^{-1}$). Sample stability at $T \leq -90$ °C is sufficient to conclude that the lower band intensity by almost one order of magnitude is an inherent property of $[\text{MesNi-Cy}]^+$. The possibility of more than one product being formed contradicts EPR data that point clearly to the generation of a major species.

Recognizing that ν_{whm} are very similar along the series $[\text{MesM-Cy}]^+$, the trend of band intensities may be attributed to the overall fit of M^{2+} to the radical-ligand along the order $\text{Pt} > \text{Pd} > \text{Ni}$ as inferred from solid-state structure, electrochemical and cw-EPR data. Notably, the energies of λ^{NIR} fit the relative order of formal redox potentials as noted in Figure 2, both qualitatively and quantitatively; $\lambda^{\text{NIR}}(\text{Pt}) \gg \lambda^{\text{NIR}}(\text{Ni}) \approx \lambda^{\text{NIR}}(\text{Pd})$ versus $E^0(\text{Pt}) \ll E^0(\text{Ni}) \approx E^0(\text{Pd})$. Further in line with electrochemical and EPR data, the nature of the R group reflects in the properties of λ^{NIR} displayed by $[\text{R}^{\text{Pt-Cy}}]^+$. The redshift of ~ 100 nm observed for $[\text{tBuPt-Cy}]^+$ (dash-dotted curve in Figure 3) corroborates the lower relative admixture of Pt inferred from EPR data. The oscillator strength that associates with the transition is equivalent to that of $[\text{MesPt-Cy}]^+$ since the twofold increase of $\nu_{\text{whm}} \approx 2100\text{ cm}^{-1}$ is balanced by the respective decrease of band intensity by one half to $\epsilon^{\text{NIR}} = 1.2 \times 10^4\text{ M}^{-1}\text{cm}^{-1}$.

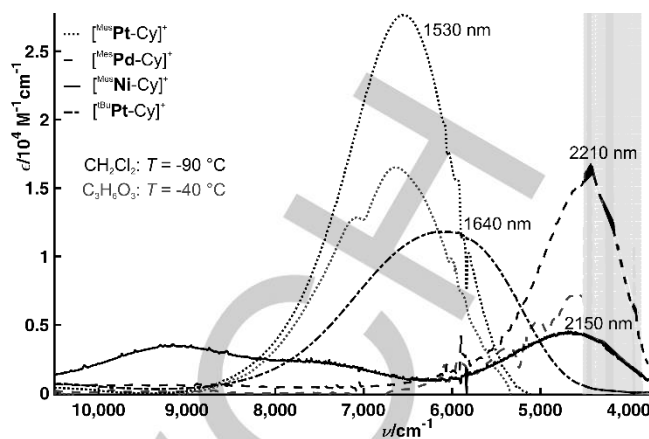


Figure 3. Distinctive low-energy electronic transitions of radical-ligand ions $[\text{R}^{\text{M-Cy}}]^+$ for M = Ni (R = Mes, solid line; sample prepared *in situ*), Pd (R = Mes, dashed line), Pt (R = Mes, dotted lines; R = ^tBu, dash-dotted line) recorded at $T = -80$ °C recorded in CH_2Cl_2 (black) and $\text{C}_3\text{H}_6\text{O}_3$ (grey) solution; bands at $\nu^{\text{NIR}} > 5000\text{ cm}^{-1}$ (grey area) result from strong IR absorptions of the solvents.

Electronic structures of radical-ligand ions $[\text{MesM-Cy}]^+$ have been addressed with DFT methods starting from structures that were optimized at the PBE0-1/3-D3(BJ)/TZP/ZORA level of theory,^[15] accounting for medium effects in a continuum approach (COSMO parameterized for CH_2Cl_2). The computational setting is suitable to match with experimentally determined solid-state structure metrics for the neutral precursors of Ni, Pd and Pt and the cations of Pd and Pt. A compromise between the typical bias of GGA functionals toward delocalization and the contrary effect of exact exchange is required for the description of potentially mixed valence systems.^[16] Very good agreement of experimental and DFT derived spectroscopic data indicates appropriate descriptions of electronic structures of radical-ligand ions $[\text{MesM-Cy}]^+$ of Pd and Pt. Calculated g_{iso} values and anisotropies Δg both match experimental EPR data with absolute deviations in g and $\Delta g < 0.03$. Calculated hyperfine splitting A_{iso} also is in very good agreement; see Table S5, SI, for details. Furthermore, TD-DFT calculations predict transitions at $\lambda^{\text{NIR}} = 1260\text{ nm}$ ($f_{\text{osc}} = 0.238$) for $[\text{MesPt-Cy}]^+$, and 1800 nm ($f_{\text{osc}} = 0.103$) for $[\text{MesPd-Cy}]^+$, in accord with experimental transition energies and intensities. Contrasting calculations for Pd and Pt, consideration of large amounts of exact exchange (33.333 % for PBE0-1/3) in the optimization of $[\text{MesNi-Cy}]^+$ has impaired convergence, resulting in substantial spin contamination and artificially distorted bond metrics. Notably, spectroscopic parameters, $g_{\text{iso}} = 2.109$ ($\Delta g = 0.028$) and $\lambda^{\text{NIR}} = 1790\text{ nm}$ ($f_{\text{osc}} = 0.125$), computed for the PBE0-D3BJ optimized structure of $[\text{MesNi-Cy}]^+$ and PBE0-1/3 agree reasonably with experimental data.

A population analysis locates $>95\%$ of the total spin for all $[\text{ArS-M-S}^{\text{Ar}}]^+$ cores. An NBO analysis provided ≤ 0.14 of metal centred spin for Pd and Pt as expected for radical-ligand character but calculated spin densities at individual atoms vary significantly with the method of population analysis chosen. Metal centred spin has been found to vary by as much as 0.06 (40 %), comparing Löwdin and Mulliken spin densities as implemented in ORCA.^[17] This method dependence renders the

validity of spin density based discussions of electronic structure of doubtful value.

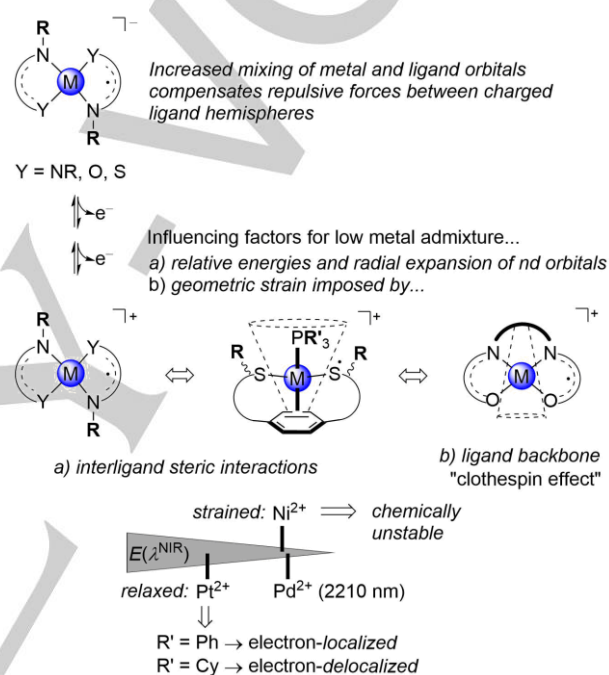
A TD-DFT analysis for $[\text{MesPt-Cy}]^+$ assigns the low-energy band λ^{NIR} to a $\beta\text{HOMO} \rightarrow \beta\text{LUMO}$ transition of a delocalized thyl/thiolate-Pt manifold, as inferred from solid-state structure and UV/vis/NIR spectroscopic data. Very similar data have been computed for $[\text{MesPd-Cy}]^+$, which agrees with band intensity and width of λ^{NIR} that are reminiscent of that of Pt but contrasts solid-state structure data. Taking the invariance of λ^{NIR} toward solvent polarity into account identifies $[\text{MesPd-Cy}]^+$ either as an electron localized Class II-III or delocalized Class III system. The computational data support that a subtle change in intramolecular steric interactions has a profound effect on the electronic structure of a given radical-ligand-metal chromophore. Critical examination of previously reported DFT-data for $[\text{MesPt-Ph}]^+$ now at the higher level of theory (PBE0-1/3 instead of BP86/single-point BLYP-35) corroborates that a subtle change of steric interactions between primary and auxiliary ligand in $[\text{MesPt-L}]^+$ correlates with a change of the electronic structure from electron-localized Class II-III for PPh_3 to delocalized Class III for PCy_3 , which, however, reflects in a marginal redshift of λ^{NIR} by 10 nm and a $\Delta\Delta g = 0.001$.

Conclusions

Salen and terphenyldithiophenol ligands differ largely with regard to their compositions of redox active and spectating donors but associated radical-ligand complex cations are remarkably similar with regard to frontier MO composition and associated electronic properties. Three general factors appear to be relevant as summarized in Scheme 1. First, the energetic order of *nd* orbitals along the triad, which is independent of the ligand used. Second, geometric strain, either as the result of the organic linker in salen ligands or of interligand interactions in terphenyldithiophenols, affects spatial overlap of metal and ligand orbitals. Third, type and number of negatively charged donors. Both frameworks combine a set composed of two anionic and neutral donors for metal coordination, a composition that associates with calculated metal spin densities ≤ 0.17 for Pt; cf. Chart S1, SI. Substituting neutral for negatively charged donors as in square planar ate complexes associates with an overall higher metal (≥ 0.2 for Pd; cf. Chart S1, SI) admixture to frontier orbitals. The higher degree of metal-ligand orbital mixing is prerequisite to counteract the repulsion of charged ligand hemispheres. Accordingly, salen- and terphenyldithiophenol-like properties should prevail for dianionic ate complexes upon successive oxidation by three electrons. Indeed, electronic and spectroscopic properties of corresponding $S = 1/2$ radical-ligand complex cations of Pd are reminiscent of those ligated by radical-salen and terphenylthiylhiophenolate.^[5] Different from Pd and Pt, the lack of a radial node renders the radial expansion of 3d orbitals similar to that of the fully occupied 3p orbitals, which adds a repulsive contribution to Ni-donor bonding.^[18] This property not only causes the electronic and chemical properties of radical-ligand complexes of Ni to respond sensitively to the type, number, and steric shielding of donors in the ligand framework as shown in Figure 1 and Scheme 1 but also renders

high-level DFT electronic structure calculations prone to spin-contamination.

The significance of relativistic effects for Pt renders the triad of group 10 metals distinct from group 9 congeners. The overall picture along the group 10 series reveals a discontinuous behaviour, placing 3d Ni in between the 4d/5d homologues with respect to all relevant experimental and theoretical descriptors of electronic structure. Contrasting the group 10 triad, a detailed analysis of the structure-property relationship of six-coordinate tris-dithiolene complexes identified a continuous increase of metal admixture from Co (0 % 3d) to Rh (17 % 4d) to Ir (26 % 5d), which renders the radical-ligand complexes increasingly resistant toward thyl-based consecutive reactivity.^[19]



Scheme 1. Unified picture of influencing factors on the chemical-electronic structure relationship of group 10 metal radical-ligand ionic complexes.

In summary, this work shifts the perspective from individual structure-property relationships of compositionally divergent radical-ligand coordination compounds of the group 10 metals to a conceptual framework that is based on three influencing factors: a) the order of *nd* orbital energies $\text{Pd} < \text{Pt} < \text{Ni}$ (orbital energy and radial match), b) total number of negatively charged donors on the ligand(s) (degree of metal orbital admixture), and c) geometrical strain of variable origins (spatial metal-ligand orbital overlap). Understanding electronic structure properties is a key prerequisite for understanding the relationship of electronic structure and chemical reactivity.

Acknowledgements

N.M.M. and A.B. acknowledge the Elite program for postdocs of the Baden-Württemberg Stiftung for financial support, and

Annika Stetter for experimental contributions to this work. M.R., G.H., and A.B. thank Prof. Martin Kaupp for discussions and computational advice in preparation of this work.

Keywords: radical-ligand complex • thiolate ligand • structure-property relationship • metal-ligand bonding • electronic structure

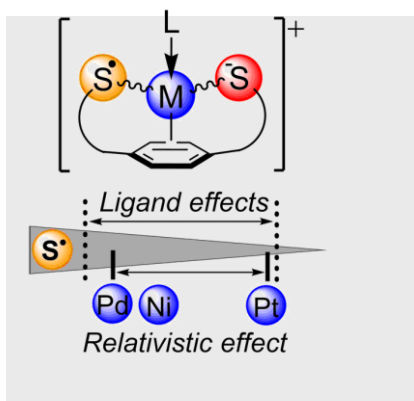
- [1] (a) N. Miyaura, A. Suzuki, *Chem. Rev.* **1995**, *95*, 2457-2483; (b) *Acc. Chem. Res.* **2008**, *41*, 1439-1564; (c) P. G. Gildner, T. J. Colacot, *Organometallics* **2015**, *34*, 5497-5508; (d) N. Hazari, P. R. Melvin, M. M. Beromi, *Nature Rev. Chem.* **2017**, *1*, 0025; (e) A. Biffis, P. Centomo, A. Del Zotto, M. Zecca, *Chem. Rev.* **2018**, *118*, 2249-2295; (f) K. M. Korch, D. A. Watson, *Chem. Rev.* **2019**.
- [2] K. Ray, T. Petrenko, K. Wieghardt, F. Neese, *Dalton Trans.* **2007**, 1552-1566.
- [3] (a) W. Kaim, *Coord. Chem. Rev.* **2011**, *255*, 2503-2513; (b) D. Herebian, E. Bothe, F. Neese, T. Weyhermüller, K. Wieghardt, *J. Am. Chem. Soc.* **2003**, *125*, 9116-9128; (c) R. M. Clarke, K. Herasymchuk, T. Storr, *Coord. Chem. Rev.* **2017**, *352*, 67-82; (d) F. Thomas, *Dalton Trans.* **2016**, *45*, 10866-10877.
- [4] (a) S. Kimura, E. Bill, E. Bothe, T. Weyhermüller, K. Wieghardt, *J. Am. Chem. Soc.* **2001**, *123*, 6025-6039; (b) K. Ray, T. Weyhermüller, F. Neese, K. Wieghardt, *Inorg. Chem.* **2005**, *44*, 5345-5360; (c) K. M. Conner, A. L. Perugini, M. Malabute, S. N. Brown, *Inorg. Chem.* **2018**, *57*, 3272-3286.
- [5] S. Kokatam, T. Weyhermüller, E. Bothe, P. Chaudhuri, K. Wieghardt, *Inorg. Chem.* **2005**, *44*, 3709-3717.
- [6] P. Chaudhuri, C. N. Verani, E. Bill, E. Bothe, T. Weyhermüller, K. Wieghardt, *J. Am. Chem. Soc.* **2001**, *123*, 2213-2223.
- [7] R. Williams, E. Billig, J. H. Waters, H. B. Gray, *J. Am. Chem. Soc.* **1966**, *88*, 43-50.
- [8] P. Chaudhuri, K. Wieghardt, in *Prog. Inorg. Chem.*, Vol. 50, **2002**, pp. 151-216.
- [9] H. Oshita, M. Kikuchi, K. Mieda, T. Ogura, T. Yoshimura, F. Tani, T. Yajima, H. Abe, S. Mori, Y. Shimazaki, *ChemistrySelect* **2017**, *2*, 10221-10231.
- [10] F. Koch, H. Schubert, P. Sirsch, A. Berkefeld, *Dalton Trans.* **2015**, *44*, 13315-13324.
- [11] N. Kaltsoyannis, *J. Chem. Soc., Dalton Trans.* **1997**, 1-12.
- [12] N. M. Mews, A. Berkefeld, G. Hörner, H. Schubert, *J. Am. Chem. Soc.* **2017**, *139*, 2808-2815.
- [13] Y. Shimazaki, T. D. Stack, T. Storr, *Inorg. Chem.* **2009**, *48*, 8383-8392.
- [14] K. Ray, S. DeBeer George, E. I. Solomon, K. Wieghardt, F. Neese, *Chem. Eur. J.* **2007**, *13*, 2783-2797.
- [15] (a) G. te Velde, F. M. Bickelhaupt, E. J. Baerends, C. Fonseca Guerra, S. J. A. van Gisbergen, J. G. Snijders, T. Ziegler, *J. Comput. Chem.* **2001**, *22*, 931-967; (b) C. Fonseca Guerra, J. G. Snijders, G. te Velde, E. J. Baerends, *Theor. Chem. Acc.* **1998**, *99*, 391-403.
- [16] M. Parthey, M. Kaupp, *Chem. Soc. Rev.* **2014**, *43*, 5067-5088.
- [17] F. Neese, *WIREs Comput. Mol. Sci.* **2012**, *2*, 73-78.
- [18] M. Kaupp, *J. Comput. Chem.* **2007**, *28*, 320-325.
- [19] (a) T. J. Morsing, S. N. MacMillan, J. W. Uebler, T. Brock-Nannestad, J. Bendix, K. M. Lancaster, *Inorg. Chem.* **2015**, *54*, 3660-3669; (b) H. Tang, E. N. Brothers, M. B. Hall, *Inorg. Chem.* **2017**, *56*, 583-593.

Entry for the Table of Contents (Please choose one layout)

Layout 1:

RESEARCH ARTICLE

A unified picture is presented for the chemical-electronic structure relationship of radical-ligand complexes of the group 10 metals. Three principal factors govern electronic properties: a) radial and energetic metal-ligand orbital match, b) metal-ligand spatial alignment (fine-tuned by spatial interligand interactions), and, c) number of charged donors per ligand.



Nicole M. Mews, Marc Reimann, Gerald Hörner, and Andreas Berkefeld*

Page No. – Page No.

Influencing Factors on the Electronic Structures of Complex Radical-Ligand Ions of the Group 10 Metal Triad

Layout 2:

RESEARCH ARTICLE

((Insert TOC Graphic here))

Author(s), Corresponding Author(s)*

Page No. – Page No.

Title

Text for Table of Contents

Influencing Factors on the Electronic Structures of Complex Radical-Ligand Ions of the Group 10 Metal Triad

Nicole M. Mews, Marc Reimann, Gerald Hörner, Hartmut Schubert and Andreas Berkefeld

Table of Contents

1	Additional Information on Group 10 Metal Radical-Ligand Coordination Compounds.....	2
2	General Information.....	3
3	Synthetic Procedures and Analytical Data.....	5
4	Additional Crystal Structure Data	10
5	Additional NMR Data.....	12
6	Additional Information on UV/Vis/NIR Spectroscopy Data.....	13
7	Additional X-Band cw-EPR Data.....	19
8	Additional Electrochemical Data.....	26
9	Additional Computational Data	30
9.1	General Information	30
9.2	Computational Results	30
9.3	Cartesian Coordinates of DFT-Optimized Radical-Ligand Complex Ion Structures.....	32
10	References	36

1 Additional Information on Group 10 Metal Radical-Ligand Coordination Compounds

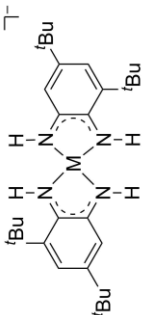
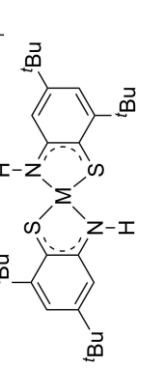
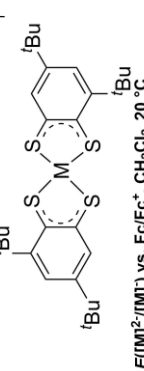
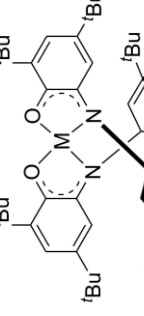
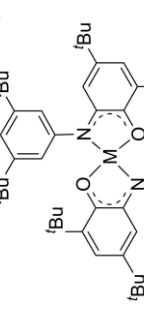
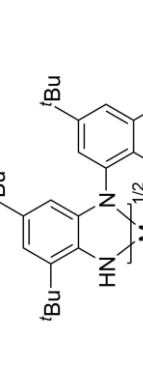
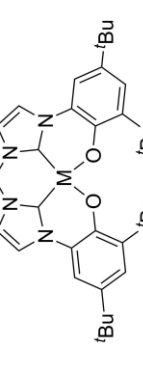
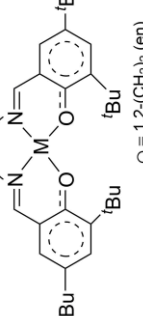
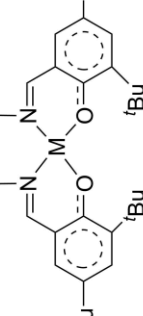
 <p>$E([M]^{2+}/[M]^{+})$ vs. Fc/Fc^{+}, MeCN, 20 °C $Ni < Pt < Pd$ $-2.22 < -2.12 < -1.86$ V</p> <p>UV/vis/NIR, CH_2Cl_2, 20 °C: λ_{max} (E/kJ mol⁻¹) $Pt < Ni < Pd$</p> <p>918 (130) 1031 (116) 1232 nm (97) EPR (X-Band): MeCN, 30 K (Ni, Pt), 10 K (Pd) g_{iso}: Pd < Pt < Ni $2.008 < 2.0165 < 2.0333$ Δg: Pd < Ni = Pt $0.038 < 0.105 < 0.108$</p> <p>Calculated spin density at M not reported</p> <p><i>J. Am. Chem. Soc.</i> 2003, 125, 9116</p>	 <p>$E([M]^{2+}/[M]^{+})$ vs. Fc/Fc^{+}, CH_2Cl_2, 22 °C $Ni < Pt < Pd$ $-1.714 < -1.527 < -1.484$ V</p> <p>UV/vis/NIR, CH_2Cl_2, -40 °C: λ_{max} (E/kJ mol⁻¹) $Ni = Pt$</p> <p>971 (123) 980 nm (122) EPR (X-Band): CH_2Cl_2, 10 K g_{iso}: Pt < Ni $2.021 < 2.067$ Δg: Ni = Pt $0.109 < 0.378$</p> <p>Calculated spin density at M not reported</p> <p><i>J. Am. Chem. Soc.</i> 2001, 123, 10012</p>	 <p>$E([M]^{2+}/[M]^{+})$ vs. Fc/Fc^{+}, CH_2Cl_2, 20 °C $Ni = Pt < Pd$ $-1.10 < -1.10 < -0.92$ V</p> <p>UV/vis/NIR, CH_2Cl_2, 20 °C: λ_{max} (E/kJ mol⁻¹) $Ni = Pt < Pd$</p> <p>890 (134) 900 (133) 1140 nm (105) EPR (X-Band): CH_2Cl_2 (Pd, Pt), DMF/CHCl₃ (Ni), 10 K g_{iso}: Pd = Pt < Ni $2.02 < 2.02 < 2.077$ Δg: Pd < Ni < Pt $0 < 0.17 < 0.41$</p> <p>Calculated spin density at M $Pd < Pt < Ni$ $21 < 24 < 34$ %</p> <p><i>Inorg. Chem.</i> 2005, 44, 5345</p>	 <p>$E([M]^{2+}/[M]^{+})$ vs. Fc/Fc^{+}, CH_2Cl_2 $Pt < Ni < Pd$ $-1.65 < -1.59 < -1.43$ V</p> <p>UV/vis/NIR, CH_2Cl_2: λ_{max} (E/kJ mol⁻¹) $Pt < Ni < Pd$</p> <p>1262 (95) 1515 (79) 1661 nm (72) EPR data: not reported</p> <p>Calculated spin density at M not reported</p> <p><i>Inorg. Chem.</i> 2018, 57, 3272</p>	 <p>$E([M]^{2+}/[M]^{+})$ vs. Fc/Fc^{+}, CH_2Cl_2 $Ni = Pt < Pd$ $-1.91 < -1.91 < -1.67$ V</p> <p>UV/vis/NIR, CH_2Cl_2: λ_{max} (E/kJ mol⁻¹) $Pt < Ni < Pd$</p> <p>1105 (108) 1321 (91) 1547 nm (77) EPR data: not reported</p> <p>Calculated spin density at M not reported</p> <p><i>Inorg. Chem.</i> 2018, 57, 3272</p>
<p>R = C₆H₅ (Ph), o-CF₃-C₆H₄ (Ph)</p> <p>$E([M]^{2+}/[M]^{+})$ vs. Fc/Fc^{+}, CH_2Cl_2, 298 K Ni (R = Ph) = Pt^a (R = Ph) < Pd^b (R = Ph) $-1.64 < -1.64 < -1.54$ V</p> <p>UV/vis/NIR, CH_2Cl_2, 25 °C: λ_{max} (E/kJ mol⁻¹) Ni (R = Ph) < Pt^a (R = Ph) < Pd^b (R = Ph) 890 (134) 1059 (113) 1564 nm (76)</p> <p>EPR (X-Band): CH_2Cl_2, 10 K g_{iso}: Pd^b (R = Ph) < Pt^a (R = Ph) $2.021 < 2.036$ Δg: Pd^b (R = Ph) < Pt^a (R = Ph) $0.0975 < 0.361$</p> <p>Calculated spin density at M Pt^a (R = Ph) = 23.7 % a <i>Inorg. Chem.</i> 2001, 123, 2213 b <i>Inorg. Chem.</i> 2002, 41, 4295</p>	 <p>$E([M]^{2+}/[M]^{+})$ vs. Fc/Fc^{+}, CH_2Cl_2, 298 K $Pd < Ni < Pt$ $-0.38 < -0.31 < -0.25$ V</p> <p>UV/vis/NIR, CH_2Cl_2, 298 K: λ_{max} (E/kJ mol⁻¹) $Pt < Ni < Pd$</p> <p>1248 (96) 1536 (78) 1644 nm (73) EPR (X-Band): solid-state, 100 K g_{iso}: Pd = Ni < Pt $1.992 < 1.992 < 1.978$ Δg^a: Pd = Ni < Pt $0.007 < 0.008 < 0.025$</p> <p>a) $\Delta g = g_{(lowest\ field)} - g_{iso}$ Calculated spin density at M not reported</p> <p><i>Eur. J. Inorg. Chem.</i> 2018, 1752</p>	 <p>$E([M]^{2+}/[M]^{+})$ vs. Fc/Fc^{+}, CH_2Cl_2, 298 K $Ni < Pd = Pt$ $0.11 < 0.21 < 0.21$ V</p> <p>UV/vis/NIR, CH_2Cl_2, 298 K: λ_{max} (E/kJ mol⁻¹) $Pt < Ni < Pd$</p> <p>2294 (52) 2390 (50) 2600 nm (46) EPR (X-Band): solid-state, 100 K g_{iso}: Pd < Ni < Pt $2.004 < 2.032 < 2.044$ Δg^b: Pd < Ni < Pt $0.017 < 0.055 < 0.096$</p> <p>a) $\Delta g = g_{(lowest\ field)} - g_{iso}$ Calculated spin density at M: B3LYP-D3/6-31g*/lanL2DZ ECP (for M) $Pd < Ni = Pt$ (Mulliken) $0.04 < 0.07 < 0.07$</p> <p><i>Inorg. Chem.</i> 2019, 58, 8030</p>	 <p>$E([M]^{2+}/[M]^{+})$ vs. Fc/Fc^{+}, CH_2Cl_2, 230 K $Pt(\eta = en) < Ni(\eta = cy) < Pd(\eta = cy)$ $0.35 < 0.37 < 0.45$ V</p> <p>UV/vis/NIR, CH_2Cl_2, 298 K: λ_{max} (E/kJ mol⁻¹) $Pt(\eta = en) < Ni(\eta = cy) < Pd(\eta = cy)$</p> <p>1834 (65) 2127 (56) 2439 nm (49) EPR (X-Band)^a: solid-state, 77 K g_{iso}: Pd(η = en) < Pt(η = en) < Ni(η = en) $2.01 < 2.03 < 2.06$ Δg: Pd(η = en) < Ni(η = en) < Pt(η = en) $0 < 0.16 < 0.56$</p> <p>Calculated spin density at M $Pd(\eta = en) < Ni(\eta = en) < Pt(\eta = en)$ $8 < 12 < 17$ %</p> <p><i>J. Am. Chem. Soc.</i> 2009, 48, 8383 ^a <i>J. Am. Chem. Soc.</i> 2007, 129, 2559</p>	 <p>$E([M]^{2+}/[M]^{+})$ vs. Fc/Fc^{+}, CH_2Cl_2, 230 K $Ni = Pt < Pd$ $0.43 < 0.44 < 0.52$ V</p> <p>UV/vis/NIR, CH_2Cl_2, 298 K: λ_{max} (E/kJ mol⁻¹) $Pt < Ni < Pd$</p> <p>1996 (60) 2325 (51) 2531 nm (47) EPR (X-Band): CH_2Cl_2, 20 K g_{iso}: Pd < Ni < Pt $2.007 < 2.040 < 2.045$ Δg: Pd < Ni < Pt $0 < 0 < 0.48$</p> <p>Calculated spin density at M $Ni = Pd < Pt$ $7 < 7 < 16$ %</p> <p><i>Dalton Trans.</i> 2011, 40, 2469</p>

Chart S1. Compilation of properties of representative radical-ligand complexes of group 10 metals (from left to right): top row, [1], [2], [3], [4]; bottom row [5], [6], [7], [8], [9].

2 General Information

All manipulations of air- and moisture sensitive compounds were carried out under an atmosphere of dry argon using standard Schlenk or glove box techniques. Literature procedures were followed for the preparation of 5',5'''-di-tert-butyl-2,2''',4,4''',6,6'''-hexamethyl-[1,1':3',1'':4'',1'''':3''',1''''-quinquephenyl]2',2'''-dithiol ($\text{Mes}_2^t\text{Bu}_2(\text{SH})_2$), $^{\text{Mes}}\text{Ni-Cy}$,^[10] *trans*-py₂PtCl₂,^[11] *trans*-py₂PdCl₂,^[12] 1,1'-diacetylferrocenium bis(trifluoromethanesulfonyl)imide,^[13] [(4-BrC₆H₄)₃N]BAR^{F24} (BAR^{F24} = (3,5-(F₃C)₂C₆H₃)₄B⁻),^[14] benzyl potassium,^[15] and 1,4-bis(4,6-di-tert-butylthiophenol-2-yl)benzene ($^t\text{Bu}_4(\text{SH})_2$).^[16]

AgClO₄ (Alfa Aesar), 1,1'-diacetylferrocene (TCI), PPh₃ (abcr) and PCy₃ were used as received. High purity ferrocene (Fc, 99.5 %; TCI) was sublimed, and stored under argon. In general, solvents were purified and dried prior to use. Propylene carbonate (PC) was pre-dried and purified by fractional distillation under reduced pressure and percolation through a column of activated neutral alumina. 1,1,2,2-C₂H₂Cl₄ was dried over and distilled from P₂O₅ and degassed. Pentane and toluene were pre-dried over activated 3 Å molecular sieves (MS) and distilled from sodium benzophenone ketyl under argon. Et₃N was distilled from and stored over 3 Å MS. Dichloromethane stabilized with EtOH (CHEMSOLUTE, Th. Geyer) was first distilled from P₂O₅, then from K₂CO₃, and finally stored over activated basic alumina. Acetonitrile (MeCN) for use in electrochemical experiments was sequentially dried over and distilled from CaH₂ and P₂O₅, and finally percolated through activated neutral alumina. 1,2-Difluorobenzene (1,2-C₆H₄F₂; abcr) was dried and purified by percolation through a column of activated neutral alumina, and distilled onto activated neutral alumina prior to use. C₆D₆ was dried over and distilled from NaK alloy. CD₂Cl₂ and CDCl₃ were dried over and vacuum transferred from 3 Å MS. In general, solvents were stored over 3 Å MS under argon. Molecular sieves and alumina were activated by heating under dynamic vacuum (10⁻³ mbar) at $T \leq 200$ °C for 24-48 h.

NMR data were acquired on a Bruker Avance III HDX 600 and an AVII+500 spectrometer (DOSY). ¹H and ¹³C{¹H}-NMR chemical shifts are referenced to the residual proton and naturally abundant carbon resonances of the solvents: 7.16/128.06 (C₆D₆), 5.32/53.84 (CD₂Cl₂), 7.26/77.16 (CDCl₃). ³¹P NMR chemical shifts are referenced to an external standard sample of 85 % H₃PO₄ set to 0 ppm. ¹⁹⁵Pt NMR chemical shifts are referenced to an external standard sample of 1.2 M hexachloroplatinate(IV) in D₂O set to 0 ppm.

EPR spectra were collected using 4 mm O.D. Wilmad quartz (CFQ) EPR tubes or 5 mm O.D. NMR tubes on a continuous wave X-band Bruker EMXmicro spectrometer, and are referenced to the Bruker Strong Pitch standard $g_{\text{iso}} = 2.0028$. EPR simulations were done with EasySpin (version 5.1.25)^[17] and MATLAB and Statistic Toolbox Release R2016a (The MathWorks, Inc., Natick, Massachusetts, United States). X-band cw-EPR spectral data were fitted using the easyfit tool included in EasySpin package (pepper for solid state and garlic for solution data).

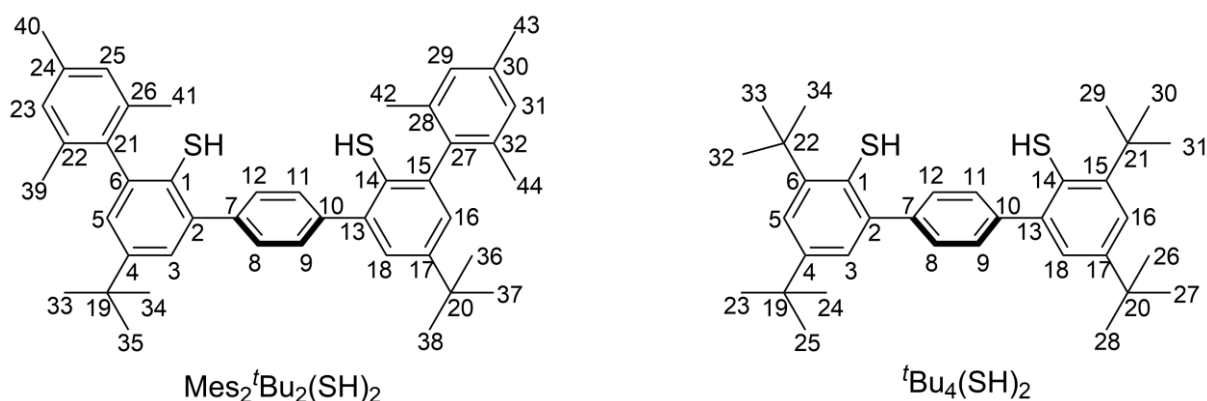
In general, the sample concentrations for electronic spectra were corrected for temperature dependent changes of solvent density ρ by using a modified form of the Rackett equation^[18]

Evan's method^[19] was employed to determine μ_{eff} in solution using a coaxial insert for 5 mm NMR sample tubes, $\chi_{\text{M}}^{\text{dia}} = -0.5 \times M$, M = dimensionless molecular weight of the sample and $\chi_{\text{M}}^{\text{dia}}(\text{CD}_2\text{Cl}_2) = -4.66 \times 10^{-5} \text{ cm}^3 \text{ mol}^{-1}$ were used to correct for diamagnetic susceptibilities of sample and solvent.^[20]

X-Ray diffraction data were collected on a Bruker Smart APEXII diffractometer with graphite-monochromated MoK_α radiation. The programs used were Bruker's APEX2 v2011.8-0, including SADABS for absorption correction and SAINT for structure solution, the WinGX suite of programs version 2013.3,^[21] SHELXS and SHELXL for structure solution and refinement,^[22] PLATON,^[23] and ORTEP.^[24] Crystals were, unless otherwise noted, coated in a perfluorinated polyether oil and mounted on a 100 μm MiTeGen MicroMounts™ loop that was placed on the goniometer head under a stream of dry nitrogen at 100 K.

Cyclic voltammetry (CV) measurements were performed under argon at 17 °C using a Julabo CF40 (resistance thermometer: Pt-100, temperature range: -40 to 50 °C) and an ECi 200 potentiostat (Nordic Electrochemistry) and BASi CV-50W voltammetric analyzer (Bioanalytical Systems, Inc.) in a gas-tight, full-glass, three-electrode cell setup. The ECi 200 potentiostat was controlled by using the EC4 DAQ (version 4.1.133.1, Nordic Electrochemistry) software, and data were treated with EC4 VIEW (version 1.2.55.1, Nordic Electrochemistry). $n\text{Bu}_4\text{NPF}_6$ electrolyte (Alfa Aesar) was recrystallized 3 times from acetone/water and employed as a 0.1 M solution in CH_2Cl_2 and MeCN. A Pt disc electrode (Deutsche Metrohm GmbH & Co. KG, electro-active area = $0.080 \pm 0.003 \text{ cm}^2$) and a 1 mm coiled Pt-wire were employed as working and counter electrodes. The Ag/Ag^+ redox couple, in the form of a 0.5 mm Ag wire in a 0.01 M $\text{AgClO}_4/0.1 \text{ M } n\text{Bu}_4\text{NPF}_6/\text{MeCN}$ solution, served as a reference electrode. Voltammograms were corrected for capacitive currents of electrolyte solutions and overall cell resistance, and potentials are reported relative to $\text{Fc}/[\text{Fc}]^+$ in CH_2Cl_2 , with $E^0(\text{Fc}/[\text{Fc}]^+ / 0.1 \text{ M } n\text{Bu}_4\text{NPF}_6 / \text{CH}_2\text{Cl}_2, 17 \text{ }^\circ\text{C}) = 0.212 \pm 0.001 \text{ V}$. The electro-active area of the Pt disc electrode was calculated from $\text{Fc}/[\text{Fc}]^+$ measurements in 0.1 M $n\text{Bu}_4\text{NPF}_6$ solution in CH_2Cl_2 at various concentrations and potential sweep rates at 295 K, using $D(\text{Fc}, \text{CH}_2\text{Cl}_2, 295 \text{ K}) = 2.2 \times 10^{-5} \text{ cm}^2 \text{ s}^{-1}$.^[25] The working electrode was rinsed with acetone, polished gently with a paste of 0.3 μm alumina (Deutsche Metrohm GmbH & Co. KG) in deionized water, rinsed thoroughly with plenty of deionized water, and finally acetone after each use. Periodic $\text{Fc}/[\text{Fc}]^+$ reference measurements verified the electro-active surface area of the Pt electrode, and the stability of the potential of the Ag/Ag^+ reference electrode.

3 Synthetic Procedures and Analytical Data



^{Mes}Pt-Cy. Ligand $\text{Mes}_2^t\text{Bu}_2(\text{SH})_2$ (500 mg, 0.78 mmol) and benzyl potassium (203 mg, 1.56 mmol) were suspended in 8.6 g toluene at r.t. The reaction mixture was stirred at r.t. until all benzyl potassium was consumed and a clear yellow solution formed (30 min). The solvent was removed under vacuum and slightly yellow solid was obtained. *Trans*-py₂PtCl₂ (330 mg, 0.78 mmol) and PCy₃ (218 mg, 0.78 mmol) were stirred in 31.89 g 1,2-C₆H₄F₂ until a white solid was formed (2 h). Ligand salt was diluted in 20 mL 1,2-C₆H₄F₂ and was added to the stirring precursor suspension. The flask was washed with 5 mL 1,2-C₆H₄F₂. After addition of the ligand salt the solution turns reddish-orange. The reaction mixture was stirred for 3 d at r.t. The green solution was centrifuged, filtered of and the remaining KCl was washed three times with 3 mL 1,2 C₆H₄F₂. The solvent was removed under vacuum and the dry green solid was diluted in 1,2 C₆H₄F₂. The solution was concentrated until some crystals were formed and stored at 8 °C to obtain a crystalline ^{Mes}Pt-Cy×(1,2-C₆H₄F₂)₂ suitable for XRD analysis. The crystals were wash with pentane and dried under vacuum, losing one equivalent 1,2-C₆H₄F₂. Yield: 564 mg (58 %) ^{Mes}Pt-Cy×1,2-C₆H₄F₂. Unit cell parameters: $a = 9.8530(2) \text{ \AA}$, $b = 31.8471(6) \text{ \AA}$, $c = 20.0163(4) \text{ \AA}$, $\alpha = 90^\circ$, $\beta = 93.0630(10)^\circ$, $\gamma = 90^\circ$, $V = 6271.93 \text{ \AA}^3$, $Z = 2$, I2/m. Elem. Anal. Calcd for C₆₉H₈₈F₂PtS₂: C, 66.53; H, 7.12; S, 5.15; F, 3.05. Found: C, 61.39; H, 7.67; S, 5.70. UV/vis/NIR [293 K, CH₂Cl₂; λ / nm ($\epsilon / 10^3 \text{ M}^{-1} \text{ cm}^{-1}$)] = 320 (33.0), 350 (16.4), 580 (0.2). ¹H NMR (CD₂Cl₂, 500 MHz): δ_{H} 7.58 (s, 4H; H8, H9, H11, H12), 7.27 (d, ⁴J_{HH} = 2.4 Hz, 2H; H3, H18), 6.87 (d, ⁴J_{HH} = 2.4 Hz, 2H; H5, H16), 6.85 (s, 4H; H23, H25, H29, H31), 2.24 (s, 6H; H40, H43), 2.00 (s, 12H; H39, H41, H42, H44), 1.47-1.39 (m, 15H; PCy₃), 1.33 (s, 18H; H33-H38), 1.31-1.18 (m, 10H; PCy₃), 1.06-0.97 (m, 3H, PCy₃), 0.75 ppm (s, 5H, PCy₃). ¹³C{¹H} NMR (CD₂Cl₂, 125 MHz): δ_{C} 145.8 (C4, C17), 140.6 (C2, C13), 140.5 (C21, C27), 140.4 (C6, C15), 137.9 (C7, C10), 136.4 (C24, C30), 136.1 (C22, C26, C28, C32), 136 (d, ³J_{CP} = 2.8 Hz; C1, C14), 128.2 (C23, C25, C29, C31), 127.8 (C5, C16), 122.3 (C3, C18), 34.4 (19, C20), 31.6 (C33-C38), 29.9 (PCy₃), 26.9 (PCy₃), 21.2 ppm (C40, C43). ³¹P NMR (CD₂Cl₂, 202 MHz): δ_{P} 31.68 (d, ¹J_{PtP} = 4398 Hz) ¹³⁵Pt NMR (CD₂Cl₂, 129 MHz): δ_{Pt} -4708 (d, ¹J_{PtP} = 4398 Hz).

^{tBu}Pt-Cy. Ligand ^{tBu}Bu₄(SH)₂ (500 mg, 0.96 mmol) and benzyl potassium (251 mg, 1.93 mmol) were suspended in 25 mL toluene at r.t., the reaction mixture was stirred until benzyl potassium was fully consumed (30 min), and final solvent removal under vacuum afforded a pale yellow solid.

Trans-py₂PtCl₂ (409 mg, 0.96 mmol) and PCy₃ (270 mg, 0.96 mmol) were stirred in 16 mL 1,2 C₆H₄F₂ until a white solid was formed (2 h) after which ligand potassium diluted in 20 mL of 1,2 C₆H₄F₂ was added, affording a reddish-orange solution. The reaction mixture was degassed by three freeze-pump-thaw cycles and stirred at 65 °C for 24 h during which the solution gradually turned dark green. The solvent was removed under vacuum, the residue dissolved in 1,2 C₆H₄F₂, the green solution centrifuged to aid the filtration of KCl by that was washed three times with 3 mL of 1,2 C₆H₄F₂. The solution was concentrated until crystals deposited and stored at 8 °C to afford crystalline material suitable for XRD analysis, and crystals were separated, washed with pentane, and finally dried under vacuum. Yield: 459 mg (47 %). Unit cell parameters: $a = 9.8047(5) \text{ \AA}$, $b = 11.4455(5) \text{ \AA}$, $c = 21.2480(9) \text{ \AA}$, $\alpha = 87.825(2)^\circ$, $\beta = 85.279(2)^\circ$, $\gamma = 81.634(2)^\circ$, $V = 2350.25 \text{ \AA}^3$, $Z = 2$, P-1. Elem. Anal. Calcd for C₅₃H₈₀PPtS₂: C, 63.19; H, 8.00; S, 6.36. Found: C, 62.17; H, 7.57; S, 6.49. UV/vis/NIR [293 K, CH₂Cl₂; λ / nm ($\epsilon / 10^3 \text{ M}^{-1} \text{ cm}^{-1}$)] = 289 (29.7), 320 (30.5), 344 (19.0), 586 (0.2), 647 (0.2). ¹H NMR (C₆D₆, 600 MHz): δ_{H} 7.65 (d, ⁴ $J_{\text{HH}} = 2.4 \text{ Hz}$, 2H; H5, H16), 7.47 (d, $J_{\text{H,H}} = 1.4 \text{ Hz}$, 4H; H8, H9, H10, H11), 7.28 (d, ⁴ $J_{\text{HH}} = 2.4 \text{ Hz}$, 2H; H3, H18), 3.00 (m, 3H; PCy₃), 1.95 (s, 18H; H29-H34), 1.91 (m, 6H; PCy₃), 1.56 (m, 15H; PCy₃), 1.36 (s, 18H; H23-H28), 1.19 (m, 6H; PCy₃), 1.03 ppm (m, 3H; PCy₃). ¹³C{¹H} NMR (C₆D₆, 150 MHz): δ_{C} 147.6 (C6, C15), 144.9 (C4, C17), 141.1 (C7, C10), 140.3 (C2, C13), 136.0 (d, ³ $J_{\text{CP}} = 3.4 \text{ Hz}$; C1, C14), 124.6 (C5, C16), 122.5 (C3; C18), 116.8 (C8, C9, C11, C12), 38.3 (C21, C22), 34.5 (C19, C20), 32.2 (d, $J_{\text{CP}} = 32.5 \text{ Hz}$; PCy₃), 31.6 (C23-C28), 31.2 (C29-C34), 29.8 (PCy₃), 27.6 (d, $J_{\text{CP}} = 11.4 \text{ Hz}$; PCy₃), 26.8 ppm (PCy₃). ³¹P NMR (C₆D₆, 242 MHz): δ_{P} 37.01 ppm (d, ¹ $J_{\text{PPt}} = 4638 \text{ Hz}$). ¹³⁵Pt NMR (C₆D₆, 129 MHz): δ_{Pt} -4638 ppm (d, ¹ $J_{\text{PPt}} = 4638 \text{ Hz}$)

^tBuPt-Ph. Synthesis protocol as for ^tBuPt-Cy using PPh₃ (253 mg, 0.96 mmol). Crystallisation from toluene afforded a greenish brown crystalline material. Yield: 333 mg (32 %) ^tBuPt-Ph·C₇H₈. Crystals suitable for XRD analysis were obtained by diffusion of pentane into a toluene solution at r.t. Unit cell parameters: $a = 11.4924(3) \text{ \AA}$, $b = 13.2351(4) \text{ \AA}$, $c = 15.9600(5) \text{ \AA}$, $\alpha = 11.4924(3)^\circ$, $\beta = 94.527(2)^\circ$, $\gamma = 99.208(2)^\circ$, $V = 2281.76 \text{ \AA}^3$, $Z = 2$, P-1. Elem. Anal. Calcd for C₅₃H₆₂PPtS₂: C, 64.35; H, 6.32; S, 6.48. Found: C, 64.10; H, 5.95; S, 6.58. UV/vis/NIR [293 K, CH₂Cl₂; λ / nm ($\epsilon / 10^3 \text{ M}^{-1} \text{ cm}^{-1}$)] = 327 (29.1), 360 (19.3), 424 (1.6), 561 (0.3). ¹H NMR (CDCl₃, 500 MHz): δ_{H} 7.61-7.57 (m, 5H; PPh₃), 7.53 (s, 4H; H8, H9, H11, H12), 7.39-7.36 (m, 3H; PPh₃), 7.34 (d, ⁴ $J_{\text{HH}} = 2.3 \text{ Hz}$, 2H; H5, H16), 7.29-7.25 (m, 8H; PPh₃), 7.22 (d, ⁴ $J_{\text{H,H}} = 2.3 \text{ Hz}$, 2H; H3, H18), 1.33 (s, 18H; H23-H28), 1.10 ppm (s, 18H; H29-H34). ¹³C{¹H} NMR (CDCl₃, 125 MHz): δ_{C} 148.0 (C6, C15), 145.1 (C4, C17), 140.6 (C7, C10), 140.2 (C2, C13), 135.5 (C1, C14), 135.4 (d, $J_{\text{CP}} = 10.8 \text{ Hz}$; PPh₃), 130.8 (PPh₃), 127.8 (d, $J_{\text{CP}} = 11.5 \text{ Hz}$; PPh₃), 124.6 (C5, C16), 121.9 (C3, C18), 115.2 (C8, C9, C11, C12), 37.4 (C21, C22), 34.5 (C19, C20), 31.5 (H33-H38), 30.3 ppm (C29-C34). ³¹P NMR (CDCl₃, 202 MHz): δ_{P} 32.70 ppm (d, ¹ $J_{\text{PPt}} = 4868 \text{ Hz}$) ¹³⁵Pt NMR (CDCl₃, 129 MHz): δ_{Pt} -4674 ppm (d, ¹ $J_{\text{P,Pt}} = 4868 \text{ Hz}$).

^{Mes}**Pd-Cy**. Ligand Mes₂Bu₂(SH)₂ (500 mg, 0.78 mmol) and benzyl potassium (203 mg, 1.56 mmol) were suspended in 17.5 g toluene at r.t. The reaction mixture was stirred at r.t. until all benzyl potassium was consumed and a clear yellow solution was formed. To this solution *trans*-py₂PdCl₂ suspended in 8.75 g toluene was added. The solution turns reddish-orange. Then PCy₃ in 8.75 g toluene was added and the solution becomes brown. After stirring for 16 h at r.t. the reaction mixture was degassed by freeze-pump-thaw technique and then heated up to 60 °C for 4 h. The brown solution was centrifuged, filtered off and the remaining KCl was washed three times with 3 mL toluene. The solvent was removed under vacuum and the brown-yellow solid was extracted with toluene. The solution was concentrated until some crystals were formed and pentane was added by slow diffusion at r.t. to obtain crystalline ^{Mes}**Pd-Cy**×C₇H₈ suitable for XRD analysis. The crystals were washed with pentane and dried under vacuum, losing half equivalent of toluene. Yield: 350 mg (40 %) ^{Mes}**Pd-Cy**×0.5C₇H₈. Unit cell parameters: *a* = 10.0757(3) Å, *b* = 16.5651(4) Å, *c* = 19.5789(6) Å, α = 108.6390(10)°, β = 97.825(2)°, γ = 105.2480(10)°, *V* = 2899.46 Å³, *Z* = 2, P-1. Elem. Anal. Calcd for C₁₃₃H₁₇₆P₂Pd₂S₄: C, 73.35; H, 8.15; S, 5.89. Found for two measurements of the same batch of crystalline material: C, 73.65/73.06; H, 7.44/8.00; S, 5.47/5.17. The high deviation could be caused by difficulties desorbing H₂O and SO₂ properly separated from the device column. Therefore spectra ¹H, ¹³C{¹H} and ³¹P spectra of this batch are included in Figure S2 and S3. UV/vis/NIR [193 K, CH₂Cl₂; λ/ nm (ε/ 10³ M⁻¹ cm⁻¹)] = 315 (17.0), 396 (33.5), 500 (0.4), 527 (0.3), 686 (0.2). ¹H NMR (CD₂Cl₂, 600 MHz): δ_H 7.61 (s, 4H; H8, H9, H11, H12), 7.31 (d, ⁴J_{HH} = 2.3 Hz, 2H; H3, H18), 6.86 (d, ⁴J_{HH} = 2.3 Hz, 2H; H5, H16), 6.85 (s, 4H; H23, H25, H29, H31), 2.56 (s, 3H; PCy₃), 2.24 (s, 6H; H40, H43), 2.00 (s, 12H; H39, H41, H42, H44), 1.50-1.39 (m, 16H; PCy₃), 1.34 (s, 18H; H33-H38), 1.25-1.16 (m, 6H, PCy₃), 1.07-0.99 (m, 3H, PCy₃), 0.86-0.70 ppm (m, 5H; PCy₃). ¹³C{¹H} NMR (CD₂Cl₂, 150 MHz): δ_C 145.9 (C4, C17), 141.3 (C7, C10), 140.7 (C6, C15), 140.6 (C21, C27), 138.8 (C1, C14), 138.4 (C2, C13), 136.4 (C24, C30), 136.1 (C22, C26, C28, C32), 128.1 (C23, C25, C29, C31), 127.3 (C5, C16), 122.4 (C3, C18), 118.1 (C8, C9, C11, C12), 34.5 (C19, C20), 31.6 (C33-C38), 30.7 (d, *J*_{PC} = 24.2 Hz, PCy₃), 30.4 (PCy₃), 27.1 (d, 6C, *J*_{PC} = 11.1 Hz, PCy₃), 26.8 (PCy₃), 21.2 (C40, C43), 20.7 ppm (C39, C41, C42, C44). ³¹P NMR (CD₂Cl₂, 243 MHz): δ_P 52.6 ppm.

^{Mes}**Pd-Ph**. Method 1: Mes₂Bu₂(SH)₂ (300 mg, 0.47 mmol), *trans*-py₂PdCl₂ (156 mg, 0.47 mmol) and PPh₃ (122 mg, 0.47 mmol) were suspended in 23 mL toluene and Et₃N (0.15 mL, 0.98 mmol) was added. The yellow suspension turns red-orange after the addition of Et₃N. The reaction mixture was degassed by three freeze-pump-thaw cycles and heated to 55 °C for 2 h. The reaction mixture was then filtered off, and the residue washed three times with toluene. The brown solution was concentrated in vacuum and diffusion of pentane afforded brown needles, which were washed with pentane and dried under vacuum. Yield: 286 mg (55 %) ^{Mes}**Pd-Ph**×C₇H₈.

Method 2: Mes₂Bu₂(SH)₂ (300 mg, 0.47 mmol) and benzyl potassium (122 mg, 0.94 mmol) were suspended in 23 mL toluene. The reaction mixture was stirred at r.t. until all benzyl potassium was consumed (30 min). Then *trans*-py₂PdCl₂ and PPh₃ were added and the reaction turns reddish. The

mixture was degassed by freeze-pump-thaw-technique and heated for 10 h at 55 °C. The brown solution was centrifuged, filtered of and the residue was washed three times with toluene. The solution was concentrated in vacuum and by diffusion of pentane brown needles of the product with one equivalent toluene were obtained. The crystals were washed with pentane and dried under vacuum. Yield: 152 mg (30 %) $^{\text{Mes}}\text{Pd-Ph}\times\text{C}_7\text{H}_8$.

Crystals suitable for XRD analysis were obtained by diffusion of pentane into a toluene solution at rt. Unit cell parameters: $a = 9.4361(7) \text{ \AA}$, $b = 34.785(3) \text{ \AA}$, $c = 17.2103(12) \text{ \AA}$, $\alpha = 90^\circ$, $\beta = 91.871(2)^\circ$, $\gamma = 90^\circ$, $V = 5646.01 \text{ \AA}^3$, $Z = 4$, P21/n. Elem. Anal. Calcd for $\text{C}_{70}\text{H}_{74}\text{PPdS}_2$: C, 75.28; H, 6.68; S, 5.74. Found: C, 74.73; H, 6.22, S, 6.06. UV/vis/NIR [293 K, CH_2Cl_2 ; λ/nm ($\epsilon/10^3 \text{ M}^{-1} \text{ cm}^{-1}$)] = 409 (27.5), 528 (0.6), 681 (0.3). ^1H NMR (CD_2Cl_2 , 400 MHz): δ_{H} 7.67 (s, 4H, H8, H9, H11, H12), 7.37 (d, $^4J_{\text{HH}} = 2.3 \text{ Hz}$, 2H; H3, H18), 7.26-7.19 (m, 9H, PPh_3), 7.12-7.07 (m, 6H, PPh_3), 6.78 (d, $^4J_{\text{HH}} = 2.3 \text{ Hz}$, 2H; H5, H16), 6.61 (s, 4H; H23, H25, H29, H31), 2.24 (s, 6H; H40, H43), 1.66 (s, 12H, H39, H41, H42, H44), 1.32 (s, 4H; H33-H38). $^{13}\text{C}\{^1\text{H}\}$ NMR (CD_2Cl_2 , 101 MHz): δ_{C} 146.1 (C4, C17), 141.1 (C7, C10), 140.8 (C6, C15), 139.6 (d, $^3J_{\text{CP}} = 9.9 \text{ Hz}$; C1, C14), 138.5 (C2, C13), 136.0 (C22, C26, C28, C32), 135.3 (C24, C30), 135.1 (d, $J_{\text{CP}} = 10.9 \text{ Hz}$; PPh_3), 130.4 (PPh_3), 127.7 (d, $J_{\text{CP}} = 11.2 \text{ Hz}$; PPh_3), 127.7 (C23, C25, C29, C31), 127.2 (C5, C16), 122.3 (C3, C18), 117.9 (C8, C9, C11, C12), 34.5 (C19, C20), 31.5 (C33-C38), 21.1 (C40, C43), 20.3 ppm (C39, C41, C42, C44). ^{31}P NMR (CD_2Cl_2 , 162 MHz): δ_{P} 49.3 ppm. Diffusion coefficient $D = 6.8 \times 10^{-10} \text{ m}^2/\text{s}$ (293 K, CD_2Cl_2).

$[\text{MesPt-Cy}] \text{NTf}_2$. To a solution of $^{\text{Mes}}\text{Pt-Cy}\times 1,2 \text{ C}_6\text{H}_4\text{F}_2$ (92 mg, 0.074 mmol) in 4 mL of CH_2Cl_2 was added $\text{Fc}^{\text{N}}\text{NTf}_2$ (41 mg, 0.074 mmol) in 2 mL of CH_2Cl_2 at r.t. The dark purple solution was stirred for 2 min and was then cannula transferred into 100 mL of vigorously stirred pentane. A dark purple solid precipitated, and the reaction mixture was stored at -28°C overnight. An orange mother liquor was removed, and the purple solid recrystallized from CH_2Cl_2 layered with pentane (1:10) at -28°C . The crystals thus obtained were washed with pentane three times and dried under vacuum. Yield: 77 mg (74 %). Crystals suitable for XRD analysis were obtained from diffusion of pentane into a 1,2 $\text{C}_6\text{H}_4\text{F}_2$ solution at -38°C . Unit cell parameters: $a = 27.4740(10) \text{ \AA}$, $b = 29.3018(10) \text{ \AA}$, $c = 10.8540(4) \text{ \AA}$, $\alpha = \beta = \gamma = 90^\circ$, $V = 8737.88 \text{ \AA}^3$, $Z = 8$, Pnma. Elem. Anal. Calcd for $\text{C}_{65}\text{H}_{84}\text{F}_6\text{NO}_4\text{PPtS}_4$: C, 55.30; H, 6.00; N, 0.99; S, 9.08. Found: C, 54.93; H, 5.93; N, 0.99; S, 9.23. $\mu_{\text{eff}} = 2.1$ (278–308 K, CD_2Cl_2 containing 1,1,2,2- $\text{C}_2\text{H}_2\text{Cl}_4$). UV/vis/NIR [293 K, CH_2Cl_2 ; λ/nm ($\epsilon/10^3 \text{ M}^{-1} \text{ cm}^{-1}$)] = 348 (15.9), 368 (17.4), 485 (2.7), 535 (2.6), 631 (1.1), 686 (0.4), 809 (0.9), 949 (0.3), 1526 (18.3).

$[\text{MesPt-Cy}]\text{BAr}^{\text{F}24}$. $^{\text{Mes}}\text{Pt-Cy}\times 1,2 \text{ C}_6\text{H}_4\text{F}_2$ (50 mg, 0.04 mmol) was dissolved in 1,5 mL of CH_2Cl_2 and cooled to -78°C in an acetone/dry ice bath, and combined with a solution of $[(4\text{-BrC}_6\text{H}_4)_3\text{N}]\text{BAr}^{\text{F}24}$ (54 mg, 0.04 mmol) in 0.5 mL of CH_2Cl_2 that was transferred by cannula. The resulting dark purple solution was layered with pentane (1:10) and stored at -28°C , affording dark purple crystals that were washed with pentane three times and dried under vacuum. Yield: 49 mg (61 %). Crystals suitable for

XRD analysis were obtained by diffusion of pentane into a 1,1,2,2-C₂H₂Cl₄ solution at -38 °C. Unit cell parameters: $a = 15.1784(6)$ Å, $b = 16.5068(6)$ Å, $c = 21.9412(8)$ Å, $\alpha = 84.293(2)^\circ$, $\beta = 72.914(2)^\circ$, $\gamma = 71.728(2)^\circ$, $V = 4989.56$ Å³, $Z = 4$, P-1. Elem. Anal. Calcd for C₉₅H₉₆BF₂₄PPtS₂: C, 57.20; H, 4.85; S, 3.21. Found: C, 57.04; H, 4.93; S, 3.18. UV/vis/NIR [293 K, CH₂Cl₂; λ / nm ($\epsilon/ 10^3$ M⁻¹ cm⁻¹)] = 349 (19.4), 367 (20.9), 486 (2.9), 533 (2.8), 636 (1.0), 812 (0.5), 1530 (21.7). UV/vis/NIR [293 K, PC; λ / nm ($\epsilon/ 10^3$ M⁻¹ cm⁻¹)] = 269 (40.8), 352 (15.1), 492 (1.7), 536 (1.8), 678 (0.7), 830 (0.8), 965 (0.7), 1511 (15.3).

[^tBuPt-Cy]NTf₂. Same procedure as for [^{Mes}Pt-Cy]NTf₂ starting from ^tBuPt-Cy (100 mg, 0.1 mmol) afforded a dark purple crystalline solid. Yield: 96 mg (75 %). Elem. Anal. Calcd for C₅₅H₈₀F₆NO₄PPtS₄: C, 51.31; H, 6.26; N, 1.09; S, 9.96. Found: C, 50.48; H, 6.18; N, 1.16; S, 10.39. $\mu_{\text{eff}} = 2.2$ (278–308 K, CD₂Cl₂ containing 1,1,2,2-C₂H₂Cl₄). UV/vis/NIR [293 K, CH₂Cl₂; λ / nm ($\epsilon/ 10^3$ M⁻¹ cm⁻¹)] = 256 (39.7), 278 (38.0), 347 (19.1), 377 (13.2), 502 (4.0), 554 (3.8), 657 (1.8), 746 (1.1), 926 (0.9), 1682 (15.4).

[^tBuPt-Ph]NTf₂. Same procedure as for [^{Mes}Pt-Cy]NTf₂ starting from ^tBuPt-PhC₇H₈ (100 mg, 0.09 mmol) afforded a dark purple crystalline solid. Yield: 41 mg (35 %). Elem. Anal. Calcd for C₅₅H₆₂F₆NO₄PPtS₄: C, 52.04; H, 4.92; N, 1.10; S, 10.10. Found: Found: C, 51.61; H, 4.85; N, 1.22; S, 10.26. $\mu_{\text{eff}} = 1.9$ (223–273 K, CD₂Cl₂ containing 1,1,2,2-C₂H₂Cl₄). UV/vis/NIR [223 K, CH₂Cl₂; λ / nm ($\epsilon/ 10^3$ M⁻¹ cm⁻¹)] = 374 (6.3), 506 (3.1), 536 (3.0), 617 (1.2), 746 (0.3), 959 (0.7), 1539 (17.1).

[^tBuPt-Ph]BAr^{F24}. Same procedure as for [^{Mes}Pt-Cy]BAr^{F24} starting from ^tBuPt-Ph×C₇H₈ (50 mg, 0.046 mmol) afforded brown crystalline material. Yield: 41 mg (48 %). Dark brown single crystals suitable for XRD analysis separated at -38 °C from a CH₂Cl₂ solution of [^tBuPt-Cy]BAr^{F24} layered with pentane. Unit cell parameters: $a = 14.4458(3)$ Å, $b = 18.4681(4)$ Å, $c = 19.6025(4)$ Å, $\alpha = 107.0010(10)^\circ$, $\beta = 108.6950(10)^\circ$, $\gamma = 100.0160(10)^\circ$, P-1. Elem. Anal. Calcd for C₈₅H₇₄BF₂₄PPtS₂: C, 55.11; H, 4.03; S, 3.46. Found: C, 54.74; H, 3.91; S, 3.86.

[^{Mes}Pd-Cy]BAr^{F24}. Procedure as for [^{Mes}Pt-Cy]BAr^{F24} starting from ^{Mes}Pd-Cy×0.5C₇H₈ (50 mg, 0.046 mmol) afforded a dark red crystalline material. Yield: 59 mg (68%). Dark reddish brown crystals suitable for XRD analysis separated at -28 °C from a CH₂Cl₂ solution layered with pentane. Unit cell parameters: $a = 15.9777(3)$ Å, $b = 17.5645(3)$ Å, $c = 19.4418(3)$ Å, $\alpha = 111.6280(10)^\circ$, $\beta = 102.1630(10)^\circ$, $\gamma = 92.6780(10)^\circ$, $V = 4525.78$ Å³, $Z = 2$, P-1. Elem. Anal. Calcd for C₉₅H₉₆BF₂₄PPdS₂: C, 59.86; H, 5.08; S, 3.36. Found: C, 59.24; H, 5.13; S, 3.30. UV/vis/NIR [293 K, CH₂Cl₂; λ / nm ($\epsilon/ 10^3$ M⁻¹ cm⁻¹)] = 277 (51.1), 302 (27.8), 412 (14.5), 442 (14.4), 544 (5.6), 852 (1.7), 2210 (13.7). UV/vis/NIR [233 K, PC; λ / nm ($\epsilon/ 10^3$ M⁻¹ cm⁻¹)] = 402 (12.8), 432 (10.3), 538 (2.9), 862 (0.7), 2210 (6.2).

4 Additional Crystal Structure Data

Table S1. Selected bond lengths [\AA] and angles [$^\circ$] of neutral complexes.

	^{Mes} Ni-Cy ^{a)}	^{Mes} Pd-Cy	^{Mes} Pt-Cy	^{tBu} Pt-Cy	^{tBu} Pt-Ph	^{Mes} Pd-Ph
M-P	2.353(2)	2.3119(6)	2.2955(4)	2.2685(6)	2.2356(8)	2.263(1)
M-S1	2.222(2)	2.3729(5)	2.3719(3)	2.3827(6)	2.3433(7)	2.348(4)
S1-Ar	1.776(4)	1.778(2)	1.773(1)	1.791(2)	1.790(3)	1.782(3)
M-S2	2.259(2)	2.3725(6)	2.3719(3)	2.3604(6)	2.3809(6)	2.361(1)
S2-Ar	1.780(4)	1.769(2)	1.773(1)	1.792(2)	1.785(3)	1.774(3)
M-Ar ^{b)}	2.179	2.305	2.273	2.271	2.254	2.313
P-M-Ar ^{b)}	171.86	173.47	177.89	167.51	171.26	161.33
M-S1-CC	4.1(4)	2.3(2)	3.5	11.3(2)	19.8(3)	12.6(3)
M-S2-CC	13.3(4)	3.8(2)	3.5	15.1(2)	20.5(2)	9.5(3)

a) Data included for the sake of better comparability and taken from ref. [10]. b) Data determined using centroid of η^2 -coordinate moiety of 1,4-disubstituted arene.

Table S2. Selected bond lengths [\AA] and angles [$^\circ$] of radical cation complexes.

	[^{Mes} Pd-Cy]	[^{Mes} Pt-Cy]	[^{Mes} Pt-Cy]	[^{Mes} Pt-Ph]	[^{tBu} Pt-Ph]
	BAr ^{F24}	BAr ^{F24}	NTf ₂ ^{a)}	NTf ₂ ^{b)}	BAr ^{F24}
M-P	2.3155(7)	2.307(1)	2.320	2.2694(7)	2.2441(7)
M-S1	2.3238(7)	2.306(1)	2.296	2.3012(9)	2.3391(6)
S1-Ar	1.772(3)	1.761(4)	1.755(5)	1.760(2)	1.786(3)
M-S2	2.3276(7)	2.314(1)	2.296	2.3149(9)	2.3410(6)
S2-Ar	1.743(3)	1.758(6)	1.755(5)	1.760(2)	1.796(3)
M-Ar	2.366	2.356	2.313	2.270	2.296
P-M-Ar	164.70	170.33	172.26	174.62	169.81
M-S1-CC	8.8(3)	8.5(5)	4.2	18.8(2)	20.3(2)
M-S2-CC	4.9(3)	4.6(5)	4.2	3.2(2)	17.4(2)

a) The Pt atom locates at an inversion centre so metrical data are likely biased by symmetry of the crystal lattice. b) Data are identical to those reported in ref. [13] and included for the sake of comparability.

5 Additional NMR Data

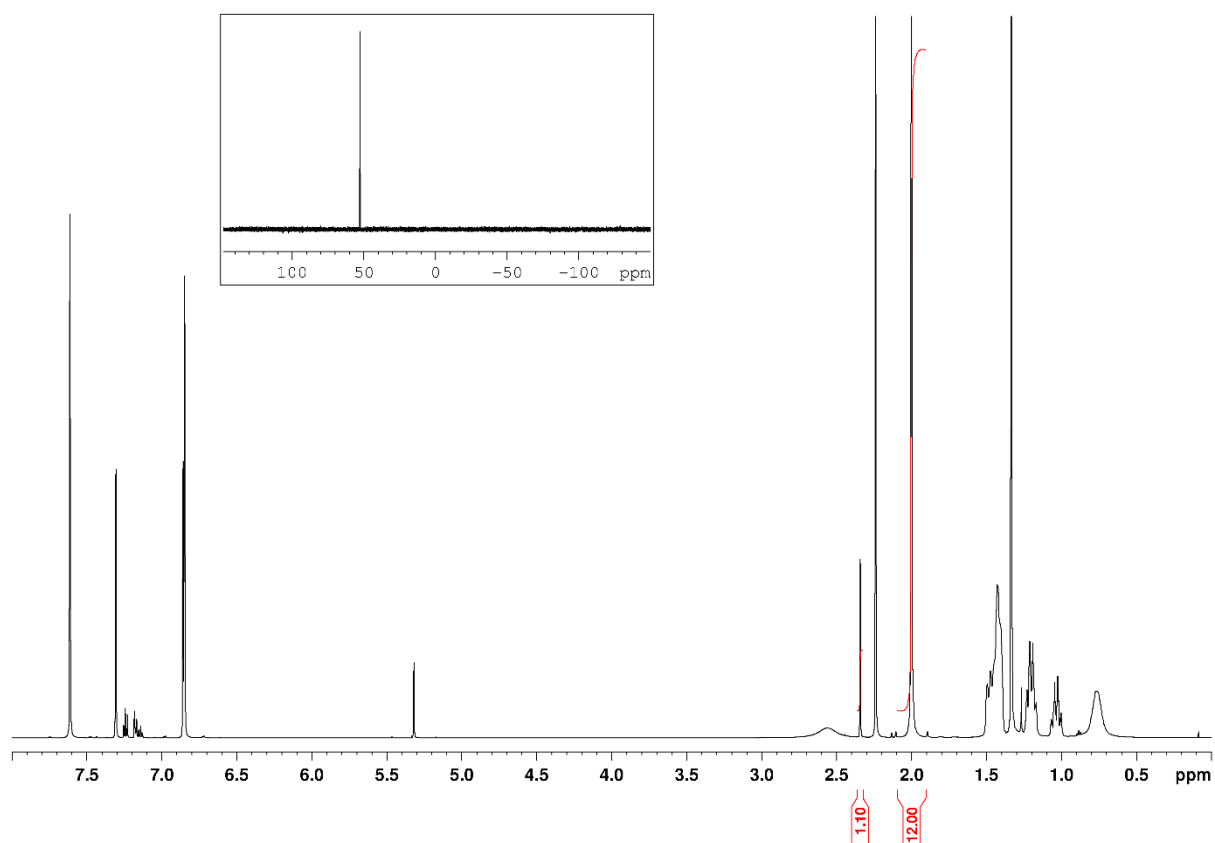


Figure S2. 600 MHz ^1H NMR (CD_2Cl_2 , 26 °C) and 243 MHz $^{31}\text{P}\{^1\text{H}\}$ NMR data (inset, CD_2Cl_2 , 26 °C): $^{\text{Mes}}\text{Pd-Cy} \times 0.5\text{C}_7\text{H}_8$.

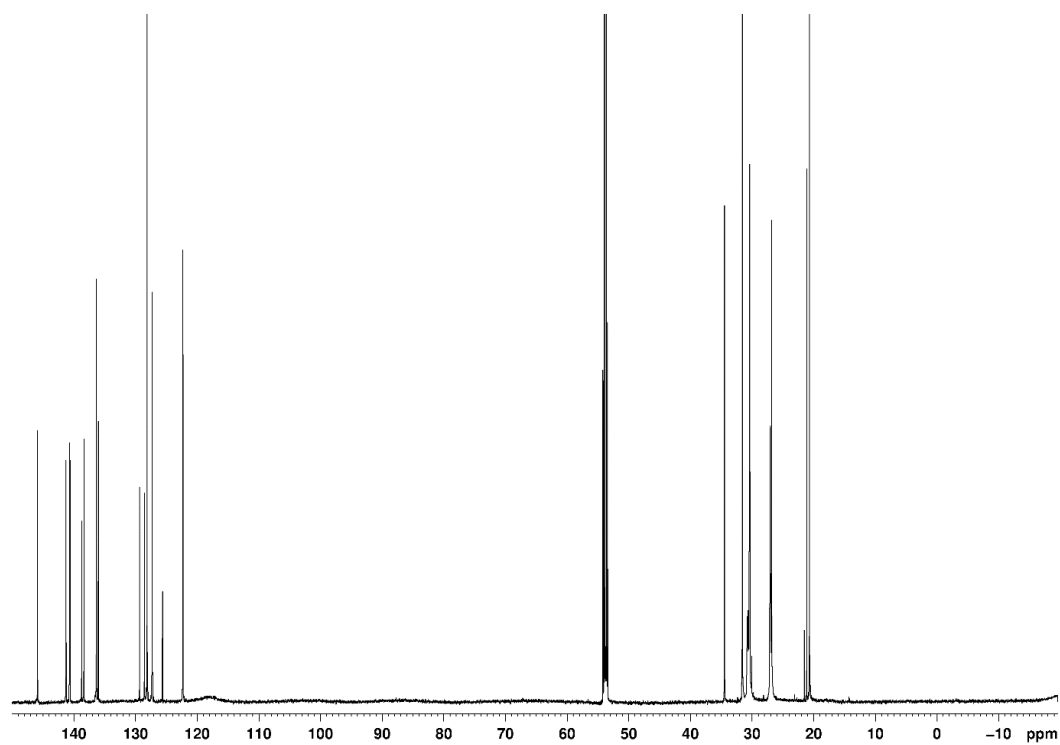


Figure S3. 150 MHz $^{13}\text{C}\{^1\text{H}\}$ NMR (CD_2Cl_2 , 26 °C): $^{\text{Mes}}\text{Pd-Cy} \times 0.5\text{C}_7\text{H}_8$.

6 Additional Information on UV/Vis/NIR Spectroscopy Data

For *in situ* generation of $[\text{MesM-L}]^+$ stock solutions of the neutral compound and the oxidizing agent in CH_2Cl_2 at r.t. were prepared. A four-sided transparent cell with a screw cap and septum was filled with 2.8 mL CH_2Cl_2 , and background spectra were recorded at $-90 \leq T \leq 20$ °C at 10 °C steps. The neutral compound is then transferred by syringe to the cuvette at $T \leq -80$ °C and a spectrum is recorded. Aliquots of 0.25 equiv., in the case of $[\text{MesNi-Cy}]^+$ one equiv., of oxidizing agent are added, and spectra were recorded after each addition. The obtained spectra were corrected by subtraction of the respective background of neat CH_2Cl_2 .

Due to insolubility at high concentrations the stock solution of $[\text{MesPd-Cy}]\text{BAR}^{\text{F24}}$ for measurements in PC were prepared in CH_2Cl_2 . 2.8 mL of PC are added to a four-sided transparent cell with a screw cap and septum, and background spectra were recorded at $-40 \leq T \leq 20$ °C. 15 μL of the stock solution is added four times and a spectrum is recorded after each addition.

Table S3. NIR data of $[\text{RM-L}]^+$ in CH_2Cl_2 solution.

	λ nm	ν cm^{-1}	$\Delta\nu_{1/2}$ cm^{-1}	$\epsilon / 10^4$ $\text{L mol}^{-1} \text{cm}^{-1}$	T K
$[\text{MesNi-Cy}]\text{NTf}_2$	2149	4653	1455	0.53	183
$[\text{MesNi-Cy}]\text{BAR}^{\text{F24}}$	2157	4636	1454	0.43	183
$[\text{MesPd-Cy}]\text{NTf}_2$	2216	4512 (4502)	1108 (1241)	1.5	193 (293)
$[\text{MesPd-Cy}]\text{BAR}^{\text{F24}}$	2210	4531 (4524)	1093 (1311)	1.5	183 (293)
$[\text{MesPd-Ph}]\text{NTf}_2$	2179	4589 (4596)	1100 (1260)	1.4	183 (293)
$[\text{MesPt-Cy}]\text{NTf}_2$	1526	6531 (6561)	1410 (1588)	1.8	193 (293)
$[\text{MesPt-Cy}]\text{BAR}^{\text{F24}}$	1530	6540 (6535)	1394 (1672)	2.2	183 (293)
$[\text{tBuPt-Cy}]\text{NTf}_2$	1682	6090 (5945)	2056 (1944)	1.5	183 (293)
$[\text{tBuPt-Ph}]\text{NTf}_2$	1539	6497 (6406)	1544 (1698)	1.7	223 (293)

^{Mes}Ni-Cy. UV/vis/NIR [183 K, CH₂Cl₂; λ/nm (ε/ 10³ M⁻¹ cm⁻¹)] = 331 (20.4), 448 (3.2), 558 (6.9), 658 (3.0), 1058 (1.3).

[^{Mes}Ni-Cy]BAR^{F24}. UV/vis/NIR [183 K, CH₂Cl₂; λ/nm (ε/ 10³ M⁻¹ cm⁻¹)] = 436 (5.1), 564 (6.3), 657 (3.0), 1089 (3.1), 1297 (2.0), 2157 (3.7).

[^{Mes}Ni-Cy]NTf₂. UV/vis/NIR [183 K, CH₂Cl₂; λ/nm (ε/ 10³ M⁻¹ cm⁻¹)] = 332 (20.2), 434 (6.8), 500 (6.1), 568 (6.7), 685 (3.3), 1098 (4.2), 1297 (2.9), 2149 (5.4).

[^{Mes}Pd-Cy]NTf₂. UV/vis/NIR [193 K, CH₂Cl₂; λ/nm (ε/ 10³ M⁻¹ cm⁻¹)] = 436 (27.0), 538 (7.2), 797 (1.2), 863 (1.8), 1131 (0.5), 2216 (20.0).

[^{Mes}Pd-Ph]NTf₂. UV/vis/NIR [183 K, CH₂Cl₂; λ/nm (ε/ 10³ M⁻¹ cm⁻¹)] = 407 (21.6), 534 (6.1), 832 (1.2), 1174 (0.8), 2179 (14.0). Diffusion coefficient *D* of Dimer = 4.8×10⁻¹⁰ m²/s (293 K, CD₂Cl₂).

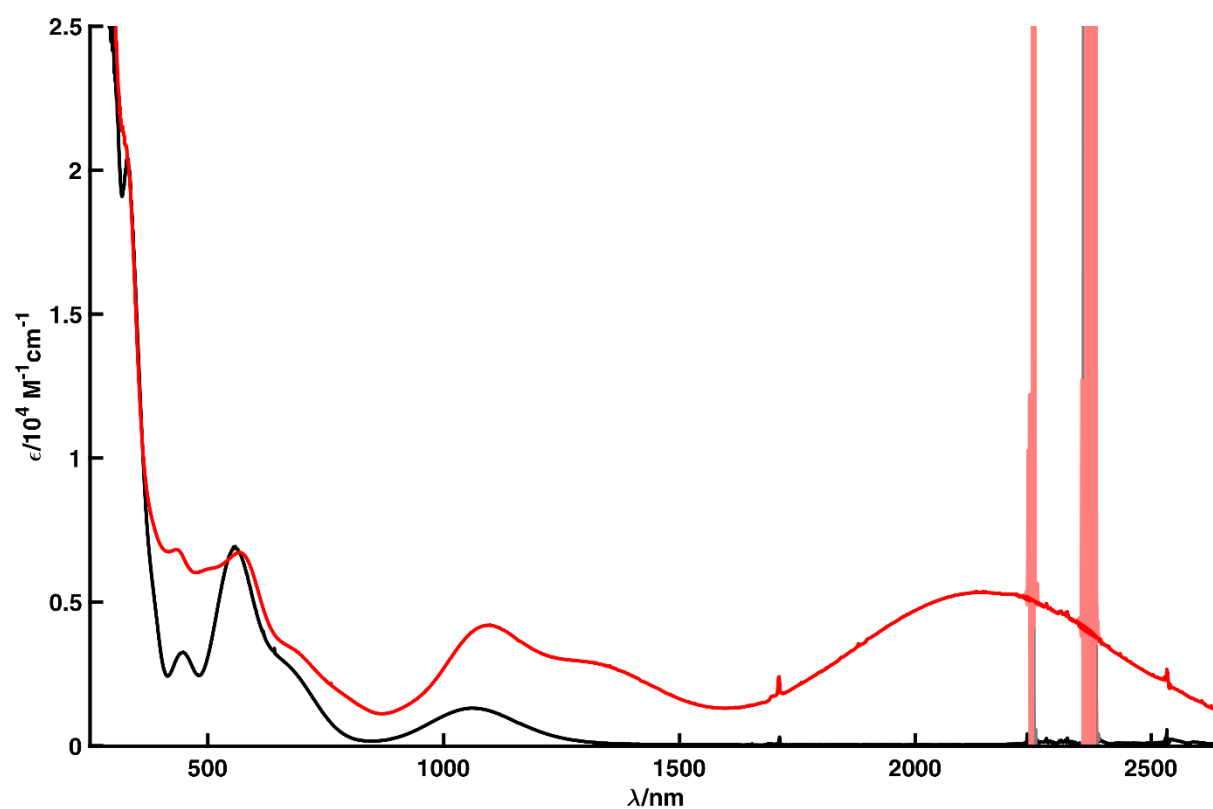


Figure S4. UV/vis/NIR spectra (-90 °C, CH₂Cl₂): 0.144 mM [^{Mes}Ni-Cy]NTf₂ (red) and 0.151 mM ^{Mes}Ni-Cy (black).

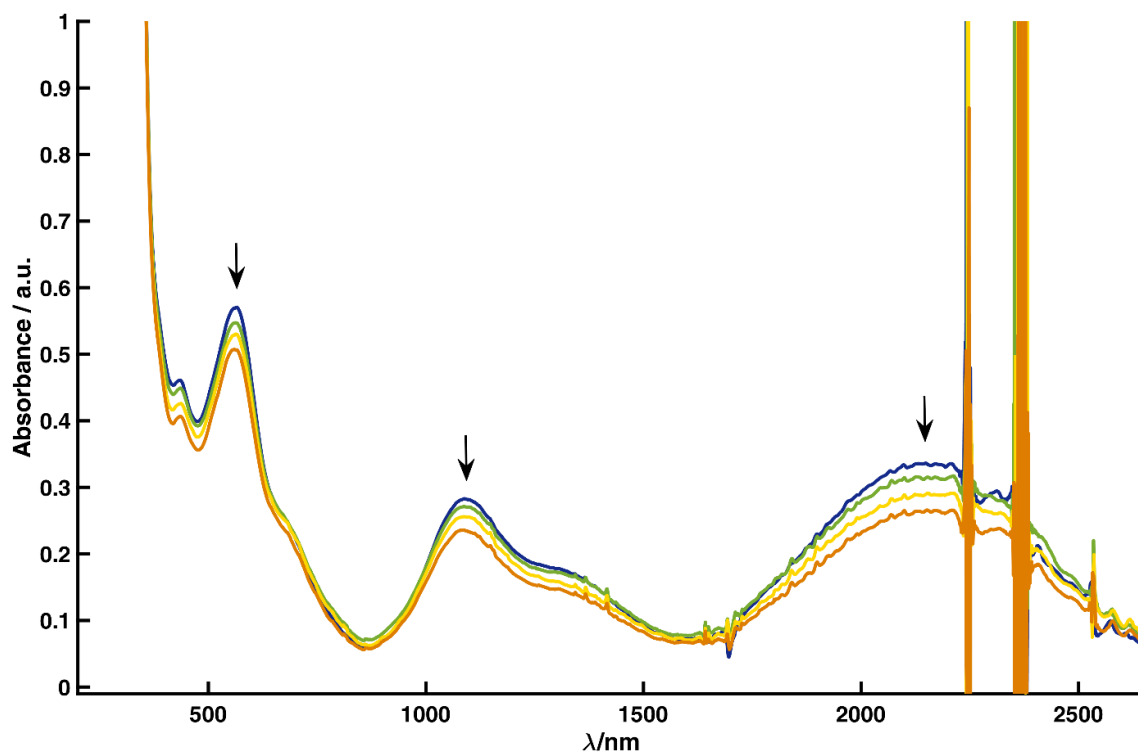


Figure S5. UV/vis/NIR spectra ($T = -90\text{ }^{\circ}\text{C}$, CH_2Cl_2): 0.087 mM $[\text{MesNi-Cy}]\text{BAR}^{\text{F}24}$, evolution of spectra monitored over 2 h.

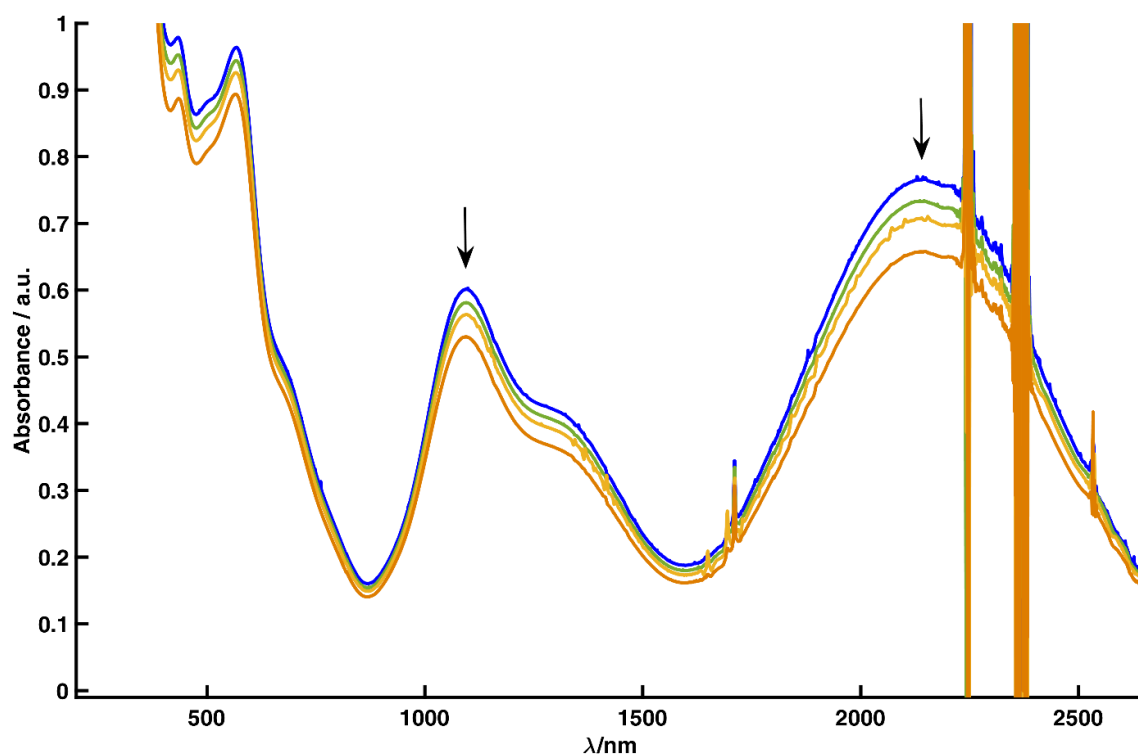


Figure S6. UV/vis/NIR spectra ($T = -90\text{ }^{\circ}\text{C}$, CH_2Cl_2): 0.144 mM $[\text{MesNi-Cy}]\text{NTf}_2$, evolution of spectra monitored over 40 min.

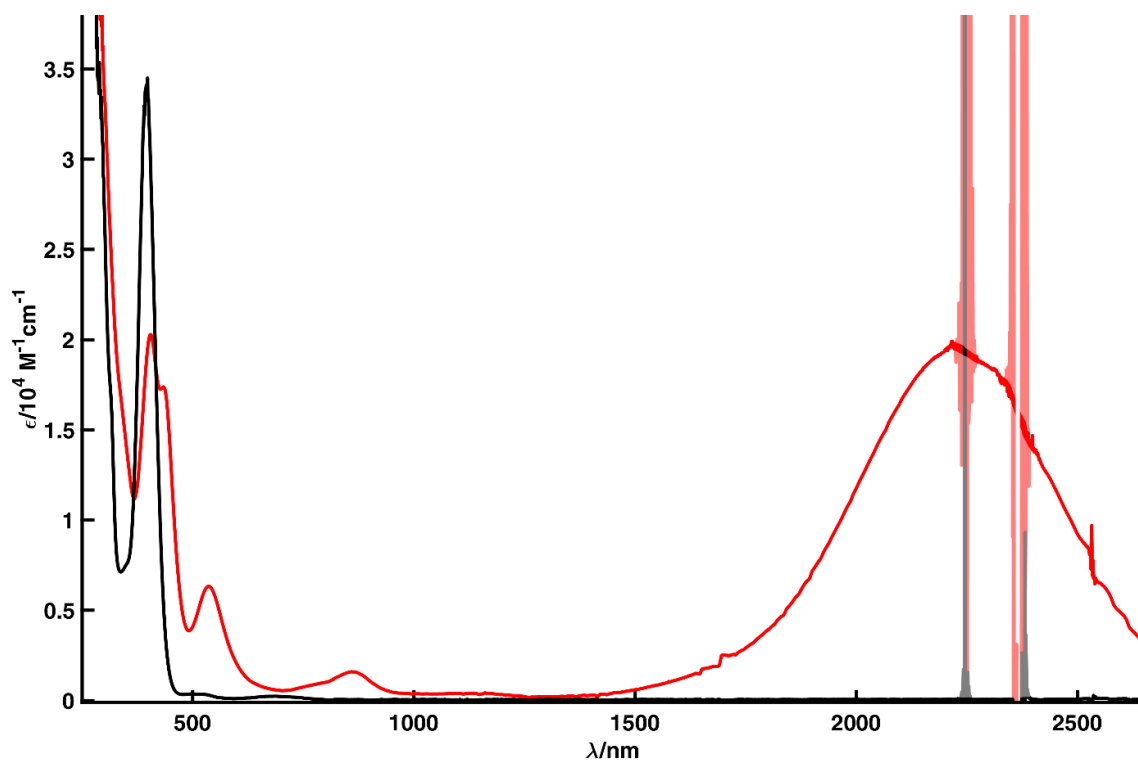


Figure S7. UV/vis/NIR spectra ($T = -80 \text{ }^\circ\text{C}$, CH_2Cl_2): $0.103 \text{ mM } [\text{MesPd-Cy}]\text{NTf}_2$ (red) and $0.111 \text{ mM } \text{MesPd-Cy} \times 0.5\text{C}_7\text{H}_8$ (black).

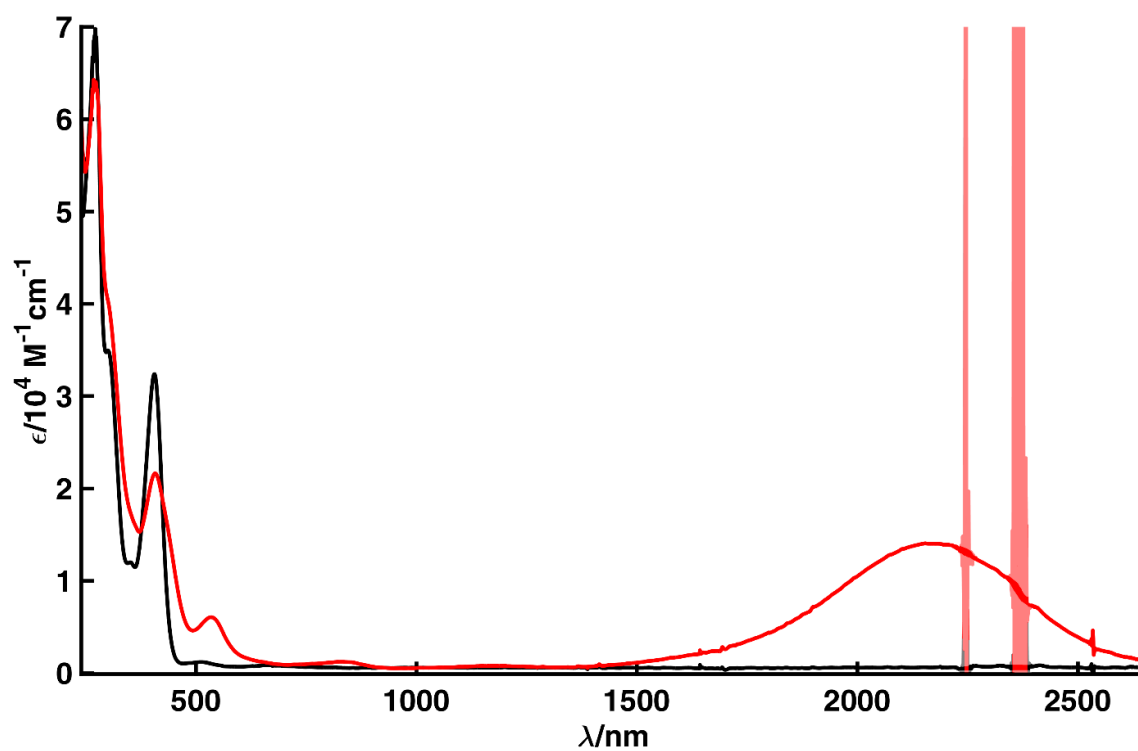


Figure S8. UV/vis/NIR spectra ($T = -90 \text{ }^\circ\text{C}$, CH_2Cl_2): $0.055 \text{ mM } [\text{MesPd-Ph}]\text{NTf}_2$ (red) and $0.054 \text{ mM } \text{MesPd-Ph} \times \text{C}_7\text{H}_8$ (black).

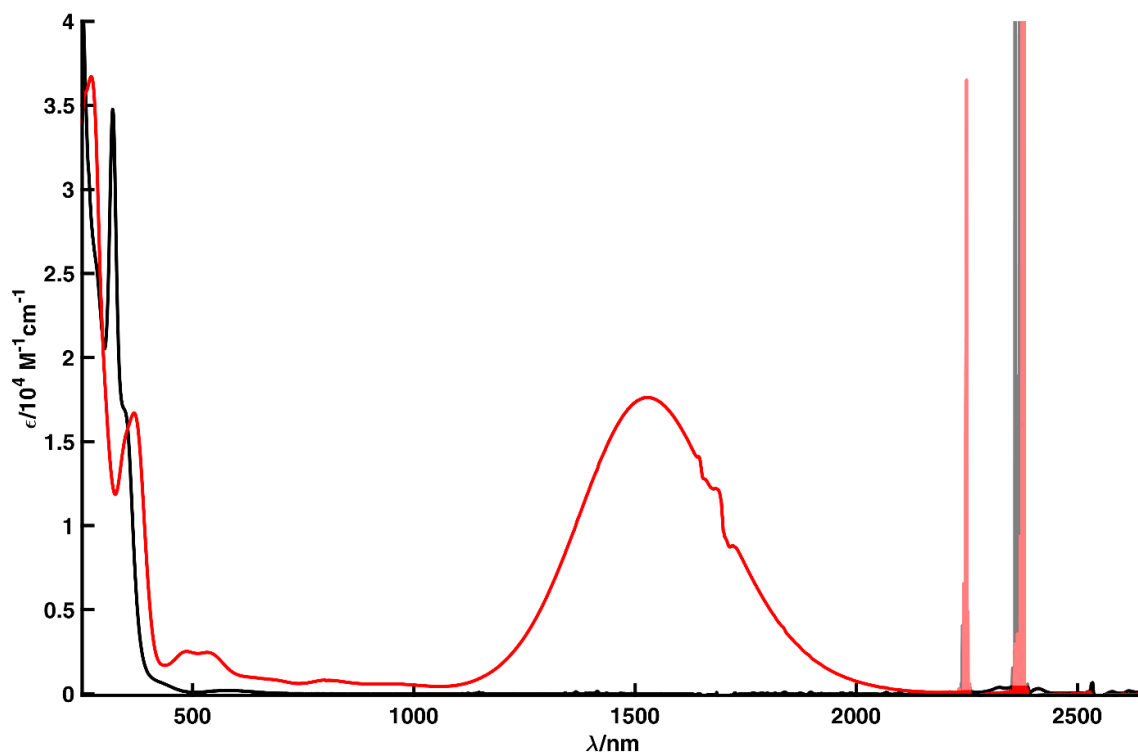


Figure S9. UV/vis/NIR spectra ($T = 20^\circ\text{C}$, CH_2Cl_2): $0.057 \text{ mM } [\text{MesPt-Cy}]\text{NTf}_2$ (red) and $0.052 \text{ mM } \text{MesPt-Cy} \times 1,2\text{-C}_6\text{H}_4\text{F}_2$.

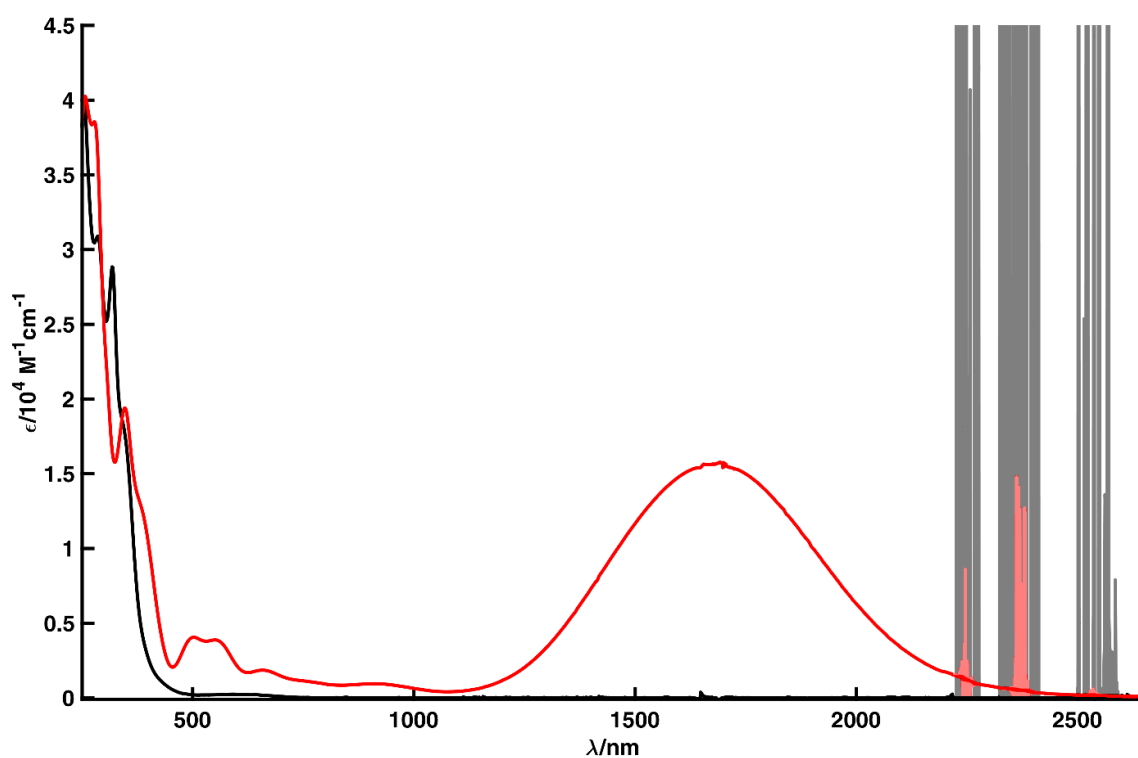


Figure S10. VT UV/vis/NIR spectra ($T = 20^\circ\text{C}$, CH_2Cl_2): $0.037 \text{ mM } [\text{tBuPt-Cy}]\text{NTf}_2$ and $0.063 \text{ mM } \text{tBuPt-Cy}$.

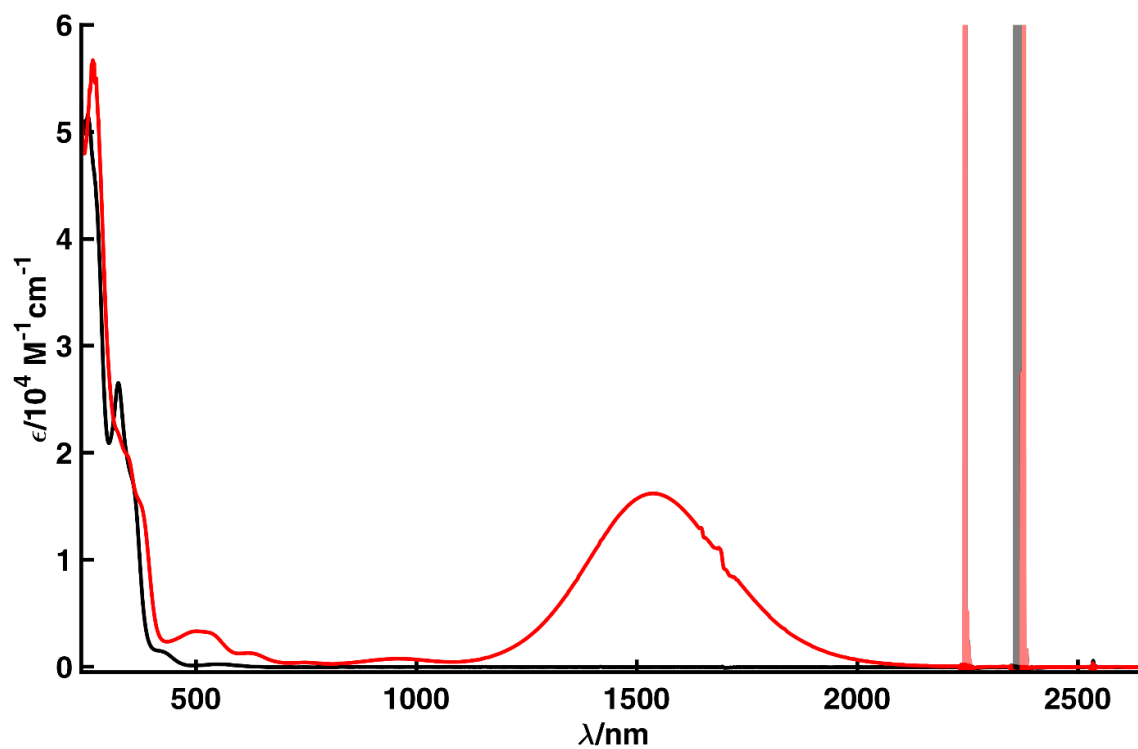


Figure S11. UV/vis/NIR spectra ($T = -50 \text{ }^\circ\text{C}$, CH_2Cl_2): $0.064 \text{ mM } [{}^{\text{tBu}}\text{Pt-Ph}]\text{NTf}_2$ and $0.065 \text{ mM } {}^{\text{tBu}}\text{Pt-Ph}\times\text{C}_7\text{H}_8$.

7 Additional X-Band cw-EPR Data

For the general *in situ* preparation, 4 mM stock solutions of the neutral complexes in toluene and of the oxidizing agent in CH_2Cl_2 were prepared at r.t. For delicate samples, 0.25 mL of the neutral compound were transferred by syringe into an NMR tube sealed with a septum and cooled in an acetone/dry ice bath at $-80\text{ }^\circ\text{C}$. To this solution, 0.25 mL of the stock solution of the oxidizing agent were added slowly. The reactant solutions were mixed agitating the tube carefully, and finally frozen in liquid N_2 .

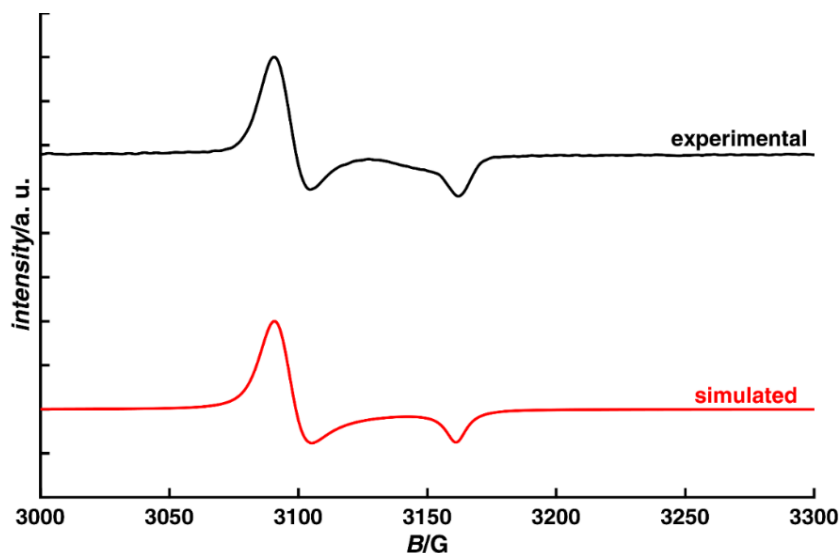


Figure S12. X-Band cw-EPR spectra (1:1 $\text{C}_7\text{H}_8/\text{CH}_2\text{Cl}_2$, 110 K): $[\text{MesNi-Cy}]\text{BAR}^{\text{F}24}$, microwave frequency = 9.256458 GHz, microwave power = 0.5024 mW, modulation amplitude = 0.2 mT, Simulated parameters: $g_x = 2.138$, $g_{y,z} = 2.092$; full line width at half maximum (Gaussian; Lorentzian) $lw = [0.127; 0.946]$ mT, $g\text{Strain} = [0.00696; 0]$.

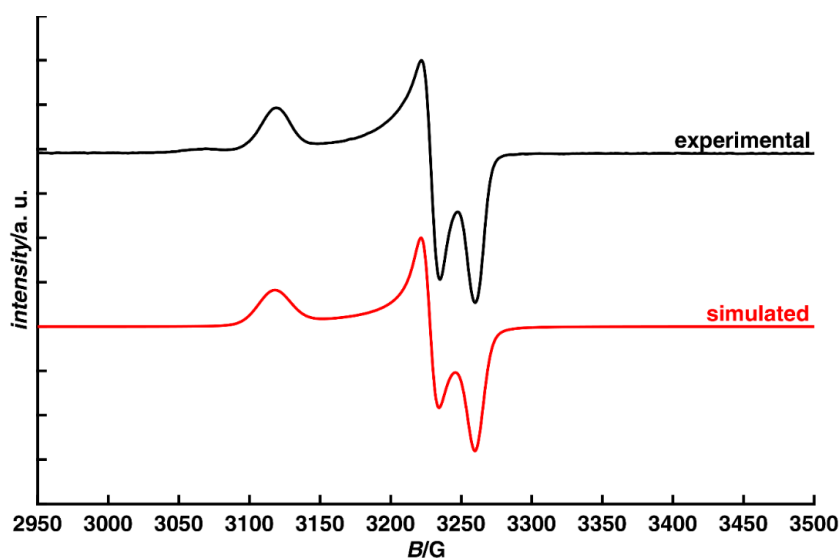


Figure S13. X-Band cw-EPR spectra (1:1 $\text{C}_7\text{H}_8/\text{CH}_2\text{Cl}_2$, 110 K): $[\text{MesNi-Cy}]\text{NTf}_2$, microwave frequency = 9.296928 GHz, microwave power = 0.7962 mW, modulation amplitude = 0.2 mT, Simulated parameters: $g_x = 2.131$, $g_y = 2.058$, $g_z = 2.038$; full line width at half maximum (Gaussian; Lorentzian) $lw = [0.929; 0.437]$ mT, $g\text{Strain} = [0.0155; 0; 0.00410]$.

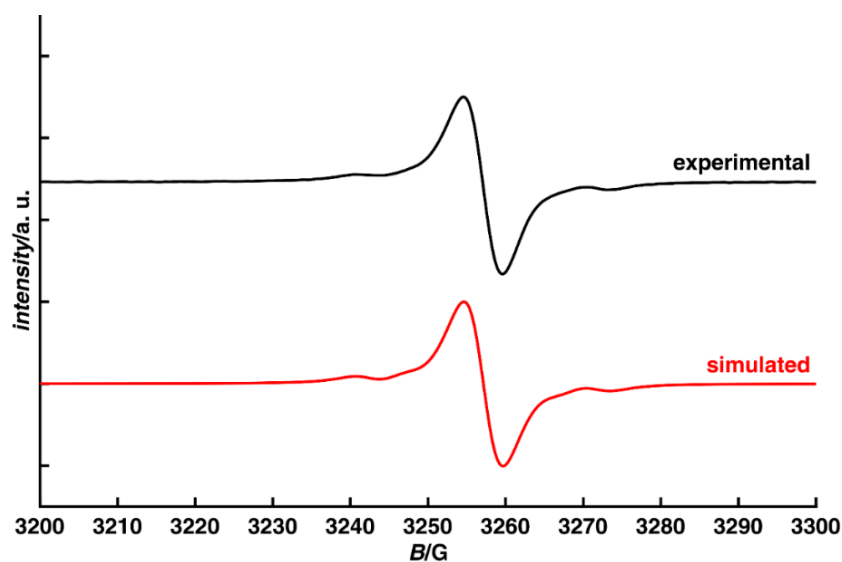


Figure S14. X-Band cw-EPR spectra (1:1 C_7H_8/CH_2Cl_2 , 293 K): $[^{Mes}Pd-Cy]NTf_2$, microwave frequency = 9.293992 GHz, microwave power = 0.0317 mW, modulation amplitude = 0.0702 mT, Simulated parameters: $g_{iso} = 2.039$, $A_{iso}(^{105}Pd) = 17$ MHz; full line width at half maximum (Gaussian; Lorentzian) $lw = [0.293; 0.634]$ mT.

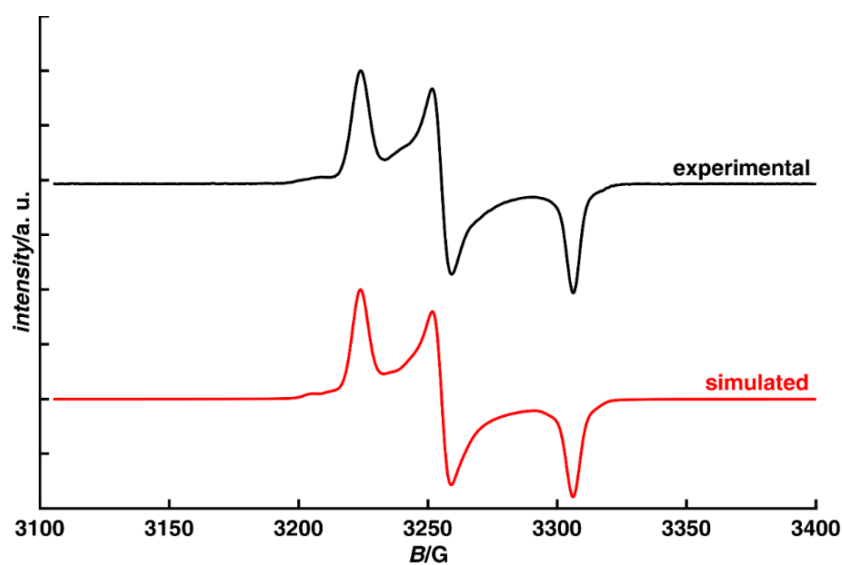


Figure S15. X-Band cw-EPR spectra (1:1 C_7H_8/CH_2Cl_2 , 110 K): $[^{Mes}Pd-Cy]NTf_2$, microwave frequency = 9.305645 GHz, microwave power = 0.1262 mW, modulation amplitude = 0.0701 mT, Simulated parameters: $g_x = 2.062$, $g_y = 2.042$, $g_z = 2.011$, $A_x(^{105}Pd) = 22$, $A_y(^{105}Pd) = 7$, $A_z(^{105}Pd) = 10$ MHz; full line width at half maximum (Gaussian; Lorentzian) $lw = [0.526; 0.172]$ mT, $gStrain = [0.00197; 0.0006; 0]$.

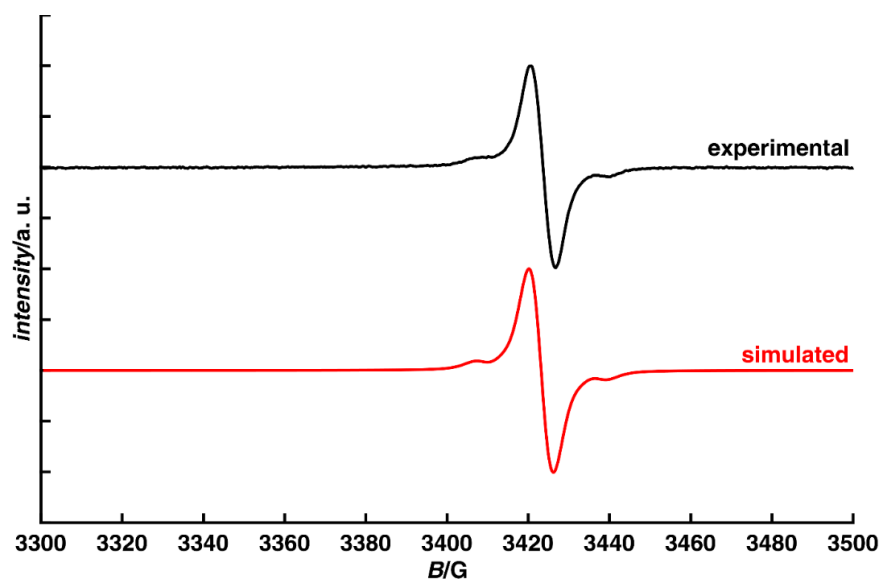


Figure S16. X-Band cw-EPR spectra (1:1 C₇H₈/CH₂Cl₂, 293 K): [MesPd-Ph]NTf₂, microwave frequency = 9.7548510 GHz, microwave power = 2 mW, modulation amplitude = 0.4767 mT, Simulated parameters: $g_{\text{iso}} = 2.036$, $A_{\text{iso}}(^{105}\text{Pd}) = 16$ MHz; full line width at half maximum (Gaussian; Lorentzian) $l_w = [0.486; 0.535]$ mT.

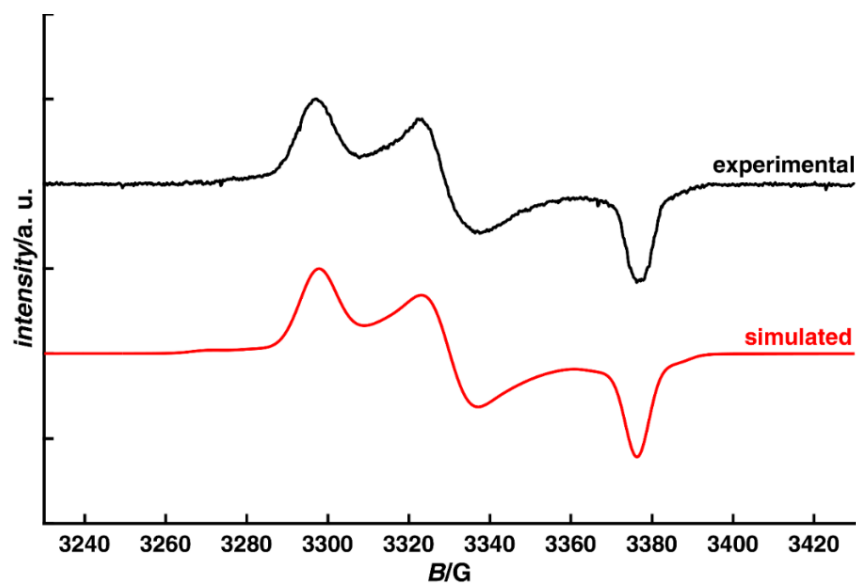


Figure S17. X-Band cw-EPR spectra (1:1 C₇H₈/CH₂Cl₂, 77 K): [MesPd-Ph]NTf₂, microwave frequency = 9.4982505 GHz, microwave power = 2 mW, modulation amplitude = 0.26804 mT, Simulated parameters: $g_x = 2.058$, $g_y = 2.038$, $g_z = 2.010$, $A_x(^{105}\text{Pd}) = 31$, $A_y(^{105}\text{Pd}) = 13$, $A_z(^{105}\text{Pd}) = 12$ MHz; full line width at half maximum (Gaussian; Lorentzian) $l_w = [0.0683; 0.0857]$ mT, $g\text{Strain} = [0.00625; 0.00711; 0.00385]$.

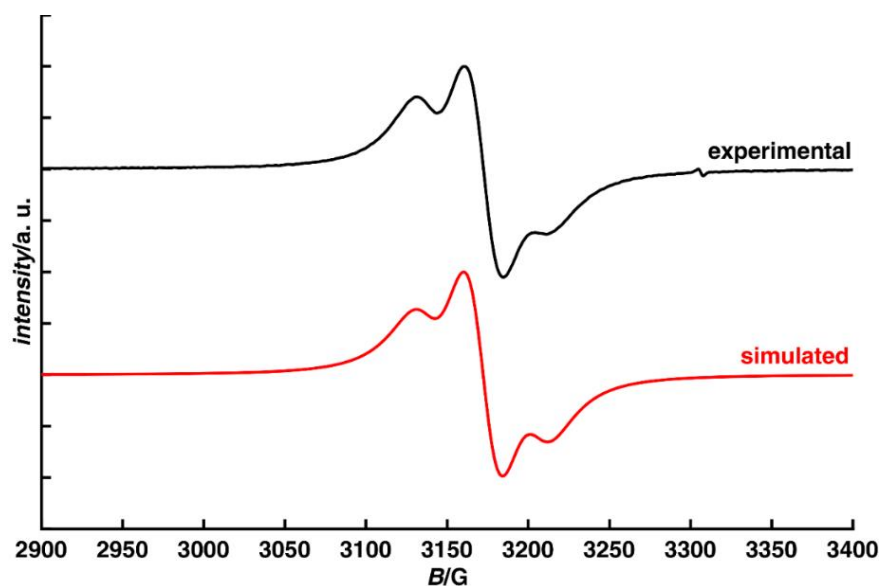


Figure S18. X-Band cw-EPR spectra (1:1 C₇H₈/CH₂Cl₂, 293 K): [MesPt-Cy]NTf₂, microwave frequency = 9.297227 GHz, microwave power = 2 mW, modulation amplitude = 0.3 mT, Simulated parameters: $g_{\text{iso}} = 2.094$, $A_{\text{iso}}(^{195}\text{Pt}) = 192$ MHz; full line width at half maximum (Gaussian; Lorentzian) $h\nu = [0.400; 4.501]$ mT.

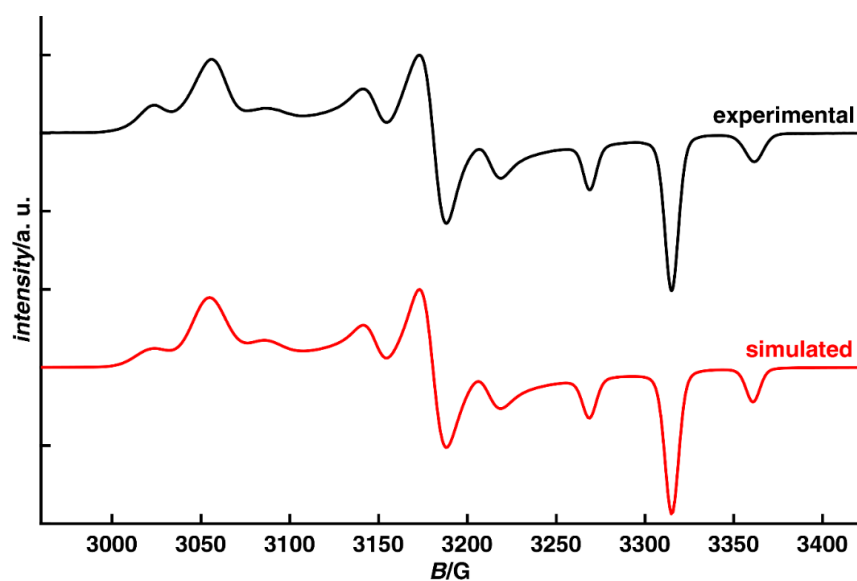


Figure S19. X-Band cw-EPR spectra (1:1 C₇H₈/CH₂Cl₂, 110 K): [MesPt-Cy]NTf₂, microwave frequency = 9.306359 GHz, microwave power = 2 mW, modulation amplitude = 0.3 mT, Simulated parameters: $g_x = 2.177$, $g_y = 2.091$, $g_z = 2.006$, $A_x(^{195}\text{Pt}) = 191$, $A_y(^{195}\text{Pt}) = 186$, $A_z(^{195}\text{Pt}) = 259$ MHz; full line width at half maximum (Gaussian; Lorentzian) $h\nu = [0.788; 0.226]$ mT, $g\text{Strain} = [0.0142; 0.00679; 0]$.

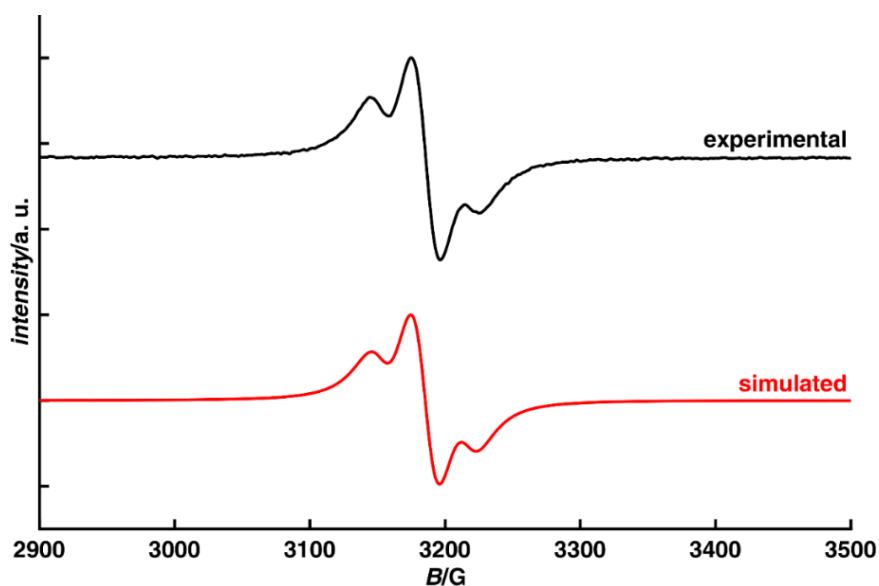


Figure S20. X-Band cw-EPR spectra (1:1 C₇H₈/CH₂Cl₂, 293 K): [tBuPt-Ph]BAR^{F24}, microwave frequency = 9.294807 GHz, microwave power = 0.5024 mW, modulation amplitude = 0.2 mT, Simulated parameters: $g_{\text{iso}} = 2.085$, $A_{\text{iso}}(^{195}\text{Pt}) = 181$ MHz; full line width at half maximum (Gaussian; Lorentzian) $lw = [0.520; 3.901]$ mT.

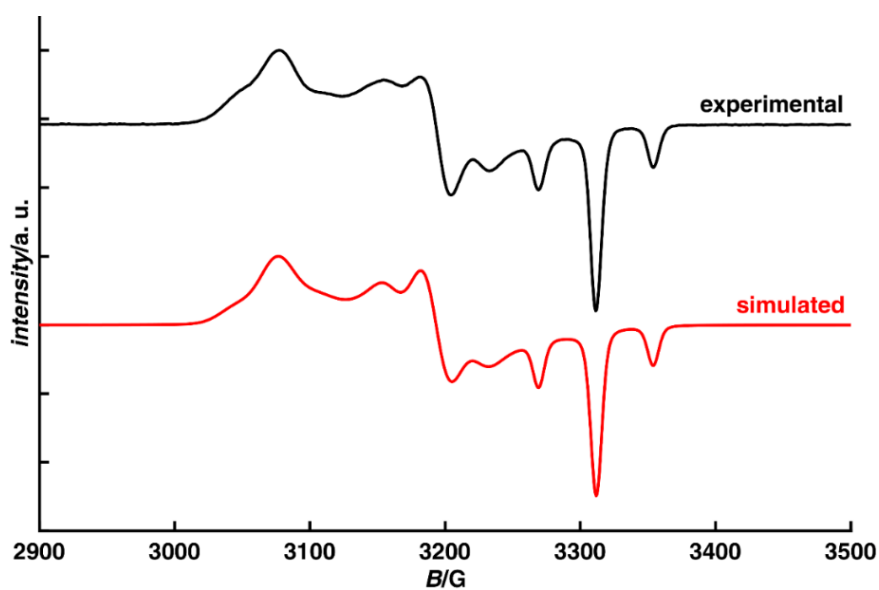


Figure S21. X-Band cw-EPR spectra (1:1 C₇H₈/CH₂Cl₂, 110 K): [tBuPt-Ph]BAR^{F24}, microwave frequency = 9.304133 GHz, microwave power = 0.5024 mW, modulation amplitude = 0.2 mT, Simulated parameters: $g_x = 2.162$, $g_y = 2.082$, $g_z = 2.007$, $A_x(^{195}\text{Pt}) = 178$, $A_y(^{195}\text{Pt}) = 177$, $A_z(^{195}\text{Pt}) = 238$ MHz; full line width at half maximum (Gaussian; Lorentzian) $lw = [0.766; 0.325]$ mT, $g\text{Strain} = [0.0194; 0.0129; 0.00122]$.

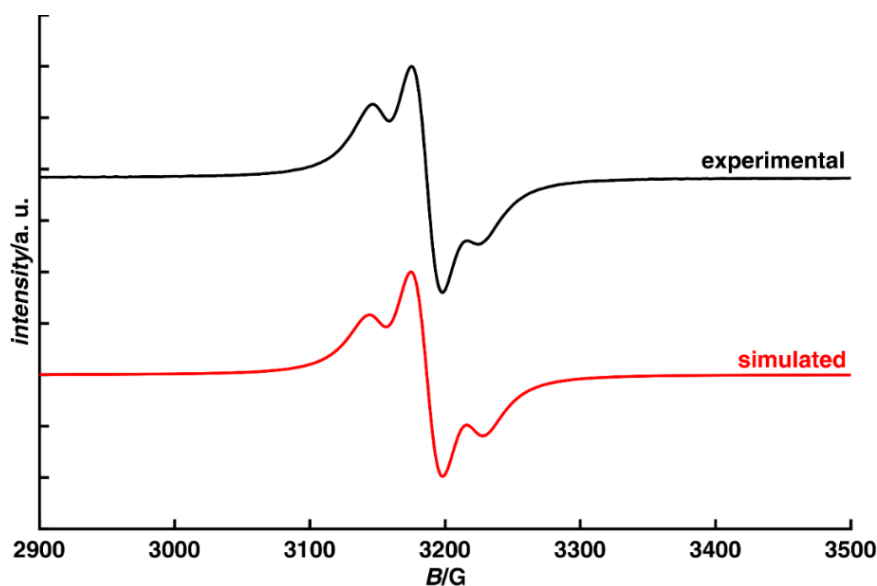


Figure S22. X-Band cw-EPR spectra (1:1 C_7H_8/CH_2Cl_2 , 293 K): $[^{tBu}Pt-Ph]NTf_2$, microwave frequency = 9.295042 GHz, microwave power = 2 mW, modulation amplitude = 0.3 mT, Simulated parameters: $g_{iso} = 2.084$, $A_{iso}(^{195}Pt) = 195$ MHz; full line width at half maximum (Gaussian; Lorentzian) $lw = [0.689; 4.221]$ mT.

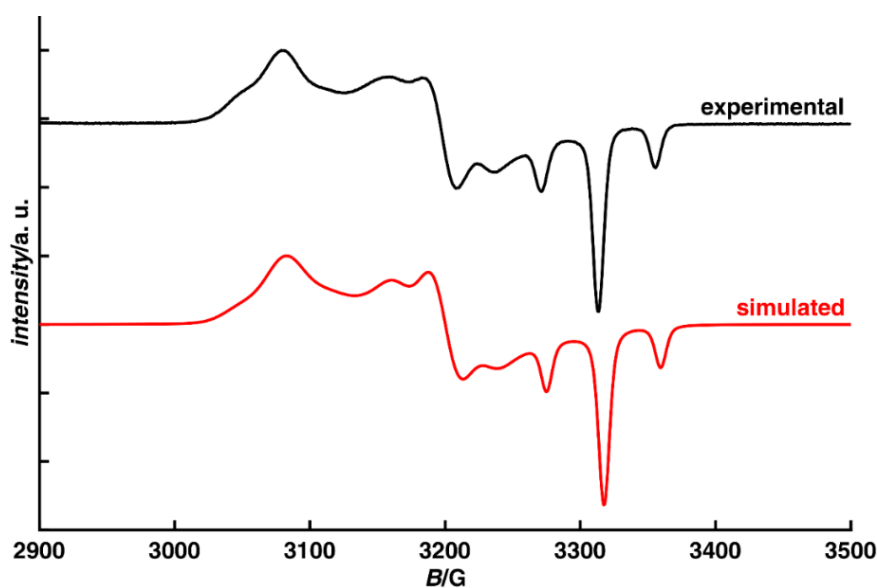


Figure S23. X-Band cw-EPR spectra (1:1 C_7H_8/CH_2Cl_2 , 123 K): $[^{tBu}Pt-Ph]NTf_2$, microwave frequency = 9.304748 GHz, microwave power = 2 mW, modulation amplitude = 0.3 mT, Simulated parameters: $g_x = 2.158$, $g_y = 2.078$, $g_z = 2.004$; $A_x(^{195}Pt) = 185$, $A_y(^{195}Pt) = 175$, $A_z(^{195}Pt) = 237$ MHz; full line width at half maximum (Gaussian; Lorentzian) $lw = [0.676; 0.455]$ mT, $gStrain = [0.0212; 0.0141; 0.000747]$.

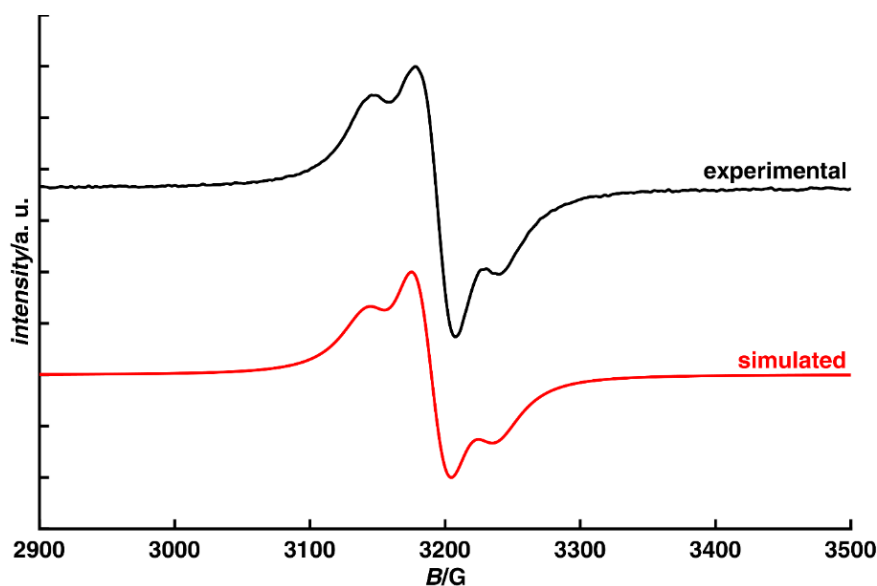


Figure S24. X-Band cw-EPR spectra (1:1 C₇H₈/CH₂Cl₂, 293 K): [tBuPt-Cy]NTf₂, microwave frequency = 9.293009 GHz, microwave power = 0.5 mW, modulation amplitude = 0.3 mT, Simulated parameters: $g_{\text{iso}} = 2.079$; $A_{\text{iso}}(^{195}\text{Pt}) = 214$ MHz, full line width at half maximum (Gaussian; Lorentzian) $l_w = [1.415 \ 4.778]$ mT.

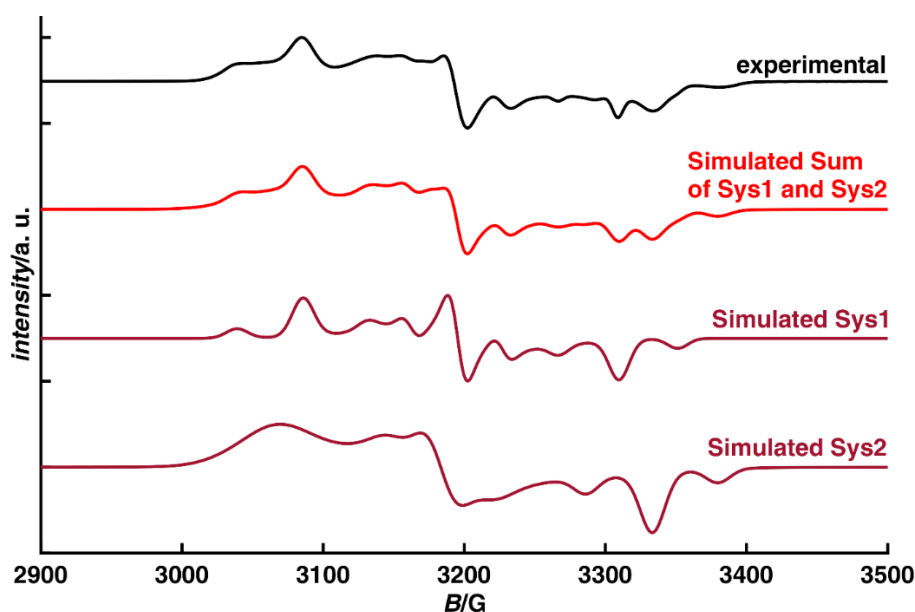


Figure S25. X-Band cw-EPR spectra (1:1 C₇H₈/CH₂Cl₂, 123 K): [tBuPt-Cy]NTf₂, microwave frequency = 9.306693 GHz, microwave power = 0.7962 mW, modulation amplitude = 0.3 mT, Simulated parameters for System 1 (Sys1): $g_x = 2.155$, $g_y = 2.081$, $g_z = 2.009$; $A_x(^{195}\text{Pt}) = 280$, $A_y(^{195}\text{Pt}) = 189$, $A_z(^{195}\text{Pt}) = 237$ MHz; full line width at half maximum (Gaussian; Lorentzian) $l_w = [1.2909; 0]$ mT, $g\text{Strain} = [0.00867; 0.00121; 0.00645]$, weight = 0.794. Simulated parameters for System 2 (Sys2): $g_x = 2.169$, $g_y = 2.089$, $g_z = 1.995$; $A_x(^{195}\text{Pt}) = 168$, $A_y(^{195}\text{Pt}) = 173$, $A_z(^{195}\text{Pt}) = 261$ MHz; full line width at half maximum (Gaussian; Lorentzian) $l_w = [1.382; 0.396]$ mT, $g\text{Strain} = [0.0328; 0.0141; 0.00748]$, weight = 1.432.

8 Additional Electrochemical Data

Table S4. CV data measured in CH₂Cl₂ at 17 °C in 0.1 M nBu₄NPF₆. *E*/ mV vs. Fc/[Fc]⁺, Fc = ferrocene; *E*(100 mVs⁻¹) for electrochemically quasi- (qr) or irreversible (ir) processes.

	<i>E</i> ⁰ ₁	<i>E</i> ⁰ ₂	Δ <i>E</i> ⁰ ₁₋₂
^{Mes} Ni-Cy	134 (ir)	941 (ir)	807
^{Mes} Pd-Cy	172	854	682
^{Mes} Pd-Ph	192	728 (ir)	536
^{Mes} Pt-Cy	32	806	774
^{Mes} Pt-Ph ^[a]	60	727	667
^{tBu} Pt-Cy	20	668	648
^{tBu} Pt-Ph	72	679 (qr)	607

[a] Data included for comparison, cf. ref. ^[13].

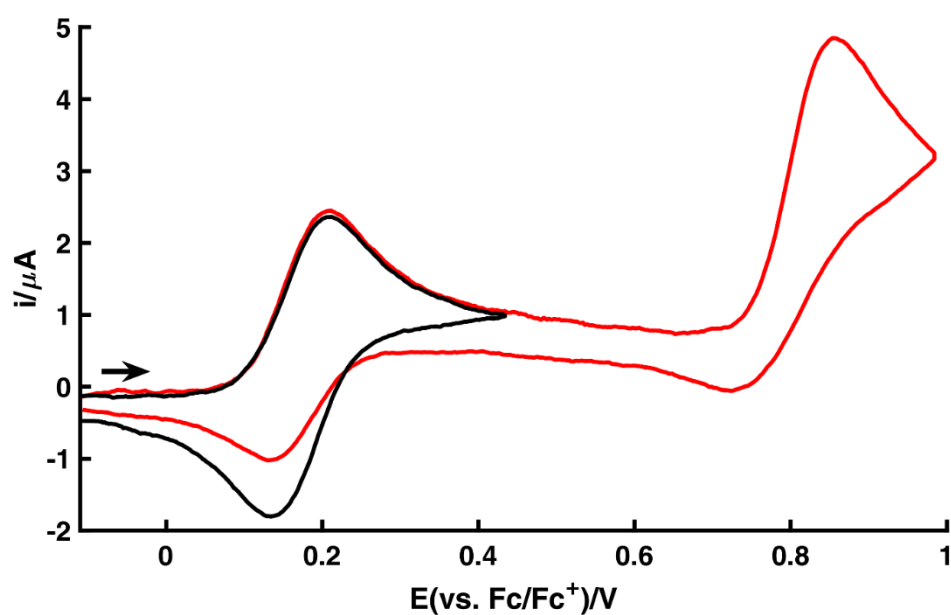


Figure S26. CV *i*-*E* curves (0.1 M nBu₄NPF₆/CH₂Cl₂, 100 mV s⁻¹, 17 °C): 0.135mM ^{Mes}Pd-Cy×0.5C₇H₈ (black, potential sweep direction reversed at 0.433 V).

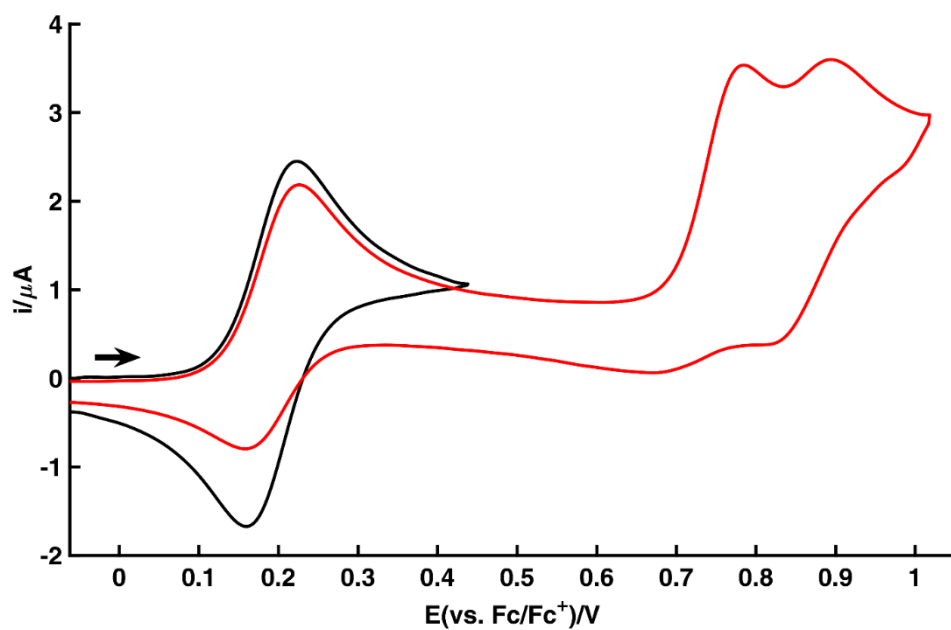


Figure S27. CV *i*-*E* curves (0.1 M nBu₄NPF₆/CH₂Cl₂, 100 mV s⁻¹, 17 °C): 0.093 mM ^{Mes}Pd-Ph (red); 0.086 mM ^{Mes}Pd-Ph (black, potential sweep direction reversed at 0.44 V).

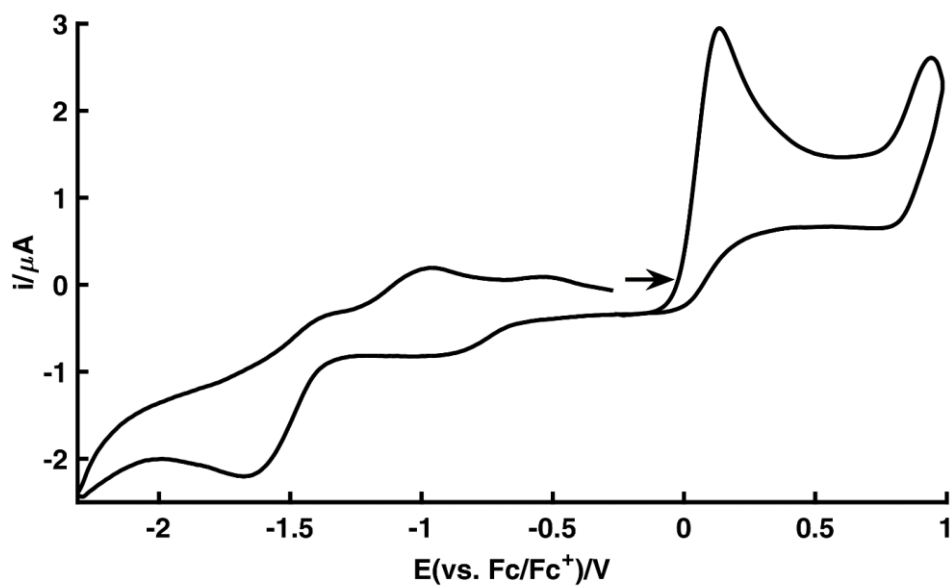


Figure S28. CV *i*-*E* curves (0.1 M nBu₄NPF₆/CH₂Cl₂, 100 mV s⁻¹, 17 °C): 0.06 mM ^{Mes}Ni-Cy.

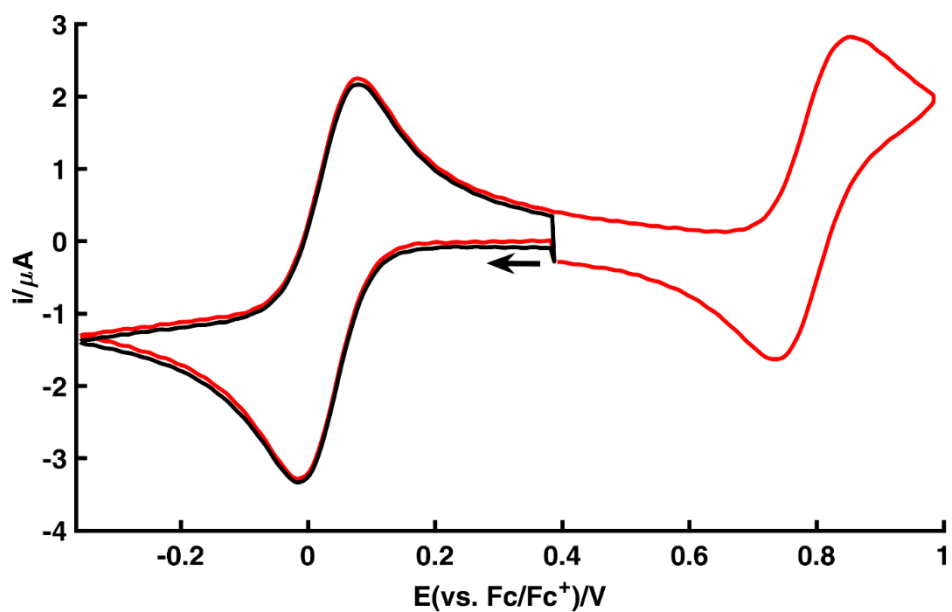


Figure S29. CV i - E curves (0.1 M $n\text{Bu}_4\text{NPF}_6/\text{CH}_2\text{Cl}_2$, 100 mV s^{-1} , $17 \text{ }^\circ\text{C}$): 0.182 mM $[\text{MesPt-Cy}]\text{NTf}_2$ (black, potential sweep finished at 0.39 V).

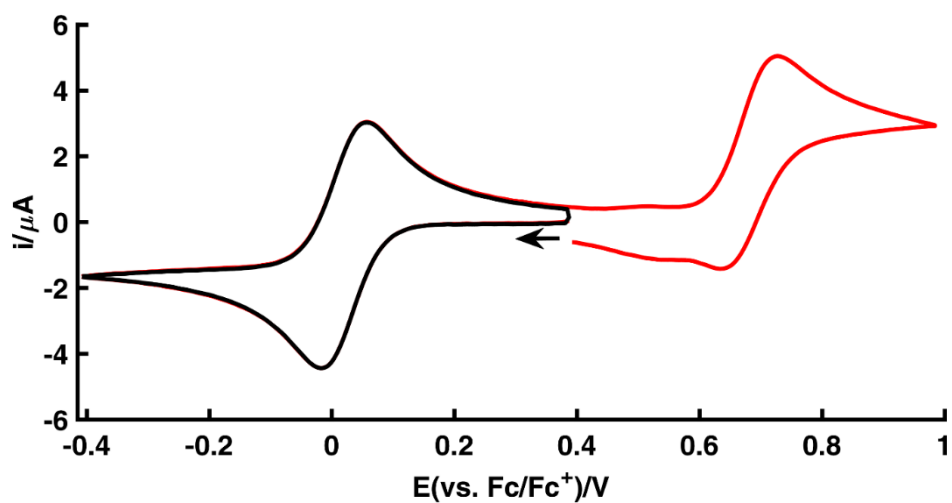


Figure S30. CV i - E curves (0.1 M $n\text{Bu}_4\text{NPF}_6/\text{CH}_2\text{Cl}_2$, 100 mV s^{-1} , $17 \text{ }^\circ\text{C}$): 0.213 mM $[\text{tBuPt-Cy}]\text{NTf}_2$ (black, potential sweep finished at 0.39 V).

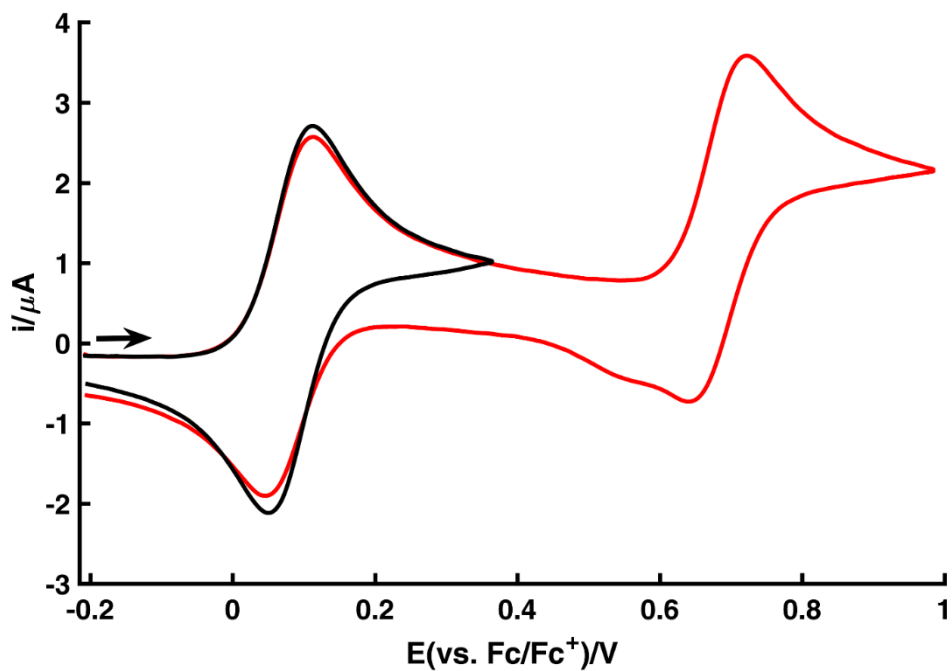


Figure S31. CV i - E curves (0.1 M nBu₄NPF₆/CH₂Cl₂, 100 mV s⁻¹, 17 °C): 0.135 mM ^tBuPt-Ph (black, potential sweep direction reversed at 0.37 V).

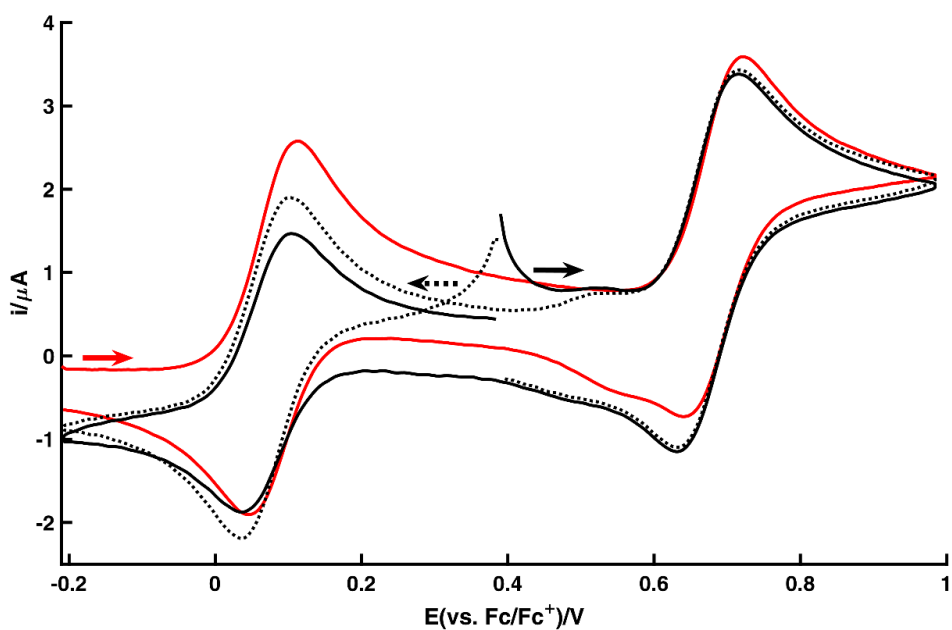


Figure S32. CV i - E curves (0.1 M nBu₄NPF₆/CH₂Cl₂, 100 mV s⁻¹, 17 °C): 0.135 mM ^tBuPt-Ph×C₇H₈ (red), and 0.189 mM [^tBuPt-Ph]NTf₂ (black, solid and dashed).

9 Additional Computational Data

9.1 General Information

All calculations were performed using the ADF2017.111 release^[26] or ORCA version 4.0.1^[27].

Structures optimization and EPR calculations were done in ADF, electronic excitations were computed using ORCA. Structures were optimized using the PBE0-1/3-D3(BJ) functional (using the PBE0-D3(BJ) parameter for the dispersion correction and 33.333 % exact exchange), ZORA and the ZORA-TZP basis set. All ADF calculations used COSMO with the parameters for CH₂Cl₂ ($\epsilon = 8.93$, $R_{\text{solv}} = 2.94$), a “good” numerical quality. The convergence criteria were set to $5e-7$ for the commutator of Fock and density matrix in the SCF and to $1e-5$ hartree for energy change and $1e-4$ hartree/bohr for gradient change in the structure optimization. EPR parameters were calculated using the collinear ZORA(SO) approach, the ZORA-TZ2P basis set and a Gaussian nuclear model.

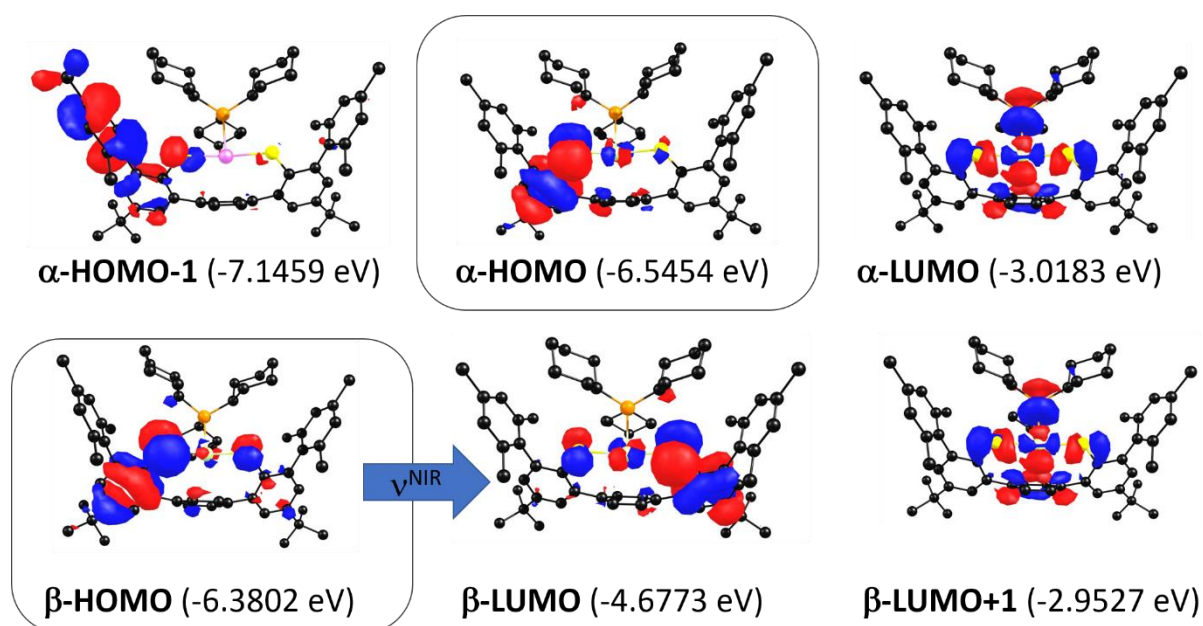
For the TD-DFT calculations, a CPCM model with the COSMO $f(\epsilon)$ and the parameters used in ADF and ZORA were used. The calculations employed the ZORA-def2-TZVPP basis sets from the internal ORCA library (old-ZORA-TZVPP for Pd and SARC-ZORA-TZVPP for Pt), the RIJCOSX approximation with the “AutoAux” function for the fitting basis sets and the “VeryTightSCF” convergence criteria, as well as a Grid5 grid and a GridX6 COSX-grid. In the TD-DFT part, 50 roots were converged. The oscillator strengths given in the main text were obtained via the transition electric dipole moment route.

By comparing NPA charges it was made certain that the wavefunctions in both programs were comparable.

9.2 Computational Results

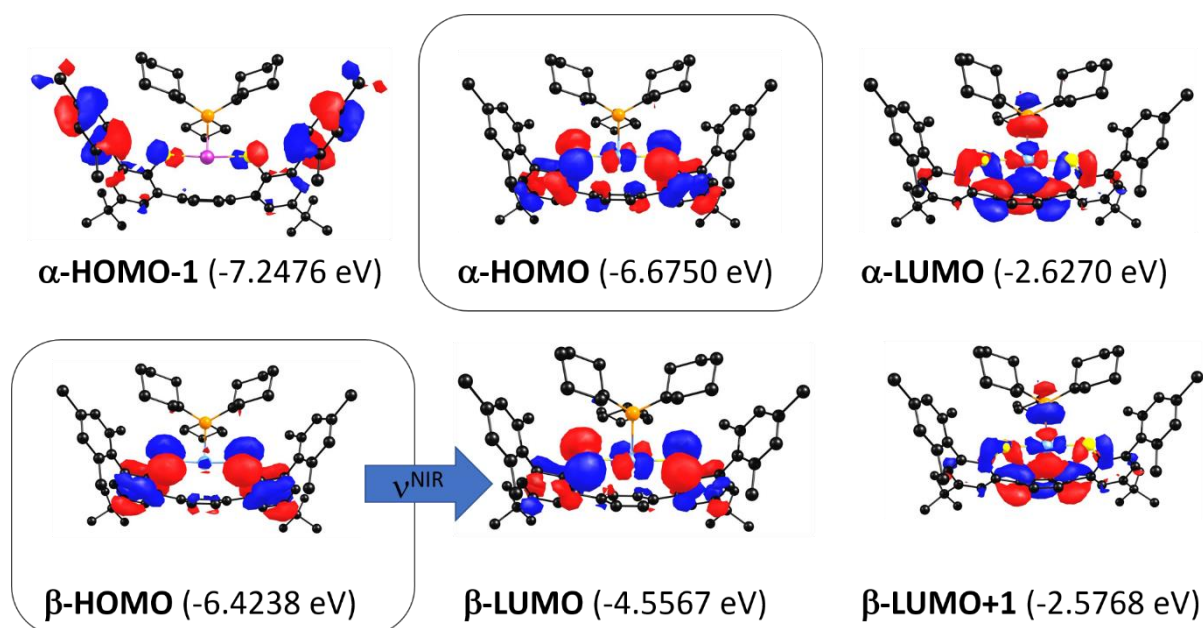
Table S5. Comparison of calculated EPR parameters and TD-DFT data.

	PBE0-1/3		
	[^{Mes} Ni-Cy] ⁺	[^{Mes} Pd-Cy] ⁺	[^{Mes} Pt-Cy] ⁺
g_{iso}	2.109	2.038	2.099
Δg	0.028	0.034	0.087
$A_{\text{iso}}/\text{MHz}$	3	15	183
$\lambda^{\text{NIR}}/\text{nm}$	1790	1800	1260
$\nu^{\text{NIR}}/\text{cm}^{-1}$	5590	5560	7940
$f_{\text{osc.}}$	0.125	0.103	0.238



Contour value of isosurfaces (neg. = blue, pos. = red) = 0.0333.

Figure S33. Kohn-Sham MOs and energies for $[\text{MesPd-Cy}]^+$ from a spin-unrestricted BPE0-1/3-D3(BJ)/ZORA DFT calculation. TD-DFT derived lowest-energy transition ($\beta\text{HOMO} \rightarrow \beta\text{LUMO}$): $\lambda^{\text{NIR}}(\text{computed}) = 1800 \text{ nm}$ (5560 cm^{-1}).



Contour value of isosurfaces (neg. = blue, pos. = red) = 0.0333.

Figure S34. Kohn-Sham MOs and energies for $[\text{MesPt-Cy}]^+$ from a spin-unrestricted BPE0-1/3-D3(BJ)/ZORA DFT calculation. TD-DFT derived lowest-energy transition ($\beta\text{HOMO} \rightarrow \beta\text{LUMO}$): $\lambda^{\text{NIR}}(\text{computed}) = 1260 \text{ nm}$ (7940 cm^{-1}).

9.3 Cartesian Coordinates of DFT-Optimized Radical-Ligand Complex Ion Structures

[^{Mes}Ni-Cy]⁺ (PBE0-D3(BJ)/ZORA/COSMO(CH₂Cl₂)):

Ni	-0.872678	5.488060	4.928744	H	3.077370	-1.248604	2.608630
S	-0.865731	7.599006	5.461450	H	2.153057	0.922277	-0.316818
S	-1.101594	3.323494	5.121298	H	2.991721	-0.626890	-0.401102
P	-3.109864	5.615703	4.662407	H	3.442788	0.542821	0.839570
C	0.221672	8.699791	4.625178	H	2.101544	2.196837	1.548770
C	1.193012	8.305852	3.686633	H	-0.284139	-0.983150	3.136188
C	1.929206	9.253087	2.983644	H	0.843347	-0.070424	6.192016
C	1.761438	10.611794	3.206743	H	0.156718	-0.114405	7.824114
C	0.801863	10.987766	4.150433	H	0.204935	1.399589	6.913621
C	0.022337	10.078233	4.845719	H	-5.410998	-1.909413	6.859681
C	1.373887	6.877780	3.464518	H	-4.975183	-0.778991	8.142995
C	1.446789	6.047977	4.606154	H	-4.154758	-2.331157	8.034761
H	1.673985	6.486175	5.569572	H	1.133219	4.477135	1.089054
C	1.355259	4.680345	4.470605	H	1.316022	6.928590	1.329291
H	1.513928	4.038242	5.327066	H	2.665645	8.897639	2.274185
C	1.174448	4.103853	3.192382	H	0.627083	12.040084	4.346436
C	1.251996	4.911994	2.074766	H	3.050365	10.484497	0.715084
C	1.355238	6.298728	2.210551	H	4.285012	10.437107	1.986997
C	0.788085	2.700333	3.142283	H	4.098622	11.876788	0.984892
C	-0.197267	2.266174	4.048086	H	3.903289	13.297200	2.978180
C	-0.574524	0.907053	4.034803	H	4.034483	11.898327	4.056334
C	0.026389	0.055884	3.123042	H	2.665367	13.007561	4.204832
C	0.982578	0.478571	2.194907	H	1.022349	12.002525	0.966082
C	1.346167	1.816609	2.224589	H	2.148263	13.354825	1.166826
C	-1.034452	10.618713	5.743316	H	0.880839	13.076134	2.364498
C	-2.202714	11.138075	5.170355	H	-4.811265	-0.782164	4.837022
C	-3.143857	11.748008	5.993252	H	-2.027408	-0.849000	8.076121
C	-2.959232	11.845818	7.367474	H	-2.819959	1.334892	2.687680
C	-1.794036	11.316974	7.913572	H	-4.318452	0.401943	2.858427
C	-0.825448	10.705408	7.125227	H	-2.834850	-0.374641	2.305793
C	-1.618350	0.344212	4.934193	H	-4.637620	13.152059	7.687577
C	-1.306092	0.019817	6.262479	H	-3.567589	12.982460	9.089889
C	-2.271859	-0.596117	7.048394	H	-4.664313	11.676669	8.652195
C	-3.539351	-0.895315	6.556182	H	-1.630649	11.385491	8.985234
C	-3.825817	-0.563691	5.238336	H	-4.050698	12.147585	5.548598
C	-2.885033	0.050830	4.415931	H	-2.272018	10.028064	3.327578
C	2.559679	11.678954	2.472078	H	-1.770304	11.694582	3.132363
C	1.576137	-0.520617	1.212696	H	-3.468538	11.330065	3.448298
C	-2.445823	11.043408	3.692392	H	1.316708	10.565301	7.266177
C	-4.011267	12.454373	8.244527	H	0.469304	9.072987	7.644648
C	0.424421	10.160411	7.748839	H	0.465795	10.402133	8.810494
C	0.048536	0.320574	6.830921	H	-1.754345	4.166015	2.390458
C	-4.576419	-1.517625	7.441589	H	-3.355822	3.473651	2.590375
C	-3.236866	0.374527	2.993471	H	-2.653018	3.454178	0.216399
C	1.589897	12.580810	1.698789	H	-4.088159	4.442157	0.445179
C	3.334195	12.519765	3.493568	H	-2.486532	5.622863	-1.020494
C	3.553283	11.074226	1.484984	H	-1.224595	5.468004	0.192062
C	2.599126	0.126582	0.284315	H	-3.818120	7.048692	0.493700
C	2.266284	-1.645046	1.993608	H	-2.208979	7.728811	0.304397
C	0.445572	-1.109297	0.360084	H	-2.917636	7.758481	2.677932
C	-3.921393	7.168668	5.236817	H	-1.493278	6.760476	2.449484
C	-5.239820	7.537527	4.552947	H	-4.355467	5.729115	2.650585
C	-5.647089	8.941829	4.990055	H	-4.385142	4.652000	7.372591
C	-5.751385	9.064898	6.503564	H	-2.795148	3.977963	7.070816
C	-4.466671	8.624346	7.189333	H	-3.780138	1.771743	6.611082
C	-4.067069	7.223467	6.756927	H	-4.262552	2.332326	8.203134
C	-4.042848	4.163069	5.295264	H	-6.184372	1.352706	6.923281
C	-3.848160	3.901366	6.791249	H	-6.458347	3.034181	7.356113
C	-4.382445	2.519500	7.132738	H	-5.558015	1.989758	4.636327
C	-5.844076	2.373980	6.732159	H	-7.129884	2.679190	5.020604
C	-6.066205	2.727243	5.267729	H	-6.076752	4.864749	5.508420
C	-5.526841	4.114785	4.933235	H	-5.688047	4.333322	3.874994
C	-3.278766	5.622541	2.830168	H	-6.024655	6.827137	4.821963
C	-2.815187	4.325534	2.173506	H	-5.142152	7.512701	3.466130
C	-3.016171	4.382505	0.665101	H	-3.138172	6.924585	7.249966
C	-2.306432	5.582515	0.056383	H	-4.842196	6.519749	7.070096
C	-2.758351	6.877536	0.714648	H	-6.583069	8.444846	6.859054
C	-2.563231	6.830329	2.223562	H	-5.987951	10.096971	6.776447
H	-0.063811	-0.324694	-0.204111	H	-3.657810	9.314880	6.938877
H	-0.296781	-1.623462	0.973086	H	-4.585689	8.653634	8.275763
H	0.854805	-1.832133	-0.349782	H	-6.597119	9.206158	4.518438
H	2.688285	-2.374525	1.298161	H	-4.900425	9.653747	4.622651
H	1.568251	-2.169204	2.648664	H	-3.196472	7.941112	4.960980
				H	-3.558152	3.332946	4.770755

[^{Mes}Pd-Cy]⁺ (PBE0-1/3-D3(BJ)/ZORA/COSMO(CH₂Cl₂)):

Pd	-0.925185	5.459680	5.029822	H	0.259599	-0.274943	-0.215226
S	-0.845691	7.747833	5.477353	H	-0.047476	-1.606046	0.901034
S	-1.138584	3.157731	5.215114	H	1.192277	-1.771559	-0.341678
P	-3.210800	5.571817	4.712468	H	2.907210	-2.354027	1.405580
C	0.231849	8.748444	4.580713	H	1.697815	-2.196196	2.678879
C	1.219891	8.282112	3.682453	H	3.196631	-1.270485	2.771923
C	1.957812	9.183700	2.935569	H	2.459365	0.984050	-0.132927
C	1.784559	10.554005	3.065675	H	3.316172	-0.551913	-0.205518
C	0.818878	11.001961	3.974145	H	3.665274	0.580553	1.096932
C	0.042680	10.147216	4.720315	H	2.248258	2.204528	1.744569
C	1.413241	6.843953	3.528433	H	-0.192069	-1.033631	3.080877
C	1.545210	6.037873	4.676840	H	0.693360	-0.450989	6.188678
H	1.776655	6.494443	5.629361	H	-0.087007	-1.088241	7.773629
C	1.451935	4.663736	4.570558	H	0.146639	1.083140	6.840192
H	1.600246	4.040239	5.440559	H	-5.699262	-1.787103	6.421616
C	1.212810	4.065470	3.318206	H	-5.130940	-0.945255	7.862370
C	1.240091	4.855119	2.186238	H	-4.512696	-2.544554	7.487710
C	1.344384	6.239150	2.289718	H	1.081574	4.402197	1.216983
C	0.837760	2.651242	3.263933	H	1.263642	6.850094	1.400758
C	-0.190556	2.185698	4.092298	H	2.704686	8.789661	2.262622
C	-0.551438	0.829159	4.004943	H	0.650523	12.063572	4.095168
C	0.114396	0.004012	3.117832	H	3.094711	10.258576	0.605796
C	1.125193	0.456565	2.273459	H	4.315920	10.296015	1.886559
C	1.463791	1.794930	2.364677	H	4.137878	11.663008	0.792747
C	-1.007110	10.726393	5.598684	H	3.928433	13.202989	2.684367
C	-2.208302	11.151730	5.028069	H	4.042765	11.884105	3.854803
C	-3.153977	11.769061	5.837040	H	2.678969	13.003580	3.911051
C	-2.937350	11.966079	7.191748	H	1.067105	11.788225	0.738436
C	-1.735112	11.531048	7.735429	H	2.192177	13.145162	0.861233
C	-0.763775	10.913874	6.962681	H	0.915476	12.949731	2.059588
C	-1.658519	0.245562	4.808930	H	-4.888112	-0.699042	4.486783
C	-1.434188	-0.172673	6.124994	H	-2.292492	-1.097486	7.844310
C	-2.467676	-0.776985	6.823687	H	-2.712140	1.455112	2.602079
C	-3.718967	-0.977387	6.253135	H	-4.227997	0.539396	2.599830
C	-3.917462	-0.557221	4.947904	H	-2.720554	-0.217164	2.091412
C	-2.906157	0.052193	4.214294	H	-4.771196	13.047617	7.460855
C	2.590134	11.563889	2.271967	H	-3.552165	13.363654	8.700209
C	1.791978	-0.506336	1.304443	H	-4.440011	11.849581	8.709918
C	-2.481954	10.956066	3.568155	H	-1.547505	11.676039	8.792984
C	-3.982413	12.595849	8.058355	H	-4.087792	12.096769	5.395645
C	0.519184	10.455944	7.583338	H	-2.247680	9.939116	3.252869
C	-0.097456	0.022419	6.770818	H	-1.870769	11.620890	2.956770
C	-4.827000	-1.600013	7.044271	H	-3.526023	11.156647	3.339603
C	-3.160353	0.483723	2.802690	H	1.382391	10.841402	7.041128
C	1.627217	12.411144	1.435795	H	0.591001	9.367217	7.569185
C	3.352438	12.466634	3.244843	H	0.586955	10.784035	8.617578
C	3.589935	10.896160	1.338180	H	-1.889295	4.205775	2.451488
C	2.869463	0.174989	0.471919	H	-3.501015	3.533609	2.585617
C	2.434344	-1.649974	2.091171	H	-2.729310	3.566573	0.237906
C	0.731886	-1.073049	0.357945	H	-4.162796	4.553447	0.452584
C	-3.925059	7.119454	5.383119	H	-2.517915	5.758086	-0.937406
C	-5.315733	7.495085	4.878950	H	-1.297452	5.576127	0.309236
C	-5.636405	8.914346	5.326330	H	-3.901151	7.135181	0.574082
C	-5.531001	9.071945	6.833668	H	-2.297003	7.830077	0.436051
C	-4.176764	8.618563	7.351771	H	-3.058391	7.801543	2.785261
C	-3.863955	7.202473	6.904951	H	-1.619622	6.819880	2.565989
C	-4.140342	4.100935	5.269490	H	-4.474621	5.784171	2.719096
C	-4.023185	3.824703	6.765708	H	-4.615935	4.550026	7.322648
C	-4.535593	2.425640	7.055898	H	-2.990947	3.927537	7.101570
C	-5.966426	2.251102	6.574494	H	-3.886674	1.704923	6.556196
C	-6.116920	2.619225	5.107712	H	-4.470090	2.223537	8.125950
C	-5.595781	4.020495	4.820015	H	-6.290145	1.221475	6.732296
C	-3.400304	5.667530	2.891727	H	-6.628415	2.885749	7.171556
C	-2.939129	4.386050	2.206535	H	-5.557332	1.904647	4.498462
C	-3.099667	4.483032	0.699151	H	-7.161828	2.548486	4.802848
C	-2.372295	5.692805	0.141046	H	-6.197905	4.749682	5.363491
C	-2.847544	6.967712	0.814277	H	-5.698516	4.243277	3.757964
C	-2.683633	6.888414	2.322312	H	-6.059058	6.808143	5.284165
				H	-5.374406	7.429754	3.792942
				H	-2.886105	6.891737	7.276207
				H	-4.597378	6.519446	7.333285
				H	-6.317167	8.479932	7.311661
				H	-5.707403	10.112136	7.110230

H	-3.397588	9.285962	6.980232	H	-4.936307	9.601073	4.843434
H	-4.149528	8.675063	8.440725	H	-3.239574	7.881918	4.998590
H	-6.635220	9.186635	4.983337	H	-3.596278	3.296709	4.767574

[^{Me}Pt-Cy]⁺ (PBE0-1/3-D3(BJ)/ZORA/COSMO(CH₂Cl₂)):

Pt	-0.946939	5.466381	4.962385	H	2.976525	-2.377690	1.493270
S	-0.899517	7.722908	5.424451	H	1.755801	-2.202834	2.752856
S	-1.174259	3.174669	5.083034	H	3.248166	-1.265279	2.839569
P	-3.235704	5.612299	4.719909	H	2.522630	0.924215	-0.118861
C	0.252848	8.724735	4.572133	H	3.384734	-0.609695	-0.156004
C	1.253598	8.270334	3.699277	H	3.723390	0.548389	1.125614
C	2.025908	9.177159	2.984728	H	2.312105	2.171250	1.747671
C	1.863328	10.543815	3.128670	H	-0.144876	-1.050047	3.104918
C	0.877852	10.978845	4.016315	H	0.726064	-0.385467	6.186280
C	0.071113	10.113855	4.726131	H	-0.057210	-0.378269	7.770296
C	1.433875	6.834144	3.534955	H	0.145589	1.123374	6.866551
C	1.446835	6.025019	4.696031	H	-5.694800	-1.705975	6.445287
H	1.640933	6.477320	5.658030	H	-5.051784	-8.768469	7.911158
C	1.356932	4.652060	4.581563	H	-4.503890	-2.560565	7.428719
H	1.481926	4.026887	5.453921	H	1.320828	4.391712	1.203556
C	1.247393	4.052352	3.304008	H	1.487451	6.837876	1.407078
C	1.387031	4.840394	2.185397	H	2.785736	8.782117	2.326294
C	1.481426	6.228902	2.300838	H	0.711437	12.039150	4.155033
C	0.877562	2.645061	3.235525	H	3.233480	10.274103	0.700535
C	-0.164893	2.185075	4.055464	H	4.421325	10.284325	2.012155
C	-0.520665	0.822016	3.997699	H	4.284201	11.666982	0.931489
C	0.154237	-0.010312	3.129661	H	4.037645	13.187606	2.837527
C	1.172953	0.436571	2.285974	H	4.113347	11.849482	3.989743
C	1.514093	1.775633	2.358807	H	2.756160	12.976498	4.029405
C	-0.994727	10.692701	5.586945	H	1.221079	11.819246	0.797893
C	-2.188649	11.115815	5.000362	H	2.348384	13.169420	0.971502
C	-3.143819	11.740285	5.793119	H	1.038487	12.959932	2.131960
C	-2.944148	11.945654	7.149188	H	-4.862828	-0.685299	4.489140
C	-1.751383	11.507823	7.711454	H	-2.268809	-1.063230	7.850526
C	-0.772165	10.883818	6.953970	H	-2.693433	1.456691	2.589011
C	-1.632057	0.251958	4.805085	H	-4.201507	0.531132	2.592337
C	-1.408314	-0.152559	6.125499	H	-2.689851	-0.219736	2.089434
C	-2.442329	-0.751993	6.826888	H	-4.788731	13.016090	7.388768
C	-3.692885	-0.956783	6.256069	H	-3.576743	13.371804	8.623748
C	-3.891885	-0.542762	4.949023	H	-4.450505	11.850243	8.666370
C	-2.879874	0.059696	4.210690	H	-1.578930	11.654668	8.771409
C	2.696830	11.561840	2.369970	H	-4.071529	12.066913	5.337969
C	1.852363	-0.540930	1.342986	H	-2.196183	9.888524	3.238923
C	-2.442839	10.906896	3.539052	H	-1.826747	11.569954	2.930527
C	-3.997741	12.585060	7.998679	H	-3.485350	11.098738	3.295221
C	0.501612	10.423913	7.592282	H	1.370188	10.862612	7.101136
C	-0.076144	0.059094	6.775105	H	0.604233	9.340568	7.516246
C	-4.798092	-1.582309	7.048599	H	0.527205	10.695087	8.644818
C	-3.133921	0.482721	2.796351	H	-1.980521	4.273432	2.377958
C	1.765562	12.428574	1.519470	H	-3.564248	3.554926	2.607118
C	3.442632	12.445964	3.371092	H	-2.940996	3.607871	0.218502
C	3.715288	10.898498	1.453117	H	-4.377224	4.567667	0.520587
C	2.932042	0.128887	0.504287	H	-2.839844	5.804044	-0.962354
C	2.493800	-1.663457	2.160808	H	-1.544176	5.643560	0.209738
C	0.800232	-1.132219	0.402024	H	-4.155931	7.154517	0.629830
C	-3.961697	7.142839	5.408160	H	-2.574981	7.878319	0.401108
C	-5.358054	7.507659	4.911061	H	-3.194865	7.833429	2.791545
C	-5.686995	8.921788	5.368478	H	-1.758584	6.874732	2.489980
C	-5.576377	9.071739	6.876300	H	-4.583411	5.788807	2.782885
C	-4.217097	8.624309	7.386343	H	-4.499122	4.559521	7.391307
C	-3.897454	7.212705	6.930483	H	-2.885641	3.947604	7.090870
C	-4.121534	4.129427	5.315062	H	-3.797540	1.721952	6.570328
C	-3.931360	3.840569	6.801663	H	-4.305102	2.227725	8.169420
C	-4.423722	2.437272	7.105521	H	-6.186232	1.226719	6.858871
C	-5.875113	2.258710	6.692256	H	-6.510511	2.886549	7.324230
C	-6.096446	2.635636	5.236948	H	-5.562730	1.928239	4.596398
C	-5.596853	4.041695	4.936480	H	-7.154028	2.561353	4.980971
C	-3.500683	5.693974	2.908141	H	-6.174265	4.762589	5.516627
C	-3.047987	4.422880	2.198062	H	-5.753205	4.273825	3.883146
C	-3.300058	4.516869	0.702873	H	-6.096481	6.813250	5.312394
C	-2.629235	5.740682	0.105515	H	-5.420186	7.451841	3.824917
C	-3.087258	7.005862	0.808633	H	-2.916109	6.906996	7.295558
C	-2.834637	6.927310	2.304366	H	-4.627674	6.523674	7.355638
H	0.326662	-0.349005	-0.190165	H	-6.356746	8.471908	7.354251
H	0.021406	-1.661262	0.949481	H	-5.758710	10.109257	7.159085
H	1.271228	-1.840258	-0.280364	H	-3.443422	9.297553	7.014375

H	-4.185712	8.675606	8.475516
H	-6.689209	9.189269	5.031515
H	-4.993213	9.615908	4.887083
H	-3.284011	7.913182	5.029940
H	-3.608701	3.327926	4.77574

10 References

- [1] D. Herebian, E. Bothe, F. Neese, T. Weyhermüller, K. Wieghardt, *J. Am. Chem. Soc.* **2003**, *125*, 9116-9128.
- [2] D. Herebian, E. Bothe, E. Bill, T. Weyhermüller, K. Wieghardt, *J. Am. Chem. Soc.* **2001**, *123*, 10012-10023.
- [3] K. Ray, T. Weyhermüller, F. Neese, K. Wieghardt, *Inorg. Chem.* **2005**, *44*, 5345-5360.
- [4] K. M. Conner, A. L. Perugini, M. Malabute, S. N. Brown, *Inorg. Chem.* **2018**, *57*, 3272-3286.
- [5] (a) P. Chaudhuri, C. N. Verani, E. Bill, E. Bothe, T. Weyhermüller, K. Wieghardt, *J. Am. Chem. Soc.* **2001**, *123*, 2213-2223; (b) X. Sun, H. Chun, K. Hildenbrand, E. Bothe, T. Weyhermüller, F. Neese, K. Wieghardt, *Inorg. Chem.* **2002**, *41*, 4295-4303; (c) S. Kokatam, T. Weyhermüller, E. Bothe, P. Chaudhuri, K. Wieghardt, *Inorg. Chem.* **2005**, *44*, 3709-3717.
- [6] N. Leconte, J. Moutet, T. Constantin, F. Molton, C. Philouze, F. Thomas, *Eur. J. Inorg. Chem.* **2018**, *2018*, 1752-1761.
- [7] R. Kunert, C. Philouze, O. Jarjayes, F. Thomas, *Inorg. Chem.* **2019**, *58*, 8030-8044.
- [8] (a) Y. Shimazaki, T. D. Stack, T. Storr, *Inorg. Chem.* **2009**, *48*, 8383-8392; (b) Y. Shimazaki, T. Yajima, F. Tani, S. Karasawa, K. Fukui, Y. Naruta, O. Yamauchi, *J. Am. Chem. Soc.* **2007**, *129*, 2559-2568.
- [9] Y. Shimazaki, N. Arai, T. J. Dunn, T. Yajima, F. Tani, C. F. Ramogida, T. Storr, *Dalton Trans.* **2011**, *40*, 2469-2479.
- [10] F. Koch, H. Schubert, P. Sirsch, A. Berkefeld, *Dalton Trans.* **2015**, *44*, 13315-13324.
- [11] G. B. Kauffman, D. O. Cowan, G. Slusarczuk, S. Kirschner, in *Inorg. Synth.*, Vol. 7 (Ed.: J. Kleinberg), John Wiley & Sons, Inc., Hoboken, NJ, USA, **1963**, pp. 239-245.
- [12] H. D. K. Drew, F. W. Pinkard, G. H. Preston, W. Wardlaw, *J. Chem. Soc.* **1932**, 1895-1909.
- [13] N. M. Mews, A. Berkefeld, G. Hörner, H. Schubert, *J. Am. Chem. Soc.* **2017**, *139*, 2808-2815.
- [14] S. V. Rosokha, C. L. Stern, J. T. Ritzert, *CrystEngComm* **2013**, *15*.
- [15] M. Schlosser, J. Hartmann, *Angew. Chem. Int. Ed. Engl.* **1973**, *12*, 508-509.
- [16] F. Koch, A. Berkefeld, H. Schubert, C. Grauer, *Chem. Eur. J.* **2016**, *22*, 14640-14647.
- [17] S. Stoll, A. Schweiger, *J Magn Reson* **2006**, *178*, 42-55.
- [18] (a) F. Murrieta-Guevara, A. Trejo Rodriguez, *Journal of Chemical & Engineering Data* **1984**, *29*, 204-206; (b) J. G. Speight, in *Lange's Handbook of Chemistry*, 16. ed. (Ed.: J. G. Speight), McGraw-Hill Education, New York, Chicago, San Francisco, Lisbon, London, Madrid, Mexico City, Milan, New Delhi, San Juan, Seoul, Singapore, Sydney, Toronto, **2005**, pp. 2.470-494.
- [19] D. F. Evans, *J. Chem. Soc.* **1959**.
- [20] G. A. Bain, J. F. Berry, *J. Chem. Educ.* **2008**, *85*.
- [21] L. J. Farrugia, *J. Appl. Cryst.* **1999**, *32*, 837-838.
- [22] (a) G. M. Sheldrick, *Acta Crystallographica Section A: Foundations and Advances* **2008**, *64*, 112-122; (b) C. B. Hubschle, G. M. Sheldrick, B. Dittrich, *J Appl Crystallogr* **2011**, *44*, 1281-1284.
- [23] A. L. Spek, *Acta Crystallographica Section D Biological Crystallography* **2009**, *65*, 148-155.
- [24] L. J. Farrugia, *J. Appl. Cryst.* **2012**, *45*, 849-854.
- [25] J. Janisch, A. Ruff, B. Speiser, C. Wolff, J. Zigelli, S. Benthin, V. Feldmann, H. A. Mayer, *J. Solid State Electrochem.* **2011**, *15*, 2083-2094.
- [26] (a) G. te Velde, F. M. Bickelhaupt, E. J. Baerends, C. Fonseca Guerra, S. J. A. van Gisbergen, J. G. Snijders, T. Ziegler, *J. Comput. Chem.* **2001**, *22*, 931-967; (b) C. Fonseca Guerra, J. G. Snijders, G. te Velde, E. J. Baerends, *Theor. Chem. Acc.* **1998**, *99*, 391-403.
- [27] F. Neese, *WIREs Comput. Mol. Sci.* **2012**, *2*, 73-78.